

**Exploring Electron Beam Induced Surface  
Activation for the Fabrication of well-defined  
Nanostructures: On the Role of Catalytic  
Processes, Substrates and Precursors.**

**Untersuchungen zur elektronenstrahlinduzierten  
Oberflächenaktivierung als Werkzeug für die Herstellung  
wohldefinierter Nanostrukturen: Die Rolle von katalytischen  
Prozessen, Substraten und Präkursoren.**

Der Naturwissenschaftlichen Fakultät der  
Friedrich-Alexander-Universität Erlangen-Nürnberg

zur Erlangung des Doktorgrades Dr. rer. nat.

vorgelegt von

**Florian Rudolf Vollnhals**

aus Ingolstadt

Als Dissertation genehmigt  
von der Naturwissenschaftlichen Fakultät  
der Friedrich-Alexander-Universität Erlangen-Nürnberg

Tag der mündlichen Prüfung: 12.12.2014

Vorsitzender des Promotionsorgans: Prof. Dr. Jörn Wilms

Gutachter: PD Dr. Hubertus Marbach

Prof. Dr. Rainer Fink

*Un bon mot ne prouve rien.*

Voltaire



---

<b>1</b>	<b>Introduction</b>	<b>1</b>
<b>2</b>	<b>Literature Review</b>	<b>5</b>
2.1	Electron Beam Induced Deposition – EBID	6
2.2	Electron Beam Induced Surface Activation – EBISA	9
2.3	Autocatalysis and Precursor Chemistry	13
2.4	Proximity Effects	14
<b>3</b>	<b>Methods &amp; Techniques</b>	<b>17</b>
3.1	Scanning Electron Microscopy	17
3.2	Auger Electron Spectroscopy	20
3.3	Scanning Tunneling Microscopy	22
3.4	Scanning Transmission X-ray Microscopy (STXM)	25
3.5	Other Techniques	26
3.6	Electron Trajectory Simulation	27
<b>4</b>	<b>Experimental Section</b>	<b>29</b>
4.1	MULTISCAN Lab UHV SEM/STM	29
4.1.1	System Layout	29
4.1.2	Preparation Chamber	30
4.1.3	Analysis Chamber	31
4.1.4	Sample Holders	35
4.2	PolLux STXM	38
4.3	Samples and Sample Preparation	39
4.3.1	Rutile TiO <sub>2</sub> (110)	39
4.3.2	Ag(111)	40
4.3.3	Silicon and Silicon oxides	40
4.3.4	Silicon Nitride Membranes	41
4.3.5	STM Tips	41
4.4	Precursors	43
4.4.1	Iron pentacarbonyl - Fe(CO) <sub>5</sub>	43
4.4.2	Cobalt tricarbonyl nitrosyl - Co(CO) <sub>3</sub> NO	44
4.4.3	Dicobalt octacarbonyl - Co <sub>2</sub> (CO) <sub>8</sub>	44
4.5	Electron trajectory simulation	46
4.6	Software and Data Processing	47
<b>5</b>	<b>Lithography</b>	<b>49</b>
5.1	General Considerations and Terminology	50

5.2	Technical aspects.....	50
5.3	Available Lithographic Systems .....	54
5.3.1	SEM Software .....	54
5.3.2	Elphy Quantum .....	55
5.3.3	Arbitrary Waveform Generators .....	57
5.4	NanoScribbler - a custom lithographic attachment.....	60
5.4.1	NanoScribbler Hard- and Software.....	60
5.4.2	Graphical User Interface Layout.....	62
5.4.3	Data Structure .....	63
5.4.4	Timing algorithm .....	64
5.4.5	Pattern Generation.....	68
5.4.6	Exposure Procedure.....	71
5.4.7	System Tests and Evaluation .....	73
5.4.8	Future perspectives.....	78
5.4.9	Summary and Conclusions .....	81
<b>6</b>	<b>Results and Discussion .....</b>	<b>83</b>
6.1	Introduction.....	83
6.2	EBID and EBISA on rutile TiO <sub>2</sub> (110).....	85
6.2.1	Introduction.....	85
6.2.2	Results and Discussion .....	86
6.2.3	Conclusions.....	95
6.3	EBID and EBISA on Ultrathin Porphyrin Layers on Ag(111).....	97
6.3.1	Introduction.....	97
6.3.2	Results and Discussion .....	98
6.3.3	Conclusions.....	110
6.4	EBID and Autocatalytic Growth using Co(CO) <sub>3</sub> NO .....	111
6.4.1	Introduction.....	111
6.4.2	Results and Discussion .....	114
6.4.3	Conclusions.....	126
6.5	EBID using Co <sub>2</sub> (CO) <sub>8</sub> .....	128
6.5.1	Introduction.....	128
6.5.2	Results and Discussion .....	129
6.5.3	Conclusions.....	133
<b>7</b>	<b>Summary.....</b>	<b>137</b>

<b>8</b>	<b>Zusammenfassung .....</b>	<b>141</b>
<b>9</b>	<b>Bibliography .....</b>	<b>147</b>
	<b>Appendix A – Communication Protocols.....</b>	<b>163</b>
	<b>Appendix B – List of Figures .....</b>	<b>168</b>
	<b>Danksagung .....</b>	<b>175</b>

## List of Abbreviations

<b>ADC</b>	Analog-to-Digital Converter	<b>LEED</b>	Low-Energy Electron Diffraction
<b>AE</b>	Auger Electron	<b>LN2</b>	Liquid Nitrogen
<b>AES</b>	Auger Electron Spectroscopy	<b>MC</b>	Monte Carlo
<b>AFM</b>	Atomic Force Microscopy	<b>MFM</b>	Magnetic Force Microscopy
<b>ALD</b>	Atomic Layer Deposition	<b>MOCVD</b>	Metal-Organic Chemical Vapor Deposition
<b>AWG</b>	Arbitrary Waveform Generator	<b>NEXAFS</b>	Near Edge X-ray Absorption Fine Structure
<b>BE</b>	Binding Energy	<b>OSF</b>	Oversampling Factor
<b>BSE</b>	Backscattered Electron	<b>PBN</b>	Pyrolytic Boron Nitride
<b>CCM</b>	Constant Current Mode	<b>PE</b>	Primary Electron
<b>CHM</b>	Constant Height Mode	<b>PMT</b>	Photomultiplier Tube
<b>CL</b>	Cathodoluminescence	<b>PVD</b>	Physical Vapor Deposition
<b>CRR</b>	Constant Retarding Ratio	<b>QMS</b>	Quadrupole Mass Spectrometry
<b>CVD</b>	Chemical Vapor Deposition	<b>RT</b>	Room Temperature
<b>DAC</b>	Digital-to-Analog Converter	<b>SAM</b>	Scanning Auger Microscopy
<b>DC</b>	Direct current	<b>SE</b>	Secondary Electron
<b>DD</b>	Dipolar Dissociation	<b>SEM</b>	Scanning Electron Microscopy
<b>DEA</b>	Dissociative Electron Attachment	<b>SFF</b>	Sampling Frequency Factor
<b>DFT</b>	Density Functional Theory	<b>SLS</b>	Swiss Light Source
<b>DI</b>	Direct Ionization	<b>STM</b>	Scanning Tunneling Microscopy
<b>EBID</b>	Electron Beam Induced Deposition	<b>STXM</b>	Scanning Transmission X-Ray Microscopy
<b>EBIE</b>	Electron Beam Induced Etching	<b>TE</b>	Transmitted Electron
<b>EBISA</b>	Electron Beam Induced Surface Activation	<b>TEM</b>	Transmission Electron Microscopy
<b>EBL</b>	Electron Beam Lithography	<b>TPP</b>	Tetraphenyl Porphyrin
<b>EDX</b>	Energy Dispersive X-ray Spectroscopy	<b>TTIP</b>	Titanium(IV) tetraisopropoxide
<b>ESD</b>	Electron Stimulated Desorption	<b>TTL</b>	Transistor-transistor-logic
<b>EUV</b>	Extreme Ultraviolet	<b>UHV</b>	Ultra High Vacuum
<b>FEBIP</b>	Focused Electron Beam Induced Processing	<b>UV</b>	Ultraviolet
<b>FFT</b>	Fast Fourier Transformation	<b>VI</b>	Virtual Instrument
<b>FIB</b>	Focused Ion Beam	<b>VUV</b>	Vacuum Ultraviolet
<b>FOV</b>	Field of View	<b>WDX</b>	Wavelength Dispersive X-Ray Spectroscopy
<b>FSE</b>	Forward Scattered Electron	<b>XAS</b>	X-ray absorption spectroscopy
<b>FWHM</b>	Full Width at Half Maximum	<b>XMCD</b>	X-Ray Magnetic Circular Dichroism
<b>GIS</b>	Gas Injection System	<b>XPS</b>	X-Ray Photoemission Spectroscopy
<b>GUI</b>	Graphical User Interface		
<b>HV</b>	High Vacuum		
<b>IMFP</b>	Inelastic Mean Free Path		
<b>ITRS</b>	International Technology Roadmap for Semiconductors		





## 1 Introduction

The technological advancement of human life has sped up considerably. Today, it is possible to buy electronic devices that have been regarded as science fiction only a few decades ago. Prominent examples are smartphones and tablet computers, which were wondrous items in classic Sci-Fi, e.g. the “tricorder” used in the Star Trek universe.

In order to achieve this kind of technological advancement, it is necessary to improve and advance on the existing as well as research new technologies, which may offer beneficial properties or even revolutionize the state of the art. This process of improving and superseding technologies is quite apparent in the field of semiconductor manufacturing, which is the basis of the modern, computerized world. In order to steadily improve the computational power, speed or memory capacity of integrated circuits, the number of individual components, e.g. transistors, on a chip is rising continuously. The trend was first noted by Moore in 1965,<sup>1</sup> in what is now known as Moore’s law: the complexity of integrated circuits doubles approximately every two years. This demand of increasing numbers can only be met if the size of the individual components shrinks considerably, which has been and still is fueling research and development.

A major aspect of the ongoing shrinking process is the improvement of the lithographic processes that define the shape of the individual components. The International Technology Roadmap for Semiconductors, ITRS,<sup>2</sup> serves as a reference for the required developments and improvements and shows that in order to honor Moore’s law, new lithography techniques have to be implemented. Currently (2014), a major technology change from 193 nm vacuum ultraviolet (VUV) to 13 nm extreme UV (EUV) radiation is approaching, which should provide the required capabilities to fabricate ever smaller structures. In addition to the improvement of the currently used processes, there is an area of research deemed Beyond

Moore's Law,<sup>3</sup> dealing with alternative approaches to chip fabrication and applications of integrated circuits.

In both cases, and in many more fields, the application of structures with at least one dimension below 100 nm is a central aspect. It is therefore necessary to study the fabrication processes, and especially the underlying principles, in great detail.

As a part of this effort, the thesis at hand will provide new insights into a field of lithographic nanofabrication subsumed under the term Focused Electron Beam Induced Processing (FEBIP).<sup>4</sup> As the name suggests, in FEBIP a focused electron beam is used to modify the properties of matter for the fabrication of well-defined, arbitrarily shaped nanostructures. The most well-known and probably also best investigated FEBIP technique is electron beam induced deposition (EBID).<sup>4</sup> In EBID, the focused electron beam of a scanning electron or transmission electron microscope (SEM/TEM) is used to locally decompose adsorbed precursor molecules on a substrate to build up a nanostructured deposit of the non-volatile dissociation products. Depending on the material system, it is also possible to etch material by electron beam induced bond formation between a solid material and a gaseous precursor and subsequent removal of the new, volatile compound in a process referred to as electron beam induced etching (EBIE).

Four years ago, the FEBIP family has seen the introduction of a novel process: electron beam induced surface activation (EBISA).<sup>5</sup> In EBISA, the electron beam is used to locally change the properties of the substrate such that the irradiated areas become chemically active towards the decomposition of certain precursor molecules, forming an initial deposit. Certain precursors have also been shown to exhibit autocatalytic decomposition at these initial deposits, which leads to the formation of a solid nanostructure with desirable properties, e.g. high purity. While the technique was studied extensively on silicon oxide surface using iron pentacarbonyl as a precursor, the general applicability of EBISA for different surfaces and precursor molecules has yet to be demonstrated. In the framework of the thesis at hand, the EBISA process is expanded to another oxide, namely  $\text{TiO}_2$ , and to organic films on  $\text{Ag}(111)$ . In addition, the EBISA and corresponding catalytic growth processes were also studied for other precursors ( $\text{Co}(\text{CO})_3\text{NO}$  and  $\text{Co}_2(\text{CO})_8$ ).

Furthermore, past experience has shown that fundamental research in any FEBIP technique requires precise control of the lithography involved in the experimental work. Therefore, one part of this thesis is dedicated to the development and testing of a custom lithographic solution that is tailored to the specific requirements and challenges of fundamental FEBIP research in ultrahigh vacuum (UHV).

This thesis is organized such that first the EBID and EBISA processes will be introduced in detail and an overview of the available literature will be given as a foundation for the discussion of the relevant aspects. This will be followed by an introduction to the relevant experimental techniques and a detailed description of the development of an electron beam lithography attachment. Once this background information is established, the experimental results will be presented.

First, it will be shown that EBISA is a viable technique also on non-SiO<sub>x</sub> surfaces by demonstrating successful fabrication of Fe nanostructures on TiO<sub>2</sub>(110) in combination with a detailed analysis of the effects of the focused electron beam on the TiO<sub>2</sub> surface using Auger electron spectroscopy (AES) and scanning tunneling microscopy (STM). Furthermore, the interaction of the electron beam with thin layers of organic molecules (Tetraphenylporphyrins) on metallic substrates and the resulting consequences for EBID and EBISA will be discussed. In addition, the fabrication of nanostructures using the precursors Co(CO)<sub>3</sub>NO and Co<sub>2</sub>(CO)<sub>8</sub> will be addressed.



## 2 Literature Review

Focused electron beam induced processing (FEBIP) is a powerful approach to the fabrication of nanostructures with lithographic control down to the nanometer regime. FEBIP subsumes a number of different techniques, which rely on the use of a highly focused electron beam of a scanning electron microscope (SEM) or scanning transmission electron microscope (TEM) to locally modify matter and material properties.<sup>4-11</sup> Two specific approaches are schematically depicted in Figure 2-1, both starting from a clean surface (a).

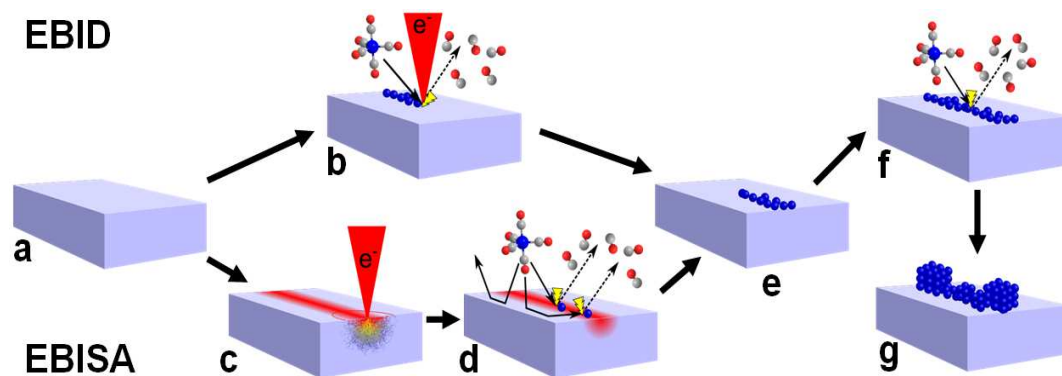


**Figure 2-1:** Electron beam induced deposition (EBID) and electron beam induced surface activation (EBISA) processes in comparison. Starting from a clean sample (a) in EBID the surface is irradiated while precursor is supplied (b), leading to the e-beam induced decomposition into volatile fragments and a nonvolatile primary deposit (e). The EBISA process involves an irradiation step under vacuum conditions (c) followed by precursor dosage and surface mediated deposition (d) of a primary deposit (e). In both cases, the primary deposit may grow autocatalytically if further precursor is supplied (f) to form the final deposit (g).

In electron beam induced deposition (EBID), the electron beam is scanned across a surface, while a suitable precursor is dosed (Figure 2-1b).<sup>4, 7, 8, 11</sup> The precursor, typically a metal organic compound with a relatively high vapor pressure, is locally decomposed by the electron beam to form a deposit of the non-volatile dissociation products (Figure 2-1b,e). The volatile precursor fragments are pumped off by the vacuum system.

The second FEBIP technique explored in our group shown in Figure 2-1 is electron beam induced surface activation (EBISA).<sup>5, 12-16</sup> In this approach, the surface is first locally irradiated with the electron beam under UHV conditions, i.e., without precursor supply (Figure 2-1c). Thereby, the irradiated surface areas are chemically modified such that they become catalytically active towards the decomposition of precursor molecules. In a second processing step, a viable precursor is dosed onto the surface (Figure 2-1d) and reacts at the activated surface areas to form an initial deposit (Figure 2-1e).

For suitable precursors, e.g.,  $\text{Fe}(\text{CO})_5$ , the initial deposits produced by EBID or EBISA continue to grow autocatalytically as long as the precursor is supplied (Figure 2-1f,g).

The following chapters shall give an overview of the state of the art, explain the theoretical background and identify the challenges associated with EBID and especially EBISA.

## 2.1 Electron Beam Induced Deposition – EBID

The effect of electron beam induced deposition of material in electron microscopy has been known for a long time, usually as carbonaceous deposits resulting from the decomposition of residual gases, e.g. originating from pump oils, in electron beam based systems.<sup>17</sup> The understanding of the EBID process has progressed from that point on and especially proceeded rapidly in the last decade.<sup>4, 7, 8, 11, 18, 19</sup> It has been demonstrated, for example, that it is possible to fabricate nanostructures with dimensions well below 10 nm;<sup>4, 9</sup> the current record is even below 1 nm (full width at half maximum, FWHM), obtained using tungsten hexacarbonyl,  $\text{W}(\text{CO})_6$ , on thin silicon nitride membranes.<sup>20</sup> Research has also shown that (some) materials can be deposited with high purity, e.g., iron from iron pentacarbonyl,  $\text{Fe}(\text{CO})_5$ ,<sup>5, 21, 22</sup> cobalt from dicobalt octacarbonyl,  $\text{Co}_2(\text{CO})_8$ ,<sup>23, 24</sup> or Au from  $\text{Au}(\text{CO})\text{Cl}$ .<sup>25</sup> In addition, EBID offers the possibility of 3D fabrication, e.g., pillars, as well as the possibility of working on non-flat substrates.<sup>4, 8, 11, 26</sup>

These aspects are the basis for a number of interesting applications of this technique. Foremost, a commercial application has been established in semiconductor industry: mask

repair of high-resolution lithographic masks.<sup>27, 28</sup> Such masks are highly complex, incorporate features of very small dimensions and cannot be fabricated completely defect free. The as-fabricated mask therefore has to undergo a repair process, in which these defects are corrected, e.g. by the addition of material (EBID) to correct clear defects or by the removal of unwanted material (etching via EBIE) to correct opaque ones. The FEBIP-based mask repair has superseded focused ion beam (FIB) techniques for the 65 nm and lower nodes and is likely to be used for the repair of EUV masks.<sup>29</sup>

EBID has also been applied for the fabrication of scanning probe tips, e.g. for applications in magnetic force microscopy (MFM)<sup>30</sup> or as nano-tweezers,<sup>31</sup> for the fabrication of nanoscale sensors, e.g. Hall,<sup>32, 33</sup> strain,<sup>34</sup> or humidity<sup>35</sup> sensors, and for other custom applications that make use of the benefits of the technique.

In most cases, EBID is performed under high vacuum (HV) conditions and the resulting metal contents of the deposit are below 60 %at.<sup>18</sup> Few exceptions have been reported, with much higher purities of >90 to 95 %at: EBID with Fe(CO)<sub>5</sub>, performed in ultrahigh vacuum (UHV),<sup>21</sup> where, in addition to EBID, autocatalytic decomposition on the Fe deposits can occur (after electron irradiation), leading to continuous clean iron structure growth as long as Fe(CO)<sub>5</sub> is supplied (Figure 2-1f and g).<sup>5, 12, 14, 16</sup> The high purity goes along with very low resistivities (below 100 μΩcm), which are not accessible otherwise.<sup>36</sup> The second exception concerns high purity cobalt deposits from Co<sub>2</sub>(CO)<sub>8</sub>, which have been reported under HV conditions,<sup>24</sup> with inconsistent reports concerning autocatalytic growth behavior.<sup>15, 37</sup> In addition, it has been reported that deposits from Au(CO)Cl or AuCl(PF<sub>3</sub>) yield gold deposits of high purity.<sup>25, 38</sup> It has also been shown that it is possible to combine EBID with a number of post-treatment techniques, including annealing processes in vacuum and in reactive gas environments<sup>39</sup> and post-deposition irradiation with electrons. Alternatively, a number of coincidental purification techniques such as elevated sample temperatures, laser irradiation or co-dosing of reactive gases was proposed.<sup>18</sup>

While the application of EBID for the fabrication of nanostructures is quite common by now, the theoretical description is still under development. This is mostly due to the complexity of the individual processes that comprise EBID, their interplay and the heterogeneity of the experimental setups, used precursors and substrates that make up the EBID knowledgebase.

The EBID process can be divided into three interaction domains: the electron beam – surface, surface – precursor and electron – precursor interactions.<sup>4</sup> Most aspects of the electron beam – surface interactions, e.g. scattering properties, are well understood and can be

predicted and simulated. Electrons are scattered in the solid according to the incident energy, the density and mean atomic number of the material and surface topography. As a result, the incident electrons lose energy and are deflected while causing excitation and ionization processes in the substrate, which result in the emission of various interaction products, e.g. X-rays or secondary electrons. These processes are also well understood, also due to their relevance for electron microscopy in general (see also Chapter 3.1).

The surface – precursor interactions include physico-chemical aspects like adsorption, desorption and diffusion, which are strongly temperature dependent, as well as chemical processes like dissociative adsorption, and (auto-) catalytic decomposition. One of the major difficulties for the description of these aspects is the inherent change of the parameters during deposition. The adsorption, desorption and diffusion characteristics may change greatly from the clean substrate to a thin EBI deposit in terms of surface chemistry and even more so once the change in surface topography becomes substantial during the deposition.

Finally, the interaction of electrons with precursor molecules is of importance. There are a number of processes that can lead to the dissociation of a precursor molecule, most prominently direct (or dissociative) ionization (DI) and dissociative electron attachment (DEA).<sup>4, 8, 11, 40</sup> There are other processes, e.g. electron induced desorption of intact precursor molecules (ESD) or other dissociation processes like dipolar dissociation (DD), which may also occur. The description of the electron induced dissociation is based on the respective cross-section, which is strongly energy dependent. In a simplified picture, DEA is the dominant process at low electron energy (few eV) and exhibits a higher cross-section, while direct ionization occurs for higher electron energies and typically lower cross-sections. Unfortunately, the cross-sections for many precursor molecules are unknown, which limits the predictive power of EBID models.

In recent years, the electron – precursor interactions have been investigated with a special focus on the relevance for EBID. These studies include gas-phase reaction studies, e.g. for a common platinum precursor (Trimethyl methylcyclopentadienyl platinum (IV), Cp'PtMe<sub>3</sub>)<sup>41</sup> or the cobalt tricarbonyl nitrosyl precursor<sup>42, 43</sup> as well as surface science studies for both the platinum<sup>44-46</sup> as well as the cobalt precursor.<sup>47</sup> These studies highlight the importance of DEA in EBID and also offer some insight into the relevance of the decomposition pathway on the deposit composition.

The state of the art of FEBIP and especially electron beam induced deposition was reviewed in a number of articles, which summarize the available data and introduce theoretical aspects in more detail.<sup>4, 7, 8, 10, 11, 16, 18</sup>

## 2.2 Electron Beam Induced Surface Activation – EBISA

Electron beam induced surface activation is closely related to EBID, as it also utilizes the focused electron beam of a SEM for the fabrication of nanostructures on surfaces. Many of the concepts derived for EBID are also valid for EBISA; especially the electron scattering aspects and other physical aspects of the electron – surface interactions are virtually identical. In this regard, the knowledgebase of EBID can serve as a basis as well as a benchmark for EBISA. The state of the art in EBISA was summarized in a recent review.<sup>16</sup>

In contrast to EBID, the irradiation in EBISA proceeds under vacuum conditions, i.e. preferably in the absence of any precursor molecules. As mentioned before, the irradiation leads to the formation of active sites on/in the surface, which can catalyze the decomposition of precursor molecules introduced at a later time. The actual fabrication of solid nanostructures then relies on secondary growth processes, which depend on the chemical properties of the precursor molecules, foremost the ability for autocatalytic decomposition and associated structure growth (as autocatalytic growth may also affect EBI deposits, a general introduction to autocatalytic growth shall be given in the next chapter).

The EBISA process was introduced by Walz et al. in 2010.<sup>5</sup> The discovery was based on the observation of autocatalytic growth of EBI deposits prepared from  $\text{Fe}(\text{CO})_5$  on a  $\text{SiO}_2(300\text{ nm})/\text{Si}$  surface under UHV conditions. During the initial stages of the growth process, i.e. directly after the electron irradiation, very little Fe deposited due to EBID is present on the surface. Instead, dark features are observed in scanning electron micrographs of the irradiated areas, leading to the suggestion that both the Fe atoms deposited during the EBID step as well as the irradiated surface itself act as catalytic agents towards the decomposition of  $\text{Fe}(\text{CO})_5$ . The assumption was confirmed experimentally by preparing irradiated surface areas under UHV conditions, i.e. in the absence of precursor molecules, followed by prolonged exposure to the precursor to allow for autocatalytic growth.<sup>5</sup> The resulting deposits were found to exhibit very high Fe contents (> 90 to 95 %at.), with minor carbon and oxygen contaminations, and consist of cube-like  $\alpha$ -Fe crystallites.

Figure 2-2 juxtaposes two series of EBID lines (A:a-g and A:h-j) and a series of EBISA line structures (B:a-f), which were part of this first publication.<sup>5</sup> The EBID series (A) contain SEM images of line structures fabricated using  $\text{Fe}(\text{CO})_5$  as a precursor and two different electron doses ( $1.9\ \mu\text{C}/\text{cm}$  and  $0.5\ \mu\text{C}/\text{cm}$ ) after different periods of autocatalytic growth after the initial EBID step (as indicated). In the EBID series, only after about 30 min of precursor dosage at a background pressure of  $3.0 \times 10^{-7}$  mbar (further specified in later publications as a

surface pressure of approx.  $9 \times 10^{-6}$  mbar<sup>14</sup>), emergence of small clusters can be detected (A:b), before larger, polycrystalline structures develop. It is apparent that the autocatalytic growth plays a major role in the nanostructure fabrication using this precursor under the given conditions. The EBISA series comprises images of lines with different electron doses and a common autocatalytic growth time of 270 min. The data shows successful fabrication of nanostructures using the EBISA protocol.

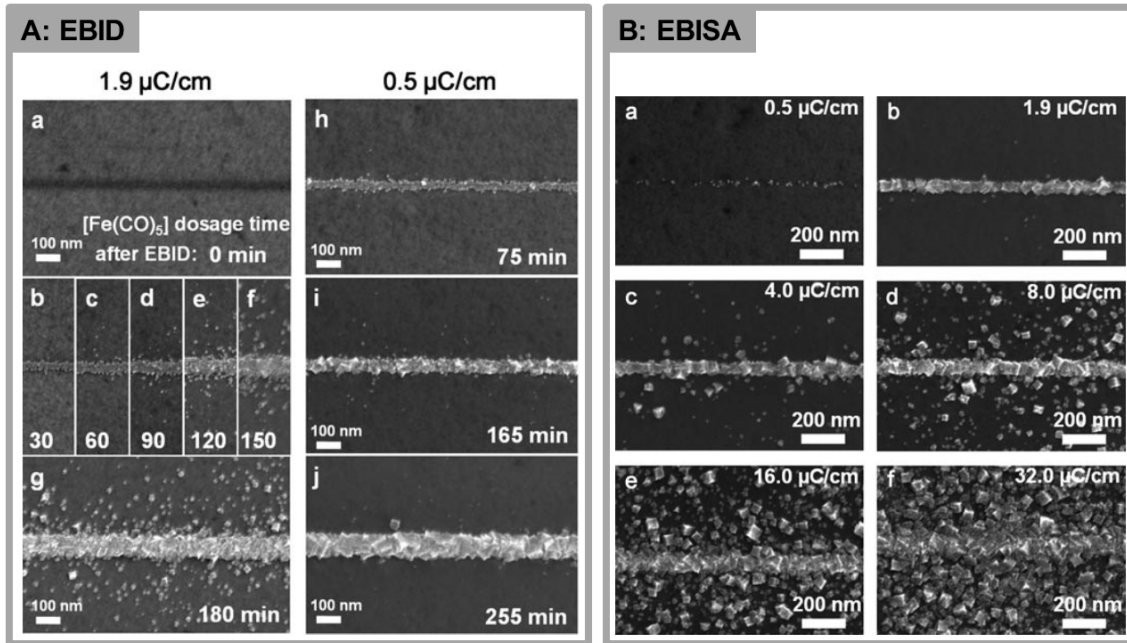


**Figure 2-2:** Examples of the autocatalytic growth observed for EBID lines prepared from  $\text{Fe}(\text{CO})_5$  on  $\text{SiO}_x(300 \text{ nm})/\text{Si}$  (A) and first published results of successful EBISA and autocatalytic growth on the same system (B). The SEM series A:a-g and A:h-j show EBID lines prepared with two different electron doses and increasing autocatalytic growth times (as indicated). The series B:a-f consists of EBISA lines prepared with increasing PE doses after identical growth times of 270 min. Figures reprinted from Walz *et al.*<sup>5</sup>

The scattered deposits close to the line structures are the result of so-called proximity effects. In this case, backscattered electrons are responsible for the loss of structure definition at higher electron dose. Proximity effects will be discussed in more detail in Chapter 2.4.

The successful fabrication of nanostructures using the EBISA protocol raises the question of the underlying mechanism of the activation. Based on prior work by Pfnür and co-workers<sup>48, 49</sup> and Watanabe and coworkers<sup>50, 51</sup> concerning a technique known as electron beam assisted selective thermal desorption (EBSTD), in which an ultrathin layer of  $\text{SiO}_x$  is

reduced in a spatially defined way to SiO by an electron beam, followed by an annealing process to selectively desorb the SiO, it was proposed that oxygen vacancies generated by electron stimulated desorption of oxygen from the SiO<sub>x</sub> surface act as the active sites for the initial decomposition of Fe(CO)<sub>5</sub>.<sup>5</sup> The electron stimulated desorption (ESD) has been attributed to a Knotek-Feibelman process, i.e., an inter-atomic Auger decay resulting in the expulsion of oxygen ions.<sup>52, 53</sup> The suggested mechanism was later substantiated by AES studies of irradiation induced oxygen desorption from ultrathin SiO<sub>x</sub> on Si and the observation of the intrinsic activity of freshly prepared SiO<sub>x</sub>/Si samples.<sup>14</sup> Physical charging of the sample was excluded under the experimental conditions (thin layer, conductive Si(100) substrate, long-term stability (>24 h) of the activation), albeit localized charges at oxygen vacancies, as e.g. observed on TiO<sub>2</sub>(110)<sup>54</sup> were mentioned as possible active sites.<sup>14</sup>

EBISA in combination with Fe(CO)<sub>5</sub> was also used as a probe for the investigation of proximity effects on thin membrane samples.<sup>12, 13</sup> The studies broaden the scope of applicable substrates to native silicon oxide layers on silicon single crystals as well as silicon nitride films (both free-standing and on Si supports), which could be activated under the same experimental conditions. It was also reported that carbonaceous layers on the SiO<sub>x</sub> surface suppress the activation process.<sup>5</sup> It has to be noted, that all of the aforementioned studies by Walz et al. have been conducted under UHV, i.e. ultraclean conditions, at room temperature using Fe(CO)<sub>5</sub> as a precursor molecule. UHV seemed to be a prerequisite for the successful application of EBISA and autocatalytic growth.

In 2012, studies by Muthukumar et al.<sup>15</sup> and Córdoba et al.<sup>37</sup> concerning EBISA and the autocatalytic growth of cobalt nanostructures from dicobalt octacarbonyl, Co<sub>2</sub>(CO)<sub>8</sub>, on silicon oxide and other surfaces were published. In both cases, the experiments were performed under high vacuum (HV) conditions at room temperature.

Córdoba et al. did not observe any successful EBISA on SiO<sub>x</sub> surfaces; autocatalytic decomposition of the precursor was only reported on in-situ prepared, freshly Ga-ion sputtered pure cobalt films; Co nanostructures prepared by EBID from Co<sub>2</sub>(CO)<sub>8</sub> did not exhibit any autocatalytic growth. Autocatalytic growth was hence ruled out as a major contributing factor in the fabrication of high purity Co nanostructures prepared from Co<sub>2</sub>(CO)<sub>8</sub> in HV.

In contrast, Muthukumar et al. reported the successful fabrication of nanostructures using the EBISA protocol using Co<sub>2</sub>(CO)<sub>8</sub> on SiO<sub>x</sub> and also report autocatalytic growth of material on plasma-cleaned SiO<sub>x</sub> surfaces. The metal content of the deposits was reported as approx. 95 % on plasma-cleaned and 76 % on electron pre-irradiated surfaces. The publication also

contains detailed DFT data concerning the adsorption and initial stages of the decomposition of  $\text{Co}_2(\text{CO})_8$  on the surface. The results suggest an activation mechanism in which the electron beam or the plasma discharge partially dehydroxylize the, under the HV conditions usually fully hydroxylated,  $\text{SiO}_x$  surface. The precursor molecule then interacts with the dehydroxylated surface and dissociates into two  $\text{Co}(\text{CO})_4$  fragments, which are stabilized by the interaction with the surface. The reported most stable structures of  $[\text{Co}_2(\text{CO})_8]$  on fully hydroxylated (Figure 2-3a, intact  $\text{Co}_2(\text{CO})_8$ ) and partially hydroxylated  $\text{SiO}_2$  (Figure 2-3b, dissociated into two  $\text{Co}(\text{CO})_4$  fragments) are juxtaposed in Figure 2-3. This initial decomposition reaction is suggested to be the first step in the deposition process.

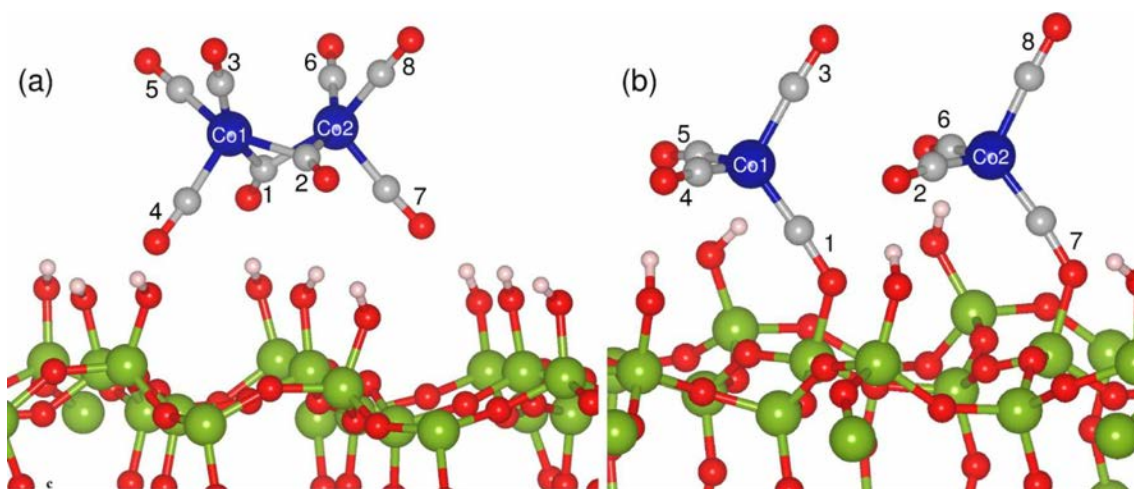


**Figure 2-3:** Most stable structures of  $[\text{Co}_2(\text{CO})_8]$  on fully hydroxylated (a) and partially hydroxylated (b)  $\text{SiO}_2$ , reprinted from Muthukumar *et al.*<sup>15</sup> The  $\text{Co}_2(\text{CO})_8$  precursor shows only minor interactions with the fully hydroxylated silica (a), but undergoes dissociation into two surface bound  $\text{Co}(\text{CO})_4$  fragments on the partially hydroxylated surface.

The calculations are setup such that individual OH groups in close proximity to CO ligands of the precursor (in various starting geometries) are removed from a hydroxyl-terminated  $\beta$ -cristobalite  $\text{SiO}_2$  slab.<sup>55</sup> Effectively, the precursor interacts with un-terminated, undercoordinated Si atoms. The notion of undercoordinated Si atoms as reactive sites is also part of the EBISA mechanism proposed by Walz *et al.*<sup>5, 12-14</sup> (“oxygen vacancy”). This suggests that both explanations are not mutually exclusive.

In summary, successful nanostructure fabrication by EBISA has been reported for iron pentacarbonyl,  $\text{Fe}(\text{CO})_5$ , on a number of  $\text{SiO}_x$ -terminated surfaces in UHV<sup>5, 12-14</sup> and recently also for  $\text{Co}_2(\text{CO})_8$  on  $\text{SiO}_x$  in HV.<sup>15</sup> The active component in the initial precursor decomposition is still under investigation, with chemically active species, like

undercoordinated atoms, being favored over physical causes such as charging. In order to broaden the understanding of EBISA, both deeper insights into the mechanism on the known systems as well as the generalization of the EBISA concept towards other precursors and substrates are necessary and shall be the aim of this thesis.

## 2.3 Autocatalysis and Precursor Chemistry

There are two requirements for a precursor to be suitable for the fabrication of nanostructures using the EBISA protocol: susceptibility to the decomposition at activated sites to start the deposition and selective autocatalytic decomposition in order to facilitate the subsequent growth. As autocatalytic growth was also observed for primary structures produced by EBID, this process is relevant for conventional EBID, and possibly for other FEBIP techniques as well, which is reflected by the acknowledgment of the phenomenon in recent review articles.<sup>4, 10, 11, 16, 18</sup>

It has to be stressed at this point that decomposition of a precursor can only be considered autocatalytic growth if the decomposition occurs selectively and continuously at already deposited material under the respective conditions (especially temperature). This distinguishes the autocatalytic growth from processes like chemical vapor deposition (CVD), which is continuous but unselective, and atomic layer deposition (ALD), which is selective but discontinuous.

In contrast to the initial surface mediated decomposition of the precursor in EBISA, the autocatalytic decomposition and growth itself can be independently investigated and have been studied to some extent, mostly in contexts other than EBID/EBISA. It has been shown for example that  $\text{Fe}(\text{CO})_5$  exhibits autocatalytic growth in a number of cases under HV<sup>56-59</sup> and UHV<sup>60-67</sup> conditions, partially at elevated temperatures. Autocatalytic growth was observed for  $\text{Fe}(\text{CO})_5$  and  $\text{Cr}(\text{CO})_6$  at elevated temperatures ( $\sim 125\text{ }^\circ\text{C}$  and  $\sim 280\text{ }^\circ\text{C}$ , respectively) on the respective metal-containing EBI deposits<sup>56-58</sup> and for  $\text{Co}_2(\text{CO})_8$  on clean Co as well as on Co-containing (EBISA-derived) deposits<sup>15, 37</sup> in high vacuum environments.

Under UHV conditions, Zaera demonstrated that  $\text{Fe}(\text{CO})_5$  decomposes catalytically on Pt(111) and exhibits autocatalytic growth starting at 275 K;<sup>64-66</sup> similar behavior was reported for  $\text{Fe}(\text{CO})_5$ ,  $\text{W}(\text{CO})_6$  on Ni(100).<sup>67</sup> Catalytic decomposition on Ni(100) has also been reported for  $\text{Cr}(\text{CO})_6$  and  $\text{Mo}(\text{CO})_6$ .

In addition, there are reports of so-called seeded growth, i.e. the increase of deposition yield of EBID in a narrow temperature window below the thermal decomposition temperature of precursor molecules, which may also be viewed for autocatalysis at elevated temperatures.<sup>23, 68</sup>

Regarding the mechanism of the (auto-)catalytic decomposition of  $\text{Fe}(\text{CO})_5$  on Pt(111), an adsorption-induced change in the molecular geometry from trigonal-bipyramidal to square planar structure was proposed, where the surface may become a sixth ligand for the central iron metal.<sup>65</sup> This is followed by the mostly reversible loss of one or two CO ligands to produce stable  $\text{Fe}(\text{CO})_4$  and  $\text{Fe}(\text{CO})_3$  on the surface even at low temperature (170 to 240 K). At higher temperatures, close to room temperature, these species either recombine with CO and desorb or decarbonylate completely to give Fe atoms. While adsorbed CO acts as a poison at low temperatures, at temperatures above 275 K an equilibrium is reached, where continuous autocatalytic growth can occur.<sup>65</sup>

In all reported cases of catalytic and autocatalytic decomposition of carbonyl precursors on metal substrates in UHV, the surface cleanliness, CO coverage on the surface, the CO partial pressure in the gas phase as well as the reaction temperature influence the growth rate, purity and morphology on the resulting film in a complex way.<sup>64-67</sup>

## 2.4 Proximity Effects

One of the main challenges in most FEBIP techniques is the unwanted deposition of material in close proximity to the impact area of the electron beam due to scattered electrons: the backscattered electron (BSE) proximity effect is well studied,<sup>4, 12, 13, 69</sup> and the resulting maximum broadening of deposits can be predicted, e.g. through Monte-Carlo simulations. For EBID, also forward-scattered electron (FSE) proximity effects can occur if the deposit exhibits a pronounced 3D shape, e.g. pillar growth. In contrast to the BSE proximity effects, the range of FSEs is larger and depends on the morphology of the irradiated area during deposition. The advantage of EBISA vs. EBID is the absence of FSE proximity effects, since the deposit only forms after the electron irradiation. Autocatalytic growth after the initial deposition step is also beneficial, as it occurs without additional electron irradiation. While the nature of the autocatalytic growth process somewhat hinders the fabrication of high aspect ratio and complex 3D structures, it opens up new possibilities, e.g. for producing defined inter-structure gaps or access to multilayer structures using a second suitable precursor.





## 3 Methods & Techniques

The following chapter will give a short introduction to the applied experimental techniques and simulation methods. Most aspects in this thesis are closely tied to the scanning electron microscope (SEM), which is the main tool for both structure fabrication and characterization. In addition, Auger electron spectroscopy and microscopy (AES, SAM) also rely on the SEM as excitation source. The second central component is scanning tunneling microscopy (STM), which is used for the atomic scale characterization of samples and nanostructures. Scanning transition X-ray microscopy (STXM) and near edge X-ray absorption spectroscopy (NEXAFS) using synchrotron radiation complement the laboratory experiments and allow for further insight into the chemical and physical properties of nanostructures. Finally, standard techniques in surface science like low-energy electron diffraction (LEED) and quadrupole mass spectrometry (QMS) will be discussed briefly followed by a short introduction to Monte-Carlo simulation of electron trajectories.

### 3.1 Scanning Electron Microscopy

Scanning electron microscopy (SEM) is the younger sibling of transmission electron microscopy (TEM) in the family of electron microscopy techniques. In SEM, a focused primary electron (PE) beam is raster scanned over a surface, i.e., the e-beam is directed to a certain position on the surface under investigation, remains stationary for a given amount of time (dwell time) during which a signal is recorded and moves to the next position. The intensity of the selected signal(s) triggered by the impact of the electron beam is then plotted versus the probe position on the surface to give a map of the respective signal(s). The achievable resolution mainly depends on the beam diameter at the point of impact. Modern

SEMs offer resolutions down to the sub-nm regime, making the SEM a most valuable tool not only in nano- and surface science. A detailed introduction to scanning electron microscopy can be found in L. Reimer: “Scanning Electron Microscopy”.<sup>70</sup>

The signal types generated during an SEM scan are manifold. Foremost, the interaction of fast electrons in the beam with the sample material leads to an emission of electrons from the surface. The electron emission is the result of elastic or inelastic scattering in the surface near region of the sample material. Emitted electrons are commonly (and somewhat arbitrarily) classified according to their energy into secondary electrons (SE,  $E_{\text{kin}} < 50$  eV) and backscattered electrons (BSE,  $E_{\text{kin}} > 50$  eV). Secondary electrons are subdivided according to their origin: SE<sub>I</sub> are caused directly by the impinging primary electrons, and confined to the immediate point of impact; SE<sub>II</sub> stem from interactions of scattered electrons (BSE) with surface atoms; SE<sub>III</sub> emerge as a result of stray electrons impinging on any surfaces inside the vacuum chamber.

The BSE regime ( $E_{\text{kin}} > 50$  eV) includes a number of specific interaction products such as Auger electrons (AE) produced by core-hole ionization and decay, or low-loss electrons (LLE) with a specific energy loss due to a certain interaction e.g. with plasmons. Such electrons carry additional information about the surface composition, albeit it is only accessible through energy-resolved detection and therefore requires a dedicated electron energy analyzer. In addition to the electron energy and the emission energy, it is also possible to detect the diffraction pattern of BSEs to yield information about (poly-) crystalline material (Electron backscatter diffraction, EBSD).

The second group of signals encompasses all types of electromagnetic radiation emitted by the sample due to excitation by the primary beam. These signals range from low-energy infrared (IR) emission over medium energy visible and ultraviolet (UV/Vis) radiation, commonly referred to as cathodoluminescence, to X-ray emission, including characteristic X-rays. The detection of such radiation again requires specialized detectors, but can give insights into surface properties that are hard to obtain otherwise with nanometer resolution. Many SEMs are equipped with energy dispersive (EDX) or wavelength dispersive (WDX) X-ray spectrometers for analysis of the chemical composition of a sample.

Emission of electrons can be measured indirectly via the current flow to ground (specimen current) or directly via dedicated detectors. Such detectors, like the well-known Everhart-Thornley detector (ET),<sup>71</sup> collect emitted electrons by a small attractive potential, accelerate them towards a scintillator and detect the thereby created photons using photomultiplier tubes (PMT), which can be mounted outside the vacuum chamber at the end of an optical fiber. The

ET detector's collection grid can also be charged negatively to repel slow electrons and thus emulate a BSE detector. In addition, it is possible to combine SEM's with electron energy analyzers, e.g. a hemispherical electron analyzer. This allows for the energy resolved detection of electrons, e.g. for Auger electron spectroscopy (AES, see later chapter) or low loss electrons, with high precision and due to the highly focused excitation source also with high lateral resolution.

All of the signals allow for the characterization of a sample with respect to a certain physical or chemical property. The most often used signals are the SE and BSE emission intensity, which is influenced by the topography and morphology of the sample surface (topographic contrast) as well as the physical and chemical properties of the sample (material contrast). Topographic contrast is observed when the emission characteristics of the surface change from position to position due to the surface tilt, the surface roughness, shadowing and edge effects. Material contrast is observed for structures of different (mean) atomic number (chemical or Z-contrast), density, work function, charging behavior, diffraction and so forth. Both types of contrast are observed simultaneously in regular SE/BSE detection mode.

Topographic contrast sums up all changes in the electron emission due to differently shaped surfaces. This includes different orientation relative to the beam axis (surface tilt contrast), edge effects, surface roughness and shadowing contrast. A uniform, flat surface does not provide any topographic contrast.

Shadowing occurs every time the signal to the detector is blocked by surface features far from the point of impact of the electron beam. The emission of electrons is increased for structures which provide a large available surface for emission such as edges and rough, i.e. edge-rich, surfaces. When the electron beam axis is not perpendicular to the surface normal, a given penetration depth results in a reduced escape depth, which in turn increases the electron emission. The different topographic contrast modes are juxtaposed in Figure 3-1.

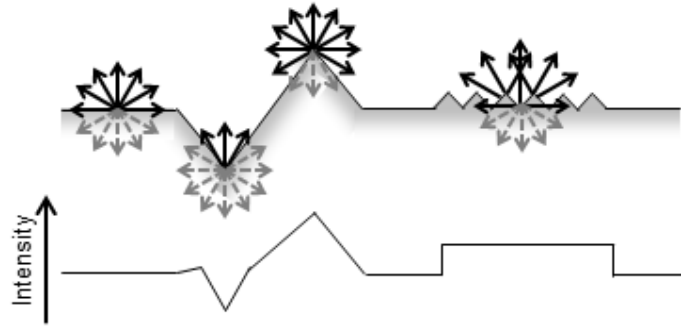


**Figure 3-1:** Topography contrast in SEM. The top scheme is a cross section of a surface with a flat section (left), a trench, a protruding edge and a rough section (right), while the bottom one represents a schematic graph of the expected image intensity. The electron emission, represented by the black arrows, differs from one surface structure to the other solely due to the topography.

The second group of contrast mechanisms is based on the physical and chemical properties of a surface rather than geometric features. The most prominent is referred to as chemical contrast and results mainly from the increase of the BSE emission coefficient  $\eta$  ( $\eta = n_{\text{BSE}} / n_{\text{PE}}$ ) with increasing atomic number  $Z$ . The contrast is more pronounced in BSE than in SE detection mode. There is also an influence of the work function on the observed contrast.<sup>72</sup> Non-conducting specimens charge up during the irradiation due to the imbalance of impinging and emitted electrons, leading to characteristic distortions and the subsequent identification of such features.

## 3.2 Auger Electron Spectroscopy

Incident primary electrons are energetic enough to excite inner shell electrons of surface atoms, resulting in an inner shell vacancy usually referred to as a core hole. The thus excited or ionized atom has two relaxation pathways that are of interest: radiative via the emission of characteristic X-rays and non-radiative via emission of Auger electrons. X-ray emission occurs when an electron from a higher shell fills the vacancy and the gained energy is emitted as an X-ray photon. Alternatively, the energy can also be transferred to another electron within the atom, which is then emitted from the atom and referred to as an Auger electron (AE). Like characteristic X-rays, Auger electrons carry information about the chemical nature of the

involved atom(s), which can be accessed via the energy-resolved detection of the electron emission. Combined with a highly focused electron beam as excitation source, AES can yield chemical information with high spatial resolution. A thorough introduction to AES can be found for example in “Practical Surface Analysis, Vol. 1 - Auger and X-ray Photoelectron Spectroscopy”, edited by Briggs and Seah.<sup>73</sup>

The energy of the Auger electron  $E_{AE}$  relative to the Fermi energy can be approximated by

$$E_{AE} = E_A - E_B - E_C^*,$$

where  $E_A$  is the binding energy (BE) of the level the hole is created in, and  $E_B$  is binding energy of the level of the electron filling that hole. The energy  $E_C^*$  represents the binding energy of the emitted electron and differs from the ground state binding energy  $E_C$  due relaxation effects in the presence of a hole in the system. This picture is a simplification, as there are additional energy shifts in the atom due to the presence of a core hole before and *two* outer shell vacancies after the emission in addition to relaxation energies.

Much like in X-ray photoelectron spectroscopy (XPS), the energy of an Auger electron shifts according to the chemical environment of the atom, which allows for the characterization e.g. of oxidation states. Also in analogy to XPS, AES is very surface sensitive. Electrons that undergo inelastic collisions on their way to the surface lose energy and therefore also the chemical information. This means that only Auger electrons originating in the immediate surface can be detected as such. The information depth depends on the kinetic energy of the Auger electron and material properties of the traversed matter via the respective inelastic mean free path (IMFP). Calculations predict that about 95 % of the signal in an AE spectrum at the respective energy stem from a depth of about three times the inelastic mean free path, which amounts to about 3 to 6 nm for typical electron energies and materials. For non-normal, grazing emission this value is even lower, as it is scaled by  $\cos(\alpha)$  with  $\alpha$  being the emission angle vs. the surface normal.

Auger emission processes are labeled using the X-ray notation of the involved orbitals in an ABC triad, where A denotes the shell of the core hole, B denotes shell of the electron that fills the hole and C the initial state of the emitted electron. To give an example, KLL transitions are a result of a hole in the K shell, which is filled by an L shell electron, while another L shell electron is emitted. Subscript number may be included to refer to specific transitions, e.g.  $KL_1L_{2,3}$ .

### 3.3 Scanning Tunneling Microscopy

The invention of the scanning tunneling microscope (STM) by Binnig (interestingly credited as “Binning” in the original publication) and Rohrer at the IBM Zurich Research Laboratory<sup>74</sup> started a new era of surface science. STM allowed, for the first time, to investigate surface structures down to the atomic level in real space on extended, flat surfaces. A review of the scientific foundations and working principles of the STM can be found e.g. in P. Sutter: “Scanning Tunneling Microscopy in Surface Science”.<sup>75</sup>

In an STM, an atomically sharp tip is raster scanned across a surface using piezo actuators for precise positioning. Electron tunneling is observed between tip and a surface, when the tip-surface distance is very small (Å to nm). This can be used to map the surface in two different ways: the tunneling current can be recorded for every point on the 2D scan raster at a given tip height (constant height mode, CHM) or the tip-surface distance can be kept constant by keeping the tunneling current constant (constant current mode, CCM).

In CHM, structures protruding from the surface plane are closer to the tip, which registers as an increased tunneling current used as the signal source. While this mode offers very fast scan speeds due to tip movement only in the x-y plane and the lack of need for any feedback system, there is a danger of touching the surface with the tip. This is known as a tip crash and severely compromises the operation of the STM.

In CCM, the z-position of the STM tip is controlled by a feedback loop to match the tunneling current setpoint. The tip therefore follows the iso-surface contour of the respective tunneling current, while the z-deflection is used as the signal source and displayed as a false-color image plot. As the tip follows the surface topology, tip crashes are avoided.

The working principle of the STM is based on the quantum mechanical tunneling effect, which gives rise to a tunneling current between objects in very close proximity. In classical mechanics, electrons can only move from one state to another if they possess enough energy to overcome the energy barrier between the two states. Quantum mechanical treatment of the electron allows for transition probability even if the energy is lower than the barrier height.

On surfaces, the electronic wave functions of surface atoms extend into the vacuum (decay length of a few nm<sup>75</sup>). An overlap with the extending wave function of objects in close proximity, e.g. a tip, allows for the tunneling of electrons without the need to overcome the barrier, i.e. the vacuum gap.

The tunneling stops when the Fermi levels of tip and surface are aligned. It is therefore necessary to apply a bias voltage (commonly referred to as gap voltage  $U_G$  or tunneling

voltage  $U_T$ ) to offset both levels by  $\Delta E = eU_T$  for continuous STM operation. As a consequence, the investigated material must show a least some conductivity to be compatible with this technique.

Figure 3-2 provides a simplified picture of a one-dimensional tunneling junction of a metallic tip and sample. The Fermi levels, i.e. energy of the highest occupied states, are offset by  $\Delta E = eU_T$  due to the applied tunneling voltage  $U_T$ . The value of  $eU_T$  is much smaller than the work function (typically 4-6 eV for common metals).

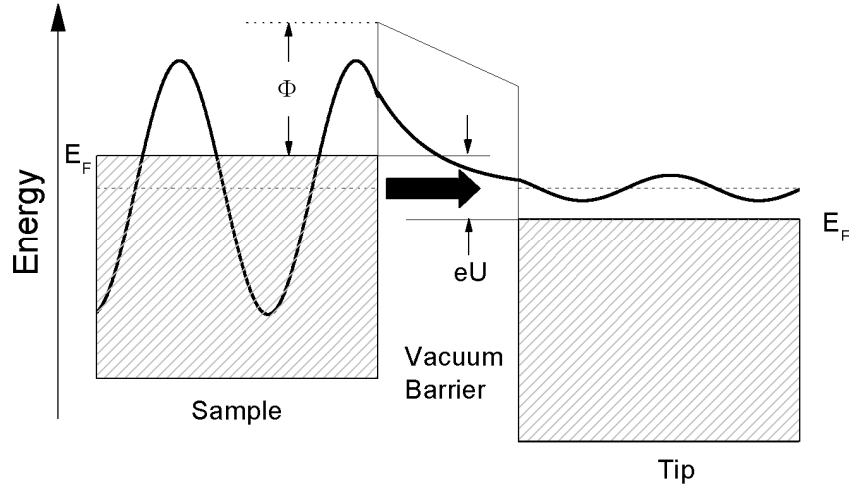


**Figure 3-2:** One dimensional metal-vacuum-metal tunneling junction (modified from ref 76). The bias voltage  $U$  offsets tip and sample Fermi level by  $\Delta E = eU_T$  with  $eU_T$  being much smaller than the work function  $\Phi$ .

The observed tunneling current is directly proportional to the number of states in the sample within the interval  $E_F$  to  $E_F - eU_T$  according to

$$I \propto \sum_{E_n=E_F-eU_T}^{E_F} |\psi_n(0)|^2 e^{-2\kappa d}$$

with  $E_n$  being the energy and  $\psi_n(0)$  the value of the  $n$ -th sample state at the sample surface,  $d$  being the surface-tip distance and  $\kappa = \hbar^{-1}\sqrt{2m\Phi}$  (electron mass  $m$  and work function  $\Phi$ ).<sup>76</sup> The sum can be replaced by the local density of states (LDOS) at the position  $z$  and the energy  $E$  as

$$\rho_S(z, E) \equiv \frac{1}{\varepsilon} \sum_{E_n=E-\varepsilon}^E |\psi_n(z)|^2$$

at the Fermi level. The LDOS is defined as the number of electrons per unit volume per unit energy, at a given point in space and at a given energy.<sup>76</sup> It follows that the tunneling current can be expressed as ( $\Phi$  in [eV])<sup>76</sup>

$$I \propto U_T \rho_S(0, E_F) e^{-2\kappa d}$$

$$\approx U_T \rho_S(0, E_F) e^{-1.025\sqrt{\Phi}d}.$$

This simplified approach is sufficient to understand the basic working principle of an STM. The tunneling depends on the applied bias voltage  $U_T$  so that a higher voltage leads to higher current. It also depends on the work function and more importantly the LDOS, which reflects the electronic structure of the surface. Most importantly for the experiment, the tunneling current depends exponentially on the tip-surface distance  $d$ . For typical values of  $\Phi$  of about 4 eV, increase of the gap by 1 Å results in a drop of the tunneling current by a factor of approx.  $e^{2\approx 7.4}$  or roughly an order of magnitude. This strong dependence of the tunneling current on the tip-surface distance is the reason for the ultimately achievable  $z$ -resolution (perpendicular to the surface) in the order of down to few 10 pm. The lateral resolution is in the order of approx. 0.1 Å and depends strongly on the tip's shape and electronic structure. Early reports assumed tips with local, spherical termination of a very low radius,<sup>77</sup> but later theories incorporated specific atomic orbitals to explain different appearances of a surface.<sup>78-80</sup> In essence, a tip terminated by an  $s$ -like orbital will give a different orbital overlap, tunneling current and resolution than  $p_z$  or  $d_{z^2}$  orbital.

For an in-depth discussion of the lateral resolution and further theoretical insights, the interested reader is referred to specialized sources, e.g. various text books<sup>75, 76</sup> and publications.<sup>77-81</sup>

### 3.4 Scanning Transmission X-ray Microscopy (STXM)

The scanning transmission X-ray microscope (STXM) is another example of a scanning probe microscopy (SPM) technique. In contrast to SEM/SAM and STM, which rely on electron as probes, the STXM uses a highly focused X-ray beam to investigate thin samples in transmission geometry.<sup>82, 83</sup> The use of synchrotron facilities as X-ray sources allows for the illumination with variable X-ray beam energies and enables elementally resolved microscopy as well as energy dependent X-ray absorption spectroscopy (XAS). Especially near edge X-ray absorption fine structure spectroscopy (NEXAFS; also known as “X-ray absorption near-edge structure spectroscopy”, XANES) is a valuable tool for sample characterization.<sup>83,84</sup>

In STXM, an X-ray beam (e.g. soft X-rays, 250 eV to few keV) is focused by a Fresnel zone plate and detected e.g. by a photomultiplier tube. Shows a schematic view of a zone plate based STXM setup.

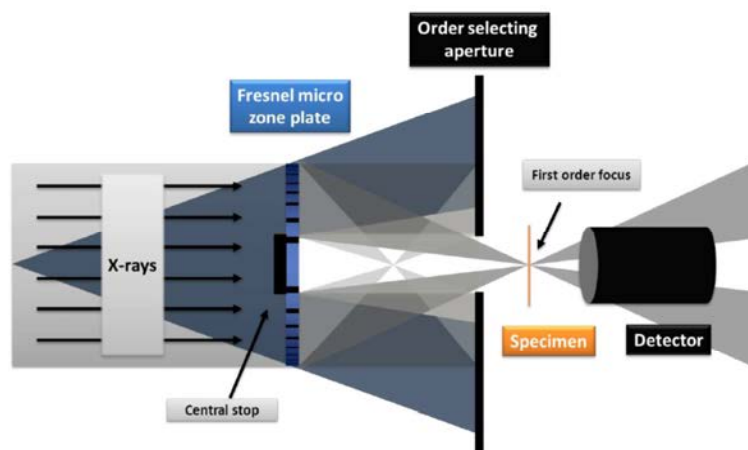


**Figure 3-3:** Schematic setup of a zone plate based STXM. Reprinted from ref. 85.

The X-rays interact with the sample material and can excite electrons into unoccupied states (resonant absorption) or into the vacuum (photoionization). The resonant transitions increase the absorption of X-rays of the respective energy and allow for elementally resolved microscopy, when the X-ray energy is set to known transition energies. Additional contrasts arise due to differences in material thickness, density, atomic number and others. Information about the electronic structure of a material can be gathered in the form of a NEXAFS spectrum. The absorption of X-rays follows the Lambert-Beer law,  $I = I_0 e^{-\mu x}$ , i.e. the transmitted intensity decays exponentially with distance  $x$  travelled within sample matter. The attenuation is strongly wavelength dependent and characterized by the attenuation coefficient

$\mu$ . Depending on the investigated system, the attenuation factor can be given as a linear attenuation coefficient  $\mu^{\text{lin}}$  in  $\text{cm}^{-1}$  or a mass attenuation coefficient  $\mu^{\text{m}}$  in  $\text{cm}^2/\text{g}$  scaled by the density  $\rho$  according to  $\mu^{\text{lin}} = \mu^{\text{m}} \times \rho$ . For a known  $\mu$ , it is possible to calculate the thickness of a material layer in transmission geometry from the transmitted signal intensity.

Using X-ray circular magnetic circular dichroism (XMCD) contrast in STXM, enables to probe the magnetic properties and dynamics of (nano-)structures with high lateral resolution. The XMCD contrast is observed when a magnetic material, e.g. Fe or Co, is probed by circularly polarized light. For resonant transitions, e.g. from 2p to unoccupied 3d levels, a difference in the transition probability depending on the photon polarization and magnetization direction can be observed.<sup>86,87</sup>

### 3.5 Other Techniques

In addition to the various microscopic techniques, a number of standard ultrahigh vacuum and surface science techniques have been used in the course of this thesis. These will not be discussed in detail but rather briefly addressed for the sake of completeness.

Low-energy electron diffraction (LEED) relies the diffraction of low-energy (few to few hundred eV) electrons at periodic surface structures, e.g. surface atoms or adsorbates.<sup>88</sup> The diffracted electrons are accelerated towards a phosphorous screen, where they produce characteristic patterns of bright spots. Simple low index surfaces like (100) or (111) give very simple, regular patterns useful for judging the surface quality. Specific structures such as the various oxygen reconstructions on Rh(110) can be identified by their characteristic pattern and selectively prepared under LEED control. It is also possible to judge the adsorbate lattice of organic molecules such as substituted porphyrins. For these applications, the fingerprint patterns are usually sufficient, although the technique allows for much deeper insights into the surface structure when more intricate data recording and processing is applied (e.g. LEED-IV).<sup>89</sup>

Quadrupole mass spectrometry (QMS) is another tool found in many UHV systems. In mass spectrometry, atoms or molecules are ionized and may subsequently break down into smaller fragments. The charged fragments, i.e. ions, are filtered according to their mass-to-charge ratio  $m/z$  and detected by a suitable detector, e.g. a Faraday cup or a secondary electron multiplier.<sup>90</sup> In QMS, the mass filter is comprised of four metallic rods in quadrupole geometry aligned along the path of the ions. A high frequency quadrupole field is applied to

the rods allowing only those ions to traverse the filter on a stable path, which are in resonance with the quadrupole field. Fragments with a non-resonant  $m/z$  value are deflected.<sup>91</sup> The observed fragments often allow for the identification of the parent molecule for simple molecules. In UHV setups, QMS is mainly used for residual gas analysis, quality control of reactive gasses and temperature programmed desorption experiments.

### 3.6 Electron Trajectory Simulation

The interaction of electrons and other charged particles with solids is of considerable interest for a number of research fields ranging from experimental particle physics to electron microscopy and lithography. For the latter purpose, a number of algorithms and programs are available that simulated the scattering of PEs in samples. Simulation programs like CASINO (“monte **C**ARlo **S**Imulation of electro**N** trajectory in **s**OLids”)<sup>92, 93</sup> allow for the evaluation of the backscattering behavior by employing Monte-Carlo methods in combination with continuum models of the sample material. In Monte-Carlo simulations, a large number of individual processes are simulated with a set of random input variables to give a large number of individual outcomes, which can be further evaluated by statistical means. CASINO simulates and tracks the trajectories of individual electrons in a Gaussian beam, randomizing the starting position, the distance of successive collisions and the scattering angle. Analytical solutions and tabulated/pre-calculated values (total/partial Cross sections, physical constants) are used to determine the corresponding trajectory. The simulation ends when the electron energy drops below 50 eV or if the electron leaves the material and becomes a transmitted or backscattered electron. Later versions also include the emission of secondary electrons.

A number of values can be extracted from the simulation results, e.g. the penetration depth into materials, the backscattering coefficient  $\eta$  or the average and maximum range of backscattered electrons. These values often are of relevance for the design and/or evaluation of and serve to improve the experiments in electron microscopy and other electron beam based techniques.



## 4 Experimental Section

### 4.1 MULTISCAN Lab UHV SEM/STM

Most experiments presented in this thesis were performed in a commercial UHV system (MULTISCAN Lab, Omicron Nanotechnology, Germany) with a base pressure of  $2 \times 10^{-10}$  mbar. The main component of the analysis chamber is a UHV-compatible electron column (Leo Gemini) for scanning electron microscopy (SEM) with a nominal resolution better than 3 nm and, in combination with a hemispherical electron energy analyzer, local AE spectroscopy (AES) and scanning Auger microscopy (SAM) with a spatial resolution better than 10 nm. In addition, an STM scanner and tip can be inserted between the pole piece of the SEM column and the sample to allow for in-situ STM measurements and tip positioning using the SEM image. The system is described in detail in the doctoral theses of Thomas Lukasczyk<sup>94</sup> and Michael Schirmer.<sup>95</sup> In the following, the main aspects will be briefly summarized.

#### 4.1.1 System Layout

The MULTISCAN Lab UHV system is divided into two main chambers for sample preparation and analysis and two auxiliary chambers for precursor gas handling and analysis (in the following referred to as “gas dosing chamber”) and fast sample exchange into and out of the system (fast entry lock). Samples can be transferred between preparation, analysis and fast entry lock using linear transfers and a series of gate valves. A system of stainless steel gas lines connects all chambers. The gas line system allows attaching precursor gasses via CF16 flanges at the gas dosing chamber side and all other gases, e.g. Ar for sputtering, via MINICAN connectors on a central hub.

The preparation and analysis chambers equipped with hot-cathode ionization vacuum gauges (VG, VIG-18) and turbo pumps (Pfeiffer Vacuum, TMU261) plus rotary vane roughing pumps (BOC Edwards, RV3) as well as ion getter pumps (Varian Inc., Analysis chamber: VacIon Plus 500; Preparation chamber VacIon Plus 150). The status of vacuum system is monitored by a central interlock system. The fast entry lock can be pumped via the turbo pump of the preparation chamber. The turbo pumps are separated from the respective chamber via interlock-controlled gate valves (VAT), which allow shutting down the vibration-inducing turbo pumps and operating the system using ion pumps only.

The gas dosing chamber is a self-constructed chamber built around a Prisma QMS/QMA200 quadrupole mass spectrometer (Pfeiffer Vacuum), with the primary task of precursor gas handling and analysis. It contains a compact full range gauge head (Pfeiffer Vacuum, PBR 260) for pressures in the range of  $10^3$  to  $5 \times 10^{-10}$  mbar, a VacIon 8l/s ion getter pump (Varian Inc.) and a self-constructed titanium sublimation pump as well as a turbo (Pfeiffer Vacuum, TMU071P) and roughing pump (Edwards, E2M2) separated from the chamber via a gate valve. Up to 6 precursors can be attached to the gas dosing line in close proximity to the gas dosing chamber and dosed into the chamber using leak valves.

The complete system (except for the roughing pumps) rests on a table that is vibrationally isolated from the building by four self-leveling laminar flow isolation legs.

Electronic devices, such as power supplies, pump controllers etc. are mounted in two 19" racks with a central power supply unit. The electronics of the Gemini SEM Column and the MATRIX STM control unit are located in separate housing units. The workspace contains three dedicated computer systems for SEM and AES/SAM, for STM and for lithography purposes (see Chapter 5.4.1).

#### **4.1.2 Preparation Chamber**

The preparation chamber houses the main sample preparation facilities. Figure 4-1 depicts photographs of the chamber and the main components. A manipulator allows for heating and cooling (via liquid nitrogen, LN<sub>2</sub>) and provides translation within the chamber. The available heating options (resistive, radiative, electron bombardment) depend on the used sample holder. The chamber contains a sputter gun (Omicron Nanotechnology, ISE 10) connected to the gas dosage line, a quartz crystal microbalance (Syscon, OSC-100A), an electron-beam evaporator for metals (Focus, EFM 3i), a self-constructed Knudsen cell evaporator for organic compounds, a quadrupole mass spectrometer (Pfeiffer Vacuum, Prisma QMS/QMA200) and a

retractable LEED system (Omicron Nanotechnology, SPECTALEED). In addition, there is a self-constructed electron gun for electron irradiation of samples.

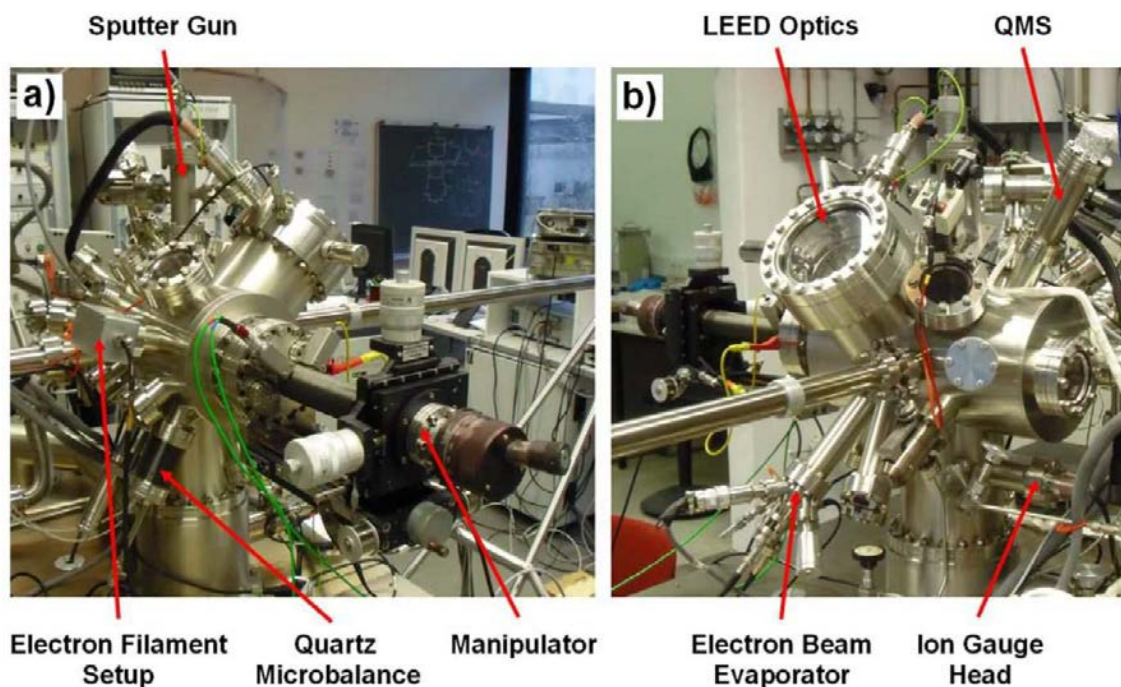


**Figure 4-1:** Photographs of the preparation chamber with labeled main components. Reprinted from ref. <sup>95</sup>.

#### 4.1.3 Analysis Chamber

The analysis chamber is depicted in Figure 4-2 and contains the main sample analysis tools. These are the UHV-compatible electron column (Zeiss/LEO, Gemini) and the Multiscan STM scanner (Omicron Nanotechnology). In addition, the analysis chamber contains a sample/tip storage facility (“Sample carousel”) for up to 12 sample/tip holders and a Prisma QMS/QMA200 quadrupole mass spectrometer for residual and precursor gas analysis.

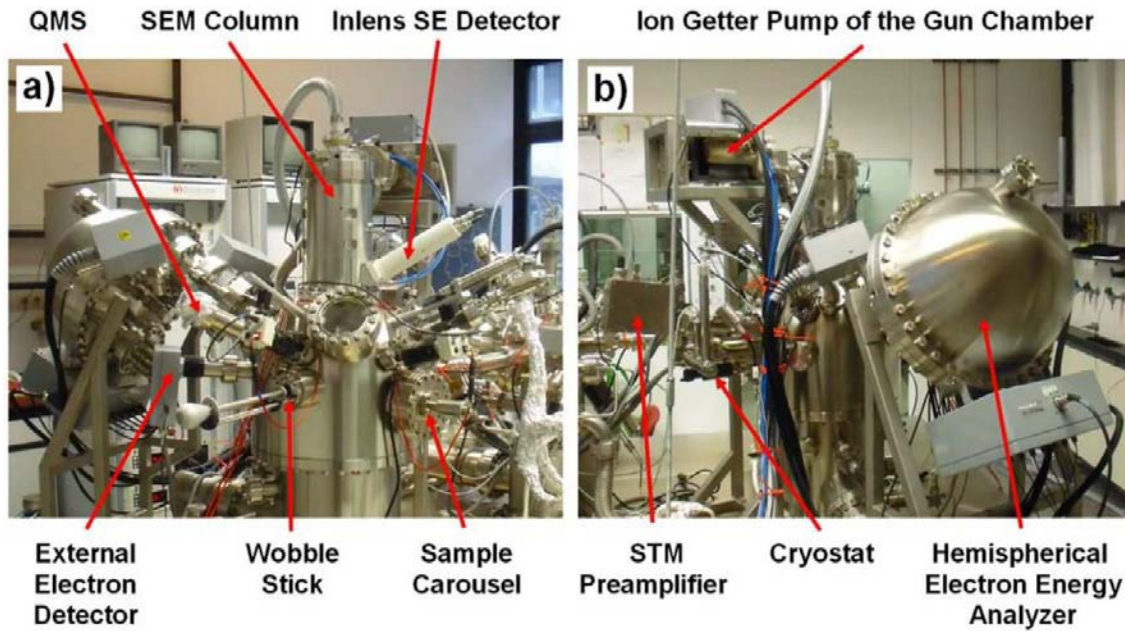


**Figure 4-2:** Photographs of the analysis chamber with labeled main components. Reprinted from ref. <sup>95</sup>.

The Gemini column allows for scanning electron microscopy with an ultimate resolution below 3 nm for 15 keV electrons at a beam current of 400 pA and working distance of approx. 9 mm. The focused electron beam of the column can also be used for electron beam based lithography (EBL, EBID, EBISA, ...; see Chapter 5) and, in combination with the hemispherical electron energy analyzer (Omicron Nanotechnology, NanoSAM) for Auger electron spectroscopy (AES) and scanning Auger microscopy (SAM) with an ultimate resolution < 10 nm.

The UHV column is based on a standard column used in commercial SEMs (SUPRA and ULTRA, Carl Zeiss SMT) with a Schottky-type (ZrO/W cathode) field-enhanced thermionic electron emitter.<sup>96</sup> The column is built with a crossover-free electron path to minimize aberrations and a beam booster to increase the beam stability for low beam energies ( $U_{\text{acc}} \leq 20$  kV). After the electrons are accelerated to the selected kinetic energy  $eU_{\text{acc}}$  by the anode, the beam booster adds 8 keV to the electron energy before they pass through the lens system ( $E_{\text{column}} = e(U_{\text{acc}} + U_{\text{booster}}) = e(U_{\text{acc}} + 8 \text{ kV})$ ). The increased energy reduces aberrations especially for low electron energies. The electron beam is decelerated to  $U_{\text{acc}}$  before it hits the sample by a retarding field. This field also acts on emitted SE and BSE, which are accelerated to the "inlens" detector situated inside the electron column. A schematic of the Gemini column is shown in Figure 4-3.

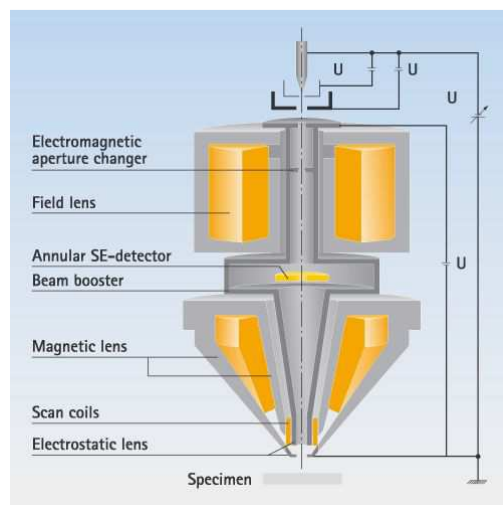


**Figure 4-3:** Schematic of the Gemini electron column as used in the MULTILAB system. The electron source is a Schottky type field-enhanced thermionic emitter. The electrons are extracted by an extractor voltage and accelerated to the final energy by the anode (top section). The beam booster adds 8 keV during the transition through the lens system only and acts as an attractive potential for the emitted SEs and BSE to the inlens-detector (“Annular SE-detector”). The beam is focused by a combination of magnetic and electrostatic lenses and feed through the column in a crossover-free trajectory. The deflection of the electron beam is realized via scan coils. Reprinted from ref. <sup>96</sup>.

The Multiscan STM scanner is mounted so that it can be inserted between the pole piece of the Gemini column and the sample surface. The scanner is a Y-shaped piezo assembly, as can be seen in Figure 4-4. The arms of the Y are formed by the independent x- and y-axis piezos which are responsible for the in-plane movement parallel to the sample surface. The z-piezo connects the scanner head / tip holder to the xy-piezos. The scan range of the STM is specified as 7  $\mu\text{m}$  for x/y- and 1.5  $\mu\text{m}$  for the z-axis, with an ultimate z-resolution of 0.01 nm.<sup>97</sup> In addition, a coarse drive allows macroscopic movement of the scanner head (Figure 4-4c).

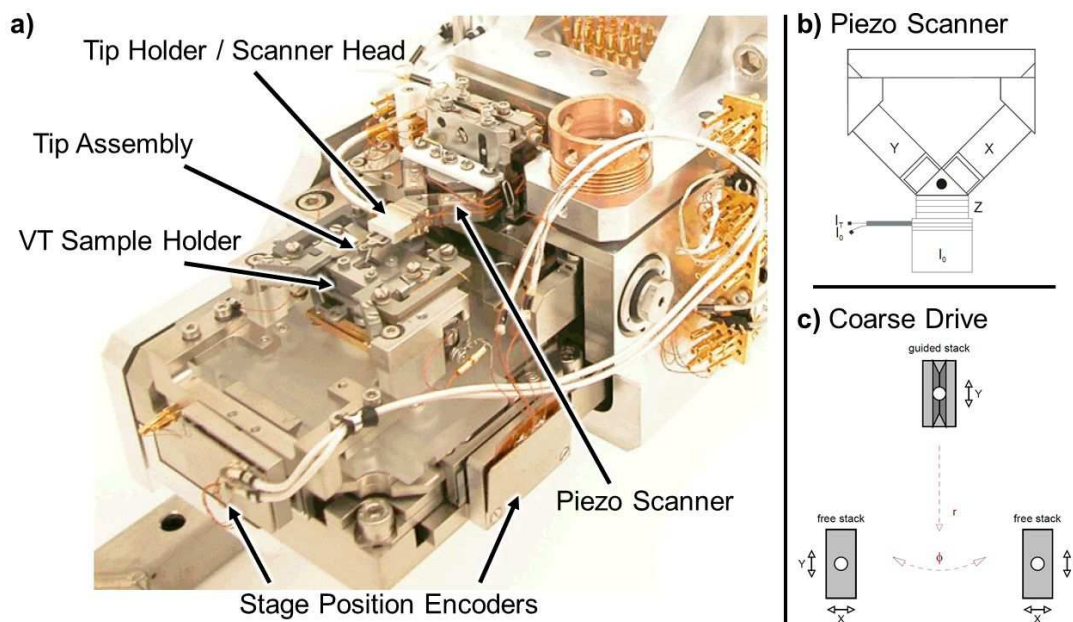


**Figure 4-4:** Photograph of the stage assembly of the MULTISCAN STM (a) and schemes of the scanner (b) and coarse drive geometry (c). The main components are indicated. The Y-shaped piezo scanner is comprised of individual piezos for in-plane movement (x/y) that form the arms of the Y while the z-piezo is directly attached to the scanner head that holds the tip assembly. The coarse drive is realized in an  $r, \phi$  geometry (c) using piezo motors as well. Tips assemblies can be exchanged without breaking the vacuum. Photograph and schemes modified from ref. <sup>97</sup>.

The tip assembly consists of a mounting (tip carrier) and a wire tip. The whole assembly (in the following referred to simply as “tip”) can be inserted into the scanner head under vacuum conditions to allow for in situ tip exchange. The tip has to be removed from the scanner head for any applications that require tilting of the stage assembly, i.e. AES and SAM.

The analysis chamber is also equipped with a gas dosage system designed for use in EBID experiments. Two precursors or reactive gases can be fed into the chamber via leak-valves, which connect to a stainless steel tube (inner diameter of 3 mm) inside the chamber. The tube assembly is mounted to a linear transfer system, which can be used to bring the end of the tube, i.e. dosing nozzle, into proximity ( $\sim 12$  mm) to the sample surface.<sup>95</sup> This is necessary to achieve the required precursor pressure on the surface during experiments. Based on simulations with the software GIS Simulator (version 1.5)<sup>98</sup> it is estimated that the local pressure increase on the sample surface is about  $30\times$  for gases like  $\text{Fe}(\text{CO})_5$  or  $\text{Co}(\text{CO})_3\text{NO}$ .

For a fixed background pressure of  $3.0 \times 10^{-7}$  mbar, this corresponds in a local pressure at the surface of about  $9 \times 10^{-6}$  mbar.<sup>95</sup>

#### 4.1.4 Sample Holders

The sample holders that can be introduced into the system can be divided into two general categories: sample plates and VT (variable temperature) sample holders. The sample plates are metal sheets that adhere to the geometry shown in Figure 4-5. They can be used to mount arbitrary specimens on top or below such a (windowed) plate if the specimen does not exceed the size limitations given by the sample transfer system.

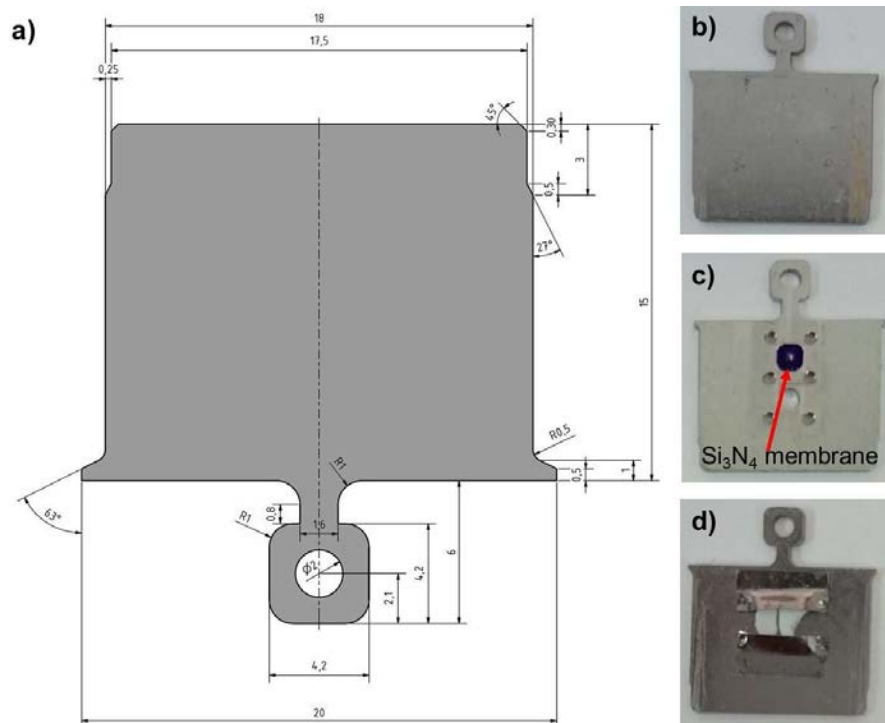


**Figure 4-5:** Technical drawing (a) and examples (b-d) of sample plates. b) Ta sample plate without specimen, for high temperatures; c) Stainless steel sample plate with windows, used for mounting standard 3 mm TEM samples, e.g.  $\text{Si}_3\text{N}_4$  membrane; d) Sample plate with MgO specimen, mounted by spot-welding it in place using of a support foil.

Sample plates can be inserted into the stage of the analysis chamber and investigated using the available techniques. For maximum compatibility especially with AES, the specimen should be mounted below a sample plate with window.

Specimens mounted on top of a sample plate can be prepared by annealing, sputtering and PVD of metals or organic compounds and analyzed by LEED in the preparation chamber using the receptacle of the manipulator. **Sample plates with features that extend below the plate, like specimens mounted below a window in the sample plate, MUST NOT be inserted into the manipulator, as they might seize.**

The sample plates (and attached specimens) can be heated radiatively or by electron bombardment using a filament that is integrated into the manipulator below the sample receptacle. Electron bombardment is realized by a negative high voltage supplied to the filament vs. the grounded sample plate. Due to the high temperatures in electron bombardment, sample plates made from refractory metals (Ta, W, Mo) are used. A manipulator temperature of 950 K / 677 °C (integrated thermocouple at copper parts) must not be exceeded; LN<sub>2</sub> cooling of the manipulator may be necessary to fulfill this requirement.

The VT sample holders present more complex but also more versatile option for mounting specimens. The basic setup of such a precursor is a molybdenum base plate with four threaded rods and a tungsten-coated ceramic top plate. The threaded rods can be fitted with spacers, contact bars, ceramic isolators and other parts to attach the specimen and provide heating/cooling options. Figure 4-6 shows an example of such a sample holder which was used for experiments on a rutile TiO<sub>2</sub>(110) single crystal. The TiO<sub>2</sub>(110) crystal is held in place by a 0.1 mm thick Ta foil, and can be heated by electron bombardment via the integrated filament. In order to accelerate the electrons, a negative potential is applied to filament and shielding foil (Figure 4-6c) vs. the grounded Ta Foil and TiO<sub>2</sub> crystal. Using this setup, sample temperatures in excess of 1000 K can be realized.

There is also the possibility of heating samples radiatively, via an integrated (resistive) PBN heater (e.g. Ag and Au single crystals), or resistively (e.g. for Si samples), via a direct current.

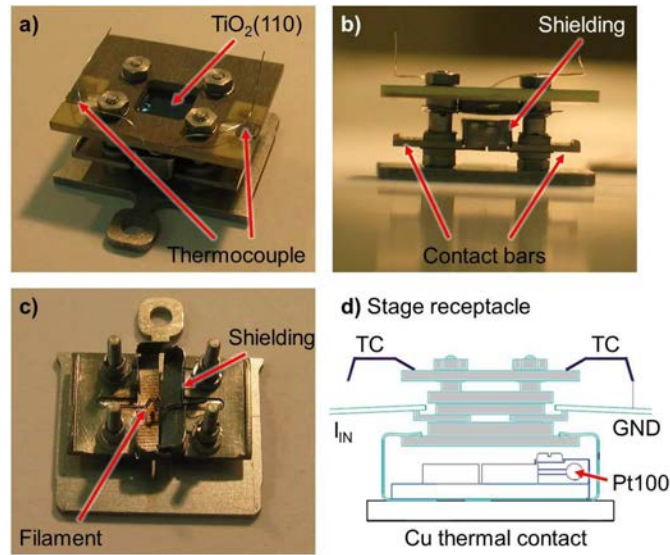


**Figure 4-6:** VT sample holder with integrated filament for heating via electron bombardment: (a) assembled sample holder with  $\text{TiO}_2(110)$  specimen, (b) side view, (c) filament level, (d) contacts.

## 4.2 PolLux STXM

Scanning transmission (soft) X-ray (spectro-)microscopic measurements were performed at the PolLux beamline located at the Swiss Light Source (SLS) in Villigen (CH).<sup>83</sup> The standard STXM setup uses high brilliance synchrotron radiation light that is focused on the sample by a Fresnel zone plate. Photographs of the PolLux beam line and schematic view of the beam focusing are presented in Figure 4-7.

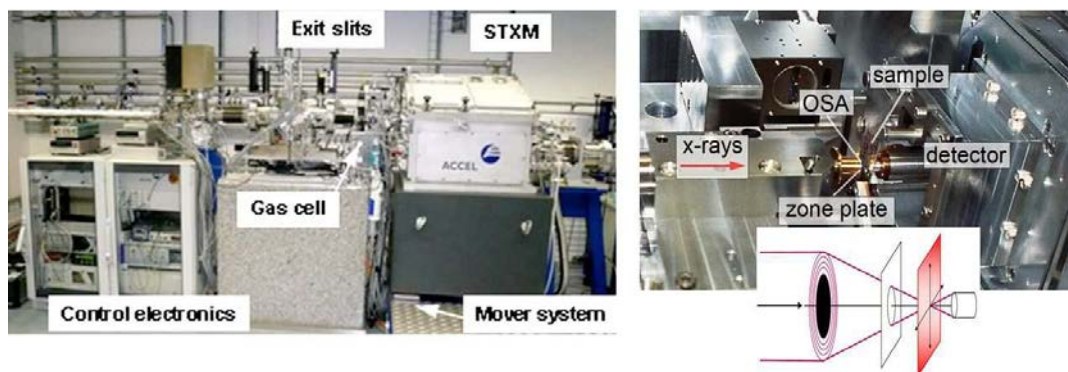


*Figure 4-7: Photographs of the PolLux beamline at the Swiss Light Source. Left: overview; right: X-ray focusing, sample stage and detector setup, including schematic.*

In order to record an image, the beam is focused for the given X-ray energy and the sample is raster-scanned through the stationary focal spot, while the transmitted photon intensity is recorded using a photo multiplier tube. The raster scan is realized via a coarse motor stage for steps larger than few  $\mu\text{m}$  and a piezo stage for smaller steps; the stage position is controlled via interferometric feedback. The lateral resolution depends on the used zone plate and can be below 10 nm.<sup>99</sup> Depending on the experimental requirements, samples can be investigated under low pressure helium or high vacuum conditions. The latter mode was used in the presented experiments in order to reduce contaminations due to X-ray or photoelectron induced deposition of residual gasses. In routine operation, 30 to 40 nm are readily achieved. Near-edge X-ray Absorption Fine structure (NEXAFS) spectra are recorded by consecutive scanning of the investigated area with varying photon energy. Magnetic properties of the sample can be studied by X-ray Magnetic Circular Dichroism (XMCD) measurements using circularly polarized X-rays, as provided by the synchrotron. An electromagnet mounted in close proximity to the sample provides the necessary magnetic fields.

### 4.3 Samples and Sample Preparation

#### 4.3.1 Rutile $\text{TiO}_2(110)$

Titanium dioxide crystals (rutile, (110)-orientation) were purchased from PiKem and Crystek. The as-received, transparent, yellowish crystals show pronounced charging in SEM due to the low conductivity of the unprepared crystal, which exhibits a band gap of approx. 3.0 eV.<sup>100</sup> During the preparation process, defects known as color centers are formed in material, which increase the conductivity.

The crystals were prepared by repeated cycles of Ar ion milling (1 keV,  $4 \times 10^{-6}$  mbar Ar pressure) and annealing. Annealing was performed in a VT sample holder or on a Ta sample plate via electron bombardment (indirect, i.e. no electron irradiation of the titania crystal itself). Temperatures were measured using a pyrometer ( $\epsilon = 0.2$ ). The annealing temperatures (1000 to 1200 K) and sputter duration (few min to 1 h) were adapted to the progress of the surface preparation, which was monitored by AES (contaminations), LEED (long range order) and STM (terrace size). The characteristic LEED pattern of the  $\text{TiO}_2(110)$ - $1 \times 1$  surface is shown Figure 4-8.

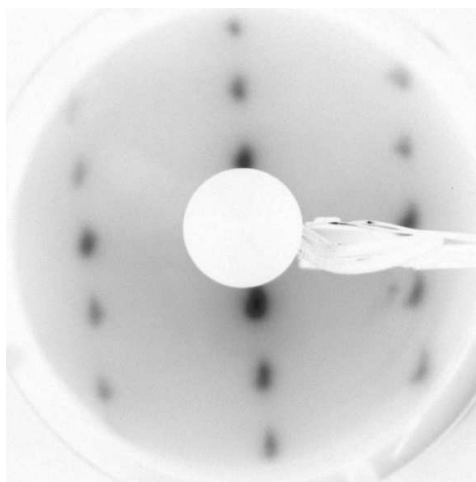


**Figure 4-8:** LEED pattern of a rutile  $\text{TiO}_2(110)$ - $1 \times 1$  surface at an electron energy of 54 eV. The samples was prepared by several ( $>10$ ) cycles of sputtering and annealing as described above.

### 4.3.2 Ag(111)

The Ag(111) single crystal ( $2 \times 10 \text{ mm}^2$ ) with an orientation accuracy  $<1^\circ$  was purchased from MaTecK GmbH, Germany. It was prepared by repeated cycles of Ar ion sputtering (1 keV,  $4 \times 10^{-6}$  mbar Ar pressure) and annealing to 850-860 K, followed by a slow cool-down (15 K / min) to RT. The annealing is performed in a VT holder equipped with a PBN heating element for radiative heating. The sample temperature is measured using a type K thermocouple inserted into a hole drilled into the side of the crystal. A Eurotherm PID controller is used to provide reproducible preparation conditions.

The surface quality was assessed using LEED, AES and SEM.

### 4.3.3 Silicon and Silicon oxides

Silicon and silicon oxide are widely used in semiconductor manufacturing and research and thus are readily available in high quality and quantity. Silicon samples used during the course of this thesis were purchased from the Materials Institute, Warsaw (PL). The laser-cut, polished (100) and (111) samples ( $10 \text{ mm} \times 1 \text{ mm}$ , thickness 500  $\mu\text{m}$ ) are stored under ambient conditions, which leads to the formation of a thin layer of silicon oxide,  $\text{SiO}_x$  (few nm, depending on the conditions). This native  $\text{SiO}_x$  layer has been shown to be suitable for EBISA without any treatment.

Clean, atomically ordered Si(100)- $2 \times 1$  and Si(111)- $7 \times 7$  can be prepared by resistive annealing of the sample in UHV. This process removes the  $\text{SiO}_x$  layer via the reaction  $\text{SiO}_2 + \text{Si} \rightarrow 2 \text{SiO}$  and subsequent thermal evaporation of the silicon monoxide.<sup>101</sup> First, the sample is degassed at red-glow ( $I_{\text{DC}} = 0.8 \text{ A}$ ,  $T_{\text{Pyrometer}} \approx 1000 \text{ K}$ ) for at least one hour. After degassing, the sample was flash-annealed, i.e. the sample was subjected to groups of five times 5 seconds of high current heating followed by 10 seconds of cool-down for increasing currents. The currents were 1.5 A ( $\approx 1200 \text{ K}$ ), 2.4 A ( $\approx 1330 \text{ K}$ ), 3.5 A ( $\approx 1430 \text{ K}$ ) and 4.2 A ( $\approx 1500 \text{ K}$ ). After a last set of flash-annealing steps, the current was set to 0.8 A and slowly reduced to zero over 10 min. This procedure yields clean (checked by AES) and well-ordered surfaces (LEED and STM) for both Si(100) and Si(111).

Thin  $\text{SiO}_2$  and  $\text{SiO}_x$  layers on Si surfaces were either purchased (300 nm thermal oxide, Crystek GmbH) or prepared by annealing the freshly prepared Si(100) surface in  $\text{O}_2$  under defined conditions.<sup>14</sup>

#### 4.3.4 Silicon Nitride Membranes

Transmission microscopy techniques such as STXM and TEM require transparent samples. Thin silicon nitride membranes are a common choice for solid supports. Such membranes (100 nm, 500  $\mu\text{m} \times 500 \mu\text{m}$ , on TEM-standard 3  $\times$  3 mm Si frames) were purchased from Plano EM, mounted on a self-constructed sample plate (see Chapter 4.1.4), and used without further treatment.

It is known that SiN membranes also exhibit a native oxidation layer when stored under ambient conditions for a prolonged time.<sup>102</sup> This native oxide has also been activated using the electron beam in the EBISA process.<sup>12,13</sup>

#### 4.3.5 STM Tips

STM tips were prepared by electrochemical etching of 0.3 mm tungsten wire using a modified wire loop approach.<sup>103,104</sup> The schematic view is given in Figure 4-9.

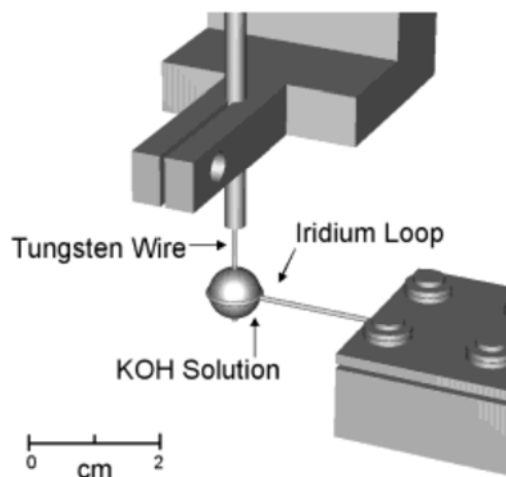


**Figure 4-9:** Schematic view of the wire loop setup for electrochemical etching of STM tips from tungsten wire. Reprinted from ref. <sup>104</sup>.

A Pt/Ir loop was used as the cathode, while the tungsten wire acts as the anode in the etching circuit. An aqueous solution of KOH (2 to 5 mol/l) is used as the etchant. In this setup, the tungsten wire extends through the drop of KOH solution suspended in the wire loop. When a DC voltage is applied, the overall reaction  $W(s) + 2 OH^- + 2 H_2O \rightarrow WO_4^{2-} + 3H_2(g)$  proceeds to dissolve the tungsten wire. The etch current is controlled in this case, as this allows to directly influence the etch rate. The solution is carefully replaced once

the evolution of hydrogen bubbles ceases. When the wire breaks due to the etching process, the lower part falls down and is collected, as this part of the etched wire yields the most promising tips.

The as-bought W wire is straightened and cleaned using isopropanol in an ultrasonic bath before use. As a first step, a rough etch is performed at 35 mA until the wire diameter is sufficiently reduced (approx. to 20% of the original diameter, approx. 3 min etch time), followed by a fine etch at 3 mA, which yields the final tip (5-10 min).

The tips are cleaned immediately by a thorough, careful rinse with distilled water and inspected using optical and scanning electron microscopy (MA40, Carl Zeiss Microscopy GmbH). Figure 4-10 shows a series of SEM images of tips prepared according to the described procedure. The tips are selected according to their sharpness and general shape (short, concave tips are preferred) using such SEM images. Suitable tips are installed into a tip assembly, which is then transferred into the MULTISCAN Lab system and used without further treatment.

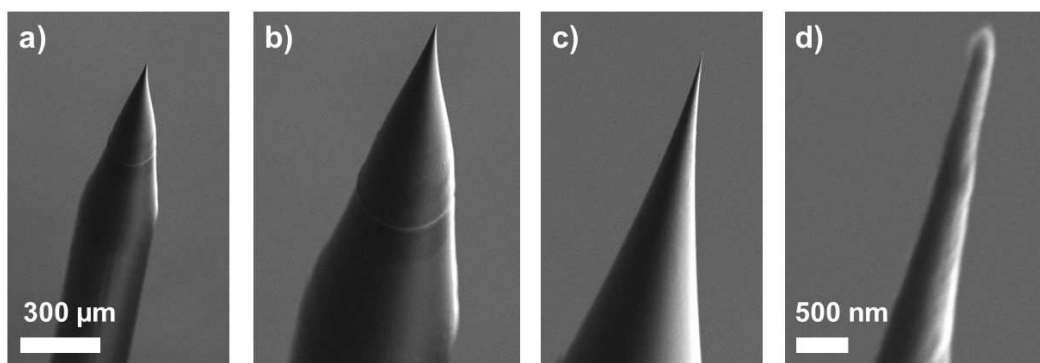


**Figure 4-10:** SE micrographs of an STM tip at increasing magnification. The tip was prepared by electrochemical etching of a tungsten wire using 2 mol/l KOH solution in a two-step rough/fine etching procedure. See text for details.

## 4.4 Precursors

### 4.4.1 Iron pentacarbonyl - $\text{Fe}(\text{CO})_5$

Iron pentacarbonyl ( $\text{Fe}(\text{CO})_5$ ) was purchased from ACROS Organics with a specified purity of 99.5%. The quality of the precursor gas was analyzed with a quadrupole mass spectrometer in a dedicated gas analysis chamber (base pressure  $2 \times 10^{-9}$  mbar). Figure 4-11 contains a mass spectrum of  $\text{Fe}(\text{CO})_5$  after purification by repeated exposure to vacuum for short amounts of time; the probable fragments are indicated. The main fragments are separated by 28 m/z, which corresponds to the loss of one CO ligand.

The purification process removes the CO that is produced due to aging, e.g. polymerization, of the precursor. In order to fabricate nanostructures in a process that involves autocatalytic growth, it was found that the Fe/CO (m/z = 56 vs. m/z = 28) peak intensity ratios can be used as an indicator for the gas quality. A ratio of at least 0.05 is required for successful growth experiments.

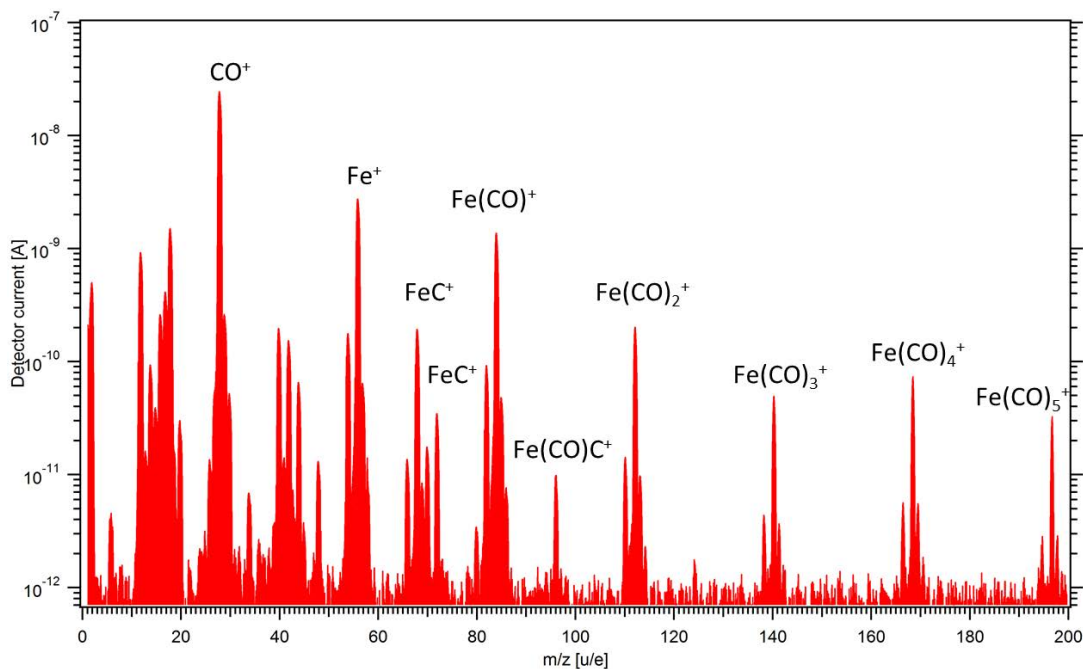


**Figure 4-11:** Mass spectrum of  $\text{Fe}(\text{CO})_5$  recorded in the gas dosing chamber at a pressure of  $3 \times 10^{-7}$  mbar. Fragment species are indicated for the most prominent m/z features. The natural isotope pattern of iron ( $^{54}\text{Fe}$  ~6%,  $^{56}\text{Fe}$  ~92%,  $^{57}\text{Fe}$  ~2%) is responsible for the peak triplet observed for Fe-containing fragments.

#### 4.4.2 Cobalt tricarbonyl nitrosyl - $\text{Co}(\text{CO})_3\text{NO}$

Cobalt tricarbonyl nitrosyl (specified purity: *for synthesis*) was purchased from abcr GmbH & Co. KG. Figure 4-12 contains a mass spectrum of the compound; probable fragments are indicated. A peak separation of 28 m/z indicates loss of a CO, 30 m/z indicates loss of NO.

Similar to  $\text{Fe}(\text{CO})_5$ , the Co/CO ratio (m/z = 59 vs. m/z = 28) was used to monitor the gas quality. The commonly observed values are greater than  $\sim 0.1$ , which is sufficient to facilitate both EBID and autocatalytic growth. Precursor gases of lower ratios have not been investigated in detail.

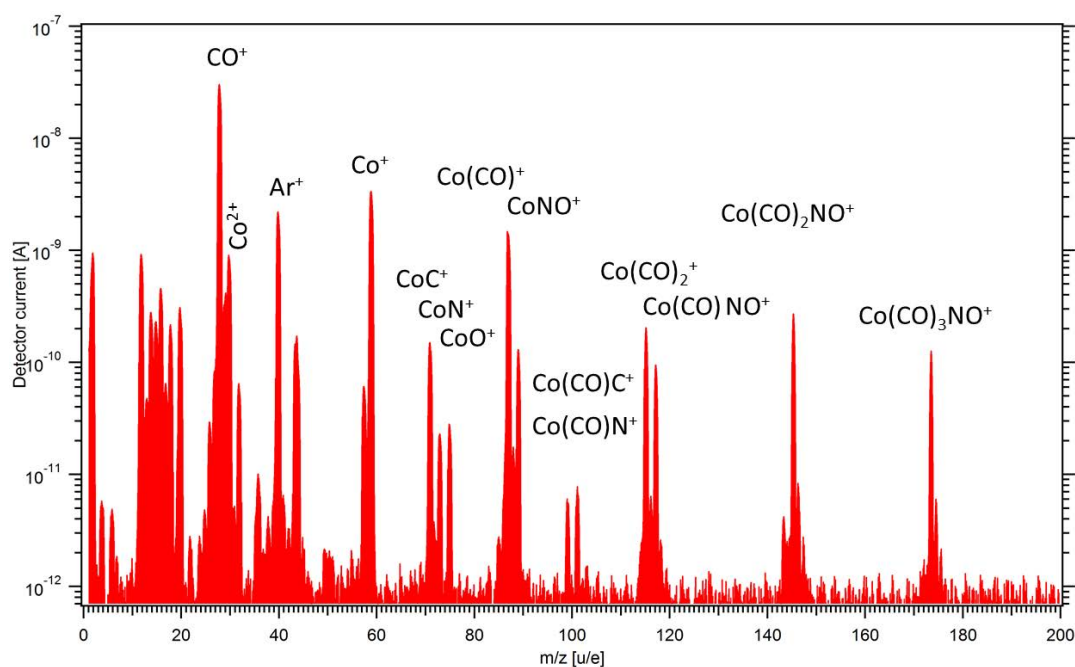


**Figure 4-12:** Mass spectrum of  $\text{Co}(\text{CO})_3\text{NO}$  recorded in the gas dosing chamber at a pressure of  $3 \times 10^{-7}$  mbar. Likely fragment species are indicated for the most prominent m/z features.

#### 4.4.3 Dicobalt octacarbonyl - $\text{Co}_2(\text{CO})_8$

Dicobalt octacarbonyl (specified purity: *for synthesis*) was purchased from Merck KGaA. The red, coarse powder is shipped under Argon and contains n-Hexane as a stabilizer. During the purification process, the n-Hexane is pumped off by careful evacuation of the precursor container. Due to the low decomposition temperature (approx. 60 °C), heat-assisted degassing is not possible. Thermal decomposition at elevated temperatures ( $>40$ -50 °C) was found to

leave a reflective Co film on the inside of the glass container due to a CVD process. At room temperature, conversion to a black powder is observed after prolonged exposure to vacuum once the stabilizer is removed. This is consistent with reports of dimerization to  $\text{Co}_4(\text{CO})_{12}$  and release of CO under vacuum conditions, e.g. studied by Tannenbaum and Bor.<sup>105</sup>

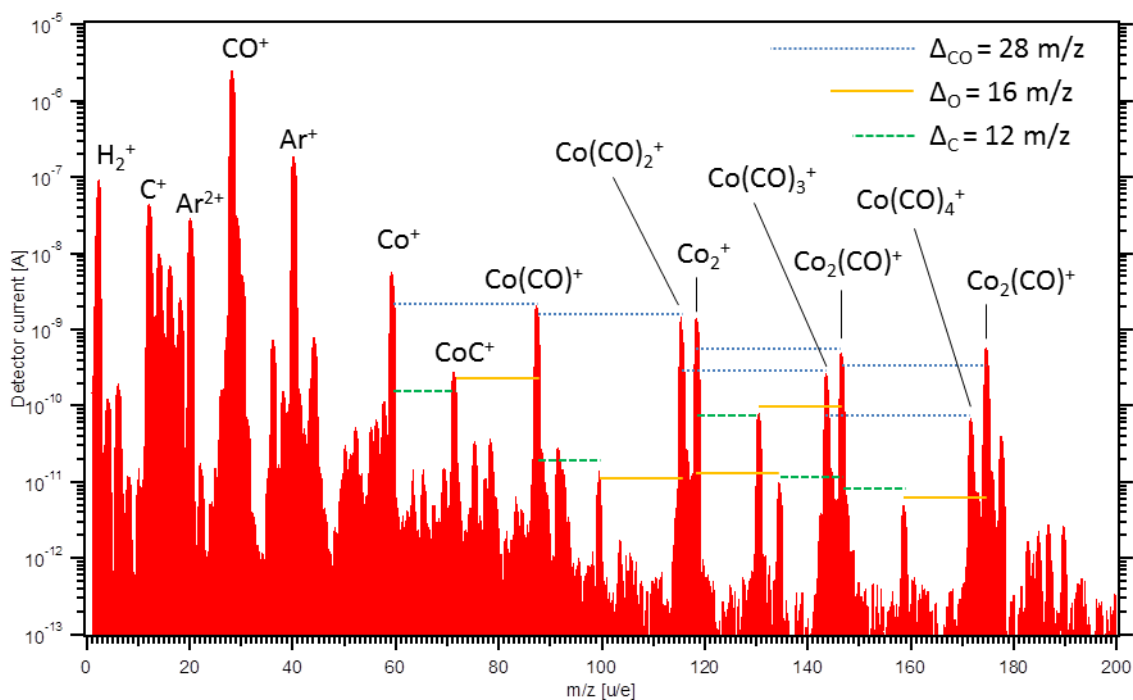


**Figure 4-13:** Mass spectrum (log scale) of  $\text{Co}_2(\text{CO})_8$  recorded in the gas dosing chamber at a pressure of  $3 \times 10^{-7}$  mbar. The separations between the peaks correspond to missing atoms or groups of atoms and are indicated by blue (CO), yellow (O) and green (C) markers.

It was observed that at low temperatures (2-6 °C) and under vacuum, stabilizer-free  $\text{Co}_2(\text{CO})_8$  powder undergoes Oswald ripening via sublimation, leading to the formation of larger (mm-sized) grains. The timescale under those conditions is months. It was observed that these grains sublime very easily under vacuum conditions and do not leave black residue. In order to exploit this behavior, an apparatus was built for more rapid vacuum recrystallization of the material. The setup is presented in Figure 4-14. A  $\text{Co}_2(\text{CO})_8$  feedstock is placed into glass vessel under inert gas ( $\text{N}_2$ ) and attached to a fine vacuum pump ( $p < 10^{-1}$  mbar). The stabilizer is removed by pumping at 20 °C for some minutes. Then, the tube bottom is placed into a heat bath (35 °C), while an ice bath is added further up the gas stream. The  $\text{Co}_2(\text{CO})_8$  sublimates at the heated bottom and solidifies at the cooler regions to form bright red, translucent crystals.

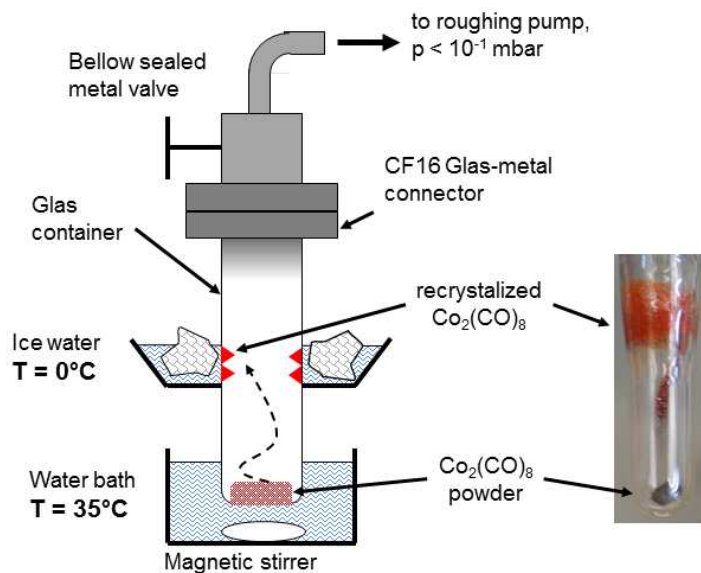


**Figure 4-14:** Setup for the vacuum recrystallization of  $\text{Co}_2(\text{CO})_8$ . The feedstock of  $\text{Co}_2(\text{CO})_8$  is carefully degassed to remove the stabilizing agent (hexane) and slowly heated up to about 35 °C under vacuum. An ice bath is added to the outside of the reaction vessel further up the gas stream. In the course of about 30 min, red  $\text{Co}_2(\text{CO})_8$  crystals are formed at the cool sections.

Unfortunately, it was not possible to evaluate the impact of the recrystallization on the EBID/EBISA behavior, as it was not possible to dose any  $\text{Co}_2(\text{CO})_8$  into the analysis chamber after the first experiment (see Chapter 6.5 for further details).

## 4.5 Electron trajectory simulation

The software package CASINO (2.42)<sup>92</sup> provides tools for the simulation of backscattered electrons (BSE) trajectories using Monte-Carlo techniques. The program version 2.42 does not allow for the simulation of secondary electrons ( $E_{\text{min}} = 50 \text{ eV}$ ).

In order to set up a simulation, one has to specify the geometry and chemical composition of the sample in a first step. The geometry in CASINO 2.42 is limited to planar samples, which can be divided into parts of different composition. Horizontal stacking of regions can be used to simulate grains boundaries, while vertical stacking of regions is a model for layered substrates. It is also possible to simulate freestanding membranes. The thickness, chemical composition and density of each layer can be specified individually. The setup of the

electron beam includes PE energy, angle of incidence and beam diameter (Gaussian beam) and number of electrons to be simulated. It is also possible to change the underlying physical models used for the simulation.

While CASINO 2.42 is a single-thread application, i.e. it does not support modern multi-core processors, it is possible to increase the simulation output by running parallel instances of the program. In the simulation, the trajectories of individual electrons are simulated, while the relevant data is collected. The software discards the trajectory data once the cut-off energy (usually  $E < 50$  eV) is reached or the electron exits the simulated model, i.e. only the resulting information is recorded.

The results of a simulation run are displayed in the GUI, mostly in the form of histograms. The histograms can be exported as images or in the form of raw data, which can be further processed in external applications to extract the BSE exit radius and other information.

## 4.6 Software and Data Processing

Scanning tunneling microscopy data was recorded using MATRIX V3.0 and V3.1 (Omicron Nanotechnology). Since MATRIX application offers no (or very limited via VERNISAGE) data processing capabilities, the micrographs are processed using WSxM (Nanotec Electronica S.L.).<sup>106</sup> WSxM is freeware and provides versatile functionality for the processing of scanning probe microscopy data, especially AFM and STM, and is able to import most standard file formats used in such environments. The most recent development versions of WSxM were used, i.e. WSxM v5.0 Develop 1.2 to 6.0.

Auger electron spectroscopic data was recorded using EIS v.2.4.24.97 and after a system upgrade using MATRIX for electron spectroscopy V3.1. The spectra were processed using Igor V6 (Wavemetrics). Commonly, the raw data was slightly smoothed using the integrated algorithms. Peak areas were determined by numerical integration.

The STXM data were analyzed using aXis2000 ([unicorn.mcmaster.ca/aXis2000.html](http://unicorn.mcmaster.ca/aXis2000.html)). aXis2000 is an IDL-based GUI for the processing of X-ray absorption micrographs and spectra, which was developed for that purpose and includes all the relevant data processing features. This includes convenient extraction of spectra from the recorded data and conversion from transmission to optical density data.



## 5 Lithography

The fabrication of arbitrarily shaped nanostructures by any focused electron beam technique, be it resist based electron beam lithography (EBL), EBID or EBISA, requires precise, spatio-temporal control of the electron beam point of impact. In industrial processes, like mask fabrication for photolithography, dedicated electron beam writing tools from companies like Raith, JEOL, Crestec or Vistec/Leica are used. Most of these systems are optimized for high electron energies (50 – 100 keV) and rely on electrostatic beam deflection. They incorporate advanced features like write field stitching, nm-precise sample positioning, proximity effect corrections and clean-room compatibility.

In contrast to these dedicated systems, there is also a possibility of using the focused electron beam of a conventional SEM for lithography. In the simplest case, this can be accomplished with the standard scan modes of the SEM imaging software, while more advanced lithography is possible by adding dedicated beam control features, pattern generators and a fast beam blanker. Such systems are referred to as lithographic attachments. There are a number of commercial systems available, e.g. NPGS (JC Naby Lithography Systems<sup>107</sup>) or Elphy Quantum (Raith GmbH<sup>108</sup>) which can be added to the SEM's external inputs to turn it into a nanofabrication tool.

In the following chapter, the lithographic systems that are available at the UHV-SEM will be discussed in detail. It will be shown that the available solutions do not allow for full control of all aspects of the electron beam, which can pose problems when used for fundamental research. This is followed by an in-depth explanation of the development and working principles of the self-constructed lithography system “NanoScribbler”, which is tailored to the specific experiments and requirements of FEBIP research, with a special focus on the MULTISCAN Lab UHV-SEM.

## 5.1 General Considerations and Terminology

In electron beam based lithography, there are a number of important input parameters and strategies which potentially define the properties of the fabricated structure on the surface and thus have to be considered when a lithographic system is used. One determining parameter for most applications is the primary electron dose, which, for standard Gauss profile beams, depends on the PE beam current and the residence time of the electron beam (dwell time,  $t_d$ ). Obviously, these parameters suffice for spot irradiations, but for line and area structures also the step size  $\Delta x$ , i.e. the distance between two adjacent beam positions on the surface, has to be defined. This means that one has to distinguish between different types of electron dose: the spot or point dose  $d_s$  (in pC or nC), the line dose  $d_L$  (in C per distance, usually cm) and the area dose  $d_A$  (in C per area, usually  $\text{cm}^2$ ).

There are two different approaches to the lithography protocol: raster scan vs. vector scan.<sup>109</sup> In raster scan mode, the electron beam is directed along the same path as it would for a raster image scan, but for all positions that are not part of the design pattern, the beam would be blanked or skipped to the next position, thereby only exposing the targeted positions to electrons. The second, more common, approach is known as vector scan. In essence, the design pattern is broken down into a list of coordinates (“vectors”), which are sequentially approached and thus exposed by the electron beam. The main advantage of the vector scan approach is the shorter writing time compared to the raster scan, as it is not necessary to raster scan every position of the surface. There are also hybrid approaches and more intricate designs like shaped beams and so forth, which will not be discussed in detail. The interested reader is referred e.g. to the Handbook of VLSI Microlithography.<sup>109</sup>

## 5.2 Technical aspects

Most commercially available SEMs feature so-called external scan inputs, which are typically occupied by X-rays spectrometer appliances (EDX or WDX). For historic reasons, EDX or WDX systems usually are not designed for digital control of the SEM but rather add their own beam positioning by supplying control signals to the SEM via an external scan interface. The external scan inputs accept DC voltages to control the beam deflection unit of the SEM and can certainly also be used for lithography purposes. Scanning a pattern can be

accomplished by supplying the appropriate beam positions as DC signals. The input voltages are generated by digital-analog-converters (DACs) and supplied to the SEM via the external inputs, where they are transformed to be fed into the beam deflection unit. Figure 5-1 contains a schematic of the internal and external connections of the SEM control electronics that are used for signal generation.

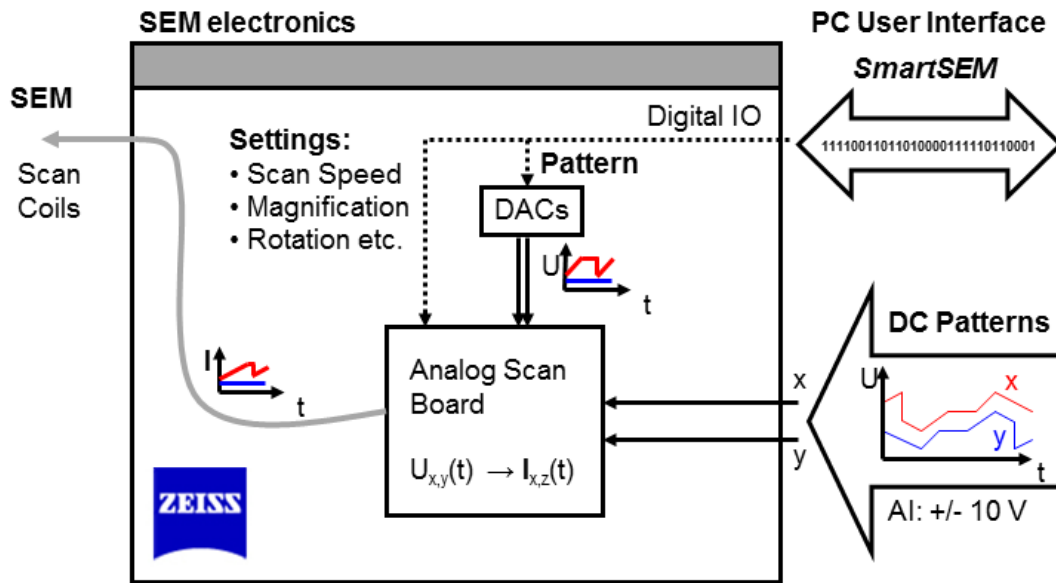


**Figure 5-1:** Schematic of the internal and external connections of the SEM control electronics used in signal generation. The digital interface (top right) connects to interface card of a PC running the SEM applications (SmartSEM, RemCon32) and supplies configuration data to the internal DACs, which supply the patterns during standard operation. The analog inputs for beam x- and y-deflection accept  $\pm 10$  V input signals via standard BNC connectors. Either type of signal is converted to the appropriate current for driving the magnetic scan coils by the analog scan board.

Zeiss SEMs work with high resistance inputs (BNC jacks) and an input voltage range of  $-10$  V to  $+10$  V for x- and y-deflection. The input voltages are interpreted as proportional deflections from the center position, i.e. the beam is centered for an input of  $0$  V for x and y. The deflection amplitude is not only dependent on the applied voltage input, but also on the magnification selected in the SEM software, so that accessible beam positions are restricted to the current field of view of the SEM image scan.

To be precise, the SEM images are recorded with an aspect ratio of 4:3, while the accessible beam position is based on a square field, i.e. 1:1 aspect ratio. This means that the

external inputs can direct the beam to some positions above and below the SEM image, but not to the left and right (see Figure 5-2).

As an example, for a magnification of 1000x corresponds (field of view: 114.3  $\mu\text{m}$  by 85.8  $\mu\text{m}$ ) an signal sweep from -10 to +10 V on the x-input (while maintaining 0 V at the y-input) produces a line of 114.3  $\mu\text{m}$  in the center of the image, while the same sweep would produce a line of 11.4  $\mu\text{m}$  for a magnification of 10 kx (field of view: 11.4 by 8.58  $\mu\text{m}^2$ ). As a consequence, the (theoretical) minimum step size  $\Delta x_{\text{min}}$  varies with the selected magnification. The minimum step size  $\Delta x_{\text{min}}$  is defined by the minimum separation of the voltage levels of the input source and represents not only the smallest separation of two adjacent beam positions, but also defines the grid of accessible points on the surface.  $\Delta x_{\text{min}}$  is equal to the FOV width divided by the number of available levels of the used digital-to-analog converter (DAC). The voltage levels are effectively pixel coordinates on a  $2^n \times 2^n$  plane, where n is the bit resolution of the applied DAC. For a 12 bit DAC, there are  $2^{12} = 4096$  different voltage levels, which corresponds to a  $\Delta x_{\text{min}}$  of 27.9 nm at 1 kx magnification and 2.79 nm at 10 kx. The different fields of view and reference systems are juxtaposed in Figure 5-2.

For lithography purposes, the magnification can be chosen to fit the size of the designed structures (AWGs, NanoScribbler) or set to certain defined fields of view (Elphy Quantum). It is also possible to set the magnification according to the required minimum step size.

The Gemini column uses an electromagnetic deflection system to feed the beam through an aperture disc with current-limiting apertures to select the beam current. In order to blank the beam, it can be directed onto a solid section of this disc where the electrons are absorbed. This electromagnetic internal beam blanker is slow ( $> 50$  ms) compared to a dedicated, electrostatic beam blanker. In addition, it can only be controlled via user interaction or via a remote interface (RS-232) of the SEM software. In either case, the latency is considerable, which limits the use for lithography.

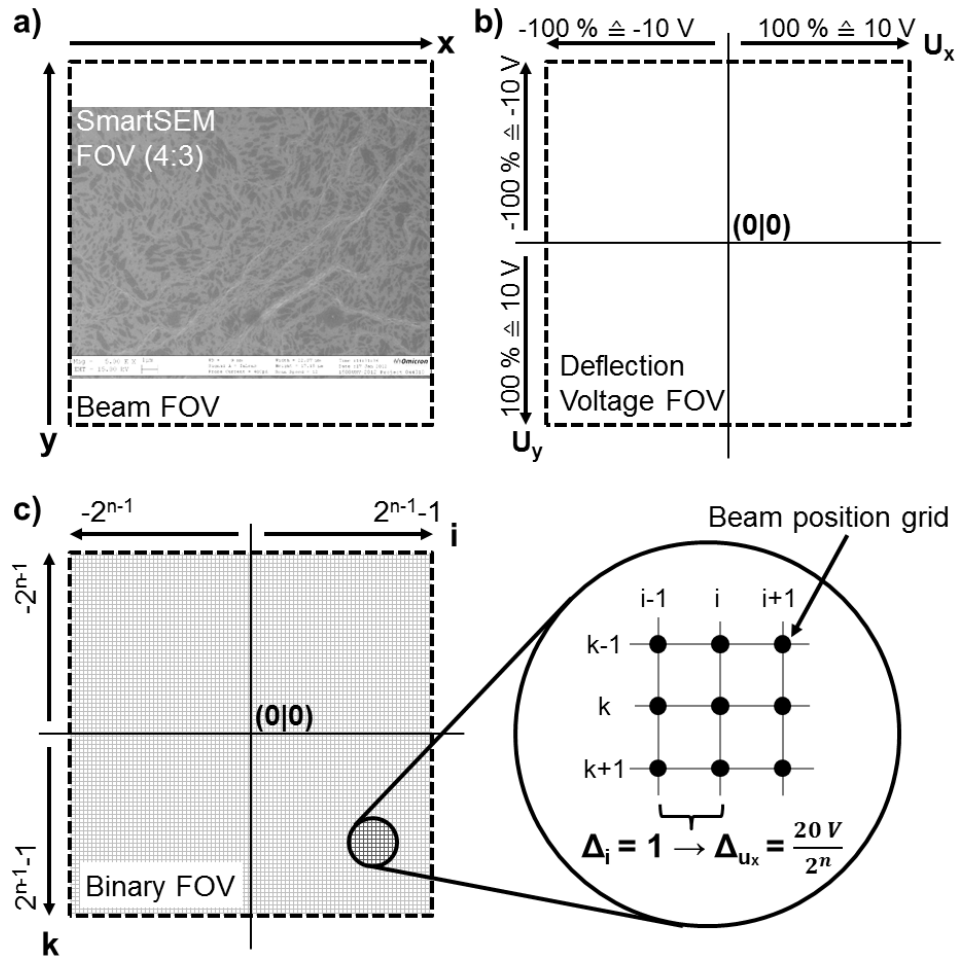


**Figure 5-2:** Reference systems for the beam position. a) SmartSEM and beam field of view (FOV) in real space coordinates ( $x/y$ ); b) Proportional deflection and corresponding DC signal ( $U_x/U_y$ ); c) Binary representation ( $i/k$ ) with  $n$  being the bit resolution of the DAC. The binary grid defines all positions on the surface the beam can target without further signal processing.

## 5.3 Available Lithographic Systems

### 5.3.1 SEM Software

The simplest form of lithographic beam control is the use of the built-in scan programs of the SEM software. The SmartSEM software provides image, line and point scans that can be used to fabricate area, line and spot irradiations. Those scan programs are optimized for imaging applications and thus using them for lithography can have serious drawbacks: there is no or very limited possibility of arbitrary shape exposures, the timing parameters are fixed and the dose calculations are far from intuitive due to waiting and replenishment times.

Two examples of EBI deposits fabricated using only the SmartSEM scan modes are presented in Figure 5-3. On the left, a peculiarly shaped crystallite on a gold (111) surface was decorated with an S-shaped feature by activating the spot mode and manually moving the cursor slowly along the desired path (a). This “hand writing” method can be considered as a simple form of lithography. The resulting feature is made up of what is usually considered as “beam damage”, i.e. most likely a thin carbonaceous deposit. Obviously, there is hardly precise control of the shape and the dwell time, i.e. the time spent at the various positions along the path, is inhomogeneous.

The image on the right shows  $\text{TiC}_x\text{O}_y$  deposits from titanium tetraisopropoxide (TTIP) on  $\text{Si}(100)$ .<sup>95, 110</sup> The imaging mode was used to expose two rectangular areas (dashed blue); the line mode was used to fabricate two crossing lines and the spot mode was used for two point irradiations (red circles). The most prominent features in that image are large deposits at the start of the line scans (green circles) and of the image scan (blue circles). These are unintentional deposits, i.e. artifacts, which were caused by the synchronization and beam settling periods that are part of the image and line scan routine.<sup>95</sup> During these periods, the beam is stationary at the starting coordinates of the respective structures, and thus, there will be an undesirable EBI deposition of material. To a lower extent this can also be seen at the beginning of each new line in the image scan (blue ellipses).

It is immediately apparent from Figure 5-3 that the use of the SEM software for lithography is restricted to preliminary and test exposures or as a measure of last resort if no alternatives are available.

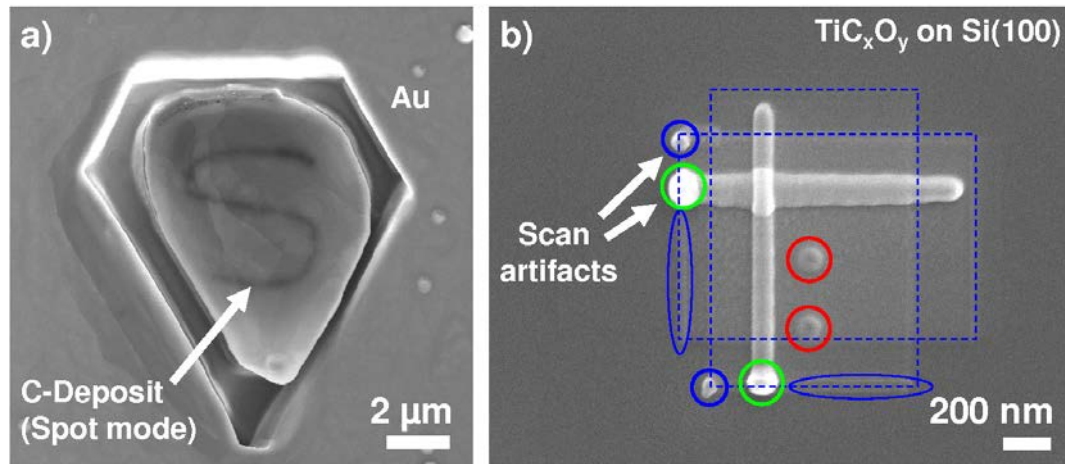


**Figure 5-3:** Examples of lithographic EBI deposits using the SEM software. (a) Au(111) single crystal surface with a conspicuous crystallite that was decorated with an S-shaped feature by dragging the spot exposure marker manual along the desired path, creating a carbonaceous deposit from residual gases. (b) TiC<sub>x</sub>O<sub>y</sub> structures by EBID of titanium tetraisopropoxide (TTIP) using the spot, line and image mode of SmartSEM. The blue and green circles and ellipses highlight artifacts (unintended deposits) due to the peculiarities of the scan modes. The red circles mark spot exposures. Reproduced from Schirmer<sup>95</sup>.

### 5.3.2 Elphy Quantum

Elphy Quantum (Raith GmbH, Germany) is a commercial lithographic attachment for SEMs and focused ion beam (FIB) systems. It consists of a software component (“Elphy”), which includes a GUI-based pattern design and exposure control application, and a dedicated PCI scan board (“Quantum board”) with 16 bit, 2.5 MHz DACs. The scan board also features additional DACs for alignment, a TTL output for controlling a (dedicated) beam blanker and an ADC to record SEM images from the SEM’s signal output BNC. In principle, this attachment can be used for any kind of e-beam based nanostructuring, but its target application is resist based electron beam lithography. In this regard, it allows for highly complex nanofabrication procedures by providing high resolution lithography, stage control, field stitching, write field alignment and so forth. The GUI based pattern design software can be used to prepare patterns to suit the need of virtually any experiment. It is also possible to import standard GDSII and other pattern files.

The system can be combined with a dedicated high-speed beam blanker. A beam blanker is a beam deflection device that is inserted into the electron column of an SEM to be able to turn the beam on and off very quickly. The use of electrostatic deflection elements allows for very

high switching frequencies and very short switching times.<sup>111</sup> The absence of such a device in the UHV-SEM limits the use for EBID experiments in some cases.

In addition, for EBL mainly the precise beam position and accurate dosing are required, while advanced timing options like fast repetitions for multiple-sweep exposures or waiting times are not supported. These timing options can play an important role in the EBID process, as e.g. replenishment times strongly influence the morphology and even the chemical composition of an EBI deposit.<sup>4, 7, 112-114</sup>

As a consequence, using Elphy Quantum for EBID in the MULTISCAN Lab can result in exposure artifacts which range from non-critical to major issues that compromise entire structures. A selection of typical artifacts in EBID structures is presented in Figure 5-4.

Figure 5-4a shows dot artifact in the top left corner (see arrow). This dot is the result of the beam being stationary during the switching of beam control from the SEM software to the lithography application. The switching process itself can take from 100 to 300 ms and requires user input, which further increases this time span.

Figure 5-4b shows several larger, circular deposits caused by the beam being stationary during the exposure as a result of data processing in a more complex pattern. Unlike before, these stationary phases are caused by the Elphy system itself as part of the lithography process. The pattern generator calculates the beam coordinates and transfers them to the DAC memory before they are exposed. Individual pattern components are computed separately and are transferred to memory one by one. If the computation is not completed before the next set of coordinates is required, the beam stops, i.e. remains stationary, to wait for further input. In a system that is equipped with a beam blanker, the beam would be automatically blanked on such occasions. In our setup, the beam remains unblanked and thus the electrons cause further deposition from precursor molecules on the surface. It is not possible to direct the beam to a non-critical position during these update times or control the timing of these events in Elphy Quantum.

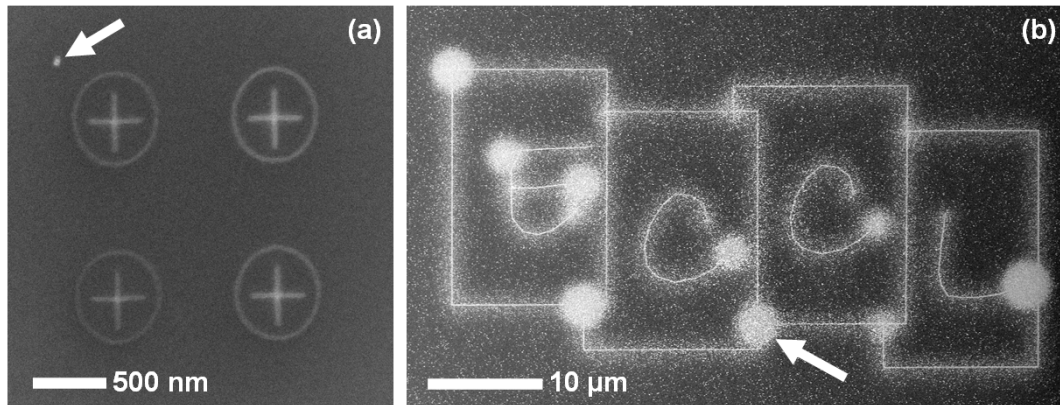


**Figure 5-4:** EBI deposits fabricated using Elphy Quantum with artifacts due to missing beam blanker. (a) Fe patterns from  $\text{Fe}(\text{CO})_5$  on  $\text{Si}(100)$  at 200 K. The white arrow marks the deposit at parking position of the electron beam that is irradiated between end of exposure and the manual beam blank. (b) Complex EBID Fe logo from  $\text{Fe}(\text{CO})_5$  on  $0.7 \text{ nm SiO}_2/\text{Si}(100)$  produced by repeatedly exposing the same structure 1000 times. The white arrow marks one of several circular artifacts due to the stationary, unblanked beam during the data processing of further elements of the pattern.

The type of artifact shown in Figure 5-4b is very pronounced for multi-sweep exposures. A multi-sweep exposure is realized by repeatedly exposing the same pattern at a fraction of the total dose, usually to avoid or reduce proximity effects. It is an uncommon mode of operation in resist based EBL and thus not natively supported by Elphy Quantum.

In summary, Elphy Quantum is a powerful tool for converting SEMs and FIBs to nanofabrication tools. It is not, however, an ideal tool for fundamental research that requires precise control of additional electron beam parameters besides the basic ones (electron dose, step size, dwell time, pattern coordinates). The lack of support for advanced timing and exposure options, like fast-repeating multisweep exposures, the inability to program a temporally defined course of events and the limited control of the beam during memory updates limits the use of the Elphy Quantum system for FEBIP in a basic research context.

### 5.3.3 Arbitrary Waveform Generators

A first step towards full control of the exposure in terms of timings, multi-sweep exposures and implementation of a continuous exposure strategy was to use arbitrary waveform generators (AWGs) for beam control. AWGs are essentially standalone DACs optimized for the generation of periodic voltage or current signals, e.g. sine or square waves or other test

signals for circuit testing, signal simulation and so forth. Using an AWG with a waveform that corresponds to a pattern in vector form, the voltage output can control the electron beam via the external inputs of the SEM. In order to use the full FOV of the SEM, a pair of AWGs (x/y) or a dual channel AWG is required.

In our setup, two HP 33120A with a DAC resolution of 12 bit (4096 unique voltage steps between -10 and +10 V) and a memory of 16,000 samples<sup>115</sup> were used mainly for line exposures in single and multi-sweep mode. For simple line exposures, a sawtooth-type wave is supplied to the x-AWG, which moves the e-beam from one edge of the FOV to the opposite one. The y-AWG is necessary for more complex shapes where y-deflection is required, i.e. essentially for all 2-dimensional structures. In addition, it was observed that there are some artifacts for line exposures at very high beam speeds, which can be partially counteracted by appropriate compensation signals on the y-channel (see Chapter 5.4.7).

The patterns were prepared either manually as a table of values in .csv format or automatically using a GUI-based software suit (Agilent IntuiLink Waveform Editor 1.6.0, 2008). The pattern, amplitude and timing information were transferred to the AWGs via an RS-232 connection. An additional TTL pulse generator (UPG 100, ELV) was used to synchronize the x- and y-AWGs. The synchronization of the two independent AWGs is not perfect, which can lead to artifacts (Figure 5-5).

With this setup it is possible to irradiate line structures in single and multisweep mode with defined step sizes, dwell times, waiting times and most importantly without artifacts due to unscheduled breaks in the pattern output. The absence of a dedicated beam blanker in the system is an issue, but the position of the beam during e.g. waiting times can now be controlled by the user. It is for example possible to direct the beam to a waiting position, where the resulting artifact does not affect the deposition of the intended nanostructure (c.f. Figure 5-5, right side).

Despite these improvements, the AWG-based lithography still suffers from a number of drawbacks that hinder the routine operation of such a setup. A major one is the limited memory size of the HP 33120A. At 16,000 samples, i.e. coordinates, the achievable complexity of the structures is quite limited and it is almost impossible to fabricate area deposits like filled squares and the like. In addition to the lack of memory, the 12 bits of output resolution translate to a minimum step size that is  $1/4096^{\text{th}}$  of the FOV width compared to the  $1/65536^{\text{th}}$  offered by the 16 bit DACs of the Quantum board. This in turn also limits the size of the structure for a given step size. A defined step size of 10 nm results in a maximum structure size of  $(40960 \text{ nm})^2$  using the AWGs, and  $(655360 \text{ nm})^2$  for Elphy Quantum.

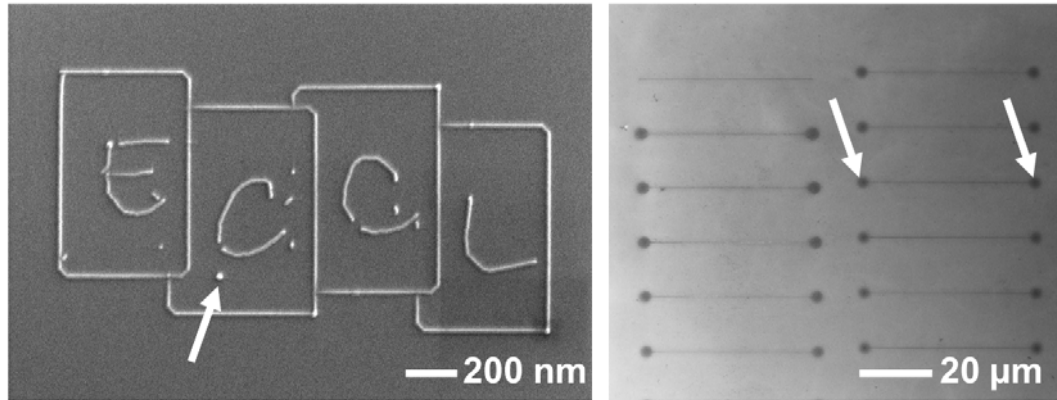


**Figure 5-5:** Examples of EBI deposits exposed using two HP 33120A arbitrary waveform generators. Left: 2D shape, multi-sweep exposure, TTIP on Si(100); right: multi-sweep line exposures, IPC on 300 nm SiO<sub>x</sub>/Si. The image on the left shows a test logo that uses half of the available memory of the AWGs. All lines are single-pixel wide. The artifacts (arrow) are attributed to synchronization issues of the x- and y-ARB. The sweep frequency is 50 Hz with a pixel dwell time of 5.6 μs. The micrograph on the right contains an array of 45 μm wide lines with 625 Hz repetition frequency. The dark areas at the start and end of every line are the result of intentional, predefined beam parking at those positions. The line segments in the middle remain unaffected by the parking artifacts.

Additional problems arise from the slow data transfer of the RS-232 connection (few seconds per pattern), the imperfections in the synchronization of two independent AWGs and also the lack of a suitable GUI for faster processing. Dedicated lithography programs calculate the U(t) pattern from the real space representation of the pattern, whereas the IntuiLink Waveform Editor requires composing waveforms directly as a U(t) pattern. This is almost impossible for complex patterns.

The AWG setup allows for more control of the exposure parameters compared to the Raith system, especially for fast multisweep exposures, works well for simple structures, and also provided valuable insights into the workings of the external-input based lithography, but still suffers from a number of hardware and software limitations.

## 5.4 NanoScribbler - a custom lithographic attachment

The experiments using the AWGs showed that it is possible to use generic DAC hardware for the control of the e-beam position via the external inputs, and that limitations due to the missing beam blanker can be overcome by the exposure design. Based on this knowledge, a lithography setup was developed with off-the-shelf hardware and self-programmed software and named “NanoScribbler”.

The aim of NanoScribbler is to provide a convenient user interface for the fabrication of nanostructures for scientific purposes with full control over all relevant parameters and no restrictions due to limitations of commercial products. The main focus of the software part of NanoScribbler is the reliable and reproducible fabrication of test patterns with high precision and versatile scanning modes, e.g. multi-sweep exposure and defined waiting times, while not relying on a dedicated beam blanker. In the following chapter, this setup and some of the development steps will be discussed in detail.

### 5.4.1 NanoScribbler Hard- and Software

The hardware of this project is comprised of a workstation computer with an off-the-shelf, PCI-express based DAC card. The requirements for the card were:

- Large memory to avoid stopped beam incidents due to data transfer (>8 MS)
- Fast sampling rate to allow for fast write speeds and flexible timings (>5 MS/s)
- Sufficient DAC resolution (>12 bit, 4096 steps).
- Synchronized dual channel output to avoid synchronization errors
- Hardware timing, i.e. OS-independent clock

The selected M2i.6021-exp (Spectrum Systementwicklung Microelectronic GmbH, Grosshansdorf, Germany) is a dual channel PCI Express card with 14 bits of output resolution, sample rate of 60 MS/s and 128 MS of onboard memory. The standard output range of  $\pm 3.3$  V is amplified to  $\pm 10$  V using a specially designed amplifier module (Mi.6xxx-Amp). The internal clock provides sampling times ranging from 1 ms ( $f_s=1$  kHz) to  $\sim 16.7$  ns (60 MHz). The supported output modes are single shot (i.e. single exposure), multi shot (i.e. multi-sweep exposure) and streaming output, in which case the onboard memory acts as a FIFO (first in first out) buffer.

In addition to the DAC card, the workstation is also equipped with a PCI board for the stage position readout (IK220, Dr. Johannes Heidenhain GmbH, Traunreut, Germany) and

another PCI board that provides four RS-232 channels. These are used for connections to various compatible devices. The most important connection is made to the SEM computer, which runs the server program RemCON32<sup>116</sup> (Appendix A – Communication Protocols) that enables remote control of the SEM. In addition, the vacuum gauges controllers (analysis chamber: PGC2; preparation chamber: NGC2, Arun Microelectronics Ltd.) provide pressure data via this interface. For future use there is also a connection to the stage control subsystem of the Matrix Control Unit (see Chapter 5.4.8). A schematic of the connections is shown in Figure 5-6.

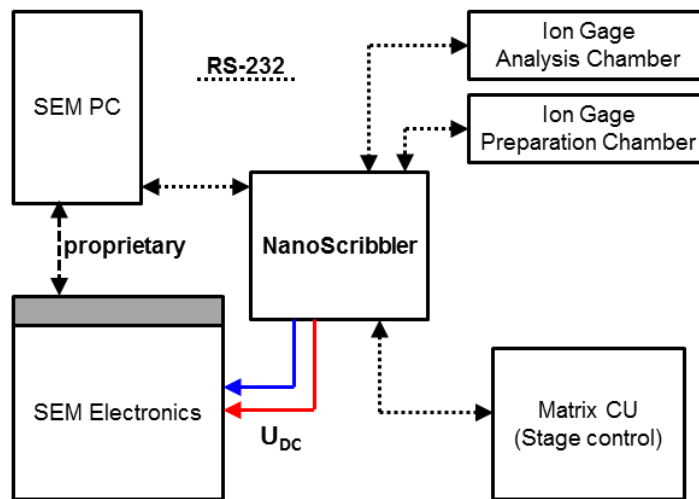


**Figure 5-6:** Connection diagram of the NanoScribbler system. RS-232 connections are available for pressure readout of the ion gauge controllers (PGC2/NGC2, Arun Microelectronics Ltd.), for stage control via the Matrix CU, and for SEM control via the RemCON32 server running on the SEM PC. The latter is connected to the SEM electronics via a proprietary interface using a standard SCSI cable. The control voltage connection  $U_{DC}$  comprises two separate coax cables (BNC on SEM electronics, SMB on DAC side).

The workstation (Core i5-660, 4 GB RAM) runs on Windows XP (32 bit) and provides a LabVIEW 8.6 (National Instruments) installation as the software development platform. LabVIEW was chosen as the development platform after some test experiments using a legacy DAC board which showed promising results. LabVIEW is well-suited to all kinds of measurement and control tasks, is an easy to learn, high level language and offers a large library of complex functions and subroutines. It also provides very simple access to the implementation of a graphical user interfaces (GUI). In addition, it makes implicit use of multiprocessor environments if applicable. Alternative programming languages like C/C++ or

others may offer faster and more optimized machine code, but as the exposure runs independently of the OS and GUI on the M2i.6021-exp board in our case, the code execution is not primarily time-critical.

### 5.4.2 Graphical User Interface Layout

NanoScribbler is designed as a compilation of tools that can be accessed from a main graphical user interface (Figure 5-7). These tools are separate entities (virtual instrument or VI in LabVIEW terminology) that are called from the main window and open up a new GUI sub-window (sub-GUI), where the respective tasks are performed. Only one sub-window can be active at a time. The sub-GUIs contain the interface elements, i.e. data in- and output fields and command structures like buttons, and provide a frontend to the algorithms.

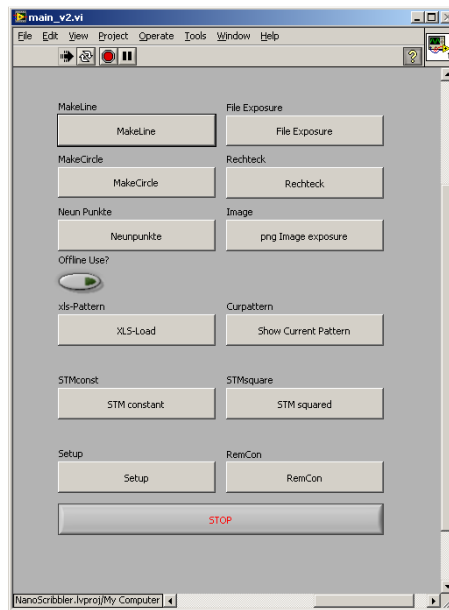


**Figure 5-7:** NanoScribbler main window. All lithography tools are accessible from this screen.

LabVIEW is a high-level graphical programming language, which means that the program code is actually a 2D diagram with functional entities representing the various elements of conventional programming. Icons represent GUI elements, functions and constants, and are connected by wires which determine the data flow and, implicitly, also the program flow. Sub programs can share program code in the form of sub-Vis, which are comparable to user-

---

defined functions in most aspects. In addition to the common properties of a function, sub-VIs can also contain a GUI.

The available tools at the time of writing were the following:

- MakeLine: line fabrication, including compensation of double lines, multi-sweep exposures, arbitrary waiting times
- MakeCircle: circle fabrication (filled circles currently unsupported)
- Rechteck: fabrication of filled rectangular shapes and dot arrays
- PNGExposure: import of bitmap data (.png)
- XLSExposure: import of coordinate arrays from spreadsheet data (.xls, .csv)
- FileExposure: exposure of saved, pre-computed patterns (currently MakeLine only)
- STMconstant/STMsquared: patterns for STM experiments
- ShowPattern: 2D display of the pattern currently stored in the LV buffer, including simple exposure animation
- Setup: COM port assignment etc.
- RemCon: legacy tool for semi-automated AWG exposures
- Neunpunkt: legacy tool for the fabrication of simple dot arrays

All exposure tools prepare pattern data according to the common data structure, transfer the data to the DAC memory, and call a common GUI for the actual exposure control. This setup allows for the fast development of new modules to expand the capabilities of the exposure program.

### 5.4.3 Data Structure

The exposure data in NanoScribbler is organized as data cluster structure that contains the necessary exposure parameters, the pattern data as well as system parameters and pattern information. The pattern data structure is set up to directly match the memory structure of the M2i.6021 DAC card. In a dual-channel output setup, as is commonly used in NanoScribbler, the internal memory is divided into two parallel arrays of output values, i.e. one array for each channel. The individual memory blocks are 2 byte, i.e. 16 bit, data words that contain the 14 bit, signed integer representation of the output voltage. The two unused upper bits will be ignored in the standard case. VIs supplied by the DAC card manufacturer allow to directly wire standard 16 bit integer arrays to be transferred to the DAC memory. *Due to technical reasons, the length of the integer array has to be a multiple of 8.* Upon exposure start, the

array values are sequentially transferred to the DAC chip and output with every clock cycle of the sampling clock.

The exposure parameter part of the data cluster contains the required sample clock and the loop count for multi-sweep exposures. The sampling clock is generated by an onboard PLL circuit from the 10 MHz master clock of the card with selectable sample clock rates ranging from 1 kHz to 60 MHz (in 1 kHz increments). The corresponding sample times range from 1 ms at 1 kHz (1 kS/s) to 16.6 ns at 60 MHz. Longer or non-matching dwell times require a workaround, which will be discussed in Chapter 5.4.4.

The loop count (lc) determines the number of repetitions of the pattern exposure. The data format is 32 bit unsigned integer, i.e.  $1 \dots 2^{32}-1$ . An lc value of 0 invokes continuous output until a certain escape condition, e.g. user abort, is met.

The last part of the data cluster provides several fields that contain pattern-related information like expected exposure duration, pattern identifier, comments, SEM parameters and pattern details like step-sizes etc. to be displayed in the exposure GUI. The use of these fields is optional, but greatly enhances the user experience.

The data cluster is part of a global variable in NanoScribbler and gets updated whenever the exposure GUI is called from a tool GUI. The exposure GUI manages the data transfer of the necessary data from the cluster global variable to the DAC card and displays the sample clock, the loop count and a number of the optional fields.

#### 5.4.4 Timing algorithm

In this chapter, a number of algorithms for the integration of the M2i.6021-exp DAC into the NanoScribbler system will be presented in more detail. The main technical constraints imposed by the M2i.6021-exp DAC card are the digital resolution of 14 bit and the minimum sampling frequency of 1 kS/s, which corresponds to a maximum sample time  $t_s$  of 1 ms. The DAC resolutions is an issue mainly for the pattern generation algorithms, which can be easily adapted to different output resolutions. In addition, it is possible to transform existing patterns into compatible data formats via interpolation (with some loss of information). The timing generation is a more complex problem. First of all, the limitation to a maximum sample time  $t_s$  of 1 ms complicates the fabrication of structures with dwell times  $t_d$  longer than that time span. In addition, it is not possible to set arbitrary values for the sampling frequency, as the input is limited to integer multiples of 1 kHz between 1 kHz and the maximum sampling rate

---

(i.e. 50 MHz = 50000 kHz). This means that it is not possible to achieve a dwell time of 0.8 ms simply by setting the sampling frequency to  $(0.8 \text{ ms})^{-1} = 1.25 \text{ kHz}$ .

Both timing issues can be resolved by the use of oversampling. Essentially, a sample ( $i/k$ ) is repeated for a number of times so that  $t_d = n \times t_s$  ( $t_d$ : dwell time;  $t_s$ : sample time), with the integer  $n$  being the oversampling factor. The repetition of identical ( $i/k$ ) pairs keeps the beam stationary for the required amount of time. Figure 5-8 juxtaposes the data structure for exposures with inactive (a) and active oversampling (b, c).

In principle, one could think of choosing a very high standard sampling frequency and adjusting dwell times via the OSF only. Choosing a sampling rate of 10 MS/s in combination with an OSF of 10000 results in a dwell time of 1 ms as much as a sampling rate of 1 kS/s and an OSF of 1. The drawback of such an approach is very high memory demand. Obviously, a pattern that is exposed with an OSF of 10000 requires 10000 memory blocks for every exposure point, resulting in a 10000-fold increase in memory consumption. As there are limitations of the available DAC onboard memory (and data transfer speed in FIFO buffer operation), it is advantageous to reduce the sampling frequency and OSFs if possible.

In NanoScribbler this problem is addressed by a central timing VI. This VI accepts the required dwell time as an input and outputs the appropriate sampling frequency factor (SFF) and OSF. This happens independently of the pattern generation. In a second step, the existing pattern data is expanded to match the OSF by another VI, which generates a new pattern array in which every sample of the input array is duplicated a number of times corresponding to the OSF.

**a)  $f_S = 1 \text{ kHz}$ , OSF = 1**

Sample No.	1	2
x-Position	$i_1$	$i_2$
y-Position	$k_1$	$k_2$

Sample time  $t_S = 1 \text{ ms}$       Dwell time  $t_d = 1 \text{ ms}$

**b)  $f_S = 5 \text{ kHz}$ , OSF = 5**

1	2	3	4	5	6	7	8	9	10
$i_1$	$i_1$	$i_1$	$i_1$	$i_1$	$i_2$	$i_2$	$i_2$	$i_2$	$i_2$
$k_1$	$k_1$	$k_1$	$k_1$	$k_1$	$k_2$	$k_2$	$k_2$	$k_2$	$k_2$

$t_S = 0.2 \text{ ms}$        $t_d = 1 \text{ ms}$

**c)  $f_S = 5 \text{ kHz}$ , OSF = 4**

1	2	3	4	5	6	7	8	9	10
$i_1$	$i_1$	$i_1$	$i_1$	$i_2$	$i_2$	$i_2$	$i_2$	$i_3 \dots$	
$k_1$	$k_1$	$k_1$	$k_1$	$k_2$	$k_2$	$k_2$	$k_2$	$k_3 \dots$	

$t_S = 0.2 \text{ ms}$        $t_d = 0.8 \text{ ms}$

**Figure 5-8:** Data structures and timeline for exposures with inactive (a) and active oversampling (b, c). Colors indicate identical coordinates. If oversampling is not activated, the dwell time  $t_d$ , i.e. the time during which the beam is stationary at  $(i/k)$ , is equal to the sample time  $t_S$ . In the case of active oversampling (b, c), identical  $(i/k)$  values are output for a number of consecutive samples. The sampling frequency is adjusted so that the dwell time is an integer multiple of the sample time (i.e.  $t_d = n \times t_S$ ). The multiplier  $n$  is referred to as oversampling factor (OSF). Both case a) and b) will yield identical output patterns for different sampling rates, as in both cases  $t_d = n \times t_S = 1 \text{ ms}$ . The third case (c) corresponds to the standard use of oversampling: synthesizing dwell times that are incompatible with the DAC board. A  $t_d$  of 0.8 ms requires  $f_S = 1.25 \text{ kHz}$ , which cannot be selected. Instead,  $t_d$  is broken down into four valid  $t_S$ -steps of 0.2 ms ( $f_S = 5 \text{ kHz}$ ,  $t_d = 4 \times t_S = 0.8 \text{ ms}$ ) to avoid invalid sampling rates. See text for more detail.

The timing VI calculates the required sampling frequency  $f_s$  according to the following algorithm:

1. Calculation of the minimum sample  $t_{s,\min}$  time via the maximum sampling frequency  $f_{s,\max}$  gives  $t_{s,\min} = 1/f_{s,\max}$
2. Calculation of the proportionality factor  $n_s = t_{s,\max} / t_{s,\min}$  with  $t_{s,\max}$  being the maximum sample time
3. Calculation of the proportionality factor  $n_d = t_d / t_{s,\min}$  with  $t_d$  being the required dwell time
4. Evaluation of the greatest common divisor of  $n_s$  and  $n_d$ :  $gcd(n_s, n_d)$
5. The sample time  $t_s$  is found via  $t_s = gcd(n_s, n_d) \times t_{s,\min}$
6. The sampling frequency is calculated as  $f_s = 1 / t_s$
7. The oversampling is calculated as  $OSF = n_d / gcd(n_s, n_d)$ .

In our case  $f_{s,\max}$  is 50 MHz and  $f_{s,\min}$  is 1 kHz, i.e.  $n_s = 10^3 \text{ s} / 2 \times 10^{-8} \text{ s} = 50000$  (step 1, 2). Assuming a required dwell time of 24  $\mu\text{s}$ ,  $n_d = 24 \times 10^{-6} \text{ s} / 2 \times 10^{-8} \text{ s} = 1200$  (step 3). This means, in essence, that if the card were running at 50 MHz, an OSF of 1200 is required to result in an output dwell time of 24  $\mu\text{s}$ . The greatest common divisor of  $n_s$  and  $n_d$  is 400 (step 3), which tells us that the required sample time  $t_s = 400 \times 2 \times 10^{-8} \text{ s} = 8 \times 10^{-6} \text{ s}$ , the sampling frequency  $f_s = 1/t_s = 125 \text{ kHz}$  and the oversampling factor is  $OSF = n_d/gcd = 1200 / 400 = 3$ .

The algorithm works for arbitrary values of  $t_d$  if  $t_d = k \times t_{s,\min}$  and  $k \in \mathbb{N}$ . The use of a maximum frequency of 50 MHz ensures compatibility with commonly used “round” numbered dwell times, but could be applied to arbitrary values as well. It yields valid sampling frequency factors SFF in kHz multiples due to the following constraints:

- I.  $t_d = k \times t_{s,\min}$  and  $k \in \mathbb{N}$
- II.  $f_{s,\max} = 50 \text{ MHz} = 2^7 \times 5^8 \text{ Hz}$ ;  $t_{s,\min} = 1/f_{s,\max} = 1/(2^7 \times 5^8) \text{ s} = 20 \text{ ns}$
- III.  $f_{s,\min} = 1 \text{ kHz} = 2^3 \times 5^3 \text{ Hz} \rightarrow t_{s,\max} = 1/(2^3 \times 5^3) \text{ s} = 1 \text{ ms}$
- IV.  $n_s = t_{s,\max} / t_{s,\min} = [1/(2^3 \times 5^3) \text{ s}] / [1/(2^7 \times 5^8) \text{ s}] = (2^7 \times 5^8) / (2^3 \times 5^3) = 2^4 \times 5^5$
- V.  $n_d = t_d / t_{s,\min} = (k \times t_{s,\min}) / t_{s,\min} = k = 2^\alpha \times 3^\beta \times 5^\gamma \times \dots$  with  $\alpha, \beta, \gamma, \dots \in \mathbb{N}_0$  (fundamental theorem of arithmetic)
- VI.  $gcd(n_s, n_d) = gcd([2^4 \times 5^5], [2^\alpha \times 3^\beta \times 5^\gamma \times \dots]) = 2^a \times 5^b$  with  $a \in \{0;1;2;3;4\}$  and  $b \in \{0;1;\dots;5\}$
- VII.  $f_s = 1/t_s = 1/[gcd(n_s, n_d) \times t_{s,\min}] = 1/[gcd(n_s, n_d)] \times 1/t_{s,\min} = 1/[gcd(n_s, n_d)] \times f_{s,\max} = 1/[2^a \times 5^b] \times [2^7 \times 5^8 \text{ Hz}] = (2^7 \times 5^8) / (2^a \times 5^b) \text{ Hz} = [(2^4 \times 5^5) \times (2^3 \times 5^3)] / (2^a \times 5^b) \text{ Hz} = (2^4 \times 5^5) / (2^a \times 5^b) \text{ kHz} = 2^{4-a} \times 5^{5-b} \text{ kHz}$

- VIII. with (VI) it follows that  $(4-a) \in \{0;1;2;3;4\}$  and  $(5-b) \in \{0;1;\dots;5\}$ ;
- IX. therefore  $(2^{4-a} \times 5^{5-b}) \in \mathbb{N}$  and  $1 \leq (2^{4-a} \times 5^{5-b}) \leq 2^4 \times 5^5 = 50000$ .

The conclusion (IX) shows that the algorithm yields only valid SFF of  $(2^{4-a} \times 5^{5-b})$  in the form of hardware-compatible integer values ( $(2^{4-a} \times 5^{5-b}) \in \mathbb{N}$ ) between 1 and 50000. The OSF is always a valid integer, as dividing  $n_d$  by the greatest common divisor of  $n_d$  and any other integer must yield an integer greater or equal to one ( $n_d \bmod \gcd(n_d, j) = 0$  with  $n_d, j \in \mathbb{N}$ ).

### 5.4.5 Pattern Generation

The functionality of the tools for pattern generation is straight forward. A GUI collects specific user input, e.g. desired step size, dwell time, sweep number and the current SEM parameters, i.e. magnification and respective FOV size, and uses this information to calculate the x- and y-coordinate arrays according to the programmed algorithm.

In the following chapter, the generation of a square shape using the Rechteck (“rectangle”) tool will be discussed as a general example. The presented concepts should be easy to transfer or adapt to other tasks. The GUI layout of the Rechteck tool is shown in Figure 5-9.

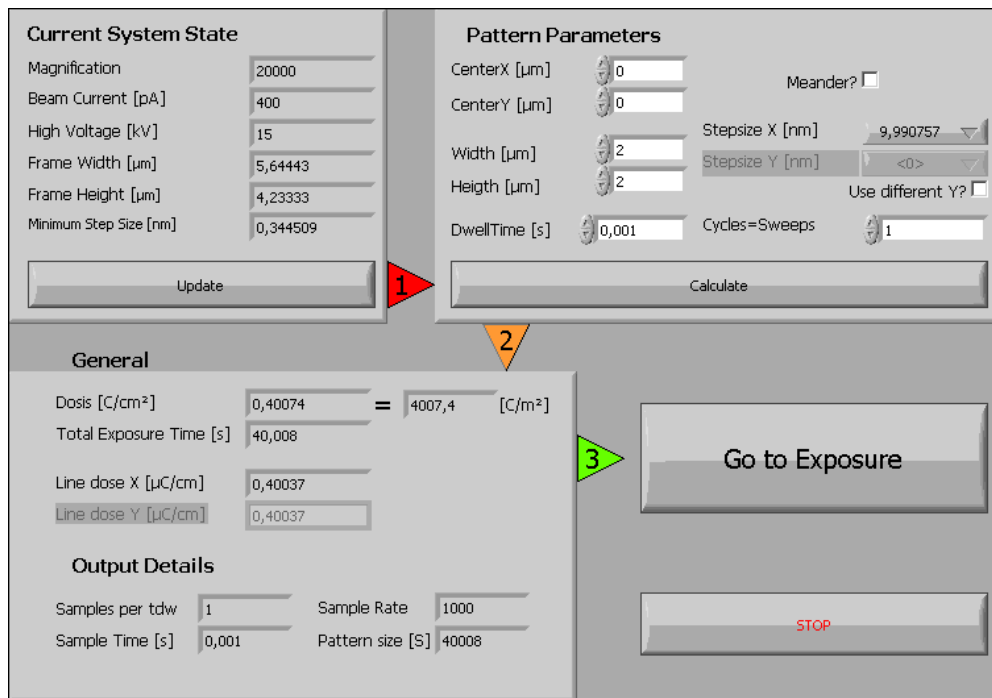


**Figure 5-9:** GUI of the Rechteck (“rectangle”) tool. Top left: system parameter collection; top right: position and parameter setup; bottom left: output pattern information.

First, the user is required to update the current system parameters by pressing the “update” button (top left). The parameters are collected via the RS-232 communication to RemCON32. For more information about the RemCon protocol, please refer to the respective section in the appendix (Appendix A – Communication Protocols) or the user manual.<sup>116</sup> The displayed minimum step size is calculated by dividing the current frame width by  $2^{14} = 16384$  (cf. Chapter 5.2).

*Note that the indicated beam current is not a reading of the actual beam current of the system, as the RemCon interface does not provide this information.* The value is fixed to the standard current of 400 pA in the LabVIEW source code (can be altered in the source code only). In order to ensure correct dose calculations etc., at the moment it is necessary to measure the beam current using of the 400 pA beam current option in the SmartSEM GUI using a Faraday cup. The beam current can be adjusted slightly by changing the extractor voltage in the SmartSEM GUI to match the target value of 400 pA.\*

The second step is the pattern setup using the various “pattern parameters” input boxes (top right). For ease of use, the position and size of the rectangle to be exposed are requested in real space coordinates [ $\mu\text{m}$ ], which will be transferred to the internally used pixel coordinates. The check box (“Meander?”) controls the writing directions of alternating lines. In standard operation, the beam moves left-to-right and jumps back to the leftmost coordinate before exposing the next line. If “Meander?” is activated, the writing direction of every second line is inverted, resulting in a continuous, snake-like path of the electron beam during the exposure. This is illustrated in Figure 5-10.

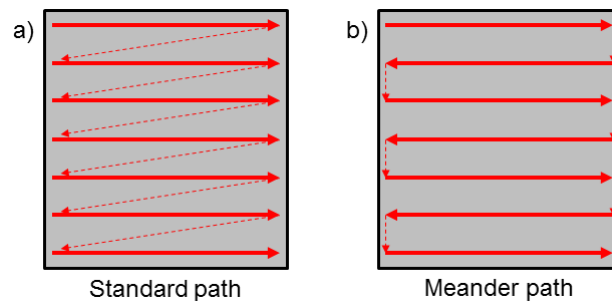


**Figure 5-10:** Standard path (a) and meander path (b) exposure. Full lines represent the active exposure path, while dashed lines show the beam repositioning between subsequent lines.

\* Future plans include reading in arbitrary values of the beam current before a lithography experiment.

The dwell time input and the multisweep counter are used to calculate the required timing configuration parameters (OSF and SFF, see Chapter 5.4.4). In this case, the dwell time  $t_d$  is regarded as dwell time per sweep, i.e. the  $t_{d,\text{total}} = t_d \times n_{\text{sweeps}}$ .

There are two options for step size selection: identical or different (“use different Y”) step size in x- and y- direction. The latter option offers a very simple way of fabricating arrays of parallel lines with defined spacing (i.e. y-step size).

A noteworthy feature of the step size input is the use of a ring control instead of a standard numerical input box. The ring control is, in essence, a list of arbitrary strings, one of which can be selected by the user from a drop-down menu. Instead of returning the selected string itself, a numerical value that is associated with the string is returned. In this case, the incremental position of the selected element within the list is returned. The strings are (re-)initialized whenever the system parameters are updated to display valid step sizes only. These are generated by multiplying the minimum step size  $\Delta x_{\text{min}}$  by the list position of the element. By doing so, the user can select the values in real space dimensions, while the actual value of the ring control, i.e. the position of the selected element, is equal to the step size in pixel coordinates and can be directly used for further calculations. In simple terms, for a minimum step size of 0.5 nm the ring control would display a list of strings like (“0.5 nm”, “1.0 nm”, “1.5 nm”, ...). If the user selects “1.5 nm”, the third element in the list, the actual value of the ring control is set to 3, which is the corresponding step size increment  $\Delta p$  in pixel space.

Once all system parameters and user inputs are gathered, pressing the “Calculate” button will start the actual pattern generation. In order to do this, the real space coordinates are converted to pixel coordinates via  $(i|k) = (\text{int} [x/w \times 2^{14}] | \text{int} [y/w \times 2^{14}])$  with x/y being the real space coordinates and w being the FOV width. The real space coordinates are defined such that the center of the current field of view represents (0|0) and the possible coordinates range from  $-\frac{w}{2}$  to  $+\frac{w}{2}$  (see Figure 5-2 for details). This results in pixel coordinates ranging from  $-2^{13} = -8192$  to  $2^{13}-1 = 8191$ .

The conversion entails small deviations due to the fact that  $(x / w \times 2^{14})$  is rounded to the nearest integer. The magnitude of the deviation for absolute coordinates is  $\Delta d_{\text{pos}} < \Delta x_{\text{min}}$  with  $\Delta x_{\text{min}}$  being the minimum step size ( $\Delta x_{\text{min}} = w / 2^{14}$ ). Conversion of distances (e.g. length of a line, height and width of a square, line spacings, ...) from real to pixel space will be off by less than one step size, i.e.  $\Delta d_{\text{dist}} < \Delta x$ .

Once the inputs have been converted to pixel space coordinates, the pattern generation algorithm starts. In the case of the rectangle program, the algorithm is fairly simple: set the

beam position to the top left corner, write  $(i_0|k_0)$  to the output array, increase  $i_n$  by  $\Delta p_x$  to give  $i_{n+1} = i_n + \Delta p_x$  while keeping  $k_{n+1} = k_n$ , append  $(i_{n+1}|k_0)$  and continue while  $i_{n+1}$  is smaller than  $i_{\max}$ , which is the x-coordinate of the right edge. The  $i$ -coordinates of the next line will be identical to the respective ones of the first row in standard mode and reversely ordered in meander mode, while all  $k$ -coordinates will be increased by  $\Delta p_y$ . This process is repeated until  $k_{\max}$  (the bottom edge coordinate) is reached. The result is an array of all coordinates of pixels to be exposed within the rectangle. The number of elements is  $j \times l$  with  $j$  being the number of pixels per line and  $l$  being the number of lines. The individual coordinates correspond to  $(i_n|k_n) = (i_0 + [n \bmod j] \times \Delta p_x | k_0 + [n \text{ div } j] \times \Delta p_y)$  for  $n < j \times l$ .

The output array is transformed to comply with the timing parameters OSF and SFF (see Chapter 5.4.4) and padded so that the number of elements is a multiple of eight (see Chapter 5.4.3).

The results of the algorithm execution are displayed in the general section on the lower left of the Rechteck GUI. They include the resulting area dose for the total pattern as well as the line doses for individual lines, the total exposure time for the pattern and hardware specific parameters such as array size, DAC frequency or oversampling factor. Pressing “Go to Exposure” transfers the pattern data and card setup parameters to the global variable and calls the exposure control GUI.

#### 5.4.6 Exposure Procedure

As mentioned before, upon completion of a pattern setup the respective tool transfers the values of the data cluster to a global variable and calls the exposure GUI that controls the actual exposure process. The GUI is shown in Figure 5-11. It contains an info box with pattern details (e.g. step size, expected time requirement, dwell time; only if provided by the respective tool), a box with card setup details (sample rate, loop count, sample count), an advanced options box and a user interaction section at the bottom.

The options box provides the following features: working without an active connection to the SEM, e.g. while the DAC is connected to an oscilloscope, (“Work offline”); adding a delay between SEM control transfer and actual start of beam movement (“EDX...delay”); and starting the exposure process immediately after the memory transfer is finished instead of manual control.



**Figure 5-11:** Exposure GUI. The info box on the left displays a number of details of the currently active pattern if provided by the respective tool. The exposure details box shows the card setup parameters sample rate, loop count and sample count. The options box provides advanced features like SEM control disable (“Work offline”). The status bar displays current status of the DAC.

The user interaction is realized via four buttons and a status bar. The “prepare” button triggers the data transfer. When pressed, the contents of the data cluster are copied from the global variable to the DAC memory (maximum data transfer rate: 160 MB/s, i.e. 40 MS/s for dual channel at 2 byte per sample) and the card is configured for output by setting e.g. sampling rate and loop count. The completion of the loading sequence enables the Start-button and disables the prepare button. If “autostart after preparation” is enabled in the options box, the exposure sequence will start immediately after the loading procedure is completed. The stop button cancels the current exposure.

Pressing the Start button starts the exposure sequence. First, the command to switch SEM beam control to the external scan inputs (“EDX 1”) is sent to RemCON32 via the RS-232 connection. When the acknowledgment of the completions is received, the optional EDX-to-write delay is enforced, before the DAC output is started by supplying a software trigger. From that point on the DAC output is completely hardware-controlled by the DAC card, i.e. the exposure runs independently of the computer OS and CPU. The card status is continually

---

read out and once the output is finished, aborted or an error is detected, the external scan is revoked via the RemCon interface (“EDX 0”) and the beam is blanked using the integrated beam blanker (“BBLK 1”).

The integrated beam blanker cannot be used during the exposure, as the command is not executed in external scan mode. Switching from external to internal scan and vice versa is quite slow (from 250 up to 400 ms have been observed), which prevents this workaround. In addition, the transmission time for the BBLK command and acknowledgment is in the order of 50 ms, which would limit the use as well.

After the exposure is finished and the beam is blanked, the exposure GUI is reset to the state before the exposure was started. The pattern data remains in the DAC memory. If desired, the exposure can be started again using the identical system parameters. If closed, the exposure control window has to be called from a pattern tool before another exposure can be started.

#### **5.4.7 System Tests and Evaluation**

The system capabilities were carefully characterized after completion of the main software components. The tests revealed that the basic concept is sound, and that all previously used lithographic solutions could be replaced by NanoScribbler. The flexibility of the system also allows for fast implementation of new pattern generators algorithms.

Using NanoScribbler, it was also possible to elucidate the technical limits of the beam control system of the Gemini column. Such limitations exist, as was already observed when the arbitrary waveform generators were used for exposures. When line structures were exposed in forward-and-backward multisweep mode, the result was a splitting into two parallel lines. If the beam was programmed to repeatedly jump back to the start after finishing the forward movement, only a single line is observed, i.e. all individual sweeps take the identical path.

Concerning the cause of this behavior, the fact that such line splitting was observed both for NanoScribbler and the arbitrary waveform generators points to an issue of the microscope rather than of faulty input signals. Within the microscope, a number of possible reasons can be considered, e.g. signal corruption or processing artifacts within the analog circuitry, or crosstalk and hysteresis effects within the magnetic scan system. Crosstalk in this context is linked to inductive coupling of the x- and y-scan coils., as e.g. fast changes in the magnetic

field generated by one set of scan coils, i.e. fast beam movement, give rise to an induced field in the other, leading to the observed behavior.

Further investigation showed that splitting can be overcome by supplying a compensation voltage to the orthogonal direction during the sweep. The double line exposure and active compensation is shown for high speed multisweep exposures in Figure 5-12.

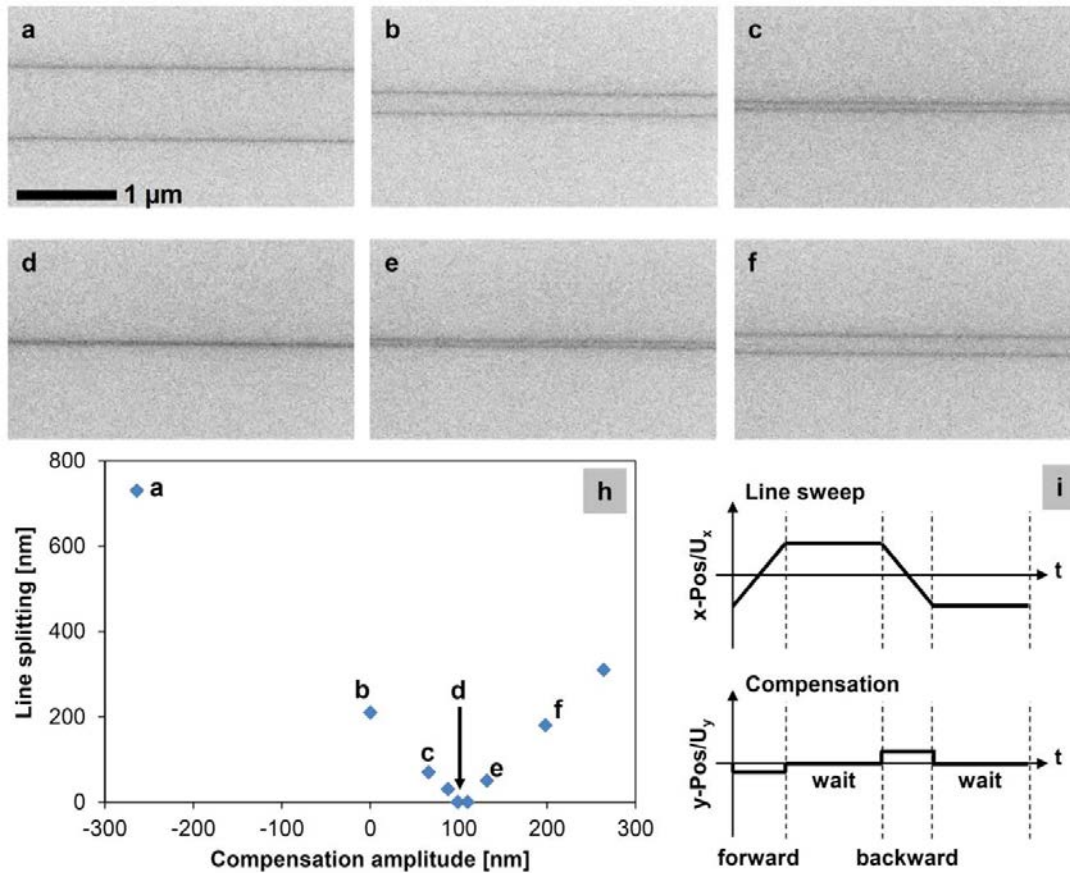


**Figure 5-12:** Line splitting of 45  $\mu\text{m}$  multisweep line exposures on 300 nm  $\text{SiO}_2/\text{Si}$ . The micrographs a)-f) show splitting of the multisweep lines for different compensations ( $b=0$ ). The correlation between compensation amplitude and observed line splitting is presented in the graph (h); corresponding images are indicated. The beam positions for the line ( $x$ -input) and compensation ( $y$ -input) during a sweep the scheme (i). The duration of a single sweep without waiting time was 500  $\mu\text{s}$ , which corresponds to a beam speed of 0.09 m/s.

The SE micrographs in Figure 5-12 a)-f) show such line splitting for different applied compensation voltages, with b) representing the line splitting without any compensation. The required compensation, as applied in Figure 5-12 d), corresponds to a beam deflection of about 100 nm, or roughly half of the observed splitting. As the compensation is applied

during both forward and backward sweep with reversed polarity, it seems likely that, without the compensation, the individual lines produced by the forward and backward sweep are offset by the same value against the centered line position.

The maximum writing speed of the Gemini Column in pixel map and continuous path exposures was tested using  $1 \times 1 \mu\text{m}^2$  square outlines as shown in Figure 5-13 (pixel map, i.e. raster scan) and Figure 5-14 (continuous path, i.e. vector scan). In both cases, the test was conducted as a multi-sweep exposure with a step size of 10 nm, and a constant total dwell time  $t_d = t_{d,\text{total}} = t_{d,\text{sweep}} \times n_{\text{sweep}}$ , resulting in identical PE doses for all structures. In the case of the pixel map exposure, the pattern is exposed likewise from top to bottom (see red arrows): first, the top bar is exposed, then the beam jumps to the topmost pixel of the left vertical bar, exposes for  $t_{d,\text{sweep}}$ , jumps to the corresponding pixel on the right vertical bar, again exposes for  $t_{d,\text{sweep}}$ , and repeats this jumping process until the lower bar, which is exposed point-by-point. It is quite obvious that this type of exposure process is prone to complications due to the jumps between the vertical bars. In fact, when there is sufficient time for the beam to stabilize, i.e. for long dwell times, no artifacts are observed, as can be seen in Figure 5-13 a)-c), while for shorter dwell time, exposure artifacts become apparent (d-f). At around  $t_d = 5 \mu\text{s}$  (Figure 5-13 d), the space between the bars is a smeared out, grey area slightly narrower than the top/bottom bars. The grey area indicates a more or less homogeneous exposure to the electron beam, i.e. the electron exposure is smeared out over the inner area. The narrowing shows that the electron beam cannot move to the intended coordinates within the given timeframe (i.e. within one  $t_d$ ). Further decrease leads to a reduction of the observed x-movement of the beam (Figure 5-13 e), resulting in shortened top/bottom bars and complete suppression of the jumping for the vertical bar section. For the shortest  $t_d$  of 50 ns, the pattern is completely distorted. The fact that there still are clearly visible dark lines shows that the electron beam still follows a defined path instead of being completely random or stationary. It is assumed that in that case, the crosstalk between the x-and y-movement and hysteresis effects cause the rounding and distortion of the pattern.

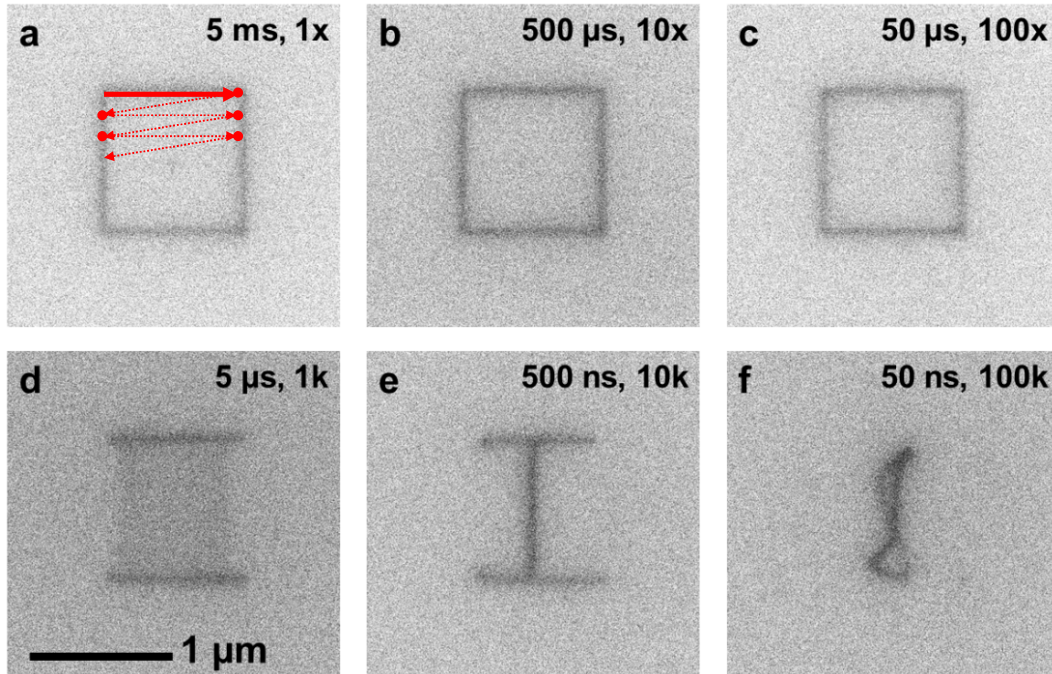


**Figure 5-13:** Beam stability test using a pixel map to fabricate a square outline ( $1 \mu\text{m} \times 1 \mu\text{m}$ ). All shapes are irradiated with the same total electron dose, but different dwell times per sweep and sweep counts, as indicated in the images. The pattern is exposed in sequential lines, i.e. the top bar is exposed first, followed by quick jumps from the left to the right vertical line and vice versa until the bottom line is reached. Images d)-f) show that the beam is not able to follow the jumping pattern for per sweep dwell times in the range of  $10 \mu\text{s}$ . The shapes in e) and f) are the result of very fast beam deflection inputs which cannot be followed by the electromagnetic scan system.

The aforementioned test with the pixel map exposure strategy clearly shows the drawbacks of that technique for short dwell times. Under the assumption that the beam position is reached and stabilized within  $t_d$  for the maximum jump distance  $\Delta x = 1 \mu\text{m}$  the maximum beam speed can be estimated to

$$v_{max} \approx \frac{\Delta x}{\Delta t_{d,min}} = \frac{1 \mu\text{m}}{50 \mu\text{s}} = 0.02 \text{ m s}^{-1},$$

as  $t_{d,min} = 50 \mu\text{s}$  is the lowest observed dwell time that leads to a stable exposure pattern (Figure 5-13c).

The limitation of the pixel map exposure (which can be considered an example of a raster scan exposure, see Chapter 5.1), can be overcome in most cases by conversion to an appropriate vector scan process. Figure 5-14 is comprised of a set of square outlines that correspond to the structures in shown Figure 5-13 in all parameters except for the applied scan strategy. In Figure 5-14, all structures were irradiated by following the outline in a continuous manner, i.e. by scanning top left – top right – bottom right – bottom left – top left (as indicated by the red arrows). Again, the patterns were exposed in multisweep mode to study the effects of fast scan speeds / low dwell times.

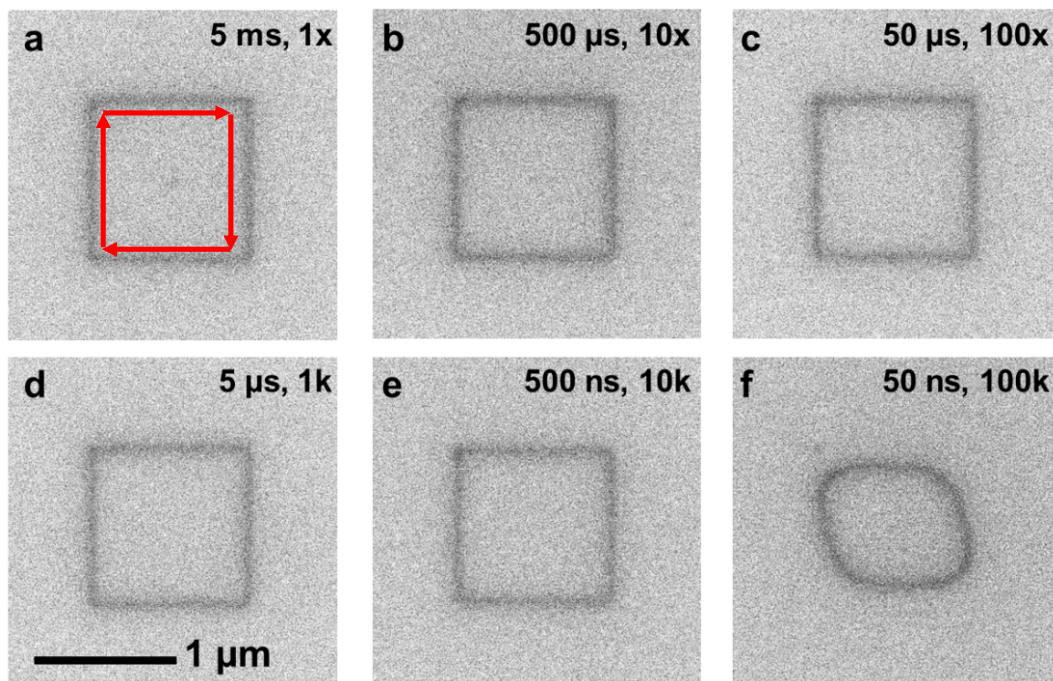


**Figure 5-14:** Beam stability test using a vector path to fabricate a square outline ( $1\ \mu\text{m} \times 1\ \mu\text{m}$ ). All shapes are irradiated with the same total electron dose, but different dwell times per sweep and sweep counts, as indicated in the images. The pattern is exposed in a continuous path, i.e. the top line is exposed first, followed by the right vertical line top to bottom and so forth. Image f) shows that the beam is not able to follow the vector path for per sweep dwell times in the range of 100 ns. The distorted shape in f) is the result of very fast beam deflection inputs which cannot be followed by the electromagnetic scan system.

As can be seen from the micrographs, the patterns remain unaffected down to a dwell time of approx.  $1\ \mu\text{s}$ , as close inspections shows a beginning edge rounding effect in Figure 5-14e ( $0.5\ \mu\text{s}$ ). In contrast to the pixel map exposure, the vector scan still produced discernible, albeit distorted patterns, even for very low dwell times of  $<500\ \text{ns}$  (Figure 5-14e,f), which

corresponds to decrease of the minimum usable dwell time by almost two orders of magnitude (50  $\mu\text{s}$  vs. 1  $\mu\text{s}$ ).

At a step size of 10 nm, a dwell time of 1  $\mu\text{s}$  corresponds to a beam speed of

$$v_{max} \approx \frac{\Delta x}{\Delta t_{d,min}} = \frac{10 \text{ nm}}{1 \mu\text{s}} = 0.01 \text{ ms}^{-1}.$$

This is in fair agreement with the assessment of the pixel map data ( $v_{max} = 0.02 \text{ ms}^{-1}$ ). The maximum beam speed for lithography purposes therefore seems to be limited to a few centimeters per second using the unmodified scan system of the Gemini column.

### 5.4.8 Future perspectives

In addition to the beam control, lithography systems often include some form of control of the sample position, i.e. stage control. This allows for fully automated exposures of multiple patterns without the need for human interaction during the process, which reduces the overall duration as well as the possibilities for operator errors.

In the case of NanoScribbler, an automated stage was planned but could not be fully implemented within the timeframe of this thesis. In order to control the sample position, an interface between the application seeking to control the stage and the stage positioning hardware is necessary. In addition, a position feedback is required. While conventional SEMs feature fully computer controlled, motorized stages with three or more degrees of freedom and corresponding feedback channels, the piezo stage in the MULTISCAN Lab is not prepared for stage control and does not feature integrated positional feedback in the standard configuration. The exchange of the standard piezo controller board of the MATRIX CU for a RS-232-enabled model (“MSCU”) allows for the control of the stage movement via a COM interface (see “MSCU Technical Reference Manual”<sup>117</sup>).

The positional feedback is realized via an interferometric sensor and IK220 PCI controller card (Heidenhain) with a precision of  $\sim 50 \text{ nm}$  and an (uncorrected) repeatability of  $< 2 \mu\text{m}$ . The position is read out by a LabVIEW program in the respective GUI (Figure 5-15). The main components are the large displays of the current x- and y- position of the sample. These values are calculated from the data of the incremental sensor and referenced to an arbitrarily chosen origin (commonly the lower left corner of the sample is used as the origin, i.e. the coordinates of the stage are mapped to positions on the sample). The buttons to the right allow setting the current position either to zero (“Zero”) or to an arbitrary value (“Set” in combination with the input box). The controls on the bottom enable the advanced functions:

RS-232 connection to the MSCU, stage control via joystick and automated stage movement (“Automove”).

In order to enable the RS-232 connection to the MSCU, the “Remote Box”, which is the standard tool used for stage and tip navigation, has to be disconnected and replaced by the RS-232 cable. A joystick module was implemented to provide manual stage control during RS-232 operation and allows to use a LabVIEW GUI or a generic joystick for stage translation (tip navigation is only possible using the Remote Box, which prevents permanent integration of the system).

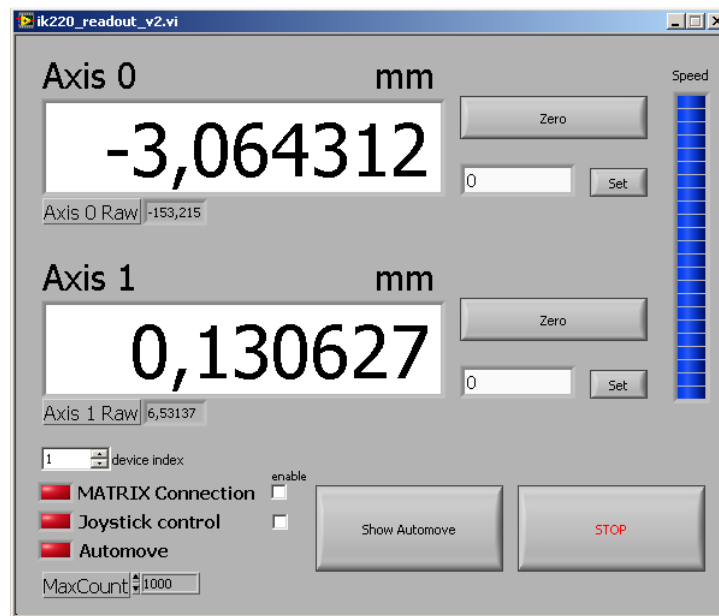


**Figure 5-15:** Graphical user interface of the stage position readout VI. The current position is displayed in the large text boxes (x/y position). The buttons on the respective right set current position to 0.0 (“Zero”) or to an arbitrary value (“Set” and input box). The vertical bar on the right indicates the current movement speed for manual stage translation using the joystick (see text). The controls on the bottom enable the MATRIX connection via RS-232, the control via the joystick and the software-controlled stage movement (“Automove”). See text for details.

The stage translation is realized via a slip-stick mechanism using piezo-actuators. In order to move the stage, the MSCU executes a number  $j$  of slip-stick cycles (“jumps”) at the selected piezo voltage  $V_p$ , which defines the distance that is travelled per jump. The system exhibits pronounced hysteresis effects and nonlinearities, and, as described before, does not

include a positional encoder. This means that it is not possible to calculate the required  $(j, V_p)$  command for a given movement before the actual translation.

The automated stage movement was therefore implemented as an iterative algorithm, which records the current position and calculates an initial  $(j_0, V_{p,0})$  command using standard parameters. After the movement is executed, the position is evaluated and the next set of commands  $(j_1, V_{p,1})$  is calculated and executed. This process is repeated until a predefined accuracy (e.g. 50 nm) is reached. As a future step, the available routines for stage movement and positional readout can be integrated into the NanoScribbler software to allow for fully automated exposures.

---

### 5.4.9 Summary and Conclusions

The fabrication of arbitrarily shaped nanostructures using focused electron beam based techniques requires precise control of all aspects of the electron beam movement and timing. While commercial lithography solutions offer high flexibility and a wide range of possible applications, they do not offer full control of all parameters to the user. In most cases, this may not be in demand, but in fundamental research of new lithography techniques like EBID, full beam control is mandatory for the realization of conclusive experiments.

As the available lithographic tools at the MULTISCAN Lab did not allow for full control of the electron beam (Elphy Quantum) or had technical limitations (Arbitrary Wave Generators), a functional lithography solution for use in fundamental FEBIP research was developed as part of this thesis.

It could be shown that it is possible to use LabVIEW and commercially available DAC hardware to design and implement such a lithography solution. The software, “NanoScribbler”, is an expandable, modular application built around the M2i.6021-exp 14-bit DAC hardware. The software-hardware interface and exposure control GUI are designed to accept arbitrary patterns in a standardized data format, which allows for easy integration of custom algorithms for pattern generation. At the time of writing, NanoScribbler includes subroutines for the generation of a number of standard patterns, e.g. dot arrays, line and square patterns and the possibility to import image data as patterns (via .png files).

Tests of the system reveal that the maximum beam speed during exposures is in the order of a few cm/s. The lower limit of the dwell time used for pattern fabrication seems to be in the order of 1 to 0.1  $\mu$ s, corresponding to a sampling rate of a few MS/s, which is well within the capabilities of the M2i.6021-exp DAC card (max. 60 MS/s). NanoScribbler is able to avoid or minimize the artifacts that were observed when other patterning tools like the SEM software, arbitrary waveform generators or the commercial Elphy Quantum solution were used. In summary, the NanoScribbler system in combination with the Gemini SEM column built into the MULTISCAN Lab is able to provide full and precise control of the relevant electron beam parameters and is therefore a valuable tool for the research of fundamental aspects in focused electron beam induced processing techniques.



## 6 Results and Discussion

### 6.1 Introduction

The following chapter will describe the main experiments and results obtained during the course of the thesis at hand in detail. The investigation of EBISA and EBID on several types of silicon oxides (300 nm and ultra-thin thermal oxide on Si(100), native oxide on Si(100) and Si<sub>3</sub>N<sub>4</sub>)<sup>5, 12-14</sup> revealed that the electron stimulated desorption of oxygen, and thus generated oxygen vacancies, is the origin of the surface activation. One of the proposed alternative mechanisms for the activation is charging of the surface upon e-beam irradiation.<sup>14</sup> This was ruled out based on observations on as-prepared, ultra-thin SiO<sub>x</sub> on Si(100). EBISA is possible on that sample, while the presence of trapped charges in the ultra-thin (< 1 nm) oxide on the doped Si substrate can be practically ruled out. The fact that the as-prepared oxide showed some activity towards the Fe(CO)<sub>5</sub> decomposition was interpreted as a consequence of the chemical nature of the active species, which is, in essence, understoichiometric SiO<sub>2-x</sub>.<sup>14</sup>

Based on this knowledge, rutile TiO<sub>2</sub>(110) was chosen as a substrate for further studies of the activation process. TiO<sub>2</sub> is, after some preparation, i.e. reduction and generation of color centers, quite conductive<sup>100</sup> and allows for the dismissal of sample charging as activation mechanism. It was also shown to be susceptible to ESD of oxygen<sup>52</sup> and serves as a step towards the use of EBISA on oxide substrates other than SiO<sub>2</sub>. In addition, for the first time, the use scanning tunneling microscopy (STM) for investigation of the activation process on an atomic scale is possible. The results of the EBISA/EBID study on TiO<sub>2</sub>(110) are presented in Chapter 6.2.

The second experimental complex deals with the use of the focused electron beam for the manipulation of functional organic layers on surfaces. It has been known that

tetraphenylporphyrin molecules adsorb in a flat geometry on many coinage metal single crystal surfaces like Ag(111), Au(111) and also Cu(111).<sup>(118 and references therein)</sup> Depending on the absence (2HTPP) or presence (e.g. CoTPP, ZnTPP, ...) of a metal center and the type of surface (inert vs. reactive metal, oxide layer etc.), the adsorption behavior differs and the resulting surface structures and ordering may vary significantly. It was also shown that porphyrin layers can alter the nucleation and growth of PVD deposited metal.<sup>119</sup> In this context, EBID/EBISA can be used to fabricate nanostructures both to investigate the absorption on (nano-)structured surfaces as well as to study the influence of the organic layer on the EBID/EBISA process. Chapter 6.3 will present results obtained on the systems 2H- and CoTPP on Ag(111) using Fe(CO)<sub>5</sub>.

The applicability and outcome of EBISA, and somewhat also of EBID, strongly depend on the chemical properties of the precursor molecules. To be suitable for EBISA, a precursor has to be susceptible to decomposition at the activated areas and show autocatalytic growth behavior. It has been established that Fe(CO)<sub>5</sub> fulfills both requirements, yielding autocatalytically grown, polycrystalline Fe of high purity (>90% at.) on a variety of substrates. In order to broaden the range of applicable precursors, related carbonyl-based metal-organic precursors were investigated during the course of this thesis. These precursors are cobalt tricarbonyl nitrosyl, Co(CO)<sub>3</sub>NO, and dicobalt octacarbonyl, Co<sub>2</sub>(CO)<sub>8</sub>.

The results of the study of the EBID/EBISA and the autocatalytic growth using Co(CO)<sub>3</sub>NO are reported in Chapter 6.4. The study includes SEM data obtained in UHV as well as scanning transmission (spectro-)microscopic (STXM) data collected at the PolLux beamline at the Swiss Light Source (SLS) synchrotron radiation facility at the Paul-Scherrer-Institut, Villigen (CH).

A brief overview of experiments using Co<sub>2</sub>(CO)<sub>8</sub> as a precursor is given in Chapter 6.5. It has been reported that Co<sub>2</sub>(CO)<sub>8</sub> can be used for the fabrication of nanostructures using the EBISA protocol on SiO<sub>2</sub> substrates in HV systems, albeit the reports being are somewhat ambiguous and contradictory.<sup>15, 37</sup> EBISA and also EBID using that precursor yield high purity Co structures; the precursor is therefore likely to be suitable for the study of EBISA and autocatalytic growth processes using surface science techniques in UHV. While the EBID results reported in literature could be reproduced, the precursor is unstable and seems not to be suitable for use in our UHV chamber.

## 6.2 EBID and EBISA on rutile TiO<sub>2</sub>(110)

### ABSTRACT

This chapter deals with the fabrication of clean iron nanostructures on rutile TiO<sub>2</sub>(110)-1×1 via electron beam induced surface activation (EBISA) in ultra-high vacuum. It will be shown that it is indeed possible to transfer the EBISA process to rutile TiO<sub>2</sub>(110) using Fe(CO)<sub>5</sub> as a precursor. On the basis of microscopic information down to the atomic scale (scanning tunneling microscopy) and local spectroscopic information (Auger electron spectroscopy/microscopy) the activation mechanism shall be investigated in great detail and shown to involving e-beam induced surface reduction and restructuring.

Results presented in this chapter have been published in “Electron Beam-Induced Writing of Nanoscale Iron Wires on a Functional Metal Oxide” by F. Vollnhals, T. Woolcot, M.-M. Walz, S. Seiler, H.-P. Steinrück, G. Thornton and H. Marbach, in the *Journal of Physical Chemistry C* (2013), vol. 117, pages 17674-17679.<sup>120</sup>

### 6.2.1 Introduction

The surface processes involved in the activation in EBISA have so far only been investigated for 300 nm thick and ultrathin (< 3 nm) silicon oxide layers on silicon and Si<sub>3</sub>N<sub>4</sub>. These link the loss of oxygen due to Electron Stimulated Desorption (ESD) to the formation of oxygen vacancies on the surface and describe these as the activation induced reactive centers. The alternative route via charging/trapped electrons was ruled out due to the observed long-term stability of the activation and the presence of a conducting substrate.

The aim of this chapter is to draw a more complete picture of EBISA using rutile TiO<sub>2</sub>(110) as a substrate in ultra-high vacuum (UHV). Surfaces of rutile TiO<sub>2</sub> have been used as model systems to explore the physics and chemistry associated with the varied applications of the material for many years,<sup>100, 121</sup> with a particular focus on the surface science associated with light harvesting processes such as photocatalysis and dye-sensitized photovoltaics. Applications in the field of molecular electronics have also been suggested, with TiO<sub>2</sub> being employed as a dielectric substrate. This has motivated studies of metal wire growth as interconnects using physical vapor deposition.<sup>122</sup> There is related interest in the generation of memristor elements on TiO<sub>2</sub>.<sup>123</sup>

The well-established surface chemistry and physics of this surface should allow for deeper insights, since the activation step can be followed at the atomic level using a Scanning Tunneling Microscope (STM). This technique has previously been employed extensively to follow the electron induced creation of defect structures as well as to examine their electronic structure and reactivity.<sup>54, 124-127</sup> Furthermore, the ESD properties of titanium dioxide are well known and have been thoroughly investigated for example by Knotek and Feibelman, resulting in the formulation of a general mechanism for ESD via core-hole Auger decay.<sup>52</sup>

In combination, these factors make TiO<sub>2</sub> a promising substrate for investigation of EBISA.

## 6.2.2 Results and Discussion

### 6.2.2.1 Structure fabrication on TiO<sub>2</sub>(110)

The first goal of this chapter was to elucidate whether the EBISA technique can be transferred to a different oxide material, namely a TiO<sub>2</sub>(110)-1×1. For that purpose, line patterns and square patterns (2 × 2 μm<sup>2</sup>) were irradiated with the focused electron beam. All electron exposures for SEM and lithography were carried out with a beam energy of 15 keV and a probe current of 400 pA. The lithographic processes were controlled by NanoScribbler (c.f. Chapter 5.4). For line exposures a single sweep with a step size of 12 nm was applied. The square patterns were exposed in a single sweep, meander-like pattern at a step size of 6 nm. The total electron dose was controlled via the respective dwell times.

Fe(CO)<sub>5</sub> was introduced at a background pressure of 3.0 × 10<sup>-7</sup> mbar after the irradiation in order to allow growth of iron structures at the irradiated positions. The surface pressure is enhanced by a factor of approx. 30 due to the dosing nozzle, according to simulations using the GIS simulator program.<sup>95, 98, 128</sup> The gas was pumped off after 270 min, corresponding to an exposure of about 1.1 × 10<sup>5</sup> L (1 Langmuir is 10<sup>-6</sup> Torr × s = 1.33 × 10<sup>-6</sup> mbar × s). Figure 6-1 shows SEM images of the resulting Fe line deposits (a-d) and Fe square deposits (e-h).

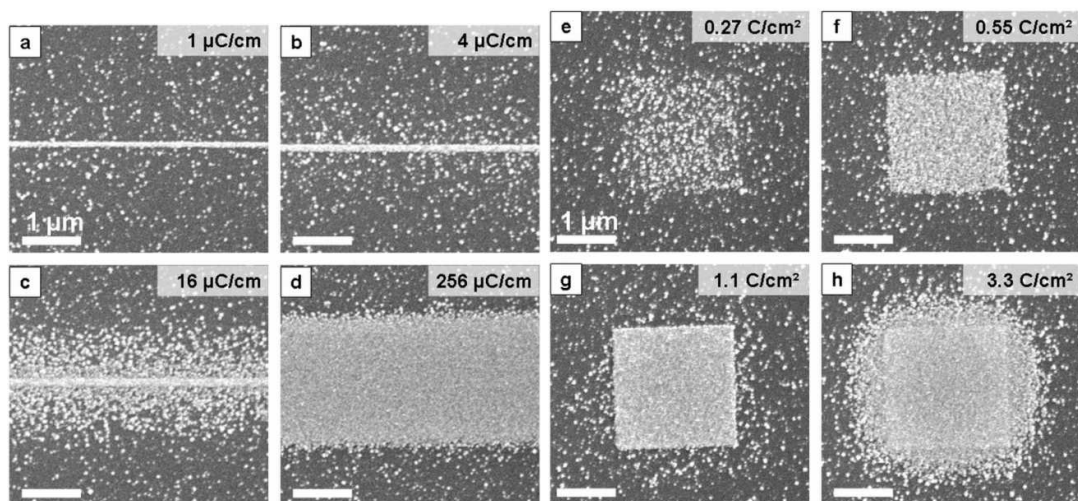


**Figure 6-1:** Line (a-d) and  $2 \times 2 \mu\text{m}^2$  square deposits (e-h) fabricated by EBISA on  $\text{TiO}_2(110)$  using  $\text{Fe}(\text{CO})_5$  as a precursor (approx.  $1.1 \times 10^5 \text{ L}$ ). Primary electron doses are indicated on the top right. The line width (FWHM, SEM intensity) increases with PE dose and range from approx. 150 nm (a) to  $2.6 \mu\text{m}$  (d). The central line is a result of activation by PEs, while the fringe is caused by BSE proximity effects. For the square fields, deposit density increases from a loose grain assembly at  $0.27 \text{ C/cm}^2$  via a close-packed assembly at  $0.55 \text{ C/cm}^2$  to a fused-grain deposit of near-ideal geometry at  $1.1 \text{ C/cm}^2$ . At even higher doses proximity effects also cause a fringe growth ( $3.3 \text{ C/cm}^2$ ). Note that scattered iron clusters are found all over the surface without electron exposure, which is attributed to active defects created during sample preparation.

The images show a strong increase of the amount of deposited iron with electron dose. AES measurements 24 hours after fabrication (Figure 6-2) indicate the purity of the iron structures to be  $> 90\%$ . For AES the electron beam of the SEM was used as the ionization source at an energy of 15 keV and a beam current of 3.0 nA. The observed purity is similar to that achieved on  $\text{SiO}_2$  substrates.<sup>5, 13, 14</sup> Those iron deposits on  $\text{SiO}_2$  exhibit a low room temperature resistivity of  $88 \mu\Omega\text{cm}$  as well as ferromagnetic behavior.<sup>36</sup> These properties can be expected to be similar on  $\text{TiO}_2$ , potentially making the corresponding iron deposits suitable for interconnects and other applications where material of a high purity is required.

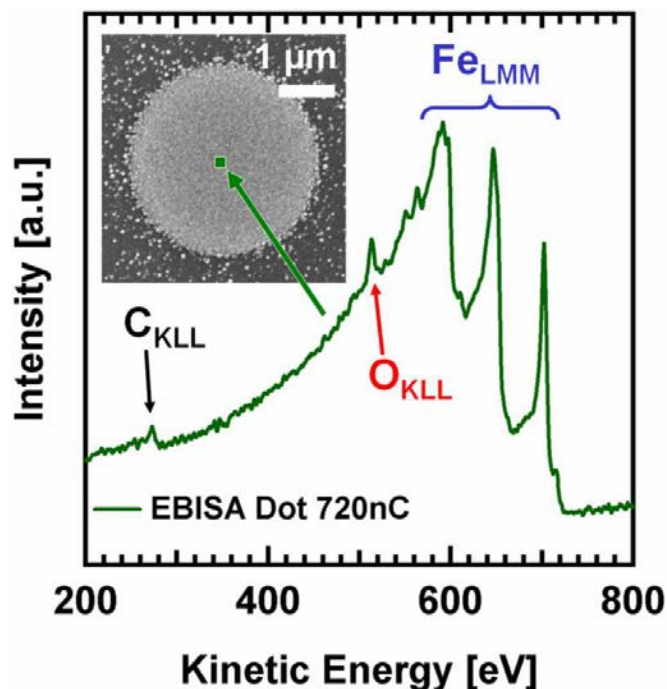


**Figure 6-2:** Local Auger Electron Spectroscopy recorded on the circular structure shown in the inset. The structure was prepared by EBISA and subsequent dosage of 270 min ( $\sim 1.1 \times 10^5$  L) of Fe(CO)<sub>5</sub>. Evaluation of the peak areas shows a content of >90%at. Fe, <7 %at. O and <3 %at. C. The thickness of the iron structure is estimated to be around 50 nm based on typical growth rates. Substrate-related Ti features are completely attenuated.

At higher SEM magnification, we observe that the structures are comprised of crystalline iron nanocubes. The density of the cubes within the line and square deposits varies with the applied electron dose while the size of the individual cubes at a given gas exposure seems to be similar. With increasing gas exposure the size of the clusters increases due to autocatalytic growth. For increased electron doses, the cubes start to merge into continuous patches, as can be seen with the 1.1 C/cm<sup>2</sup> square deposit (Figure 6-1g) or the line deposits (Figure 6-1a and b). Higher electron doses mark the start of proximity effects, i.e. unintended deposits near the irradiated patterns due to electron scattering.<sup>4, 13, 129</sup> Pronounced proximity effects are present at the 3.3 C/cm<sup>2</sup> square irradiation doses (Figure 6-1h) and the higher line doses (Figure 6-1c, d). For EBISA, all of the observed proximity effects can be attributed solely to backscattered electrons (BSE) and associated secondary electrons (SE).<sup>13</sup> Proximity effects from forward scattered electrons (FSE) do not occur in EBISA, since no deposit is formed during the e-beam exposure step.<sup>13</sup>

At the given experimental conditions, the growth rate of the deposited iron structures due to the autocatalytic decomposition of Fe(CO)<sub>5</sub> is below 1 nm per minute. By changing the

experimental parameters, i.e. by reducing the precursor pressure, it should be possible to further decrease the catalytic growth rate. This opens up the vista to fabricate electrodes with controlled extremely small gap openings, e.g. to contact individual molecules.

Figure 6-3 shows a section of the  $\text{TiO}_2(110)$  surface that was not irradiated by electrons before the dosage of 270 min of  $\text{Fe}(\text{CO})_5$ . The observation of homogeneously scattered cubes on the non-irradiated surface in Figure 6-3 (also visible in the non-irradiated areas in Figure 6-1a, b and e) points to the presence of non-electron-beam induced nucleation points on the as-prepared  $\text{TiO}_2(110)$  surface (cf. Figure 6-7). The defects are oxygen vacancies, which typically are present at an initial concentration of 5% ML (1 ML is the number of surface unit cells). The vacancies react with water in the residual vacuum to form the second major form of defects, bridging hydroxyls (one water molecule reacts with one vacancy to produce two hydroxyls).<sup>130</sup> Both defect types may be responsible for the initial  $\text{Fe}(\text{CO})_5$  decomposition.

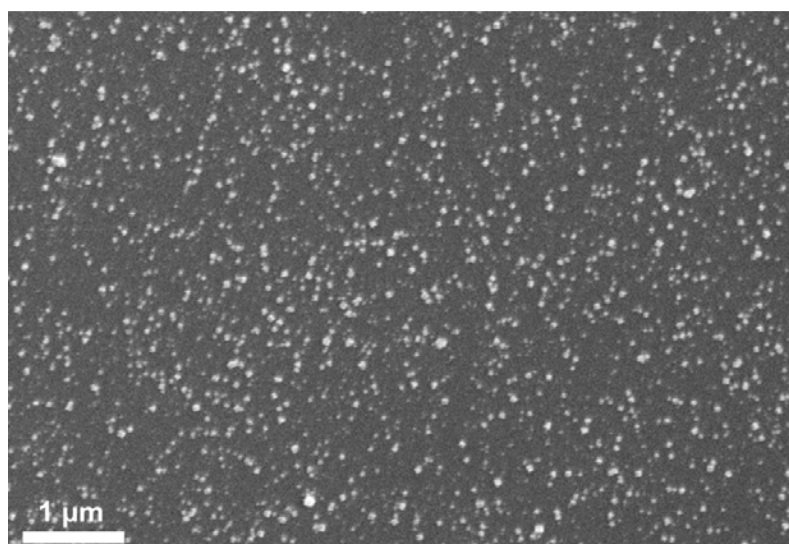


**Figure 6-3:** Non-irradiated surface of  $\text{TiO}_2(110)$  after dosage of 270 min ( $\sim 1.1 \times 10^5$  L) of  $\text{Fe}(\text{CO})_5$ . The bright features correspond to Fe crystallites, which nucleate at intrinsic defect sites on the surface and grow autocatalytically while  $\text{Fe}(\text{CO})_5$  is supplied.

#### 6.2.2.2 Activation Mechanism - AES

Turning to the EBISA mechanism, the effect of the 15 keV electron beam on the reduction state of the surface was studied. As  $\text{TiO}_2$  was one of the substrates that was heavily investigated concerning the electron simulated desorption (ESD) processes already in the late

1970s by Knotek and Feibelman,<sup>52</sup> it is not surprising that ESD is observed when the surface is irradiated with 15 keV electrons from the SEM.

Figure 6-4 a) and b) show Auger electron spectra of a freshly prepared TiO<sub>2</sub>(110) surface after irradiation with a comparably low electron dose (red, “pristine”) and a high local electron dose (blue, “reduced”).

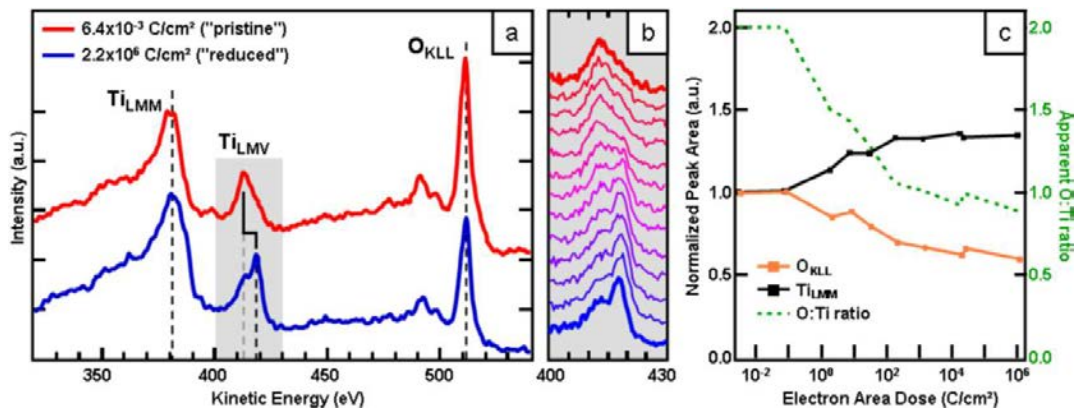


**Figure 6-4:** (a) AE spectra of pristine (red) and electron irradiated, reduced TiO<sub>2</sub> samples in non-derivative mode. The loss of oxygen KLL intensity is a clear indication of oxygen loss, i.e. ESD, while the intensity shift of the titanium LMV peak from lower to higher kinetic energy is an indication of a shift from fully oxidized Ti<sup>4+</sup> towards more reduced states like Ti<sup>3+</sup> or even lower. The gradual shift of the peak shape with increasing electron dose is shown in (b), top to bottom. (c) Quantitative evaluation of the normalized Ti<sub>LMM</sub> (blue) and O<sub>KLL</sub> peak areas and apparent O:Ti ratio (green) versus applied electron dose. The apparent O:Ti ratio (green) is set to 2:1 (TiO<sub>2</sub>) for very low electron doses, i.e. a pristine substrate. Electron stimulated desorption causes a loss of oxygen atoms, i.e. signal intensity, which simultaneously leads to an increase in the relative intensity of the Ti<sub>LMM</sub> signal.

The most prominent features of the spectra in Figure 6-4 are the Ti<sub>LMM</sub> and Ti<sub>LMV</sub> peaks at 383 and 413-419 eV, respectively and the O<sub>KLL</sub> peaks at 491 and 511 eV. It is immediately apparent that the oxygen signal is considerably smaller for the strongly irradiated surface (blue) than for the almost pristine surface (red); the Ti signals show the opposite trend, albeit not as pronounced. This behavior evidences the electron beam induced desorption of oxygen from the surface and is in line with that expected from Electron Stimulated Desorption (ESD) results from TiO<sub>2</sub> at lower electron beam energies.<sup>52, 131</sup> In addition, the change of the peak shape of the Ti<sub>LMV</sub> signal allows for insight into the chemical state of the Ti atoms of the surface. As discussed by Nishigaki<sup>132</sup> and Göpel,<sup>133</sup> the LMV Auger peak consists of two

components: 413 eV for  $\text{Ti}^{4+}$  and 419 eV for  $\text{Ti}^{<4+}$ . In a simplified picture, for  $\text{Ti}^{4+}$ , in complete absence of a Ti 3d valence electron, the valence electron in the LMV Auger process stems from an interatomic transition of an O 2p electron with higher binding energy; contrary, for  $\text{Ti}^{<4+}$  at least a partial electron charge remains in the Ti 3d level (at lower binding energy than the O 2p level) and thus participates in an intraatomic Auger transition observed at higher kinetic energy. The observed intensity shift from the low- to the high-kinetic energy contribution of the  $\text{Ti}_{\text{LMV}}$  peak therefore is a direct indication for a reduction of the  $\text{Ti}^{4+}$  by the electron beam. The evolution of the LMV peak shape upon increasing electron irradiation is illustrated in Figure 6-4 (b) from top (pristine, red) to bottom (reduced, blue).

In Figure 6-4 (c), the normalized ( $I_{\text{pristine}} = 1$ ) peak areas of the  $\text{Ti}_{\text{LMM}}$  (black) and  $\text{O}_{\text{KLL}}$  (orange) signals and the O:Ti peak ratio (green) are plotted versus the primary electron dose (note the logarithmic scale). The apparent O:Ti peak ratio is normalized so that the value for the pristine surface is set to 2, i.e.  $\text{TiO}_{2.0}$ . For doses lower than  $0.1 \text{ C/cm}^2$ , the peak ratio does not change, i.e. the applied dose is not sufficient to induce a reduction of the surface detectable in AES. After crossing the  $0.1 \text{ C/cm}^2$  threshold, the oxygen intensity and the O:Ti ratio drop rapidly until a lower limit at  $\sim 0.9$  is approached at doses larger than  $10^3 \text{ C/cm}^2$ . The corresponding relative oxygen intensity is 0.6 of the initial value of the pristine surface. The obtained O:Ti ratio of 0.9 indicates an average surface composition of roughly  $\text{TiO}_{0.9}$ . Note that the chemical composition of the surface is likely to be non-uniform after the reduction process; therefore the detected Auger signal is a convolution of different Ti oxidation states. In addition, decreased damping due to the loss of oxygen atoms from the topmost layers has to be taken into consideration when assessing the  $\text{Ti}_{\text{LMM}}$  intensity. Nevertheless, the O:Ti ratio serves as an indicator for the degree of e-beam induced reduction of the surface.

### 6.2.2.3 Activation Mechanism - STM

The Auger spectra indicate that above  $0.1 \text{ C/cm}^2$ , the stoichiometry of the surface changes gradually from  $\text{TiO}_2$  to  $\text{TiO}_{0.9}$  at  $10^3 \text{ C/cm}^2$ . As for the accompanying morphology change, Figure 6-5 shows the effect of the electron beam as viewed by STM. Note that the image has been high-pass filtered to improve visibility of the defects using the fast Fourier transform (FFT) algorithm of WSxM to suppress the low frequency contribution. A centered Blackman-Harris function with a range of approx.  $1/k = 1 \text{ nm}$  was chosen as the cut-off.

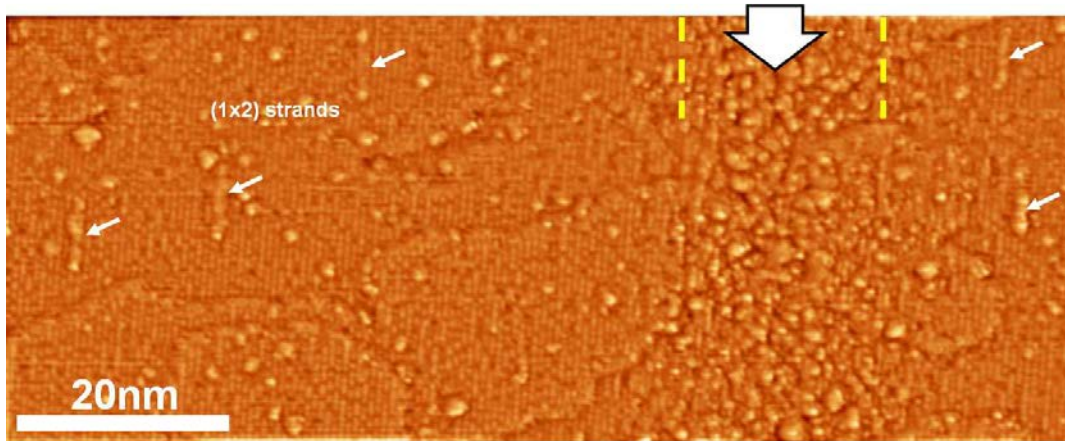


**Figure 6-5:** High resolution STM micrograph ( $I = 280$  pA,  $U = 1.2$  V, moderately high pass filtered) of an e-beam line irradiation ( $50 \mu\text{C}/\text{cm}$ ), marked by the large arrow and yellow lines. The surface on the left shows only minor damage; the typical row pattern of the TiO<sub>2</sub>(110) surface is preserved. Defects include (1×2) reconstructed sections (small arrows), dark defects in the row structure and isolated protrusions. On the right, a disordered section running top to bottom was identified as the result of a line irradiation with a primary electron dose of  $50 \mu\text{C}/\text{cm}$ . The (1×1) structure is barely retained in the highly damaged area; no characteristic defects can be identified in the irradiated area. The loss of long and short range order corresponds to an electron induced surface amorphisation.

Prior to e-beam exposure, the STM image shows bright rows along the [001] direction, separated by 0.65 nm, that corresponds to Ti atoms.<sup>100, 134</sup> A line exposure (electron energy 15 keV, beam current 400 pA, step size 12 nm, dwell time 150 ms, line dose  $50 \mu\text{C}/\text{cm}$ ), corresponding to a primary electron area dose of approx.  $60\text{-}100 \text{ C}/\text{cm}^2$ , should result in an O:Ti ratio of 1.1 to 1.2 at the irradiated positions. The exposed region can be clearly identified in the STM image in Figure 6-5 as an area with a disordered appearance and a strongly increased number of protrusions (bright) arranged within a vertical line with a width of approximately  $20 \pm 5$  nm (indicated by dotted yellow lines); this width is  $\sim 7$  times larger than the nominal beam diameter of 3 nm (Gauss profile, 20/80 criterion), indicating the well-known broadening due to SE and BSE proximity effects. The apparent surface roughness (root mean square, rms) of the exposed area (0.12 nm) in STM is double that of the non-irradiated surface. The left hand side of the image in Figure 6-5 resembles the as-prepared surface; the characteristic Ti row structure in [001] direction is clearly visible. However, there are additional defects in the form of isolated protrusions and in-row-depressions that can be attributed to proximity effects. Apart from the increase in mean roughness, the e-beam induced disorder does not cause a significant increase in average apparent height. This

indicates the absence of unintentionally formed deposits, for example EBI deposition of a carbonaceous layer from residual gases.

Figure 6-6 comprises a contrast enhanced SE micrograph (a) as well as STM images of a  $50 \mu\text{C}/\text{cm}$  line pattern before (b) and after (c) dosing of approx. 10 L of  $\text{Fe}(\text{CO})_5$  at background pressures below  $10^{-8}$  mbar (surface pressure: low  $10^{-7}$  mbar). The position of the line irradiation is indicated by the yellow markers. Note that all images share the indicated scale bar.

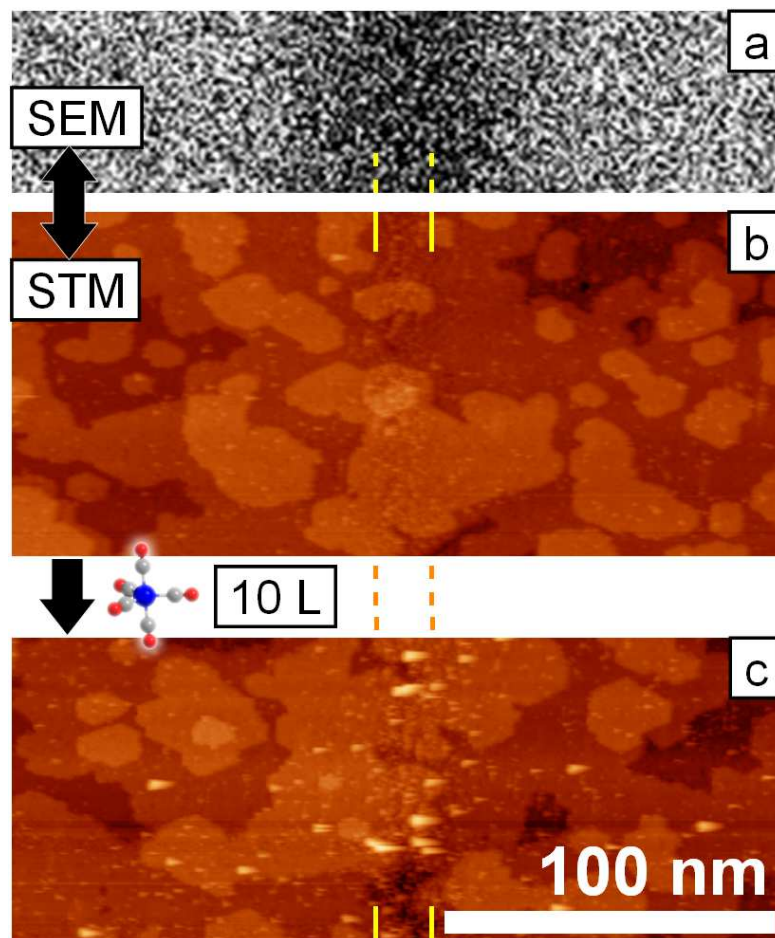


**Figure 6-6:** SEM scan (a) and STM topography (b) of the  $\text{TiO}_2(110)$  surface after line irradiation with  $50 \mu\text{C}/\text{cm}$  and after initial Fe growth from  $\text{Fe}(\text{CO})_5$  (c). The line position is indicated by yellow markers. The strongly contrast enhanced scanning electron micrograph (a) shows a dark feature at the position of the line irradiation, conventionally attributed to carbon deposition from residual gases. STM reveals a high degree of disorder at the line position, while the surrounding surface remains fairly unaffected by the irradiation. Upon exposure to about 10 L of  $\text{Fe}(\text{CO})_5$ , clusters form predominantly at the irradiated surface area (c). Cluster formation next to the line exposures is attributed to defects induced by backscattered electrons, i.e. common proximity effects.

The center of the SEM image in Figure 6-6a clearly shows a significant e-beam induced darkening. Previous studies showed that this darkening of irradiated areas is an intrinsic feature of e-beamed oxide surfaces and is not indicative of contamination.<sup>5</sup> These results indicate that the modifications to the TiO<sub>2</sub>(110) morphology and subsequent reaction with Fe(CO)<sub>5</sub> are a result of e-beam induced oxygen loss.

After the gas exposure the formation of iron deposits in the form of clusters is observed, primarily in the regions irradiated with electrons (indicated by yellow lines). Larger clusters appear as slightly asymmetric protrusions in the image, a consequence of the applied scanning speed. The higher number of large clusters at or near the line irradiation clearly shows that the disordered, defect rich surface that is caused by the electron irradiation is indeed highly active towards the initial Fe(CO)<sub>5</sub> decomposition.

In addition to the clusters observed within the yellow lines in Figure 6-6, some deposits are also found in non-irradiated areas on both sides of the irradiated line. These clusters originate from growth due to the intrinsic surface defects in TiO<sub>2</sub>(110) (see above), as well as from growth due to BSE proximity effect induced defects. The BSE exit range of TiO<sub>2</sub>, here defined as the distance from the point of impact that includes 99% of all emitted BSEs ( $r_{99}$ ), was simulated with the program *CASINO V2.42* (see also Chapter 3.6 and ref. <sup>92</sup>) and amounts to about 1050 nm. For the simulations (using the CASINO standard physics models) a PE number of  $10^7$  and a beam radius of 1.5 nm were applied.

All of the scanned area in Figure 6-6c is well within this exit range. The BSEs ( $E > 50$  eV by definition) are able to induce ESD of oxygen atoms within the Knotek-Feibelman framework ( $E_{\text{min,ESD}} = \sim 34$  eV),<sup>52</sup> thus creating isolated defects. Therefore, it is not possible to definitely attribute the scattered clusters to either intrinsic defects or BSE-related EBISA.

Figure 6-7 juxtaposes high magnification examples of the surface after line irradiation (a) and after cluster growth (b). The irradiated surface (indicated by yellow lines) is disordered and defect-rich, as was already observed before (Figure 6-5). The observed large clusters are mainly located at or close to the position of the line irradiation and have a typical diameter of  $3.2 \pm 0.3$  nm (including tip convolution) and an apparent height of  $1.2 \pm 0.1$  nm (see inset in Figure 6-7). This corresponds to clusters containing 650 to 1000 Fe atoms. The WSxM flooding tool was used to evaluate the apparent volume of clusters on the surface.

The state of the surface of the latter sites of these cluster is indicated by solid white circles in Figure 6-7a. It is not possible to assign active sites from the available STM data, as the amount of disorder is too high to identify individual atoms or surface structures.

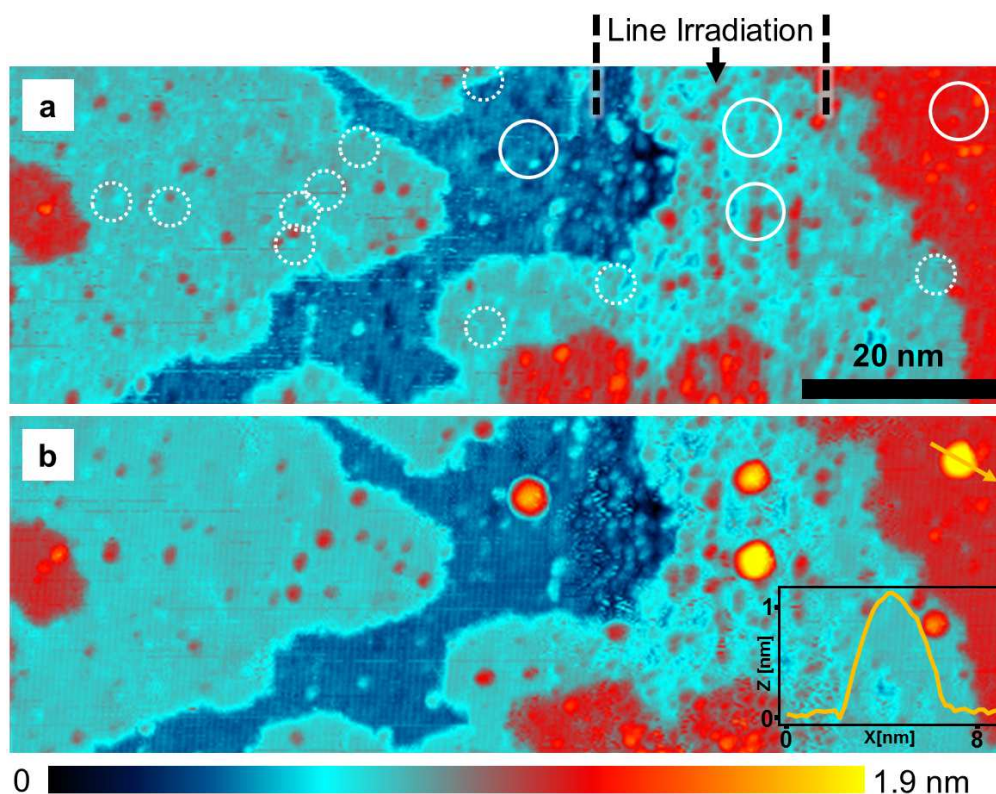


**Figure 6-7:** STM images of a line exposure (right part of the images, marked by black lines) imaged before (a) and after  $\text{Fe}(\text{CO})_5$  dosage (b). White circles in (a) mark the location of corresponding deposits in (b); the inset shows the apparent height profile of the top right Fe cluster marked by the orange arrow. The image shows the known, striped rutile surface with the parallel rows running in  $[001]$  direction (top to bottom). The identification of single defects is not possible for the irradiated line structure due to the pronounced disorder. The more intact region on the left shows some isolated bright and dark spots which could be attributed to missing O or OH defects produced by scattering processes, i.e. proximity effects.

### 6.2.3 Conclusions

The EBID and EBISA study on  $\text{TiO}_2(110)\text{-}1\times 1$  has elucidated that it is indeed possible to activate the titania surface using the 15 keV electron beam so that it becomes active towards the decomposition of  $\text{Fe}(\text{CO})_5$ . In addition, the observation of growth time dependent morphology as well as massive, polycrystalline final state of the structures in combination with the high purity confirms that autocatalytic growth of  $\text{Fe}(\text{CO})_5$  occurs on this surface. The observation of both factors demonstrates that the EBISA protocol is a viable nanofabrication technique also on  $\text{TiO}_2$ , which broadens the scope of substrates and suggests EBISA to be a general process on oxide surfaces.

In addition to the selective growth due to the electron irradiation, random growth of Fe clusters was observed all over the surface, which has been attributed to intrinsic defects, e.g. oxygen vacancies, of the TiO<sub>2</sub>(110) surface.

Auger electron spectroscopy of areas irradiated with different electron doses confirmed electron stimulated desorption of oxygen from the surface. The simultaneous observation of Ti<sup><+4</sup> species clearly shows a reduction of the surface.

The reduction process and results were also investigated using STM, revealing a strong surface disordering for relevant electron doses. Individual defects, such as the known oxygen vacancies reported in literature, could not be observed within the activated area due to the disorder. It was shown, however, that the growth of Fe clusters proceeds predominantly at or in close proximity to the disordered, reduced surface regions.

In essence, the mechanism of the EBISA process on TiO<sub>2</sub>, and likely also on other oxide surfaces, involves reduction and restructuring of the substrate due to electron stimulated desorption of oxygen.

## 6.3 EBID and EBISA on Ultrathin Porphyrin Layers on Ag(111)

### ABSTRACT

This chapter demonstrates how a focused electron beam can be used to chemically activate porphyrin layers on Ag(111) such that they become locally reactive towards the decomposition of iron pentacarbonyl,  $\text{Fe}(\text{CO})_5$ . This finding considerably expands the scope of Electron Beam Induced Surface Activation (EBISA) and also has implications for Electron Beam Induced Deposition (EBID) as well. The influence of the porphyrin layer thickness on both processes is studied in detail using scanning tunneling microscopy (STM), scanning electron microscopy (SEM) as well as Auger electron spectroscopy (AES) and Scanning Auger microscopy (SAM). While a closed monolayer of porphyrin molecules does exhibit some activity towards  $\text{Fe}(\text{CO})_5$  decomposition after electron irradiation, a growth enhancement is found for bi- and multilayer films. This is attributed to a partial quenching of activated centers in the first layer due to the close proximity of the silver substrate. In addition, it will be demonstrated that the catalytic decomposition of gaseous  $\text{Fe}(\text{CO})_5$  on Ag(111) can be effectively inhibited by introducing a densely packed monolayer of 2H-tetraphenylporphyrin (2HTPP) molecules.

Results presented in this chapter have been published in “Electron Beam Induced Surface Activation of ultrathin porphyrin layers on Ag(111)” by F. Vollnhals, P. Wintrich, M.-M. Walz, H.-P. Steinrück and H. Marbach, in *Langmuir* (2013), vol. 29, pages 12290-12297.<sup>135</sup>

### 6.3.1 Introduction

Recently, the activation mechanism in EBISA was explored both experimentally and theoretically. UHV studies show that the irradiation step causes electron stimulated desorption (ESD) of oxygen atoms, from oxide surfaces ( $\text{SiO}_x$  and  $\text{TiO}_2$ , see Chapter 6.2),<sup>5, 14, 120</sup> via the Knotek-Feibelman mechanism.<sup>52</sup> The resulting oxygen vacancies have been identified as the active sites.<sup>5, 120</sup> For  $\text{Co}_2(\text{CO})_8$  activation on fully and partially hydroxylated christobalite  $\text{SiO}_2$  surfaces, loss of hydroxyl groups has been suggested as additional process, based on DFT studies;<sup>15</sup> in the corresponding experiments the surface was activated by an electron beam or plasma discharge.

The substrate surface also has been shown to play a key role in the FEBIP process. For example, carbon rich layers were identified as starting point of EBI depositions in UHV

experiments using  $\text{Fe}(\text{CO})_5$  as precursor,<sup>21</sup> and a freshly prepared carbonaceous layer was found to increase the deposition yield of  $\text{Co}_2(\text{CO})_8$ .<sup>23</sup> These observations underline the demand for a general understanding of the influence of the physical and chemical properties of the substrate, and especially the electron beam/surface interactions, beyond the electron scattering properties. It is obvious that well-defined substrates and ultraclean conditions, such as single crystal surfaces and UHV environment, are highly favorable for such studies.

One possible way to tune the surface properties is the modification by ultrathin layers, as these will have only a minor effect on the mainly bulk-dependent electron scattering properties, but allow elucidating the influence of the vacuum interface. Examples are the introduction of thin oxide layers or the deposition of molecular layers, e.g. self-assembled monolayers (SAMs).<sup>136</sup> SAMs are composed of molecules which spontaneously form ordered layers upon adsorption onto a surface. Classical SAM-forming molecules are comprised of a reactive anchor group, e.g. a thiol group for SAMs on gold substrates, and a tail group, e.g. an aliphatic chain, that can carry further functional moieties. Such self-assembled monolayers can be used for the modification of surface properties, e.g. wetting behavior or chemical resistance. In addition, it is possible to use SAMs in combination with techniques such as micro-contact printing and optical or electron beam lithography for nanostructuring purposes.<sup>6, 136-140</sup> An alternative approach towards surface functionalization is the use of ordered molecular layers prepared in UHV. Promising molecules in this context are porphyrins, e.g. tetraphenylporphyrin (TPP). Their high thermal stability and sufficient vapor pressure in combination with their self-organizing properties make them ideal materials for the investigation in UHV systems. Furthermore, they have been studied in great detail concerning their interaction with different substrates, molecule-molecule interactions, ordering aspects and reactivity.<sup>141, 142</sup> The wide range of available functionalities makes them ideal candidates for the design of functional molecular architectures.

In this chapter, ultrathin 2H-tetraphenyl porphyrins (2HTPP) layers are investigated as a means to modify a Ag(111) surface with a focus on the fabrication of nanostructures by EBID and EBISA.

### 6.3.2 Results and Discussion

EBID and EBISA experiments using  $\text{Fe}(\text{CO})_5$  were performed on bare Ag(111), and on Ag(111) covered with 2HTPP layers of different thickness: (a) a close-packed, self-assembled monolayer (MonoL), (b) a multilayer (MultiL), and (c) a partial “bilayer” (BiL), i.e. a

monolayer partially covered with islands of 2<sup>nd</sup> layer molecules, which combines characteristics of the mono- and the multilayer. In this chapter, the term “monolayer” shall always refer to a single, close-packed layer of molecules. 2H-tetraphenylporphyrin powders were purchased from Porphyrin Systems GbR, Germany, and deposited onto the freshly prepared Ag substrate via a self-constructed Knudsen cell evaporator, at an evaporation temperature of approx. 560-580 K. All experiments were performed at room temperature; electron irradiation was performed using a primary electron (PE) energy of 15 keV and a beam current of 400 pA (AES: 15 keV, 3 nA). NanoScribbler was used to control the lithographic processes. For line irradiations, a single sweep with a step size of 12 nm was applied. Dot exposures were prepared using a spot mode.

### 6.3.2.1 EBID on Ag(111)

First, EBID on the bare, freshly prepared Ag(111) surface was studied by irradiating different patterns while dosing Fe(CO)<sub>5</sub> through a nozzle (approx.  $9 \times 10^{-6}$  mbar); the sample was held at room temperature and the total exposure after 4.5 hours was approx.  $1.1 \times 10^5$  L. Figure 6-8a shows an SEM image after the EBID process: Interestingly, no specific structures can be unequivocally recognized and surface regions irradiated by the electron beam and not irradiated by the electron beam display appear basically identical. The fact that areas irradiated during the precursor dosage (EBID) are hardly distinguishable from the rest of the surface indicates that electron irradiation has only very minor (if any) effect on the Fe growth on Ag(111). Therefore, EBID is not suitable for the selective fabrication of Fe nanostructures on Ag(111). This is attributed to an intrinsic catalytic activity of the bare Ag(111) surface towards the dissociation of Fe(CO)<sub>5</sub>, yielding Fe deposits which then continue to grow autocatalytically at RT. There are studies reporting the thermal, photolytic and electron-induced decomposition of low coverages of Fe(CO)<sub>5</sub> on Ag(111), which indeed suggest some reactivity of the pristine silver surface.<sup>143, 144</sup> Overall, the observed behavior is similar to findings on Rh(110), Pt(111) and Ni(100), at room temperature or below.<sup>63, 65-67</sup>

The SEM image in Figure 6-8a shows needle-like structures, aligned in three directions, rotated by 120° to each other. Auger electron spectroscopy on the deposited film (Figure 6-8b) reveals that the surface is composed mainly of iron with about 7-9% at. of oxygen and no indication of carbon. The observed hetero-epitaxial iron growth is in very good agreement with literature and is attributed to the coplanar alignment of the bcc-Fe(110) and the fcc-Ag(111) plane, so that the Fe[002] lattice vector is parallel to the Ag<110> directions.<sup>145, 146</sup>

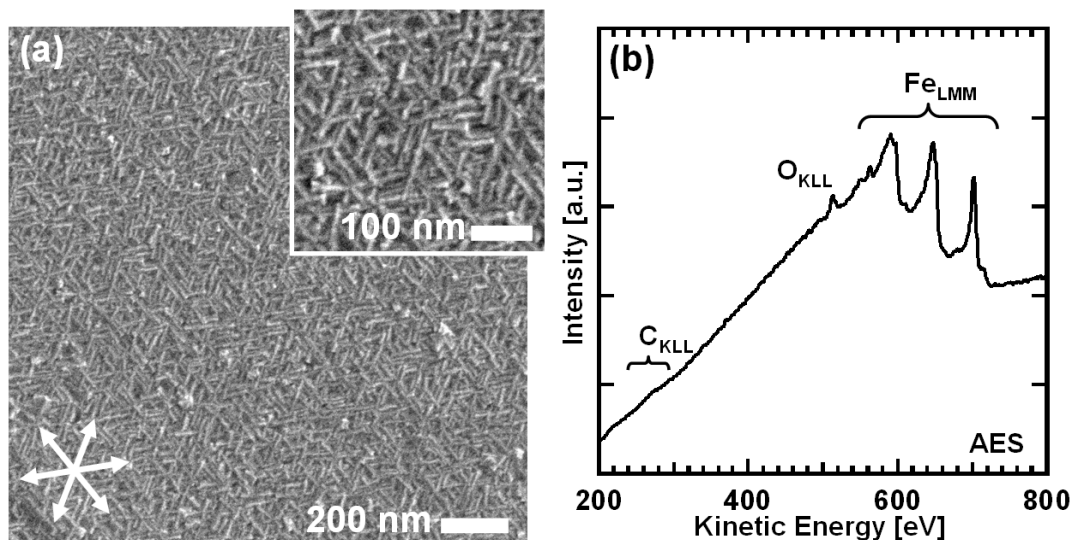


**Figure 6-8:** (a) SE micrograph and high magnification image (inset) of the iron layer on the non-irradiated Ag(111) surface after dosage of approx.  $\sim 1.1 \times 10^5$  L of  $\text{Fe}(\text{CO})_5$ , and (b) the corresponding Auger electron spectrum. Fe forms needle-like structures, oriented with angles of  $120^\circ$  with respect to each other. The observed features correspond to the known growth mode of Fe on Ag(111). The Auger spectrum shows pronounced  $\text{Fe}_{\text{LMM}}$  peaks and a small  $\text{O}_{\text{KLL}}$  contribution ( $< 8\%$ at.), while the  $\text{C}_{\text{KLL}}$  signal is below the detection limit. The Ag substrate signal is completely damped by the Fe layer.

The strain induced by lattice mismatch results in the formation of aligned bcc-Fe crystallites (Stranski-Krastanov growth).<sup>145-147</sup> These are found to be orientated in three directions, rotated to each other by  $120^\circ$ , as visible in Figure 6-8a. Thus, despite the fact that EBID with  $\text{Fe}(\text{CO})_5$  is not suitable to selectively deposit nanostructures on clean Ag(111), our study demonstrates that  $\text{Fe}(\text{CO})_5$  is an excellent precursor for standard chemical vapor deposition to produce clean iron layers on Ag(111), as an alternative to physical vapor deposition of Fe for the preparation of corresponding iron layers.

### 6.3.2.2 Preparation and characterization of porphyrin layers on Ag(111)

To quench the autocatalytic decomposition and thereby to make the FEBIP process selective, one might think of introducing a “protective layer” of organic molecules, namely 2HTPP. The choice of this particular molecule was motivated mainly by the detailed knowledge of its adsorption behavior on Ag(111).<sup>141, 142</sup> In the monolayer on Ag(111), tetraphenylporphyrins (e.g., 2HTPP, CuTPP, CoTPP, FeTPP, ZnTPP) generally adsorb such

that the plane of the macrocycle is parallel to the surface; they form a square lattice (lattice constant 1.4 nm), which is triggered by T-type interactions between the phenyl groups of neighboring molecules.<sup>141</sup> The 2HTPP monolayer (MonoL) on Ag(111) was prepared via deposition of a surplus of molecules and subsequent multilayer desorption at ~523 K.<sup>141, 148, 149</sup> It corresponds to a coverage of 0.037 molecules per surface atom.<sup>141</sup> The corresponding STM image in Figure 6-9a shows the square arrangement, in two (out of three) different domains, rotated to each other by 120°. In the corresponding LEED pattern depicted in Figure 6-9b one can extract the three rotational domains, which reflect the registry of the 2HTPP lattice with the three main crystallographic directions on Ag(111). For the closely related MnTPP with an axially coordinated Cl<sup>-</sup> ligand on Ag(111), a point-on-line (POL) superstructure  $\begin{pmatrix} b_1 \\ b_2 \end{pmatrix} = \begin{pmatrix} 5.44 & 1.46 \\ 1.46 & 5.44 \end{pmatrix} \begin{pmatrix} a_1 \\ a_2 \end{pmatrix}$  was deduced from LEED and STM measurements by Beggan et al.<sup>150</sup>

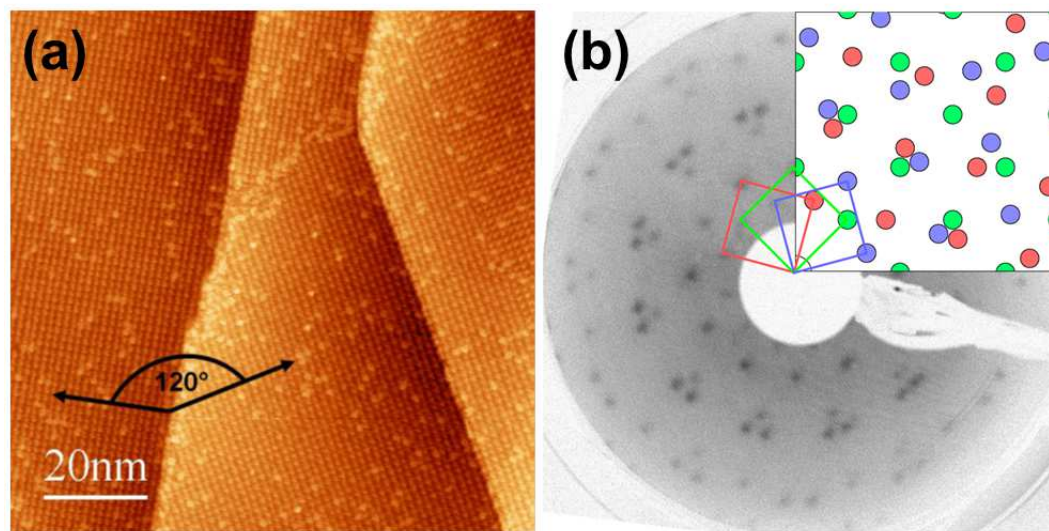


**Figure 6-9:** (a) STM image ( $U = +1$  V,  $I = 50$  pA) of a 2HTPP monolayer on Ag(111); arrows indicate orientations of the square domains. (b) LEED pattern of closed layer of 2HTPP molecules on Ag(111) recorded at  $E = 15.0$  eV. The inset shows a simulated pattern for the  $(1.46, 5.44 | 5.44, 1.46)$  superstructure with color-coded rotational domains.

Our results confirm this structure also for the 2HTPP monolayer on Ag(111), as is evident from the excellent agreement of the diffraction pattern and a corresponding simulation in Figure 6-9b. Further characterization was done by estimating the thickness of the porphyrin layer by the damping of the Ag<sub>MNN</sub> Auger signal. The corresponding analysis for the MonoL

film yielded a layer thickness of 0.4 to 0.5 nm. The thicker films were prepared by direct deposition of the required amount of molecules *without further thermal treatment* of the samples. The average thickness of the multilayer (MultiL), as determined by AES, was 2.5 nm, and that of the partial bilayer (BiL) 0.5-0.6 nm, i.e. roughly 1.2× the amount determined for the MonoL.

The SEM images of the as prepared films are depicted in Figure 6-10: the MonoL (a) appears mainly featureless, while the BiL (b) and MultiL (c) show areas of bi- and multimodal appearance.

The Auger line scan on a BiL surface (Figure 6-10d) reveals that the dark areas in SEM correspond to increased  $C_{KLL}$  and reduced  $Ag_{MNN}$  signals, and *vice versa* for the bright areas. This allows for the identification of the dark areas as 2<sup>nd</sup> layer islands of TPP molecules on top of the closed first layer (MonoL). Along the same line of argumentation, the multimodal appearance of the multilayer film is assigned to varying TPP layer thicknesses.

In principle, the observed contrast could be due to Z-based contrast in the BSE or due to differences in the SE emission coefficients. Monte-Carlo simulations using CASINO 2.42,<sup>92</sup> where individual porphyrin layers were approximated with a composition of  $C_{44}H_{30}N_4$  and a density of 1.27 g/cm<sup>3</sup> (single crystal value<sup>151</sup>), indicate virtually no influence on the BSE emission behavior for porphyrin layers thinner than 5 nm. This is a strong indication that the observed contrast is not due to Z dependence. It therefore seems likely that the contrast is related to a modified SE emission behavior of the second and higher layers, e.g. due to work function changes.

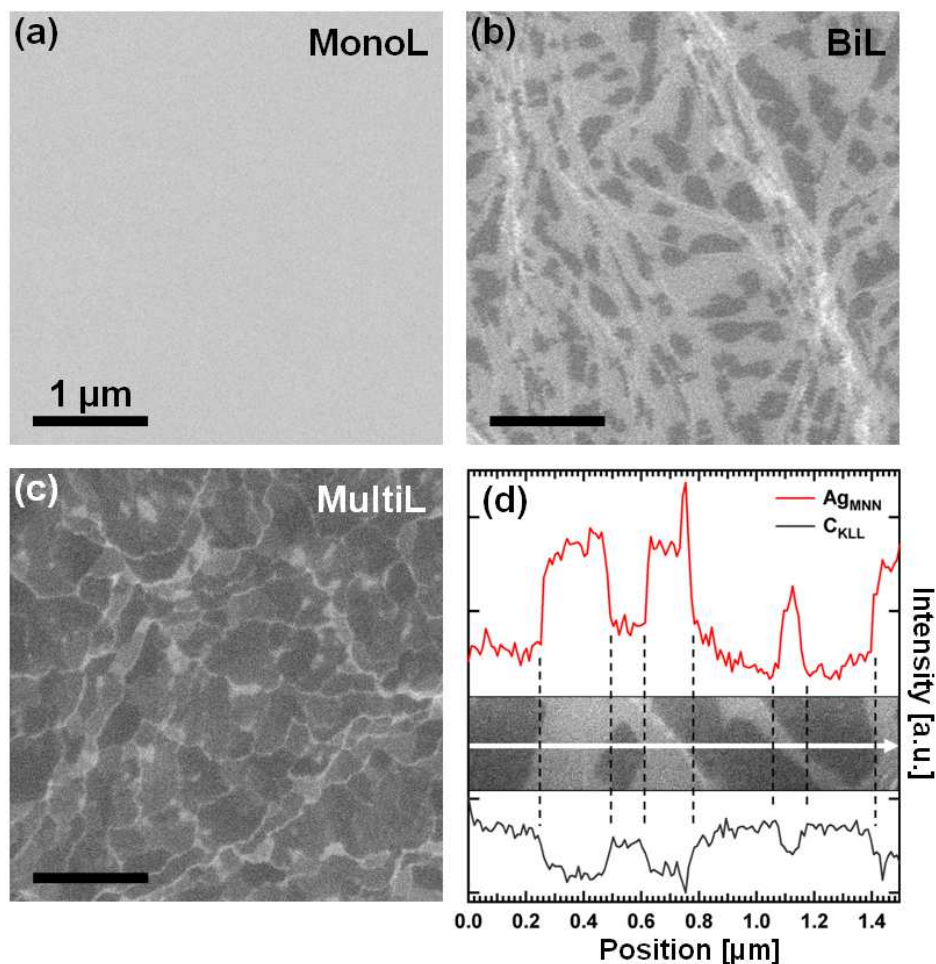


**Figure 6-10:** SE micrographs of monolayer (a), partial bilayer (b) and multilayer (c) films of 2HTPP and Auger line scan data of the BiL film (d). The monolayer (a) appears as featureless grey area, while the bilayer (b) exhibits a bimodal distribution of greyscales. The Auger data (d) shows that the dark areas correspond to higher carbon intensity (black curve) and significant damping of the Ag signals (red curve). The inverse situation is observed for the bright areas. The dark areas can therefore be identified as second-layer islands of TPP molecules on the first layer (bright). The multimodal appearance of multilayer (c) is attributed to different 2HTPP layer thicknesses on the respective terraces. Note that the contrast of the SEM images was adjusted for visibility such that the grayscale intensities are not directly comparable between images.

### 6.3.2.3 EBID and EBISA on porphyrin-precovered Ag(111)

After preparation of the porphyrin films, dot and line patterns were irradiated before (EBISA) and also during  $\text{Fe}(\text{CO})_5$  dosage (EBID). Due to prolonged exposure, initial iron

decomposition is followed by autocatalytic growth. Note that therefore the autocatalytic growth time of EBID structures varies slightly from structure to structure.

The SEM images of selected EBID structures in Figure 6-11 clearly show that Fe deposition on the porphyrin layers is a selective process, i.e. deposition only occurs in areas affected by the electron beam; the scattered small deposits in non-irradiated areas of the MonoL (Figure 6-11, left column) are assigned to imperfections of the monolayer film such that the underlying Ag surface is exposed, leading to growth catalyzed by the silver surface (see Chapter 6.3.2.1). Overall, it can be stated that the idea of quenching the catalytic activity of the Ag(111) surface towards of  $\text{Fe}(\text{CO})_5$  decomposition using 2HTPP layers was successfully implemented.

In the upper row of Figure 6-11, SEM images of dot deposits on MonoL, BiL and MultiL 2HTPP layers are depicted, after irradiation with 48 nC. For these structures only the central spots with the diameter of the electron beam ( $\sim 3$  nm) were irradiated with primary electrons. The obvious enlargement results from BSE and FSE proximity effects. The largest deposit is found for the thickest 2HTPP layer (MultiL), while the smallest is observed for the thinnest layer (MonoL), indicating that the EBID process is more effective for thicker layers. This conclusion is corroborated by the SEM image of the corresponding line exposures ( $8 \mu\text{C}/\text{cm}$ ) in the bottom row of Figure 6-11: Again the amount of deposited material in the line deposit increases with layer thickness, i.e., from left to right. This is particularly evident for the BiL, where monolayer areas (bright) coexist with second layer islands (dark). Inspection of Figure 6-11e and the corresponding inset reveals that indeed enhanced deposition is observed on the second layer islands, i.e. the thicker region.

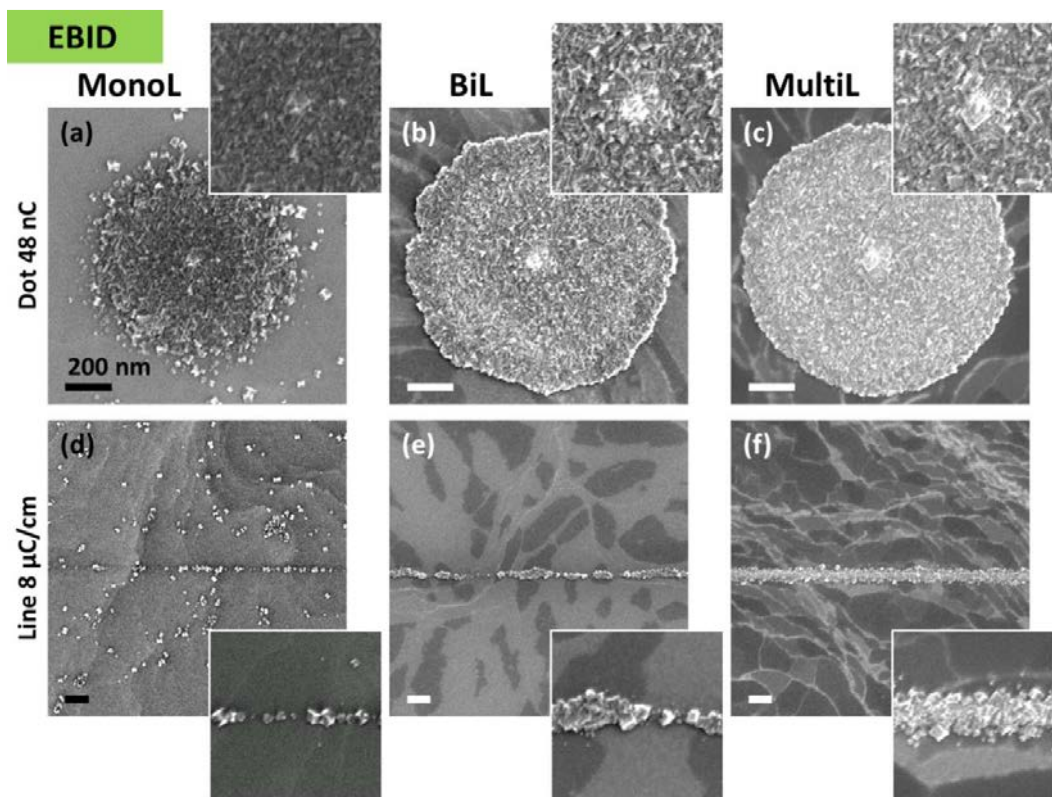


**Figure 6-11:** Dot (top row, a-c) and line deposits (bottom row, d-f) prepared by EBID on monolayer (MonoL: a, d), partial bilayer (BiL: b, e) and multilayer (MultiL: c, f) 2HTPP films on Ag(111). The electron dose was 48 nC for the dots and 8  $\mu\text{C}/\text{cm}$  for the line structures ( $E = 15 \text{ keV}$ ,  $I = 400 \text{ pA}$ ), while the precursor dose after EBID was approx.  $1.0 \times 10^5 \text{ L}$  for the dots and  $0.95 \times 10^5 \text{ L}$  for the lines. The insets contain higher magnifications of the respective structures. For a given electron dose, reduced structure growth can be observed on the MonoL compared to BiL and MultiL. The appearance of individual clusters on the MonoL surface (a, d) is attributed to incomplete coverage of the reactive silver sites, e.g. step edges, by the porphyrin film.

The cubic shape of the structures is typical for the autocatalytic growth of clean iron bcc crystallites from  $\text{Fe}(\text{CO})_5$  in UHV (see also Chapter 2.2).<sup>5, 14, 120</sup>

In a next step, it could be demonstrated that it is also possible to prepare dot and line deposits on the different porphyrin layers using the EBISA protocol. After the initial electron irradiation in UHV, the surface was exposed to  $\sim 9 \times 10^{-6} \text{ mbar}$   $\text{Fe}(\text{CO})_5$  for 270 min (approx.  $1.1 \times 10^5 \text{ L}$ ). The corresponding SEM images are shown in Figure 6-12.

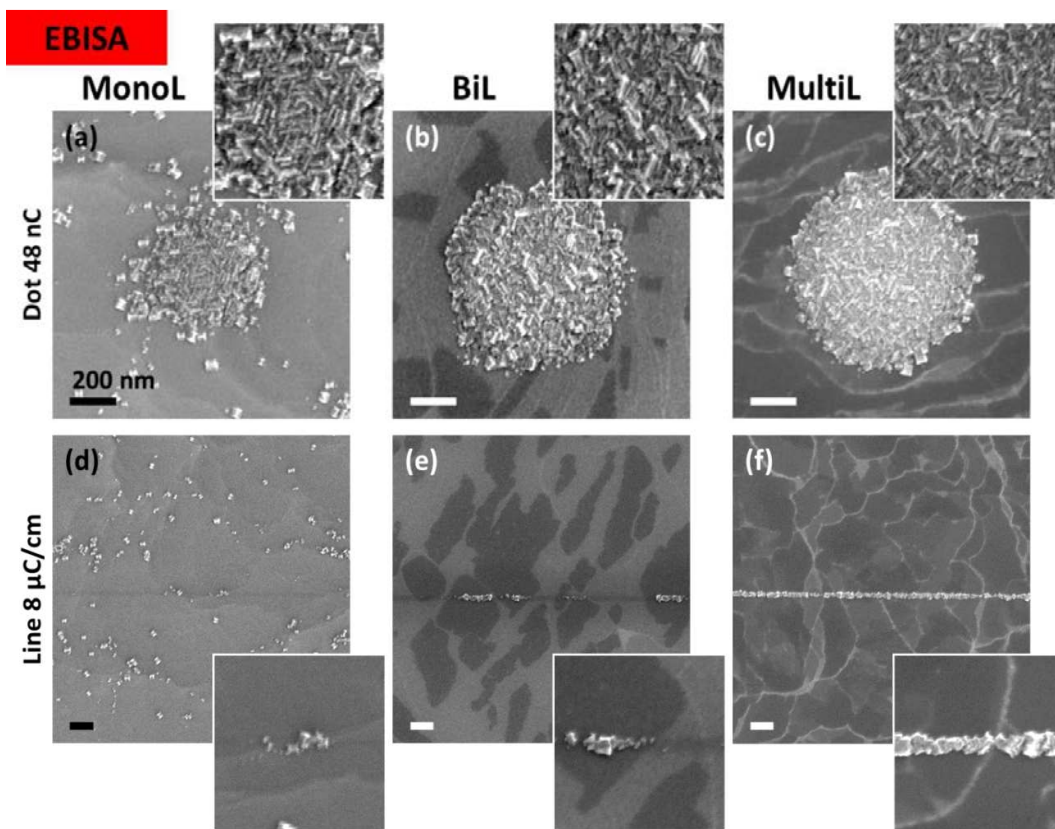


**Figure 6-12:** Dot (top row, a-c) and line deposits (bottom row, d-f) prepared by EBISA on monolayer (MonoL: a, d), partial bilayer (BiL: b, e) and multilayer (MultiL: c, f) 2HTPP films on Ag(111). The electron dose was 48 nC for the dots and 8  $\mu\text{C}/\text{cm}$  for the line structures ( $E = 15 \text{ keV}$ ,  $I = 400 \text{ pA}$ ), while the precursor dose after the surface irradiation was approx.  $1.1 \times 10^5 \text{ L}$  for all structures. The insets contain higher magnifications of the respective structures. For a given electron dose, reduced structure growth can be observed on the MonoL compared to BiL and MultiL. In image (e) structure growth is only observed on the dark, bilayer covered islands. The appearance of individual clusters on the MonoL surface (a, d) is attributed to incomplete coverage of the reactive silver sites, e.g. step edges, by the porphyrin film.

The dot deposits in the top row (Figure 6-12a-c) were irradiated with a primary electron dose of 48 nC. The resulting deposit diameters on BiL and MultiL are comparable (to within  $\pm 10\%$ ). For the MonoL, the deposits are always smaller, as is evident from the comparison of Figure 6-12a and 6b/c. In Figure 6-12d-f line patterns obtained with primary electron doses of  $8\mu\text{C}/\text{cm}$  are depicted. On the MonoL, a dark line is visible along with very few clusters, while on the MultiL a continuous wire of fused crystallites is observed. The BiL exhibits a mixture of both structures: a dark line and reduced growth on the brighter first layer sections, and pronounced wire growth on the darker bilayer sections. Obviously, the EBISA process is more effective on the thicker 2HTPP layer, similar to the overall behavior found for EBID.

While the applied local electron doses in Figure 6-11 and Figure 6-12 are identical, the precursor exposure times are somewhat shorter for EBID (dots approx. 8% shorter; lines approx. 14% shorter). Despite that, the deposits produced by EBID are significantly larger, indicating a more effective deposition by EBID. To quantify this behavior, the dot diameter is plotted vs. applied primary electron dose in Figure 6-13. The solid lines represent the EBID dot structures and the dashed lines the EBISA dot structures. The line colors indicate the type of the porphyrin layer. The graph reveals that EBID is more effective than EBISA for a given PE dose. The comparison of the relative sizes for the different porphyrin layers shows that the sizes on the BiL and the MultiL are similar, while on the MonoL a smaller size is found for a given PE dose. As discussed before, the increase of the EBISA dot deposits with electron dose is caused solely by BSE proximity effects.<sup>4, 13, 69</sup> The maximum range of BSEs (and therefore the maximum size of deposits due to proximity effects) can be predicted by Monte-Carlo simulations using CASINO 2.42 and is indicated by the grey horizontal line in Figure 6-13. The EBISA structures follow this prediction well and approach the size limit for very high doses (720 nC). In contrast to that, the EBID structure fabricated using a PE dose  $> 50$  nC exceed this BSE size limit. As those structures contain central protrusions, i.e. the onset of pillar growth, their increased size is attributed to FSE proximity effects which do not occur in EBISA.

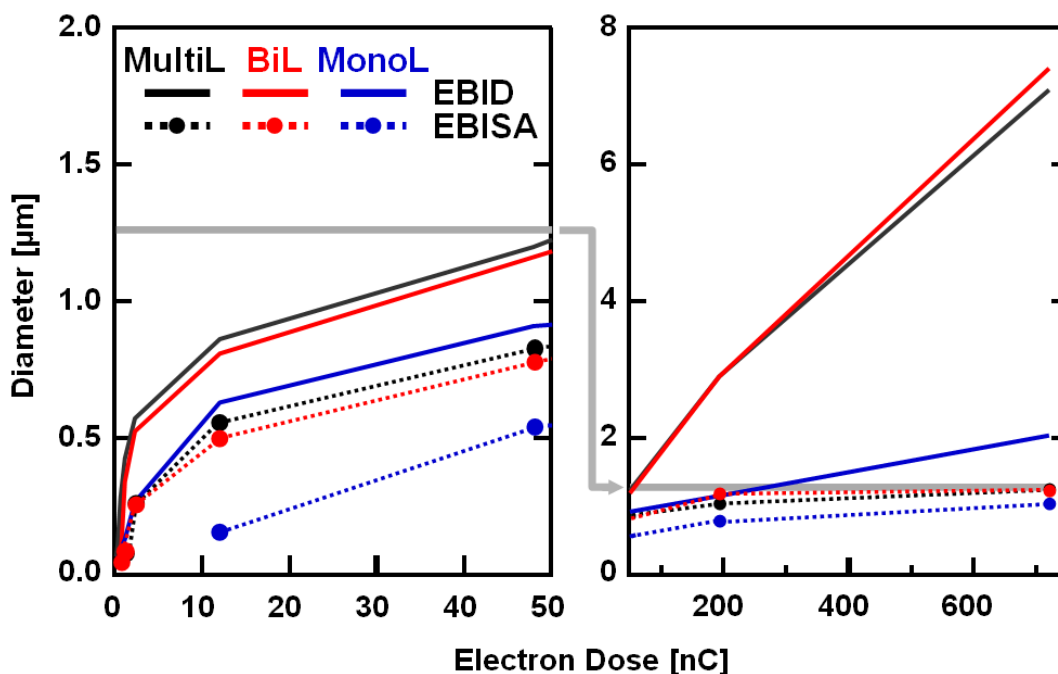


**Figure 6-13:** Diameter of EBID (solid lines) and EBISA (dashed) dot structures for multilayer (MultiL, black), partial bilayer (BiL, red) and monolayer (MonoL, blue) 2HTPP films on Ag(111) versus applied PE dose. The grey line represents the theoretical size limitation due to the BSE proximity effect. EBID deposits can overcome this limitation by FSE proximity effects. The diameters on MultiL and BiL are almost identical ( $\pm 10\%$ ) for EBID and EBISA, while on the MonoL, the diameter is significantly reduced. In general, the EBID deposits are larger than their EBISA counterparts.

EBISA has been demonstrated only for oxide surfaces (e.g.  $\text{SiO}_x$  and  $\text{TiO}_2$ ) so far; the activation was attributed to electron beam induced defects on the surface, i.e. loss of oxygen via ESD or removal of hydroxyl groups.<sup>5, 15</sup> Considering the absence of oxygen in the porphyrin layers, a different mechanism must be in operation. One possibility would be the local removal of the porphyrin layer via electron stimulated desorption of TPP molecules (or decomposition with subsequent fragment desorption) and subsequent autocatalytic growth on the uncovered Ag(111) patches. Such a mechanism can be excluded by the fact that the activation is much more pronounced on the thicker porphyrin layers; in addition, TPP are carbon rich and unlikely to yield volatile decomposition products upon electron irradiation.

To explain the observed behavior, a chemical modification of the TPP molecules by the electron beam is assumed, such that the molecules become chemically reactive. This mechanism is schematically sketched in Figure 6-14, with the activated porphyrins referred to as  $\text{C}_x\text{H}_y\text{N}_z^*$ . The observed differences for deposition on the bi-/multilayer and the monolayer

substrates can be explained by the proximity of the activated species to the silver substrate. While the close-packed first layer is in direct contact with the substrate, second and higher layer molecules are effectively decoupled from the substrate. Therefore, within the first layer, the activation process or the reactivity of the activated porphyrins can be quenched, e.g. by electron transfer from/to the substrate or the formation of fragment-surface bonds, which is not the case for second or higher layers. The substrate-induced quenching is in line with spectroscopic evidence e.g. for fluorescence quenching in differently substituted porphyrin derivatives on gold films and its reduction by the introduction of a spacer layer.<sup>152</sup>

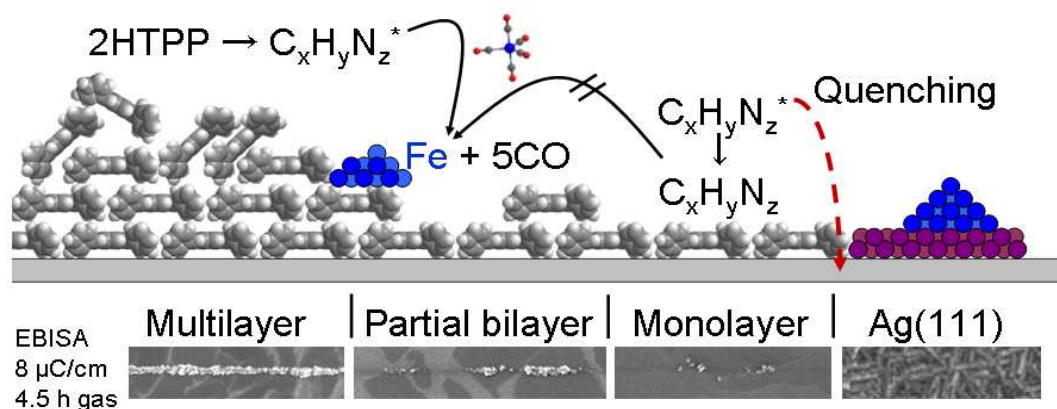


**Figure 6-14:** Summary of EBISA-based nanostructure fabrication results on organic layers on Ag(111). On pristine Ag(111),  $\text{Fe}(\text{CO})_5$  is catalytically decomposed to form a closed film of needle-like Fe crystallites (far right), which can be suppressed by a layer of TPP molecules. When these TPP films are irradiated with a focused electron beam, molecules are chemically modified ( $\text{C}_x\text{H}_y\text{N}_z^*$ ) and the films become active towards the decomposition of  $\text{Fe}(\text{CO})_5$ , which facilitates nanostructure growth. This activation is quenched on the monolayer (middle), presumably due to the close proximity to the Ag(111) support. On bi- and multilayer (left) the first molecular layer effectively decouples the activated molecules from the support and avoids the quenching (left).

Electron-induced activation of chemical bonds has been found e.g. upon electron irradiation of self-assembled monolayers (SAM)<sup>136</sup> for the fabrication of lateral nanostructures<sup>140</sup> or ultrathin carbon membranes.<sup>6, 139</sup> e.g., for biphenyl-thiol SAMs on gold electron induced dehydrogenation (and thus chemical modification) has been proposed with subsequent crosslinking via the formation of C-C single and double bond between phenyl groups of neighboring molecules.<sup>153</sup> Concerning the interaction of porphyrins with electrons, only limited information is available presently: In the gas phase, irradiation of  $\text{ClFeTPP}$  with

70 eV electrons lead to the loss of phenyl groups, possibly as benzene or biphenyl, and dehydrogenation among other processes.<sup>154</sup> In the condensed phase several reaction pathways are discussed for smaller molecules<sup>155</sup> and biomolecules,<sup>156</sup> but to the best of my knowledge, no studies on the electron beam induced decomposition of porphyrins on surfaces are available. Thus, the detailed chemical nature of the active species remains speculative. Possible reactive intermediates include radical species, anions, cations, reactive groups, unsaturated bonds, etc. Most of these intermediates *R* are likely to be able to substitute CO in Fe(CO)<sub>5</sub> to give *R*-Fe(CO)<sub>*x*</sub>,<sup>157, 158</sup> which can undergo further decarbonylation steps and start the autocatalytic growth of the iron structures.

### 6.3.3 Conclusions

In most FEBIP related studies the role of the substrate is reduced to its electron scattering properties, and its surface is treated only as a passive ingredient. In this study, it is demonstrated that the physical and chemical properties of the surface can play a significant role in FEBIP, and that the surface properties can be modified by thin organic layers. Both the EBID and the EBISA protocol are found to be suitable for the controlled fabrication of clean iron structures on Ag(111) precovered with 2HTPP-layers, using Fe(CO)<sub>5</sub> as a precursor and also as probe molecule. While the pristine Ag(111) surface is catalytically active towards Fe(CO)<sub>5</sub> at room temperature, this activity is quenched by pre-adsorbed porphyrin layers, so that the FEBIP processes become selective again. The EBID process is found to be more effective than the EBISA process, which is in line with previous studies.<sup>12</sup> The results expand the concept of electron beam induced surface activation, which was until now only reported for oxidic samples, to organic layers. The activation of the porphyrin molecules on Ag(111) is significantly reduced for the monolayer due to the close proximity to the support, while activation in the second layer is decoupled from the substrate and thus more effective. The chemical nature of active species that is formed during the electron beam irradiation remains speculative and should be investigated further, e.g. by theoretical methods, in order to be able to predict and possibly design the reactivity for new applications and processes.

## 6.4 EBID and Autocatalytic Growth using $\text{Co}(\text{CO})_3\text{NO}$

### ABSTRACT

The autocatalytic growth of arbitrarily shaped nanostructures fabricated by electron beam induced deposition (EBID) and electron beam induced surface activation (EBISA) is studied and compared for iron pentacarbonyl,  $\text{Fe}(\text{CO})_5$ , and cobalt tricarbonyl nitrosyl,  $\text{Co}(\text{CO})_3\text{NO}$ . Different deposits are prepared on silicon nitride membranes and silicon wafers under ultrahigh vacuum conditions, and are studied by scanning electron microscopy (SEM) and scanning transmission X-ray microspectroscopy (STXM), including near edge X-ray absorption fine structure (NEXAFS) spectroscopy. It has previously been shown that  $\text{Fe}(\text{CO})_5$  decomposes autocatalytically on Fe seed layers (EBID) and on certain electron beam-activated surfaces, yielding high purity, polycrystalline Fe nanostructures (c.f. Chapters 2.2, 2.3, 6.2 and 6.3).  $\text{Co}(\text{CO})_3\text{NO}$  is found to exhibit autocatalytic growth on Co-containing seed layers. The growth yields granular, oxygen-, carbon- and nitrogen-containing deposits. In contrast to  $\text{Fe}(\text{CO})_5$  no decomposition on electron beam-activated surfaces is observed. In addition, it will be shown that the autocatalytic growth of nanostructures from  $\text{Co}(\text{CO})_3\text{NO}$  can also be initiated by an Fe seed layer, which presents a novel approach to the fabrication of layered nanostructures.

Results presented in this chapter have been published in “Electron-beam induced deposition and autocatalytic decomposition of  $\text{Co}(\text{CO})_3\text{NO}$ ” by F. Vollnhals, M. Drost, F. Tu, E. Carrasco, A. Späth, R. H. Fink, H.-P. Steinrück and H. Marbach, in the *Beilstein Journal of Nanotechnology* (2014), vol. 5, pages 1175-1185.<sup>159</sup>

### 6.4.1 Introduction

Most of the previous EBISA studies as well as some EBID studies used  $\text{Fe}(\text{CO})_5$  as precursor, which yields practically pure, (poly-)crystalline Fe on different substrates and can be reliably used as a probe molecule to detect e-beam induced reactivity.<sup>5, 12-14, 120, 135</sup> In addition,  $\text{Co}_2(\text{CO})_8$  was also identified as a suitable precursor.<sup>15</sup> Since other precursors may show a similar behavior, one relevant candidate concerning autocatalytic growth, namely cobalt tricarbonyl nitrosyl,  $\text{Co}(\text{CO})_3\text{NO}$ , shall be investigated in more detail. This precursor was chosen as it is more stable and easier to handle than the related  $\text{Co}_2(\text{CO})_8$  (see Chapter 6.5). In addition to the study of the decomposition susceptibility at the irradiated,

activated surfaces and the autocatalytic growth behavior, also the possibility of the fabrication of arbitrarily shaped, layered nanostructures was explored. Such layered structures could be realized via subsequent EBID/EBISA steps, which would require precise alignment of the irradiation position, or via the subsequent autocatalytic growth of different precursors. This concept of “tertiary growth” and its connection to the EBID and EBISA processes and autocatalytic growth is shown schematically in Figure 6-15.

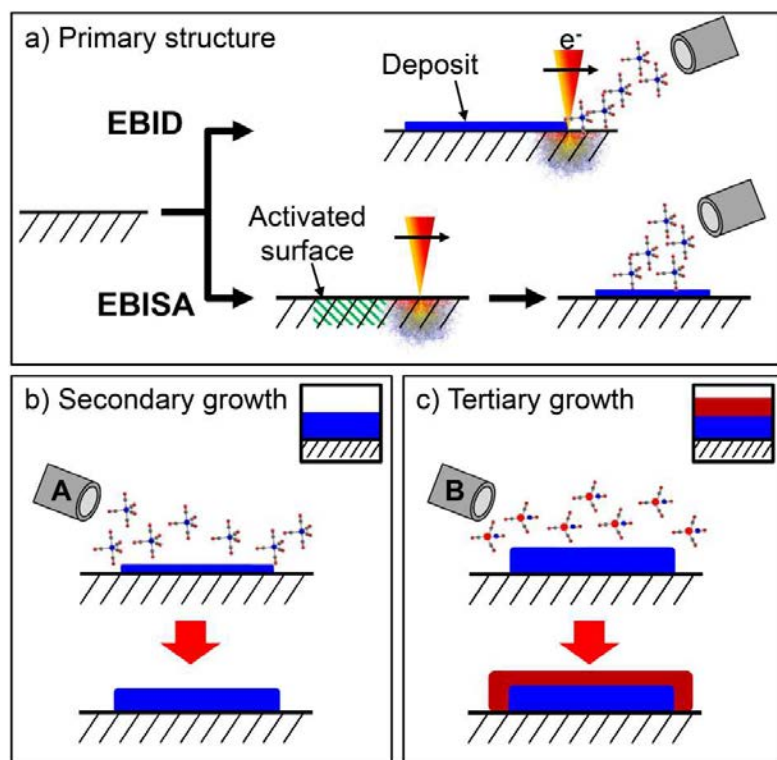


**Figure 6-15:** Fabrication and secondary/tertiary growth of nanostructures. The deposits can be fabricated by electron irradiation of a surface in the presence of a precursor (EBID) to form a thin primary deposit (a, top). In the absence of a precursor (a, bottom), some surfaces can undergo selective electron beam induced surface activation (EBISA), also yielding a primary deposit upon post-exposure to the precursor. If the primary deposits are exposed to the precursor in a successive step, autocatalytic decomposition can lead to further secondary autocatalytic growth of the deposit (b). In the case that a different precursor is supplied, tertiary autocatalytic growth can occur, leading to a layered nanostructure (c). The icons in b) and c) will be used to indicate the respective process throughout this publication.

Cobalt tricarbonyl nitrosyl was studied before concerning its ionization properties in the gas phase,<sup>42, 43</sup> the electron induced decomposition under surface science conditions in

UHV,<sup>47</sup> and the fabrication and characterization of EBID nanostructures under high vacuum conditions.<sup>68, 160, 161</sup>

In the gas phase, the decomposition proceeds via direct ionization or dissociative electron attachment depending on the kinetic energy of the involved electrons. Dissociative electron attachment is mainly observed for low-energy secondary electrons (<10 eV) and yields incompletely decomposed fragments, mostly  $[\text{Co}(\text{CO})_2\text{NO}]^-$ . Direct ionization occurs for  $E > 10$  eV and results in smaller fragments like  $\text{Co}^+$  or  $[\text{CoCO}]^+$ .<sup>42, 43</sup> It was suggested that the direct ionization route leads to deposition of incompletely dissociated precursor molecules, which in turn influences the content of non-metallic contaminants.<sup>43</sup>

Based on the irradiation of cold (105 K)  $\text{Co}(\text{CO})_3\text{NO}$  films of ~2.5 nm thickness on amorphous carbon and Au substrates with 500 eV electrons under UHV conditions the following decomposition mechanism was proposed: At low electron dose ( $<5 \times 10^{16}$  e<sup>-</sup>/cm<sup>2</sup>), one or two CO molecules are released and the NO ligand decomposes, yielding an adsorbed  $(\text{CO})_x\text{OCoN}$  species.<sup>47</sup> Upon further electron irradiation at low temperatures, decomposition of CO ligands is observed, yielding carbon-rich  $(\text{CoO}_y\text{N})\text{C}_{\text{ads}}$ . If instead the initially produced  $(\text{CO})_x\text{OCoN}$  species is annealed above 244 K, the thermally unstable CO ligands desorb without decomposition, yielding carbon free  $\text{CoO}_y\text{N}$ .<sup>47</sup>

At room temperature, EBID using  $\text{Co}(\text{CO})_3\text{NO}$  in a standard high-vacuum SEM setup yields deposits consisting of about 40-50 %at. Co, 25-35 %at. O, 10-15%at. N and 10-15 %at. C as determined by energy-dispersive X-ray spectroscopy (EDX).<sup>68, 160, 161</sup> The composition is almost independent of the applied beam current and energy, apart from a slight increase in oxygen content for increasing beam power.<sup>160</sup> The deposition yield decreases for higher electron energy, and increases strongly above 403 K substrate temperature.<sup>160</sup> A more detailed study addressed the temperature dependence for various precursors. For  $\text{Co}(\text{CO})_3\text{NO}$  and  $\text{Co}_2(\text{CO})_8$  three distinct regimes were proposed: (1) EBID only, (2) seeded growth, i.e. enhancement of deposition rate and autocatalytic growth, and (3) spontaneous decomposition and film growth, i.e., chemical vapor deposition (CVD).<sup>68</sup> For  $\text{Co}(\text{CO})_3\text{NO}$ , EBID was found up to ~393 K, followed by seeded growth up to ~403 K and spontaneous decomposition at higher temperature. In the EBID regime, increasing the temperature from 293 to 323 K lowered the carbon content by a factor of 3. In addition, the oxygen content decreased and the nitrogen content increased with temperature, while the cobalt content remained almost constant. In the seeded and spontaneous growth regimes, the composition remained constant with about 50 %at. Co, 20-25 %at. O and N, and few %at. C.

In this chapter, the autocatalytic growth of nanostructures using  $\text{Co}(\text{CO})_3\text{NO}$  at room temperature is investigated and compared to that using  $\text{Fe}(\text{CO})_5$ . EBID structures prepared from  $\text{Co}(\text{CO})_3\text{NO}$  in a UHV environment are exposed to additional  $\text{Co}(\text{CO})_3\text{NO}$  to induce autocatalytic growth; the resulting deposits are characterized by SEM and scanning transmission X-ray microscopy (STXM). STXM allows for the non-destructive quantitative spectromicroscopic characterization of the individual layers with nanoscale resolution and high contrast due to the possibility of resonant imaging.<sup>162</sup> The EBI deposits are compared to deposits produced by EBISA with  $\text{Co}(\text{CO})_3\text{NO}$ , and to deposits prepared by autocatalytic growth of  $\text{Co}(\text{CO})_3\text{NO}$  on iron seed layers, which were prepared beforehand by EBID with  $\text{Fe}(\text{CO})_5$ . The latter process opens up a novel approach for the localized fabrication of arbitrarily shaped bilayer and even multilayer nanostructures.

## 6.4.2 Results and Discussion

### 6.4.2.1 EBID plus autocatalytic growth

EBID structures were deposited from  $\text{Co}(\text{CO})_3\text{NO}$  on native  $\text{SiO}_x$  on Si(100) and 100 nm  $\text{Si}_3\text{N}_4$  membranes, and on commercially available, thermal  $\text{SiO}_2$  (300 nm) on Si(100). Electron irradiation was controlled by NanoScribbler using a beam energy of 15 keV at a beam current of 400 pA; the step size was 6.2 nm.

Figure 6-17 displays SEM images of square structures ( $1 \times 1$ ,  $2 \times 2$  and  $4 \times 4 \mu\text{m}^2$ ) on the native oxide on  $\text{Si}_3\text{N}_4$ , which were irradiated with primary electron (PE) doses ranging from 0.02 to 0.5 C/cm<sup>2</sup>. The precursor,  $\text{Co}(\text{CO})_3\text{NO}$ , was dosed onto the surface through a dozing nozzle during the irradiation at a background pressure of  $3.0 \times 10^{-7}$  mbar, which corresponds to a local pressure at the surface of about  $9 \times 10^{-6}$  mbar<sup>128</sup> based on simulations using GIS Simulator v1.5 (see also Chapter 4.1).<sup>98</sup>

The irradiation of each individual structure was performed by successively sweeping the same area 10 times. This procedure enhances the uniformity of the fabricated structures, which otherwise shows a pronounced asymmetry due to proximity effects. An example is shown in Figure 6-16.

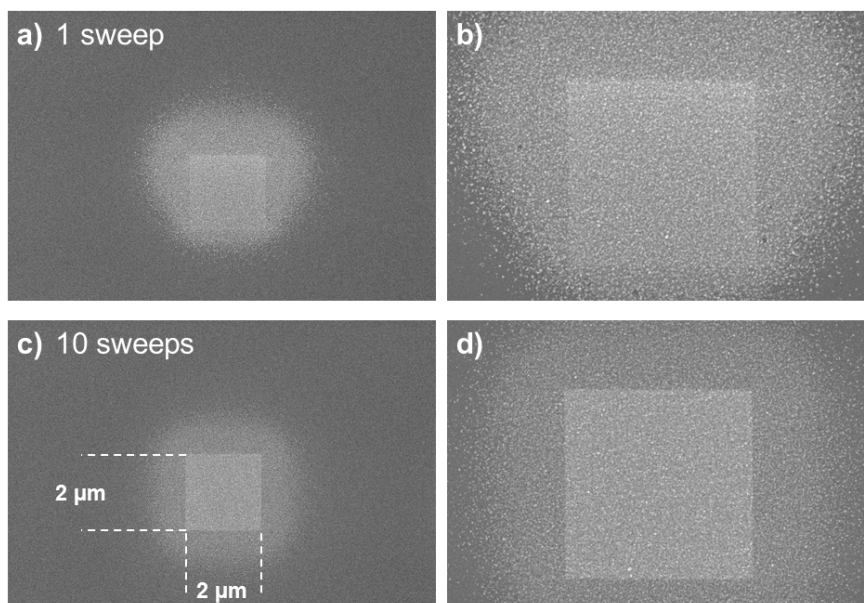


**Figure 6-16:** SEM of  $2 \times 2 \mu\text{m}^2$  deposits prepared by EBID and autocatalytic growth using  $\text{Co}(\text{CO})_3\text{NO}$  on a  $100 \text{ nm Si}_3\text{N}_4$  membrane (a, c) and corresponding high resolution data (b, d). The total PE dose is  $0.55 \text{ C/cm}^2$ , applied in one sweep with a dwell time of  $0.5 \text{ ms}$  (a) or in ten sweeps with a dwell time of  $0.05 \text{ ms}$  per sweep (c). In the single top-to-bottom sweep case (a) the top edge appears brighter and is surrounded by a pronounced bright fringe, while the bottom edge fades into the background. This behavior is attributed to proximity effects caused by electron scattering at already deposited material. In the case of multisweep irradiations, the deposit presents a more uniform distribution of material. The lower dwell time per sweep hinders the formation of a pronounced starting edge deposit, reducing the proximity effects. The high resolution images b) and c) also confirm the granular nature of the autocatalytically grown  $\text{CoO}_x\text{N}_y\text{C}_z$  deposit. The less pronounced granularity observed in d) is attributed to the lower growth time (a/b: 260 min, c/d: 220 min).

In Figure 6-17 the electron dose increases from left to right, and the size from top to bottom. The structures were written sequentially, left-to-right and row-by-row in one experimental run: the EBID process lasted 32 min, and thereafter, the precursor pressure was maintained to induce autocatalytic growth. The deposition process, including the EBID step, lasted 230 min, which corresponds to an accumulated precursor dose of  $\sim 9.3 \times 10^4$  Langmuir ( $1 \text{ L} = 10^{-6} \text{ Torr} \times \text{s} \approx 1.33 \times 10^{-6} \text{ mbar} \times \text{s}$ ). Since EBID of the individual deposits was performed sequentially, the respective times for autocatalytic growth after EBID vary from 230 min for the low dose structures on the top left corner (exposed first) to 198 min for the high dose structures on the bottom right (exposed last). The structures appear brighter for

higher doses: while below  $0.05 \text{ C/cm}^2$  no structure can be unequivocally identified, a dose of  $0.5 \text{ C/cm}^2$  marks the start of observable proximity effects in the form of fringes around the structures. Closer inspection of the structures shows that, despite the same electron dose was applied per surface area, larger squares are brighter and more defined compared to the smaller ones, which points to a deposition that is influenced by proximity effects.<sup>4</sup>

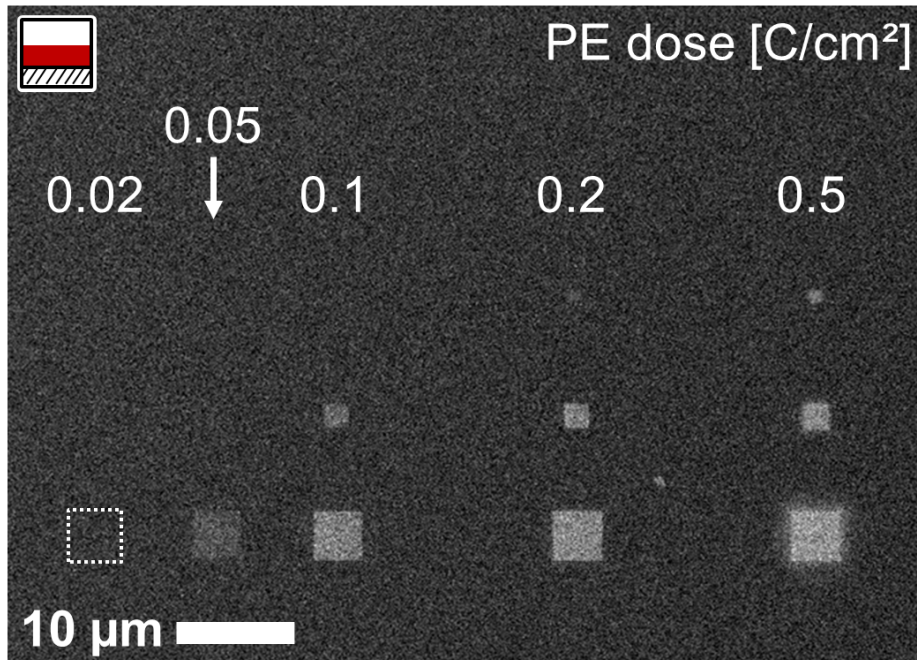


**Figure 6-17:** SEM micrograph of square EBID structures of different sizes and primary electron doses (as indicated), prepared on a  $100 \text{ nm Si}_3\text{N}_4$  membrane using  $\text{Co}(\text{CO})_3\text{NO}$ . The structures were prepared in one experimental run, from left to right, top to bottom. After the EBID step, the precursor was further supplied to allow for autocatalytic growth. The total growth time increases from  $198 \text{ min}$  (bottom right structure) to  $230 \text{ min}$  (top left structure). The minimum electron dose for detectable deposition is  $\sim 0.05 \text{ C/cm}^2$ , while a dose of  $0.5 \text{ C/cm}^2$  marks the start of proximity effect-induced loss of structure definition (fringe surrounding bottom right structure).

In addition to the dose dependence, the growth time-dependent appearance of the structures was investigated. Figure 6-18 compares SEM images of square deposits fabricated by EBID and autocatalytic growth, using  $\text{Co}(\text{CO})_3\text{NO}$  as precursor. The growth time,  $t_G$ , was varied from  $25$  to  $160 \text{ min}$ . In each of the six images (a) – (f), the two squares in the right column were irradiated with a primary electron dose of  $0.2 \text{ C/cm}^2$ , and the square in the left column with  $0.1 \text{ C/cm}^2$ . The inset in each case shows the morphology of the respective structures at  $44\times$  higher magnification.

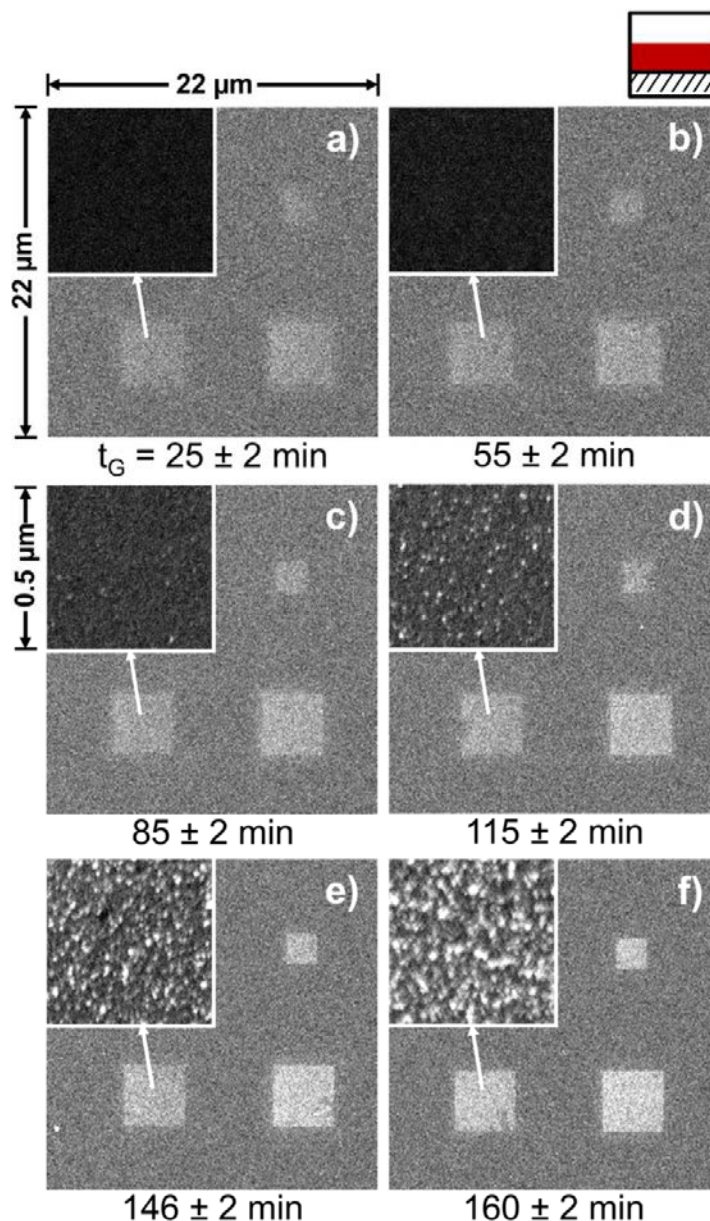


**Figure 6-18:** Nanostructures prepared by EBID plus autocatalytic growth using  $\text{Co}(\text{CO})_3\text{NO}$  on  $\text{Si}_3\text{N}_4$  with different growth times, as indicated below the images. The electron dose during EBID was  $0.2 \text{ C/cm}^2$  for the structures in the right column of every image; the dose of the lower left square was  $0.1 \text{ C/cm}^2$ . The insets show higher magnification images of the respective structures directly below. With increasing growth time the images appear brighter, and the granular nature of the deposits is more pronounced.

The data in Figure 6-18 shows a direct correlation between the brightness of the structures in SEM and the applied growth time, indicating increased material deposition. The brighter appearance of the deposited structures at larger growth times is attributed to an enhanced yield of backscattered electrons (BSE) and thereby induced secondary electrons. Indeed,

Monte-Carlo simulations using the software CASINO (v. 2.42)<sup>92</sup> show an increase in the BSE emission coefficient by >20 % for a 5 nm layer of  $\text{Co}_{0.51}\text{O}_{0.24}\text{N}_{0.14}\text{C}_{0.11}$  (composition reported by Gazzadi et al.<sup>160</sup>) and by >40 % for a 5 nm layer of pure Co compared to the bare 100 nm  $\text{Si}_3\text{N}_4$  membrane. The high-magnification insets in Figure 6-18 reveal the formation of a strongly corrugated, granular deposit, which can be interpreted as the growth of small clusters of material. Both the increase in the brightness of the deposits and the cluster growth mode are in line with the autocatalytic growth of EBID deposits upon dosage of additional  $\text{Co}(\text{CO})_3\text{NO}$ .

The samples were further characterized at the PoLux Soft X-ray STXM beamline<sup>83</sup> at the Swiss Light Source using a zone plate with a nominal resolution of 30 nm and a photomultiplier tube (PMT) behind the specimen for x-ray detection in transmission mode (see also Chapters 3.4 and 4.2). The STXM was operated under high-vacuum conditions (low  $10^{-6}$  mbar range) to avoid contamination from the decomposition of residual gases. In Figure 6-19, Co  $L$ -edge spectra of deposits prepared by EBID ( $0.2 \text{ C}/\text{cm}^2$ ) and autocatalytic growth using  $\text{Co}(\text{CO})_3\text{NO}$  are presented for different growth times. The left panel shows an overview of the Co  $L_{2/3}$  region; the right panel an enlargement of the  $L_3$  region along with the spectrum of a layer of pure cobalt (grey) that was produced by physical vapor deposition (PVD).

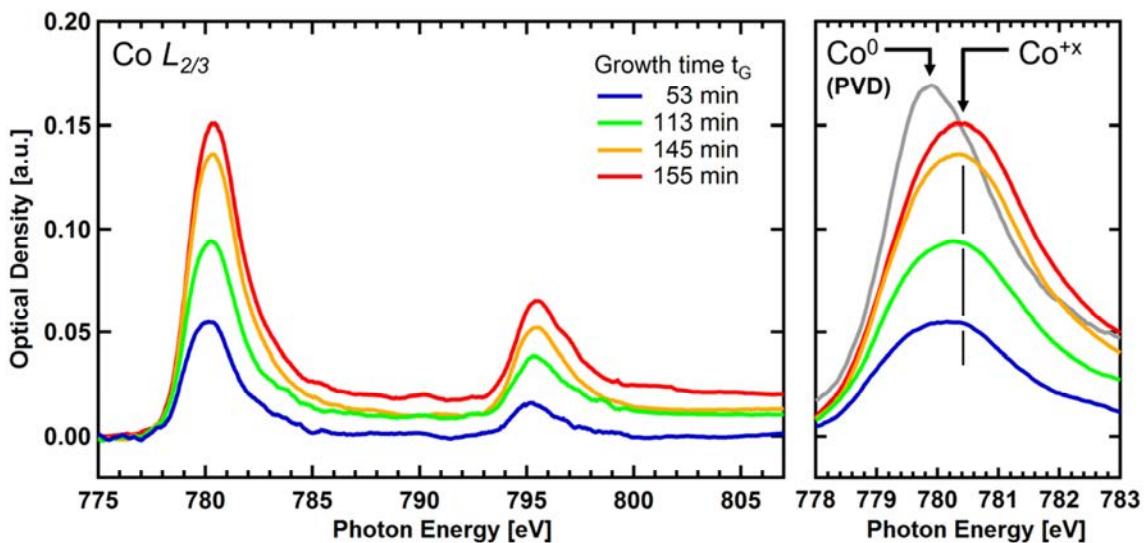


**Figure 6-19:** (left) Co  $L$ -edge X-ray absorption spectra of deposits prepared on a  $\text{Si}_3\text{N}_4$  membrane by EBID ( $0.2 \text{ C}/\text{cm}^2$ ) plus autocatalytic growth using  $\text{Co}(\text{CO})_3\text{NO}$ , with different growth times (indicated by colors); the spectra were vertically shifted to a common pre-edge baseline; (right)  $L_3$  edge of the deposits at an enlarged photon energy scale, along with the spectrum of a Co layer produced by PVD as reference (grey).

The comparison of the Co peak positions (maxima) of the metallic cobalt film prepared by PVD (779.9 eV, Co<sup>0</sup>) and the structures prepared by EBID plus autocatalytic growth (780.4 eV) reveals a chemical shift of ~ 0.5 eV, which is indicative of cobalt in an oxidized state.<sup>163-165</sup> This suggests a composition like CoO<sub>x</sub>N<sub>y</sub>(C<sub>z</sub>), in line with previous reports for comparable EBID structures by Gazzadi et al.<sup>160, 161</sup> and Mulders et al.<sup>68</sup>

The observed intensities in Figure 6-19 are a direct measure of the layer thickness of the deposits on the Si<sub>3</sub>N<sub>4</sub> membrane. In transmission X-ray microscopy or NEXAFS spectroscopy in transmission mode, the absorbance (or optical density, *OD*) is derived from:

$$OD = \mu(E) \times d = -\ln(I/I_0) = \ln(I_0/I),$$

with  $I_0$  and  $I$  being the incident and the transmitted intensities, respectively,  $d$  represents the sample thickness and  $\mu(E)$  the photon energy dependent linear absorption coefficient. The peak shape and the energy of the resonant Co  $L_3$  transition are similar for all deposits, which supports a common attenuation coefficient for this energy. The spectral intensities in Figure 6-19 also indicate that the layer thickness increases with growth time. As the analysis is based on the Co  $L_3$  signal, this increase is unequivocally related to the growth of a Co-containing layer by autocatalytic decomposition of Co(CO)<sub>3</sub>NO.

In order to quantify the absorption of the deposits, images were recorded at the resonant transition peak at 780.4 eV. The resonant transition yields the strongest element-specific absorption and thus maximizes the image contrast for ease of evaluation. The optical density of the structures was calculated by averaging the signal over the area of the respective structure (in the STXM micrograph) and referencing the signal to the background, i.e. the signal of the pristine membrane near the deposit. The granular structure of the deposits, which was observed in SEM (c.f. Figure 6-18), could not be observed in STXM due to the limited resolution approx. 30 nm for the applied zone plate.

As the exact chemical composition of the deposit is not known, the linear absorption coefficient for the deposited material,  $\mu_{\text{deposit}}$ , is also unknown. As an approximation, the value of pure Co,  $\mu_{\text{Co}}$ , is used instead and the derived thickness value is denoted as apparent cobalt thickness,  $d_A$ , which is calculated using Equation (1). Since the oxygen, nitrogen and carbon contributions are small compared to resonant Co  $L_3$  signals,  $d_A$  is considered a meaningful value, reflecting the nominal thickness of a pure Co layer. The real thickness of the deposit is certainly underestimated, but since the composition of the different EBID deposits is very likely the same, a comparison of the deposits obtained with different growth times is possible.

The value for the absorption coefficient at the resonant transition was determined by fitting the spectrum of a PVD Co layer to a calculated X-ray absorption spectrum (X-ray Form Factor, Attenuation, and Scattering Tables; NIST<sup>166-168</sup>), which does not account for resonant transitions. The fit is accomplished by scaling the optical density of the measured spectrum of the PVD Co layer to match the pre-edge and post-edge region of the calculated spectrum of a 1 nm thick layer of pure Co. The scaled measured spectrum, which contains the resonant transition, then allows to determine  $\mu(E)$  values.

The linear attenuation coefficient for Co at the resonant transition was found to be  $\mu_{\text{Co}}(779.9\text{eV}) = 0.103 \pm 0.02 \text{ nm}^{-1}$ . For the quantification of the apparent cobalt thickness of the  $\text{CoO}_x\text{N}_y\text{C}_z$  deposits, it is assumed that the absorption coefficient of the resonant peak intensity is comparable for pure Co and  $\text{CoO}_x\text{N}_y\text{C}_z$ , i.e.  $\mu_{\text{Co}}(779.9\text{eV}) \approx \mu_{\text{CoO}_x\text{N}_y\text{C}_z}(780.4\text{eV})$ . The absolute thickness of the  $\text{CoO}_x\text{N}_y\text{C}_z$  deposits may be 3-5 $\times$  larger than the reported apparent Co thickness, as estimated from calculated spectra of a set of various  $\text{CoO}_x\text{N}_y\text{C}_z$  with different atomic ratios and densities. The absorption coefficient  $\mu_{\text{Fe}}(708.7 \text{ eV}) = 0.050 \pm 0.01 \text{ nm}^{-1}$  was also determined using the described fitting procedure.

Figure 6-20 summarizes the thickness analysis for several deposits produced by EBID plus autocatalytic growth as a function of the primary electron dose during EBID and the growth time,  $t_G$ , during which  $\text{Co}(\text{CO})_3\text{NO}$  was continually supplied. The 3D plot in Figure 6-20a shows the optical density (left vertical axis) and apparent Co layer thickness (right vertical axis) vs. growth time and primary electron dose (log scale), and Figure 6-20b and d show the detailed plots against the latter two parameters. The STXM micrograph (transmitted intensity) in Figure 6-20c displays a set of square deposits fabricated with the indicated primary electron doses and a growth time of  $\sim 160$  min. The data in Figure 6-20 are in line with our previous observations: the optical density increases with both electron dose and autocatalytic growth time. The dependence on primary electron dose in Figure 6-20b can be linearly extrapolated to zero, in order to obtain the minimum dose required for direct EBID, yielding a value of  $0.03 \pm 0.01 \text{ C/cm}^2$  or  $1.8 \pm 0.6 \times 10^3$  electrons per  $\text{nm}^2$ . The dependency of the optical density on the growth time in Figure 6-20d (for a given primary electron dose) initially exhibits an almost linear behavior, but for  $t_G > 150$  min a strong nonlinear increase is apparent. The morphology of the deposits in Figure 6-18 indicates that growth proceeds in a granular fashion and not by homogeneous layer-by-layer growth. For this complex growth process, during which the number of available sites, the (local) precursor concentration or both may vary, a nonlinear behavior is not unexpected.

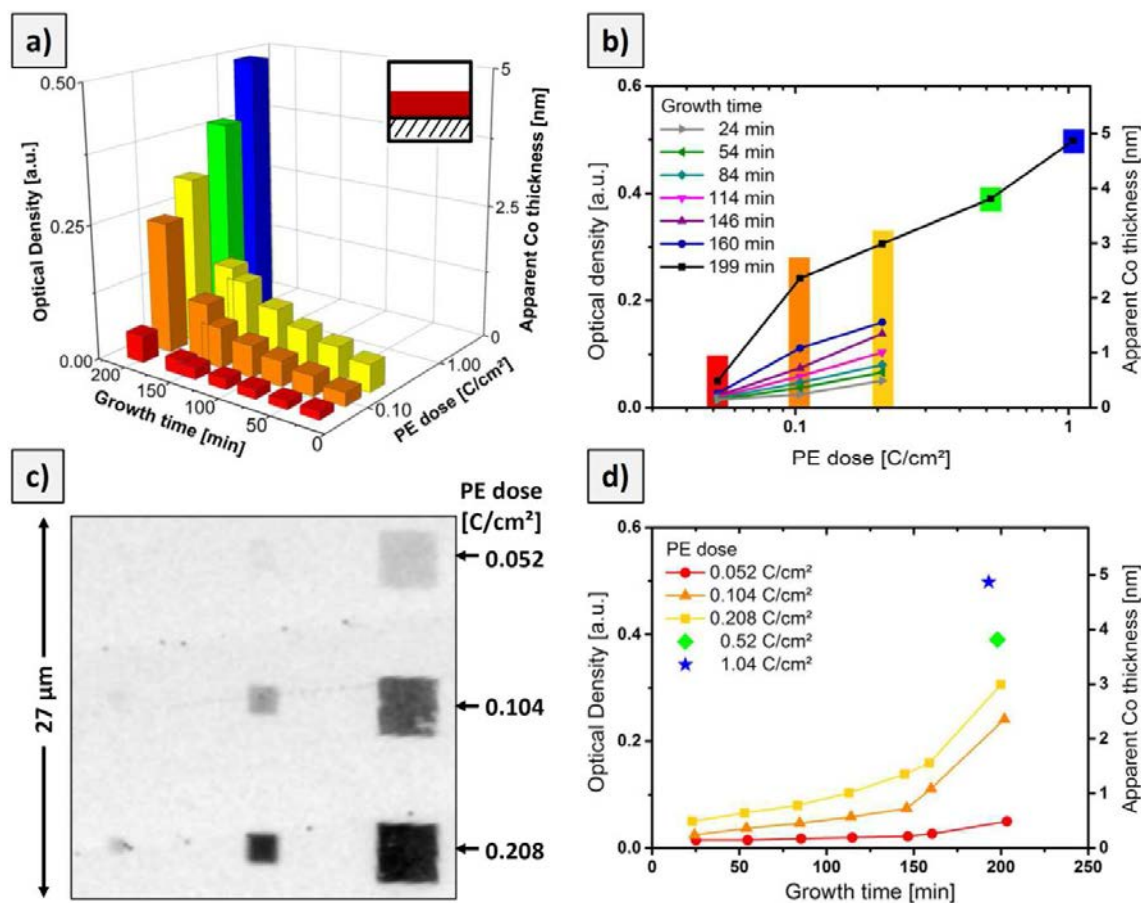


**Figure 6-20:** XAS evaluation of the growth of Co-containing deposits by EBID plus autocatalytic growth upon  $\text{Co}(\text{CO})_3\text{NO}$  dosage. a) Optical density (left vertical axis) and apparent Co thickness (right vertical axis) of  $4 \times 4 \mu\text{m}^2$  squares vs. growth time and PE dose during EBID. b) and d) detailed graphs of the observed growth behavior; the color code identifies the respective data set. c) STXM micrograph (transmitted intensity) of a set of deposits prepared with different PE doses, but the same growth time of  $\sim 160$  min obtained at a photon energy of 780.4 eV. See text for the definition of the apparent Co thickness.

#### 6.4.2.2 EBISA plus autocatalytic growth

The susceptibility to decomposition by an electron beam-activated surface or via an autocatalytic process is a prerequisite for the successful application of a precursor for EBISA-based fabrication of nanostructures. In order to study the suitability of  $\text{Co}(\text{CO})_3\text{NO}$ , a number of test patterns were irradiated on different surfaces under UHV conditions and subsequently exposed to  $\text{Co}(\text{CO})_3\text{NO}$ . The investigated surfaces were  $\text{SiO}_x$ -layers on Si(100) and  $\text{Si}_3\text{N}_4$ , both of which are suitable substrates for EBISA using  $\text{Fe}(\text{CO})_5$ .<sup>5, 12</sup> On these surfaces, electron stimulated desorption of oxygen and the thereby generated oxygen vacancies were

identified as the active sites for the initial decomposition of  $\text{Fe}(\text{CO})_5$ .<sup>5, 14</sup> However, the corresponding experiments with  $\text{Co}(\text{CO})_3\text{NO}$  as a precursor in EBISA were not successful, i.e., deposition of material on the activated surfaces was not observed (data not shown). It thus has to be concluded that  $\text{Co}(\text{CO})_3\text{NO}$  is not suitable as precursor for nanostructure fabrication using EBISA on silicon oxide surfaces.

An alternative approach could be to use different substrates for EBISA: it was shown in Chapter 6.3, that it is possible to activate thin layers of large organic molecules (2H-tetraphenyl porphyrin) on metal single crystals for  $\text{Fe}(\text{CO})_5$  decomposition.<sup>135</sup> The proposed activation mechanism involves the electron beam induced formation of reactive organic moieties, which might be reactive also towards the initial decomposition of  $\text{Co}(\text{CO})_3\text{NO}$ .

#### 6.4.2.3 Autocatalytic growth on iron seed layers

In addition to the experiments described before, the fabrication of layered nanostructures by EBID using both  $\text{Fe}(\text{CO})_5$  and  $\text{Co}(\text{CO})_3\text{NO}$  was explored. In the course of these experiments, it was observed that  $\text{Co}(\text{CO})_3\text{NO}$  does not only decompose autocatalytically on Co-containing deposits, but also on high purity Fe nanostructures. The latter can be prepared from  $\text{Fe}(\text{CO})_5$  by EBID or EBISA, plus successive autocatalytic growth as was shown in the previous chapters.

The iron structures are typically composed of very pure (>90-95%at.) cubic crystallites, as a result of the autocatalytic growth process.<sup>5, 12-14, 120, 135</sup> The morphology ranges from scattered clusters for low electron doses and shorter growth times, to fused, polycrystalline patches of cubic crystallites for high electron doses and long growth times.<sup>5, 12-14, 120, 135</sup> After preparation of the Fe deposits with  $\text{Fe}(\text{CO})_5$ ,  $\text{Co}(\text{CO})_3\text{NO}$  was introduced into the chamber for a given growth time that was identical for all Fe seed deposits. Thereafter, the samples were investigated by SEM (not shown) and STXM. For the STXM analysis, images were acquired at the Fe  $L_3$  and Co  $L_3$  absorption edges. To determine the thickness of the Co layer, the absorption by the Fe layer underneath has to be considered: whereas the absorption by Co at the Fe  $L_3$  edge (708.7 eV) is low and thus treated as negligible, the absorption by Fe at the Co  $L_3$  edge (780.4 eV) is considerable. By comparison of the optical density (OD) of pure iron deposits at both energies, a contribution of  $25 \pm 5 \%$  of the Fe intensity at the Fe  $L_3$  edge is determined for the Co  $L_3$  edge, i.e.

$$\begin{aligned} \text{OD}_{\text{Co}}(\text{Co } L_3) &= \text{OD}_{\text{total}}(\text{Co } L_3) - \text{OD}_{\text{Fe}}(\text{Co } L_3) \\ &= \text{OD}_{\text{total}}(\text{Co } L_3) - 0.25 \text{OD}_{\text{Fe}}(\text{Fe } L_3) \end{aligned}$$

---

This correction was taken into account to determine the thickness of the Co-containing layer for the Fe/CoO<sub>x</sub>N<sub>y</sub>C<sub>z</sub>-bilayer.

As the first step, the autocatalytic growth of the iron structures was investigated. Figure 6-21 shows an overall linear increase of the optical density (left vertical axis) and the average thickness (right vertical axis) with autocatalytic growth time for the Fe *L*<sub>3</sub> edge. For electron doses above 0.05 C/cm<sup>2</sup>, the data for different PE doses are very similar. This indicates that the Fe layer thickness is mainly determined by the autocatalytic growth time, with an autocatalytic growth rate of  $0.5 \pm 0.1 \text{ \AA}$  per minute (approx.  $1.3 \times 10^{-3} \text{ \AA/Langmuir}$ ). The observation that for electron doses of 0.05 C/cm<sup>2</sup> and below only reduced thicknesses are obtained indicates that the threshold for creating a homogeneously reactive initial deposit by EBID is not yet reached. Thus, only for electron doses exceeding 0.05 C/cm<sup>2</sup>, the number of catalytically active sites per area approaches a saturation value. This induction period is followed by a constant rate of autocatalytic precursor decomposition, which results in constant height growth. It is likely that the deposit formed in the induction period is a closed layer of iron on the surface. These results clearly demonstrate that continued deposition of Fe is possible on the initial layer prepared by EBID with comparatively low electron doses and thus short fabrication times.

In a next step, the high purity Fe structures are exposed to Co(CO)<sub>3</sub>NO. This results in the deposition of a Co-containing layer on top of the Fe structure in a tertiary growth process. The deposition is selective, i.e. the Co-containing layer is only observed on the Fe structures while the pristine membrane remains uncovered. The composition of the Co-containing layers is most likely again CoO<sub>x</sub>N<sub>y</sub>C<sub>z</sub>, which is supported by the shift of the Co *L*<sub>3</sub> peak to higher energy, and by Auger electron spectroscopy of comparable structures on SiO<sub>x</sub>/Si(100) (not shown); note that severe charging prevents Auger electron spectroscopy on the Si<sub>3</sub>N<sub>4</sub> membrane samples.

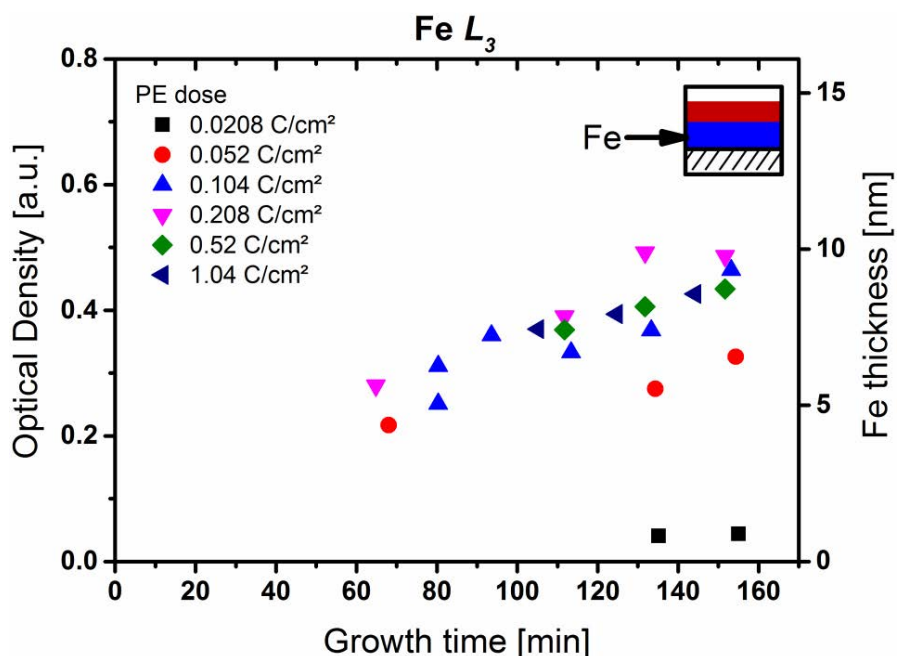


**Figure 6-21:** Optical density at the  $\text{Fe } L_3$  edge at 708.7 eV (left vertical axis) and average thickness of the iron layer (right vertical axis) of various  $\text{CoO}_x\text{N}_y\text{C}_z$  / Fe nanostructures versus autocatalytic growth time for  $\text{Fe}(\text{CO})_5$ . The different symbols indicate different primary electron (PE) doses. Above 0.05  $\text{C}/\text{cm}^2$ , the thickness/optical density increases linearly with the growth time at a rate of  $0.5 \pm 0.1 \text{ \AA}/\text{min}$  irrespective of the applied PE dose. Lower PE doses (red, black) exhibit reduced thickness.

Figure 6-22 shows the optical density (left vertical axis) at the  $\text{Co } L_3$  edge and average apparent Co thickness  $d_A$  (right vertical axis) of  $\text{CoO}_x\text{N}_y\text{C}_z$  layers grown on iron seed layers of increasing thickness (corresponding to the layers in Figure 6-21). In all cases the same total growth time (210 min) using  $\text{Co}(\text{CO})_3\text{NO}$  was applied. On top of Fe layer thicker  $>4 \text{ nm}$ , a comparable optical density of  $0.76 \pm 0.08$  is observed for the autocatalytically grown  $\text{CoO}_x\text{N}_y\text{C}_z$  layers, independent of the thickness of the initial Fe layers. The corresponding apparent cobalt thickness is  $7.4 \pm 0.8 \text{ nm}$ ; the average growth rate is  $0.35 \pm 0.05 \text{ \AA}/\text{min}$ . It is likely, however, that the growth on Fe seeds exhibits non-linear behavior, as was observed above for the autocatalytic growth on the cobalt seed layer (cf. Figure 6-20).

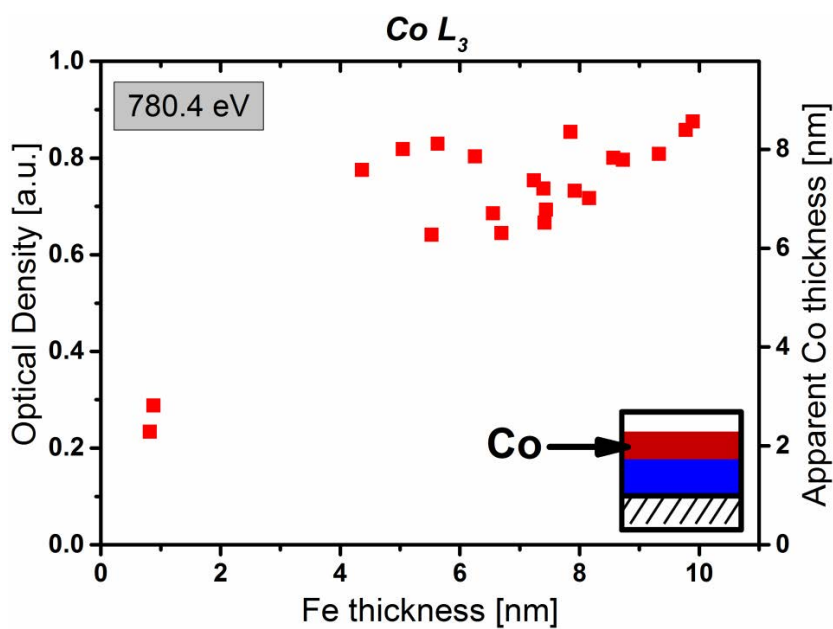


**Figure 6-22:** Optical density at the  $\text{Co } L_3$  edge and apparent cobalt thickness of  $\text{CoO}_x\text{N}_y\text{C}_z$  layers grown autocatalytically from  $\text{Co}(\text{CO})_3\text{NO}$  on Fe layers plotted against the Fe layer thickness. The Fe layers were prepared by EBID and autocatalytic growth using  $\text{Fe}(\text{CO})_5$ . In a second step,  $\text{Co}(\text{CO})_3\text{NO}$  was dosed for 210 min to produce the  $\text{CoO}_x\text{N}_y\text{C}_z$  layers via (auto-)catalytic decomposition. The optical density and thickness are corrected to account for the absorption of the Fe deposit underneath (see text). The OD of the cobalt containing layer is almost independent of the Fe layer thickness for Fe layers thicker than 4 nm.

Comparing the growth behavior of  $\text{Co}(\text{CO})_3\text{NO}$  and  $\text{Fe}(\text{CO})_5$ , the presented data (Figure 6-21 vs. Figure 6-20d) suggest two very different growth modes for the different precursors under otherwise identical reaction conditions. On the one hand, the autocatalytic decomposition of  $\text{Fe}(\text{CO})_5$  proceeds at a constant rate and produces high purity Fe deposits, which (above a threshold) are almost independent of the applied PE dose. On the other hand, the autocatalytic decomposition of  $\text{Co}(\text{CO})_3\text{NO}$  exhibits pronounced non-linear, possibly even exponential behavior and is strongly influenced by the applied primary electron dose during the initial EBID step. In contrast to  $\text{Fe}(\text{CO})_5$ , the decomposition yields an oxygen-, nitrogen- and carbon-rich  $\text{CoO}_x\text{N}_y\text{C}_z$  deposit instead of pure cobalt. Besides the involved chemistry, which is likely to be quite different, yet difficult to study with the available techniques, the deposits structure seems to have a strong influence on the growth behavior. The iron structures fabricated by EBID/EBISA plus autocatalytic growth are composed of cubic crystallites of  $\alpha\text{-Fe}(\text{bcc})$ . These crystallites are quite regular, and their vacuum interfaces consist mainly of low index  $\{100\}$  faces of these cubes. In the case of  $\text{Co}(\text{CO})_3\text{NO}$ , not very

well-defined granular structures are observed after the autocatalytic growth step, indicating a rather amorphous and defect rich deposit with a high surface area. Such structures are likely to show different, possible increased reactivity compared to ordered, flat surfaces. Indeed, the observed decomposition of  $\text{Co}(\text{CO})_3\text{NO}$  on the nominally flat Fe seed layers is less pronounced than on the Co seed layer produced with very high primary electron doses.

### 6.4.3 Conclusions

The electron beam induced decomposition of  $\text{Fe}(\text{CO})_5$  and  $\text{Co}(\text{CO})_3\text{NO}$  and the subsequent secondary growth via selective autocatalytic decomposition upon further precursor dosage was investigated in this chapter. The two precursors show very different growth characteristics under the applied reaction conditions.  $\text{Fe}(\text{CO})_5$  exhibits a constant growth rate of  $0.5 \pm 0.1 \text{ \AA}/\text{min}$ , which above a threshold of  $0.05 \text{ C}/\text{cm}^2$  is almost independent of the electron dose applied during the initial EBID step. The deposits prepared by EBID/EBISA and autocatalytic growth from  $\text{Fe}(\text{CO})_5$  are composed of polycrystalline, high purity Fe (typically >90-95% at.). While the electron irradiation defines the shape of the deposit, the thickness of the prepared structures is governed mainly by the autocatalytic growth process. The practical separation of shape definition and deposit formation has some advantages, most obviously the reduction of proximity effects due to lower required electron dose as compared to the EBID-only process.

Structure fabrication using  $\text{Co}(\text{CO})_3\text{NO}$ , on the other hand, is strongly affected by the applied electron dose in the EBID step and subsequent autocatalytic growth time. The influence of the electron dose follows a logarithmic trend, while the autocatalytic thickness growth shows non-linear, possibly exponential behavior with growth time. This is explained by the observed granular morphology of the deposits and the associated high surface area, defect rich, and reactive deposit-vacuum interface. The analysis of the chemical composition of the structures prepared from  $\text{Co}(\text{CO})_3\text{NO}$  points to an oxygen-, nitrogen-, and carbon-rich  $\text{CoO}_x\text{N}_y\text{C}_z$  composite material, with the Co  $L_3$  peak shifted towards an oxidic state. In order to fully understand the underlying mechanism of the autocatalytic decomposition especially of  $\text{Co}(\text{CO})_3\text{NO}$ , it is necessary to conduct further studies on model systems using complementary surface science techniques, e.g. X-ray photoelectron spectroscopy (XPS) or infrared absorption spectroscopy (IR/IRAS), and expand the work that has been done on the electron beam induced decomposition to include the autocatalytic growth.

Our study also shows that the EBISA approach on  $\text{SiO}_x$  does not work with  $\text{Co}(\text{CO})_3\text{NO}$  as a precursor: while  $\text{Fe}(\text{CO})_5$  decomposes on activated, i.e., electron pre-irradiated, areas of  $\text{SiO}_x$  surfaces and forms a deposit, this behavior was not observed for  $\text{Co}(\text{CO})_3\text{NO}$ . Interestingly,  $\text{Co}(\text{CO})_3\text{NO}$  decomposes autocatalytically on Fe seed layers, which opens up a number of fabrication possibilities. As the fabrication of Fe structures by EBISA plus autocatalytic growth has been shown to be a successful approach not only on  $\text{SiO}_x$  surfaces, but also on  $\text{TiO}_2$  and on substrates pre-covered with organic layers, such Fe-layers could be generally considered as seeding layers for precursors that are not susceptible to decomposition by the electron beam-activated surface. Furthermore, the fabrication of layered nanostructures without the necessity for multiple electron beam exposure steps could be demonstrated. It is likely that such a seeding concept also works for other precursor combinations. The known autocatalytic growth of high purity Co deposits from  $\text{Co}_2(\text{CO})_8$  makes that precursor a likely candidate for the successful fabrication of layered Fe/Co nanostructures with arbitrary shapes.

Thus, the presented results considerably expand the possibilities of FEBIP-based nanofabrication techniques. Also, the results suggest that the potential for (auto-)catalytic decomposition of typical EBID precursors needs to be studied in detail. This approach is necessary to gain a deeper understanding of the underlying processes, the consequences of autocatalytic growth for EBID experiments and, subsequently, to develop new or improved methods for the fabrication of FEBIP-based nanostructures.

## 6.5 EBID using $\text{Co}_2(\text{CO})_8$

### ABSTRACT

Dicobalt octacarbonyl,  $\text{Co}_2(\text{CO})_8$ , was studied concerning its application in EBID and EBISA under UHV conditions. The material contains hexane as a stabilizer, which has to be removed prior to use by degassing, and is prone to thermal and catalytic decomposition. Preliminary results suggest autocatalytic growth and susceptibility towards defects, while EBID results in deposition of Co-rich (70 %at.) material on the surface.

### 6.5.1 Introduction

Dicobalt octacarbonyl has been used for the fabrication of nanostructures by EBID for some time.<sup>15, 24, 30, 33, 37, 68, 169-174</sup> It is known that this precursor is susceptible to oxygen, water vapor, prone to thermal decomposition above approx. 70 °C (e.g. Mulders et al.<sup>68</sup>). The decomposition reaction includes polymerization and release of CO,<sup>173, 175, 176</sup> which can lead to build-up of pressure in the precursor container.

Nevertheless, it has been shown that it is possible to deposit material ranging from granular Co in a carbonaceous matrix<sup>171</sup> to almost pure Co.<sup>174</sup> The deposits exhibit magnetic properties<sup>24, 30, 33, 169-172, 174</sup> and can be used to fabricate devices like hall sensors<sup>32, 33</sup> and tips for magnetic force microscopy (MFM).<sup>30</sup> Magnetic EBID nanostructures prepared from  $\text{Co}_2(\text{CO})_8$  have also been used to investigate magnetic phenomena such as magnetoresistance.<sup>169</sup>

Studies of the autocatalytic growth under high-vacuum conditions are somewhat ambiguous: a number of studies suggest autocatalytic effects without further details; one study<sup>37</sup> finds no autocatalytic growth on Co-containing EBID seeds on  $\text{SiO}_x/\text{Si}$ , while on Co seeds prepared by PVD (and additional processing, cf. ref<sup>37</sup>) autocatalytic effects are observed; and another study<sup>15</sup> shows that catalytic decomposition and subsequent autocatalytic growth are observed at pretreated  $\text{SiO}_x/\text{Si}$  surfaces (plasma cleaned and EBISA).

In order to clarify this issue, the autocatalytic growth of cobalt nanostructures prepared by EBID or EBISA using this precursor was to be studied in UHV. This should yield additional insights in to the autocatalytic growth processes, including a comparison of the  $\text{Fe}(\text{CO})_5$  and the  $\text{Co}_2(\text{CO})_8$  precursor. In addition, the susceptibility to catalytic decomposition at primary deposits prepared from the respective other precursor could be investigated (see Chapter 6.4

for the interaction of  $\text{Co}(\text{CO})_3\text{NO}$  with Fe deposits). The following chapter will discuss the results as well as the issues discovered during the course of the experimental work.

### 6.5.2 Results and Discussion

Dicobalt octacarbonyl was filled into a standard glass precursor container under inert gas ( $\text{N}_2$ ). The container consists of a glass tube attached to a CF 16 flange and is attached to the stainless steel gas dosing lines (Swagelok, 6 mm) via a below-sealed valve. The gas line was carefully evacuated to remove the  $\text{N}_2$  from the as-filled container before the compound was studied using the QMS of the gas dosing chamber. The main components of the gas mixture consisted of carbon monoxide and of n-hexane, which is added as a stabilizing agent by the manufacturer in an undisclosed amount. The presence of large amounts of CO in the absence of Cobalt signals indicates some decomposition of the precursor even at room temperature under vacuum conditions. In order to reduce the amount of hexane and CO, the precursor was subjected to high-vacuum in the precursor container for various timespans (30 s to approx. 10 min) at low (273 K) and room temperature.

Processing at slightly elevated temperature (318 K, 45° C) under HV resulted in the formation of a reflective, metallic layer on the inside of the glass tube. Essentially, the  $\text{Co}_2(\text{CO})_8$  undergoes thermal decomposition to metallic Cobalt and CO under the applied conditions (318 K, pressure below approx.  $10^{-4}$  mbar) in a CVD-like process, which demonstrates the aforementioned difficulties in handling this precursor. In order to avoid the decomposition, the temperature was limited to room temperature.

It was also observed that the length of the gas line and the number of valves to be passed by the precursor gas has an influence on the gas composition. While it was possible to observe  $\text{Co}_2(\text{CO})_8$  signals in mass spectra in the gas dosing chamber, which is located in close proximity to the precursor container, it was not possible to observe the signals in the analysis chamber. Moderate heating of the gas dosing line to decrease the sticking did not circumvent this issue. It has to be assumed that the Co-precursor undergoes decomposition, possibly catalyzed by the tubing or valve material, during transport. It is likely, for example, that there is a decomposition at the copper gaskets used in CF16 connectors and leak valves, as clean Cu surfaces are known to act as active sites in CVD of Co films from various precursors, including  $\text{Co}_2(\text{CO})_8$ .<sup>177</sup>

While it is not possible to introduce a  $\text{Co}_2(\text{CO})_8$  container into the UHV system to reduce the length of the tubing as much as possible (as is commonly practiced in HV setups), it is

possible to reduce the outside length of the tubing. This was achieved by adding a T-junction in close proximity to the leak valve feeding into the analysis chamber. The refined gas dosing setup for  $\text{Co}_2(\text{CO})_8$  is shown in Figure 6-23.

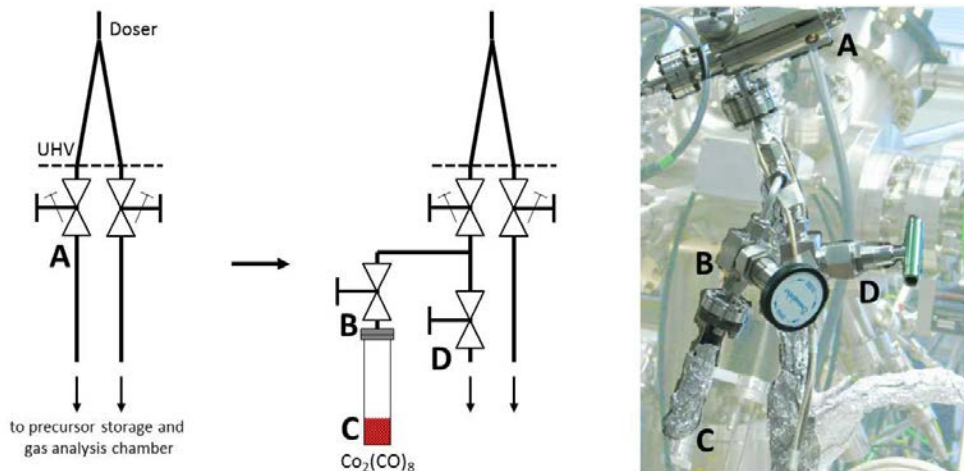


**Figure 6-23:** Scheme (left) and image of the reduced-length tubing for the  $\text{Co}_2(\text{CO})_8$  precursor. In the standard setup, the leak valve (A) connects to precursor via the length of the gas line ( $>2$  m). The new setup introduces a T-junction to directly attach the precursor container (C) via a bellows-sealed valve (B) and adds another valve (D) to seal off the remaining gas line during precursor dosing. The length of the line is reduced to about 15 cm.

Using this shortened gas line setup in combination with pre-treat, recrystallized  $\text{Co}_2(\text{CO})_8$  (see Chapter 4.4.3), it was possible to deposit a Co-rich material in an EBID experiment. This was achieved by irradiation of a rectangular field on an amorphous silicon sample while the precursor was dosed at a background pressure of  $3.0 \times 10^{-7}$  mbar. The amorphous Si sample was prepared from a Si(100) wafer by Ar sputtering and was free of carbon and oxygen contamination (as determined by AES). Electron irradiation (15 keV, 400 pA) was realized via the SmartSEM GUI in a multi-sweep fashion with a frame duration of 1.36 s/frame (including line and frame settling periods). The irradiation duration of 10 min corresponds to an accumulated primary electron dose of approx.  $1.4 \text{ C/cm}^2$  ( $\sim 3.2 \text{ mC/cm}^2$  per sweep). The precursor supply was turned off 2 min after the end of the irradiation in order to reestablish the vacuum conditions required for analysis. The resulting EBID structure is shown in Figure 6-24, accompanied by an SEM image of the non-irradiated surface.

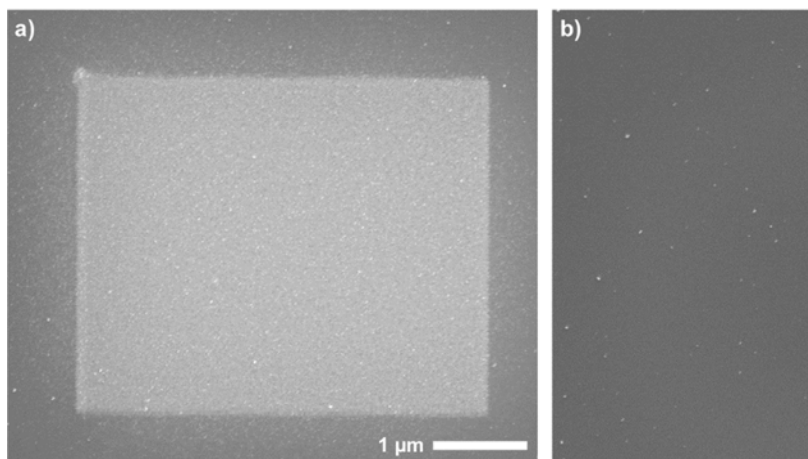


**Figure 6-24:** SEM images of a Co-rich EBID deposit prepared from  $\text{Co}_2(\text{CO})_8$  (a) and of the non-irradiated silicon surface (b). The bright square was irradiated with a primary electron dose of  $1.4 \text{ C/cm}^2$  at a precursor background pressure of  $3.0 \times 10^{-7} \text{ mbar}$ . Note that the image contrast and brightness cannot be directly compared.

It is immediately apparent that the irradiated area exhibits higher brightness compared to the surrounding surface. This is evidence for material deposition by EBID in general, and more importantly, also an indication for the deposition of high Z, i.e. Co containing, material. The deposit seems to be comprised of a homogeneous grey foundation and sparse, granular features on top. The presence of enhanced deposition at the top left corner and left edge results from the use of the SmartSEM software for beam control (c.f. Chapter 5.3.1). The non-irradiated surface (Figure 6-24) shows some individual, bright clusters, presumably from defect-induced activity.

As discussed in the previous chapters, granular features are often observed in combination with autocatalytic growth and therefore indicate that such growth also occurs for the  $\text{Co}_2(\text{CO})_8$  precursor on the respective EBID deposits in the UHV setup. The presence of the clusters on the non-irradiated surface further corroborates this assumption.

The deposit was further characterized by AES (beam settings: 15 keV, 3 nA; scan area:  $2.3 \times 1.8 \mu\text{m}$ ) to elucidate the chemical composition of the deposit. The resulting spectrum of the deposit (black) and a spectrum of a non-irradiated area on the surface (red) are presented in Figure 6-25, both in normal (top) and derivative mode. Characteristic Auger transitions are indicated for carbon, oxygen and cobalt.

The chemical composition of the deposit is calculated to 75 %at. Co, 15 %at. C and 10 %at. O (+/- 5%at.), which is well within the range of compositions reported for HV EBID using  $\text{Co}_2(\text{CO})_8$ .<sup>24, 68, 171</sup>

As discussed before, autocatalytic effects seem not to play a dominant role under the applied EBI deposition conditions (low beam current, high energy, short time for growth), which may explain a lower purity than e.g. for the autocatalytically grown Fe deposits. In addition, the high purity Co deposits from  $\text{Co}_2(\text{CO})_8$  reported in literature are commonly fabricated using higher beam currents (few nA) and higher precursor pressures (e.g. background pressure  $\sim 2 \times 10^{-6}$  mbar; not considering pressure enhancement due to dosing nozzles).<sup>170</sup>

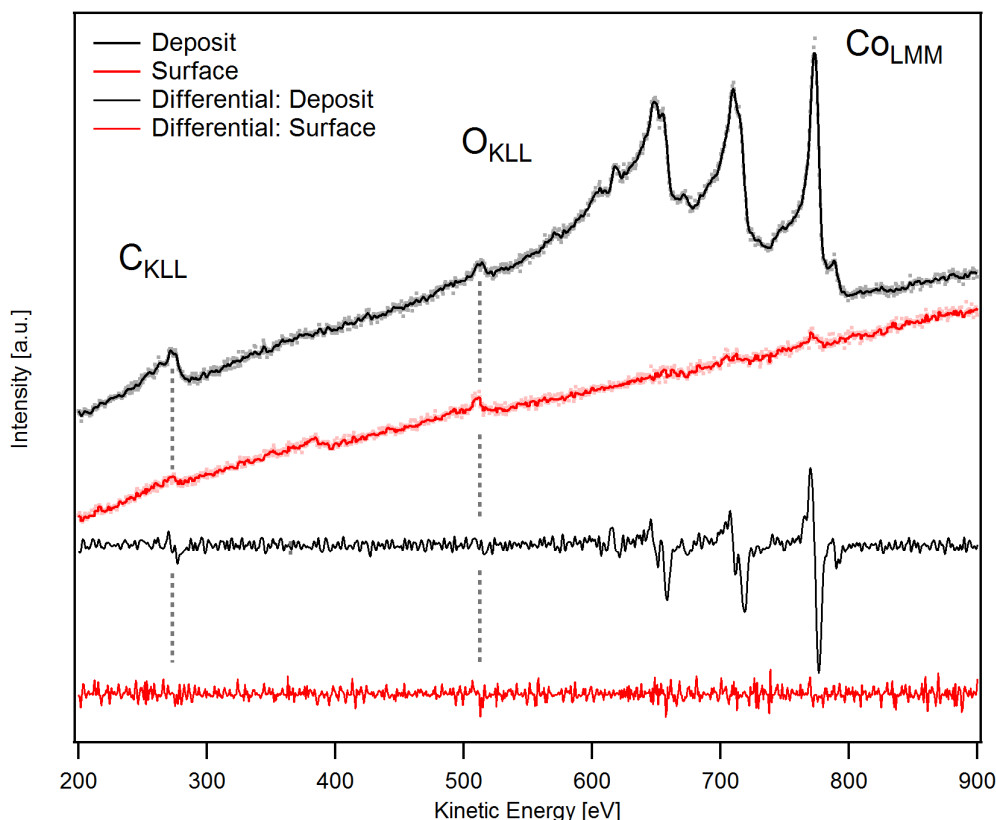


**Figure 6-25:** Auger electron spectra (as recorded, top, and smoothed & differentiated, bottom) of the nanostructure prepared by EBID using  $\text{Co}_2(\text{CO})_8$  as a precursor (black curves) and of the non-irradiated silicon surface after precursor dosage (red curves). The deposit contains 75% cobalt, approx. 15% carbon and 10% oxygen ( $\pm 5\%$ ).

The spectrum of the non-irradiated silicon surface in Figure 6-25 (red) contains faint carbon, oxygen and cobalt peaks. The signals may be due incompletely dissociated, non-volatile  $\text{Co}_x(\text{CO})_y$  species or deposition due to scattered clusters on the surface (c.f. Figure 6-24 b). The signal intensity is not sufficient to reliably assign a chemical composition to that spectrum.

In order to evaluate the applicability of  $\text{Co}_2(\text{CO})_8$  for the EBISA, and the autocatalytic growth behavior, dedicated experiments, e.g. using varying growth times, are necessary. Unfortunately, even using the shortened gas line, it was not possible to repeat any experiments using the precursor in the analysis chamber within the allotted time frame.

As described before, decomposition of the precursor en route to the sample surface is fairly likely. If the decomposition results in deposition of high purity Co layers inside the gas dosing line, these layers may induce the autocatalytic decomposition of further  $\text{Co}_2(\text{CO})_8$  into Co and CO.<sup>15, 37</sup> One has to assume that, in essence, the inside surface of the gas dosing line is being covered with catalytically active Co material during gas dosage, accompanied by a release of CO. As all subsequent molecules will be decomposed inside the line before they can reach the sample surface, this would account for the fact that no intact  $\text{Co}_2(\text{CO})_8$  is observed in the analysis chamber after the initial experiment, and can only be solved if a reliable way of dosing  $\text{Co}_2(\text{CO})_8$  onto the sample surface can be implemented. Possible solutions may include:

- use of passivation agents to reduce the reactivity of the gas line walls, e.g. oxidation or passivation by  $\text{O}_2$ , NO, possibly in combination with a thermal treatment, as proposed e.g. by Henderson et al.<sup>178</sup> for  $\text{Fe}(\text{CO})_5$ ;
- exchange of reactive materials, e.g. polymer tubing instead of steel lines and use of polymer gaskets;
- introduction of precursor containers into the UHV system (in analogy to the GIS systems used in HV-SEMs), as proposed e.g. by Klingenberger and Huth.<sup>179</sup>

### 6.5.3 Conclusions

The present chapter discusses the application of  $\text{Co}_2(\text{CO})_8$  as a precursor for FEBIP in the MULTISCAN Lab UHV system. The precursor is of interest for EBID and EBISA research, as it has been suggested to exhibit autocatalytic growth much like  $\text{Fe}(\text{CO})_5$ . In order to facilitate the experiments,  $\text{Co}_2(\text{CO})_8$  precursor containers have been added to the system's gas dosing line in different ways.

QMS data shows that hexane, used as a stabilizer in the as-purchased precursor, is the main component in the gas phase prior to purification efforts. After purification by vacuum recrystallization in combination with a redesign of the gas dosing line, a successful EBI deposition experiment was conducted. The deposited material consists of a homogeneous (as observed by SEM) base layer with some indication for beginning growth granular, possibly

crystalline, material. Using AES, a Co content in the order of 75 %at. was determined, with carbon (15 %at.) and oxygen accounting for the remainder. Such a composition is well in the range of EBI deposits under HV conditions. The deposition process was shown to be selective on amorphous Si, with the exception of few scattered clusters of material on the Si surface and faint traces of material in AES.

The observation of these scattered clusters in combination with the indication of granular growth in the EBI deposit is an indication for autocatalytic decomposition and growth.

The deposition and growth processes could not be studied in more detail, as it was not possible to reliably dose the precursor into the vacuum system. This was attributed to (auto-) catalytic decomposition of the precursor within the gas dosing line, i.e. before the precursor reaches the surface. A number of possible solutions was proposed, but could not be implemented within the timeframe of this thesis.





## 7 Summary

In the course of this thesis, fundamental aspects of nanostructure fabrication using electron beam induced surface activation (EBISA) and electron beam induced deposition (EBID) were investigated in detail. EBISA is a recently (2010) discovered process that makes use of a focused electron beam to activate a surface towards the decomposition of precursor molecules, which are supplied to form deposits at the pre-irradiated areas in a subsequent processing step. In the closely related EBID technique, precursor molecules are directly decomposed by the impact of an electron beam. As the probe size of the electron beam is in the nanometer regime, both processes can be exploited to fabricate nanostructures on surface. To guarantee full control of the beam in regard to the specific requirements of the experiments conducted in the thesis at hand, an important task was the successful development and implementation of a corresponding lithographic attachment to the ultrahigh vacuum scanning electron microscope (Chapter 5).

Compared to EBID, which has been in the focus of research especially in the last decade, the understanding of EBISA was in its infancy at the beginning of this thesis. Successful nanostructure fabrication had been demonstrated on various silicon oxide surfaces using iron pentacarbonyl,  $\text{Fe}(\text{CO})_5$ , as a precursor and it had been proposed that the surface activation of silicon oxide surfaces is due to electron stimulated desorption (ESD) of oxygen, which forms reactive oxygen vacancies that subsequently mediate the decomposition of precursor molecules.

In the work at hand, the EBISA concept could be successfully expanded to titania (single crystal, rutile  $\text{TiO}_2(110)\text{-}1\times 1$ , Chapter 6.2) and quite different “organic” surfaces (2H- and Co-tetraphenylporphyrin layers on  $\text{Ag}(111)$ , Chapter 6.3). The corresponding experiments provided new insights into processes relevant for EBISA, which were mainly investigated by SEM, STM and AES. On both types of substrates, nanostructure fabrication following the EBISA protocol with iron pentacarbonyl was performed and revealed that EBISA is not

limited to  $\text{SiO}_x$  surfaces and the principle activation mechanism is not restricted to generation of oxygen vacancies.

It could be shown that on the titania surface, much like on silica, the activation is linked to the electron stimulated desorption of oxygen and the thereby created reactive oxygen vacancies (or reactive Si dangling bonds, depending on the point of view), which are responsible for the initial decomposition of precursor molecules. Therefore, it is suggested that EBISA might generally work on similar metal oxides as substrates.

On the organic surface, 2HTPP on Ag(111), a completely different mechanism is proposed: the molecules are excited or ionized by the electron irradiation, either direct or via backscattered and secondary electrons, which leads to the formation of non-volatile, reactive organic fragments, radicals or ions. In the experiment, the reactivity of these species is quenched by the silver support for the first layer of molecules; a single closed layer of molecules is sufficient to decouple reactive species in upper layers and conserve their reactivity. This observation also bears new strategies to reduce usually occurring proximity effects due to backscattered electrons and thus to potentially fabricate better defined and smaller nanostructures.

The second part focusses on the behavior of various precursors in the context of nanofabrication using EBID and EBISA. Iron pentacarbonyl,  $\text{Fe}(\text{CO})_5$ , has been identified as a viable precursor already during the initial experiments that lead to the development of the EBISA protocol. It is susceptible towards decomposition at active sites on  $\text{SiO}_x$  surface and exhibits autocatalytic growth, i.e. selective autocatalytic decomposition and deposition of high purity (> 90 - 95 %at.) Fe. As discussed before,  $\text{Fe}(\text{CO})_5$  has subsequently been used for the successful fabrication of Fe nanostructures by EBISA on  $\text{TiO}_2(110)$  and 2HTPP/Ag(111) and was also found to catalytically decompose on clean Ag(111). In order to broaden the range of applicable precursors, cobalt tricarbonyl nitrosyl,  $\text{Co}(\text{CO})_3\text{NO}$ , and dicobalt octacarbonyl,  $\text{Co}_2(\text{CO})_8$ , were used to conduct EBISA related experiments. The selection of the two Co precursors was made due to their apparent chemical resemblance to  $\text{Fe}(\text{CO})_5$  and the interesting properties of cobalt nanostructures, e.g. the magnetic behavior.

When  $\text{Co}(\text{CO})_3\text{NO}$  is used in experiments using the EBISA protocol on  $\text{SiO}_x$  substrates, no discernible nanostructures are formed. In EBID experiments, however, not only the direct deposition but also autocatalytic growth is observed (c.f. Chapter 6.4). Unlike autocatalytic decomposition of  $\text{Fe}(\text{CO})_5$ , which results in polycrystalline, highly pure metal deposits, autocatalytic decomposition of  $\text{Co}(\text{CO})_3\text{NO}$  results in granular, cobalt-containing, and oxygen, nitrogen and carbon rich  $\text{CoO}_x\text{N}_y\text{C}_z$  deposits with an approximate composition of 50

%at. Co, 25 % O, 15 % N and 10 % C. This composition suggests that of all decomposed precursor molecules, about 30 % of the NO ligands, and about 7 % of the CO ligands are decomposed and co-deposited.

Further comparative studies of the respective growth behavior were conducted using synchrotron radiation scanning transmission X-ray microscopy (STXM) and X-ray absorption spectroscopy (XAS). Iron growth from iron pentacarbonyl was found to occur at a constant growth rate of  $0.5 \pm 0.1 \text{ \AA}/\text{min}$  (at RT, approx.  $9 \times 10^{-6}$  mbar pressure at the surface), and was independent of the electron dose used during EBID/EBISA for all but the lowest doses necessary required for nanostructure fabrication. In contrast, the autocatalytic growth of  $\text{CoO}_x\text{N}_y\text{C}_z$  nanostructures from  $\text{Co}(\text{CO})_3\text{NO}$  is strongly dependent on the electron dose applied during the EBID step. It proceeds in a non-linear fashion and shows a, possibly exponential, increase in deposition rate upon longer precursor dosage. Furthermore, XAS shows that the deposits are comprised mainly of Co in an oxidized state along with oxygen, nitrogen and carbon co-deposits. It has to be concluded that  $\text{Co}(\text{CO})_3\text{NO}$  is not suitable for the use in EBISA and for the fabrication of high purity, metallic Co nanostructures using EBID.

Interestingly, sequential deposition experiments using  $\text{Fe}(\text{CO})_5$  and  $\text{Co}(\text{CO})_3\text{NO}$  revealed that selective autocatalytic growth of  $\text{CoO}_x\text{N}_y\text{C}_z$  deposits occurs also on iron nanostructures prepared by EBID and EBISA using  $\text{Fe}(\text{CO})_5$ . This finding suggests a potential fabrication process for layered nanostructures via sequential autocatalytic growth steps using different precursors. Furthermore, if a precursor exhibits  $\text{Co}(\text{CO})_3\text{NO}$ -like decomposition behavior, i.e. autocatalytic growth and catalytic decomposition at Fe nanostructures but no susceptibility to EBISA sites,  $\text{Fe}(\text{CO})_5$  could be used as a sensitizer. First, the pattern would be defined via EBISA, then developed using low amounts of  $\text{Fe}(\text{CO})_5$  to form Fe seeds, which would initialize the autocatalytic growth of the second precursor.

In the last part, another Co-precursor, dicobalt octacarbonyl,  $\text{Co}_2(\text{CO})_8$  was studied (Chapter 6.5). The precursor is susceptible both to thermal ( $T > 50\text{-}60 \text{ }^\circ\text{C}$ ) and catalytic decomposition, and poses a number of handling difficulties. Initial experiments suggest that the precursor is susceptible to decomposition at activated sites as well as show autocatalytic growth behavior.

In summary, the thesis at hand expands the range of applicable substrates and precursor molecules for the fabrication of nanostructures based on electron beam induced surface activation and underlines the importance of both surface and precursor chemistry for EBISA as well as EBID. In addition the achieved results indicate different novel pathways for the fabrication of well-defined nanostructures which should be further explored in the near future.



## 8 Zusammenfassung

Im Verlauf der vorliegenden Arbeit wurden grundlegende Aspekte der Nanostrukturherstellung mittels elektronenstrahlinduzierter Oberflächenaktivierung (Electron Beam Induced Surface Activation, EBISA) und elektronenstrahlinduzierter Abscheidung (Electron Beam Induced Deposition, EBID) untersucht. EBISA bezeichnet hierbei einen kürzlich (2010) entdeckten Prozess, bei dem ein fokussierter Elektronenstrahl genutzt wird, um eine Oberfläche so zu aktivieren, dass die aktivierten Bereiche in einem zweiten Schritt die Zersetzung von bestimmten Molekülen, den sogenannten Präkursoren, initiieren können und so eine Abscheidung erzeugen. Im verwandten EBID-Prozess werden solche Präkursoren direkt durch den Elektronenstrahl zersetzt. Der Durchmesser des verwendeten Elektronenstrahls liegt im einstelligen Nanometer-Bereich, weshalb beide Prozesse genutzt werden können, um Nanostrukturen auf Oberflächen herzustellen. Um die speziellen Anforderungen an die Elektronenstrahlsteuerung in Bezug auf EBID und EBISA zu erfüllen, wurde als wichtiger Schritt innerhalb dieser Arbeit ein System für die Elektronenstrahlsteuerung als Erweiterung des eingesetzten Ultrahochvakuum-Rasterelektronenmikroskops entwickelt wurde (siehe Kapitel 5).

Verglichen mit dem in der letzten Dekade verstärkt untersuchten EBID-Prozess war das Verständnis von EBISA zu Beginn dieser Arbeit begrenzt. Es war gezeigt worden, dass es möglich ist, Nanostrukturen auf Siliziumoxidoberflächen mit dem Präkursor Eisenpentacarbonyl,  $\text{Fe}(\text{CO})_5$ , herzustellen; als Aktivierungsmechanismus wurde die Erzeugung von reaktiven Sauerstofffehlstellen durch energetische Elektronen über elektronenstimulierte Desorption (ESD) von Sauerstoff aus dem Siliziumoxid vorgeschlagen.

Als signifikante Erweiterung dieser Beobachtungen konnte in der vorliegenden Arbeit gezeigt werden, dass das EBISA-Konzept auf andere Substrate übertragen werden kann. Bei den neu eingeführten Substraten handelt sich um  $\text{TiO}_2(110)$ -Einkristalle (siehe Kapitel 6.2)

und dünne Tetraphenylporphyrin-Schichten auf Silber(111)-Einkristallen (siehe Kapitel 6.3). Auf beiden Substraten wurden, ausgehend vom Präkursor Eisenpentacarbonyl,  $\text{Fe}(\text{CO})_5$ , erfolgreich Nanostrukturen mittels EBISA hergestellt und mit SEM, STM und AES untersucht. Dabei zeigte sich, dass das EBISA-Konzept nicht auf  $\text{SiO}_x$ -Oberflächen beschränkt ist und dass auch andere Aktivierungsmechanismen, die nicht auf der strahlinduzierten Erzeugung von Sauerstofffehlstellen beruhen, möglich sind.

Auf dem Titanoxidsubstrat wurde, analog zum Siliziumoxid, die Aktivierung der elektronenstrahlinduzierten Sauerstoffdesorption und die damit einhergehende Erzeugung von reaktiven Sauerstofffehlstellen (oder, je nach Blinkwinkel, von ungesättigte Bindungen) zugeschrieben, die wiederum für die initiale Zersetzung der Präkursoren verantwortlich sind. Daher ist anzunehmen, dass EBISA auch auf anderen, ähnlichen Oxidoberflächen einsetzbar ist.

Der Aktivierungsmechanismus der dünnen Porphyrinschichten ist notwendigerweise ein anderer. Aus den experimentellen Befunden wird geschlossen, dass die Moleküle durch den Elektronenbeschuss, entweder direkt oder über Rückstreu- und Sekundärelektronen, angeregt oder ionisiert werden und nichtflüchtige, reaktive organische Fragmente, Ionen oder Radikale bilden. Im Experiment wird diese Reaktivität in der ersten Porphyrinlage durch das darunter liegende Silbersubstrat unterdrückt, wobei aktive Spezies in höheren Lagen durch die erste Lage abgeschirmt werden und so ihre Reaktivität erhalten bleibt. Potentiell könnte diese Beobachtung also dazu beitragen, sogenannte Proximity-Effekte, also Strukturverbreiterungen, meist bedingt durch gestreute Elektronen, zu reduzieren und so besser definierte oder kleinere Nanostrukturen herzustellen.

Der zweite Teil der vorliegenden Arbeit beschäftigt sich mit dem Verhalten verschiedener Präkursoren im Kontext von EBID und EBISA. Wie bereits bekannt, wurde Eisenpentacarbonyl bereits zu Beginn der EBISA-Forschung als geeigneter Präkursor identifiziert, da es sich an aktivierten Stellen zersetzt und im Weiteren autokatalytisches Wachstum zeigt, d.h. sich selektiv autokatalytisch an vorhandenen Eisenkeimen zersetzt und so zur Abscheidung von sehr reinem (> 90 - 95 %at.) Eisen führt. Wie bereits gezeigt, kann  $\text{Fe}(\text{CO})_5$  auch zur Herstellung von Eisen-Nanostrukturen auf  $\text{TiO}_2(110)$  und auf Porphyrinschichten auf Silber genutzt werden. Außerdem zersetzt es sich katalytisch auf frisch präpariertem Silber(111).

Um nun die Bandbreite an verwendbaren Präkursoren und damit auch abscheidbaren Materialien für EBISA zu erhöhen, wurden die potentiellen Cobalt-Präkursoren Cobalt-tricarbonylnitrosyl,  $\text{Co}(\text{CO})_3\text{NO}$ , und Dicobaltoktacobonyl,  $\text{Co}_2(\text{CO})_8$ , hinsichtlich ihrer

Eignung untersucht. Die Auswahl erfolgte dabei sowohl auf Grund der chemischen Ähnlichkeit zu  $\text{Fe}(\text{CO})_5$  als auch in Betracht der interessanten, z.B. magnetischen, Eigenschaften von Cobalt-Nanostrukturen.

Wird  $\text{Co}(\text{CO})_3\text{NO}$  analog zu  $\text{Fe}(\text{CO})_5$  in einem EBISA-Experiment auf  $\text{SiO}_x$  genutzt, bilden sich keinerlei erkennbare Nanostrukturen. In EBID-Experimenten beobachtet man jedoch zusätzlich zur direkten Abscheidung ein autokatalytisches Wachstum (siehe Kapitel 6.4). Anders als  $\text{Fe}(\text{CO})_5$ , das sehr reine, polykristalline Eisenabscheidungen bildet, führt die autokatalytische Zersetzung von  $\text{Co}(\text{CO})_3\text{NO}$  zur Abscheidung von granulearem, Cobalt enthaltenden, sauerstoff-, stickstoff- und kohlenstoffreichem Material mit einer ungefähren Zusammensetzung von 50 %at. Co, 25 % O, 15 % N und 10 % C. Diese Zusammensetzung legt nahe, dass etwa 30 % der NO- und 7% der CO-Liganden zersetzt und mitabgeschieden werden.

Das Wachstumsverhalten der Präkursoren wurde auch mit Rastertransmissionsröntgenmikroskopie (STXM) und Röntgenabsorptionsspektroskopie (XAS) untersucht. Das Wachstum von Eisen aus  $\text{Fe}(\text{CO})_5$  verlief dabei bei Raumtemperatur und ca.  $9 \times 10^{-6}$  mbar Präkursor- und -druck an der Oberfläche mit einer konstanten Abscheidungsrate von  $0.5 \pm 0.1$  Å/min, unabhängig von der Elektronendosis, die während des EBID- oder EBISA-Schritts aufgebracht wurde (Ausnahme: sehr kleine Dosen). Im Gegensatz dazu weist das Wachstum der  $\text{CoO}_x\text{N}_y\text{C}_z$ -Nanostrukturen aus  $\text{Co}(\text{CO})_3\text{NO}$  eine starke Abhängigkeit von der Elektronendosis auf und verläuft deutlich nichtlinear mit möglicherweise exponentiell ansteigender Wachstumsrate. Mittels Röntgenabsorptionsspektroskopie kann außerdem nachgewiesen werden, dass die Abscheidungen hauptsächlich Cobalt in höheren Oxidationsstufen enthalten. Aus den vorliegenden Befunden wird geschlossen, dass sich  $\text{Co}(\text{CO})_3\text{NO}$  unter den gegebenen Bedingungen nicht für die Herstellung von sauberen Cobalt-Nanostrukturen mittels EBID oder EBISA eignet.

Interessanterweise konnte bei Experimenten zur aufeinanderfolgenden Abscheidung von Strukturen mit  $\text{Fe}(\text{CO})_5$  und  $\text{Co}(\text{CO})_3\text{NO}$  beobachtet werden, dass sich  $\text{Co}(\text{CO})_3\text{NO}$  selektiv auf vorher mittels EBID/EBISA und  $\text{Fe}(\text{CO})_5$  abgeschiedenen Eisenstrukturen zersetzt und zu autokatalytischem Wachstum von  $\text{CoO}_x\text{N}_y\text{C}_z$  führt. Diese Beobachtung kann potentiell zur Herstellung von geschichteten Nanostrukturen durch aufeinanderfolgende Wachstumsschritte mit verschiedenen Präkursoren genutzt werden. Außerdem könnte  $\text{Fe}(\text{CO})_5$  als Aktivitätsvermittler für andere Präkursoren dienen, die wie  $\text{Co}(\text{CO})_3\text{NO}$  zwar autokatalytisches Wachstum und katalytische Zersetzung an Eisenkeimen, aber keine Zersetzung an aktivierten Oberflächen zeigen. Dabei würde dann die Belichtungsmuster

mittels EBISA definiert, mit wenig  $\text{Fe}(\text{CO})_5$  vermittelt und schließlich mit dem zweiten Präkursor entwickelt.

Im letzten Abschnitt (Kapitel 6.5) wurde ein weiterer Cobaltpräkursor, nämlich Dicobaltoktacobonyl,  $\text{Co}_2(\text{CO})_8$ , untersucht. Dieser Präkursor ist empfindlich gegenüber thermischer ( $T > 50 - 60 \text{ }^\circ\text{C}$ ) und katalytischer Zersetzung und stellt somit einige Anforderungen an die Handhabung. Vorexperimente zeigen, dass der Präkursor sowohl autokatalytisches Wachstum als auch Zersetzung an aktiven Zentren zeigt.

Zusammenfassend erweitert die vorliegende Arbeit also die Bandbreite an anwendbaren Substraten und Präkursoren für Herstellung von Nanostrukturen mittels EBISA und zeigt die Wichtigkeit beider Komponenten sowohl für EBISA wie für EBID. Weiterhin zeigen die Ergebnisse neue Ansätze für die Herstellung von definierten Nanostrukturen, die weiter untersucht werden sollten.





---

## 9 Bibliography

- (1) Moore, G. E., Cramming more components onto integrated circuits. *Electronics* **38** (1965), 114.
- (2) International Technology Roadmap for Semiconductors. <http://www.itrs.net/> (Accessed: 02.05.2014).
- (3) Cumming, D. R. S.; Furber, S. B.; Paul, D. J., Beyond Moore's law. *Phil. Trans. R. Soc. A* **372** (2014), 20130376.
- (4) van Dorp, W. F.; Hagen, C. W., A Critical Literature Review of Focused Electron Beam Induced Deposition. *J. Appl. Phys.* **104** (2008), 081301.
- (5) Walz, M.-M.; Schirmer, M.; Vollnhals, F.; Lukasczyk, T.; Steinrück, H.-P.; Marbach, H., Electrons as Invisible Ink: Fabrication of Nanostructures by Local Electron Beam Induced Activation of SiO<sub>x</sub>. *Angew. Chem. Int. Ed.* **49** (2010), 4669.
- (6) Götzhäuser, A.; Eck, W.; Geyer, W.; Stadler, V.; Weimann, T.; Hinze, P.; Grunze, M., Chemical nanolithography with electron beams. *Adv. Mater.* **13** (2001), 806.
- (7) Huth, M.; Porrati, F.; Schwalb, C.; Winhold, M.; Sachser, R.; Dukic, M.; Adams, J.; Fantner, G., Focused Electron Beam Induced Deposition: A Perspective. *Beilstein J. Nanotechnol.* **3** (2012), 597.
- (8) Randolph, S. J.; Fowlkes, J. D.; Rack, P. D., Focused, Nanoscale Electron-Beam-Induced Deposition and Etching. *Crit. Rev. Solid State Mater. Sci.* **31** (2006), 55.
- (9) Silvis-Cividjian, N.; Hagen, C. W.; Kruit, P., Spatial resolution limits in electron-beam-induced deposition. *J. Appl. Phys.* **98** (2005), 084905.
- (10) Utke, I.; Götzhäuser, A., Small, Minimally Invasive, Direct: Electrons Induce Local Reactions of Adsorbed Functional Molecules on the Nanoscale. *Angew. Chem. Int. Ed.* **49** (2010), 9328.
- (11) Utke, I.; Hoffmann, P.; Melngailis, J., Gas-assisted focused electron beam and ion beam processing and fabrication. *J. Vac. Sci. Technol., B* **26** (2008), 1197.
- (12) Walz, M.-M.; Vollnhals, F.; Rietzler, F.; Schirmer, M.; Kunzmann, A.; Steinrück, H.-P.; Marbach, H., Thin membranes versus bulk substrates: investigation of proximity effects in focused electron beam-induced processing. *J. Phys. D: Appl. Phys.* **45** (2012), 225306.

- (13) Walz, M.-M.; Vollnhals, F.; Rietzler, F.; Schirmer, M.; Steinrück, H.-P.; Marbach, H., Investigation of Proximity Effects in Electron Microscopy and Lithography. *Appl. Phys. Lett.* **100** (2012), 053118.
- (14) Walz, M.-M.; Vollnhals, F.; Schirmer, M.; Steinrück, H.-P.; Marbach, H., Generation of Clean Iron Nanocrystals on an Ultra-Thin SiO<sub>x</sub> Film on Si(001). *Phys. Chem. Chem. Phys.* **13** (2011), 17333.
- (15) Muthukumar, K.; Jeschke, H. O.; Valentí, R.; Begun, E.; Schwenk, J.; Porrati, F.; Huth, M., Spontaneous Dissociation of Co<sub>2</sub>(CO)<sub>8</sub> and Autocatalytic Growth of Co on SiO<sub>2</sub>: A Combined Experimental and Theoretical Investigation. *Beilstein J. Nanotechnol.* **3** (2012), 546.
- (16) Marbach, H., Electron beam induced surface activation: a method for the lithographic fabrication of nanostructures via catalytic processes. *Appl. Phys. A* **117** (2014), 987.
- (17) Stewart, R. L., Insulating Films Formed Under Electron and Ion Bombardment. *Phys. Rev.* **45** (1934), 488.
- (18) Botman, A.; Mulders, J. J. L.; Hagen, C. W., Creating pure nanostructures from electron-beam-induced deposition using purification techniques: a technology perspective. *Nanotechnology* **20** (2009), 372001.
- (19) Silvis-Cividjian, N.; Hagen, C. W., Electron-Beam-Induced Nanometer-Scale Deposition. In *Advances in Imaging and Electron Physics*, Silvis-Cividjian, N.; Hagen, C. W. (Eds.), Elsevier, (2006).
- (20) van Dorp, W. F.; van Someren, B.; Hagen, C. W.; Kruit, P.; Crozier, P. A., Approaching the Resolution Limit of Nanometer-Scale Electron Beam-Induced Deposition. *Nano Lett.* **5** (2005), 1303.
- (21) Lukasczyk, T.; Schirmer, M.; Steinrück, H.-P.; Marbach, H., Electron-Beam-Induced Deposition in Ultrahigh Vacuum: Lithographic Fabrication of Clean Iron Nanostructures. *Small* **4** (2008), 841.
- (22) Gavagnin, M.; Wanzenboeck, H. D.; Belić, D.; Bertagnolli, E., Synthesis of Individually Tuned Nanomagnets for Nanomagnet Logic by Direct Write Focused Electron Beam Induced Deposition. *ACS Nano* **7** (2013), 777.
- (23) Belova, L. M.; Dahlberg, E. D.; Riazanova, A.; Mulders, J. J. L.; Christophersen, C.; Eckert, J., Rapid electron beam assisted patterning of pure cobalt at elevated temperatures via seeded growth. *Nanotechnology* **22** (2011), 145305.
- (24) Fernández-Pacheco, A.; De Teresa, J. M.; Córdoba, R.; Ibarra, M. R., Magnetotransport properties of high-quality cobalt nanowires grown by focused-electron-beam-induced deposition. *J. Phys. D: Appl. Phys.* **42** (2009), 055005.

- 
- (25) Mulders, J. J. L.; Veerhoek, J. M.; Bosch, E. G. T.; Trompenaars, P. H. F., Fabrication of pure gold nanostructures by electron beam induced deposition with Au(CO)Cl precursor: deposition characteristics and primary beam scattering effects. *J. Phys. D: Appl. Phys.* **45** (2012), 475301.
- (26) Koops, H. W. P.; Hoinkis, O. E.; Honsberg, M. E. W.; Schmidt, R.; Blum, R.; Böttger, G.; Kuligk, A.; Liguda, C.; Eich, M., Two-dimensional photonic crystals produced by additive nanolithography with electron beam-induced deposition act as filters in the infrared. *Microelectron. Eng.* **57–58** (2001), 995.
- (27) Edinger, K.; Becht, H.; Bihl, J.; Boegli, V.; Budach, M.; Hofmann, T.; Koops, H. W. P.; Kuschnerus, P.; Oster, J.; Spies, P.; Weyrauch, B., Electron-beam-based photomask repair. *J. Vac. Sci. Technol., B* **22** (2004), 2902.
- (28) Liang, T.; Freundberg, E.; Lieberman, B.; Stivers, A., Advanced photolithographic mask repair using electron beams. *J. Vac. Sci. Technol., B* **23** (2005), 3101.
- (29) Bret, T.; Jonckheere, R.; Van den Heuvel, D.; Baur, C.; Waiblinger, M.; Baralia, G. In *Closing the gap for EUV mask repair*, Proc. SPIE, 2012; pp 83220C.
- (30) Utke, I.; Hoffmann, P.; Berger, R.; Scandella, L., High-resolution magnetic Co supertips grown by a focused electron beam. *Appl. Phys. Lett.* **80** (2002), 4792.
- (31) Bøggild, P.; Hansen, T. M.; Tanasa, C.; Grey, F., Fabrication and actuation of customized nanotweezers with a 25 nm gap. *Nanotechnology* **12** (2001), 331.
- (32) Boero, G.; Utke, I.; Bret, T.; Quack, N.; Todorova, M.; Mouaziz, S.; Kejik, P.; Brugger, J.; Popovic, R. S.; Hoffmann, P., Submicrometer Hall devices fabricated by focused electron-beam-induced deposition. *Appl. Phys. Lett.* **86** (2005), 042503.
- (33) Gabureac, M.; Bernau, L.; Utke, I.; Boero, G., Granular Co–C nano-Hall sensors by focused-beam-induced deposition. *Nanotechnology* **21** (2010), 115503.
- (34) Schwalb, C. H.; Grimm, C.; Baranowski, M.; Sachser, R.; Porrati, F.; Reith, H.; Das, P.; Müller, J.; Völklein, F.; Kaya, A.; Huth, M., A Tunable Strain Sensor Using Nanogranular Metals. *Sensors* **10** (2010), 9847.
- (35) Kolb, F.; Schmoltner, K.; Huth, M.; Hohenau, A.; Krenn, J.; Klug, A.; List, E. J. W.; Plank, H., Variable tunneling barriers in FEBID based PtC metal-matrix nanocomposites as a transducing element for humidity sensing. *Nanotechnology* **24** (2013), 305501.
- (36) Porrati, F.; Sachser, R.; Walz, M.-M.; Vollnhals, F.; Steinrück, H.-P.; Marbach, H.; Huth, M., Magnetotransport Properties of Iron Microwires Fabricated by Focused Electron Beam Induced Autocatalytic Growth. *J. Phys. D: Appl. Phys.* **44** (2011), 425001.

- (37) Córdoba, R.; Sesé, J.; Ibarra, M. R.; De Teresa, J. M., Autocatalytic Growth of Co on Pure Co Surfaces Using  $\text{Co}_2(\text{CO})_8$  Precursor. *Appl. Surf. Sci.* **263** (2012), 242.
- (38) Brintlinger, T.; Fuhrer, M. S.; Melngailis, J.; Utke, I.; Bret, T.; Perentes, A.; Hoffmann, P.; Abourida, M.; Doppelt, P., Electrodes for carbon nanotube devices by focused electron beam induced deposition of gold. *J. Vac. Sci. Technol., B* **23** (2005), 3174.
- (39) Schirmer, M.; Walz, M.-M.; Vollnhals, F.; Lukasczyk, T.; Sandmann, A.; Chen, C.; Steinrück, H.-P.; Marbach, H., Electron-beam-induced deposition and post-treatment processes to locally generate clean titanium oxide nanostructures on Si(100). *Nanotechnology* **22** (2011), 085301.
- (40) Böhler, E.; Warneke, J.; Swiderek, P., Control of chemical reactions and synthesis by low-energy electrons. *Chem. Soc. Rev.* **42** (2013), 9219.
- (41) Engmann, S.; Stano, M.; Matejčík, S.; Ingólfsson, O., Gas phase low energy electron induced decomposition of the focused electron beam induced deposition (FEBID) precursor trimethyl (methylcyclopentadienyl) platinum(IV) ( $\text{MeCpPtMe}_3$ ). *Phys. Chem. Chem. Phys.* **14** (2012), 14611.
- (42) Engmann, S.; Stano, M.; Matejčík, Š.; Ingólfsson, O., The Role of Dissociative Electron Attachment in Focused Electron Beam Induced Processing: A Case Study on Cobalt Tricarbonyl Nitrosyl. *Angew. Chem. Int. Ed.* **50** (2011), 9475.
- (43) Engmann, S.; Stano, M.; Papp, P.; Brunger, M. J.; Matejčík, Š.; Ingólfsson, O., Absolute cross sections for dissociative electron attachment and dissociative ionization of cobalt tricarbonyl nitrosyl in the energy range from 0 eV to 140 eV. *J. Chem. Phys.* **138** (2013), 044305.
- (44) Rosenberg, S. G.; Landheer, K.; Hagen, C. W.; Fairbrother, D. H., Substrate temperature and electron fluence effects on metallic films created by electron beam induced deposition. *J. Vac. Sci. Technol., B* **30** (2012), 051805.
- (45) van Dorp, W. F.; Wnuk, J. D.; Gorham, J. M.; Fairbrother, D. H.; Madey, T. E.; Hagen, C. W., Electron induced dissociation of trimethyl (methylcyclopentadienyl) platinum (IV): Total cross section as a function of incident electron energy. *J. Appl. Phys.* **106** (2009), 074903.
- (46) Wnuk, J. D.; Rosenberg, S. G.; Gorham, J. M.; van Dorp, W. F.; Hagen, C. W.; Fairbrother, D. H., Electron beam deposition for nanofabrication: Insights from surface science. *Surf. Sci.* **605** (2011), 257.
- (47) Rosenberg, S. G.; Barclay, M.; Fairbrother, D. H., Electron Beam Induced Reactions of Adsorbed Cobalt Tricarbonyl Nitrosyl ( $\text{Co}(\text{CO})_3\text{NO}$ ) Molecules. *J. Phys. Chem. C* **117** (2013), 16053.

- 
- (48) Block, T.; Pfnür, H., Generation of ultrasmall nanostructures in oxide layers assisted by self-organization. *J. Appl. Phys.* **103** (2008), 064303.
- (49) Pfnür, H.; Zielasek, V.; Tegenkamp, C.; Block, T.; Kallassy, Z., Geometrical and electronic properties of ultra thin epitaxial metal nanowires on flat and vicinal Si surfaces. *Mater. Sci.-Pol.* **23** (2005), 861.
- (50) Watanabe, H.; Fujita, K.; Ichikawa, M., Thermal decomposition of ultrathin oxide layers on Si(111) surfaces mediated by surface Si transport. *Appl. Phys. Lett.* **70** (1997), 1095.
- (51) Fujita, S.; Maruno, S.; Watanabe, H.; Ichikawa, M., Nanofabrication using selective thermal desorption of SiO<sub>2</sub>/Si induced by electron beams. *J. Vac. Sci. Technol., A* **15** (1997), 1493.
- (52) Knotek, M. L.; Feibelman, P. J., Ion Desorption by Core-Hole Auger Decay. *Phys. Rev. Lett.* **40** (1978), 964.
- (53) Niehus, H.; Losch, W., ESD on metal oxides and oxygen adsorption layers: Evidence for different mechanisms in electron stimulated desorption. *Surf. Sci.* **111** (1981), 344.
- (54) Papageorgiou, A. C.; Beglitis, N. S.; Pang, C. L.; Teobaldi, G.; Cabailh, G.; Chen, Q.; Fisher, A. J.; Hofer, W. A.; Thornton, G., Electron traps and their effect on the surface chemistry of TiO<sub>2</sub>(110). *Proc. Natl. Acad. Sci. U.S.A.* **107** (2010), 2391.
- (55) Muthukumar, K.; Opahle, I.; Shen, J.; Jeschke, H. O.; Valentí, R., Interaction of W(CO)<sub>6</sub> with SiO<sub>2</sub> surfaces: A density functional study. *Phys. Rev. B* **84** (2011), 205442.
- (56) Kunz, R. R.; Allen, T. E.; Mayer, T. M., Selective area deposition of metals using low-energy electron beams. *J. Vac. Sci. Technol., B* **5** (1987), 1427.
- (57) Kunz, R. R.; Mayer, T. M., Catalytic growth rate enhancement of electron beam deposited iron films. *Appl. Phys. Lett.* **50** (1987), 962.
- (58) Kunz, R. R.; Mayer, T. M., Electron beam induced surface nucleation and low-temperature decomposition of metal carbonyls. *J. Vac. Sci. Technol., B* **6** (1988), 1557.
- (59) Zhang, W.; Shimojo, M.; Takeguchi, M.; Che, R. C.; Furuya, K., Generation Mechanism and in situ Growth Behavior of  $\alpha$ -Iron Nanocrystals by Electron Beam Induced Deposition. *Adv. Eng. Mater.* **8** (2006), 711.
- (60) Adams, D. P.; Mayer, T. M.; Chason, E.; Kellerman, B. K.; Swartzentruber, B. S., Island structure evolution during chemical vapor deposition. *Surf. Sci.* **371** (1997), 445.

- (61) Adams, D. P.; Mayer, T. M.; Swartzentruber, B. S., Selective area growth of metal nanostructures. *Appl. Phys. Lett.* **68** (1996), 2210.
- (62) Adams, D. P.; Tedder, L. L.; Mayer, T. M.; Swartzentruber, B. S.; Chason, E., Initial Stages of Fe Chemical Vapor Deposition onto Si(100). *Phys. Rev. Lett.* **74** (1995), 5088.
- (63) Lukasczyk, T.; Schirmer, M.; Steinrück, H.-P.; Marbach, H., Generation of Clean Iron Structures by Electron-Beam-Induced Deposition and Selective Catalytic Decomposition of Iron Pentacarbonyl on Rh(110). *Langmuir* **25** (2009), 11930.
- (64) Zaera, F., A thermal desorption and x-ray photoelectron spectroscopy study of the surface chemistry of iron pentacarbonyl. *J. Vac. Sci. Technol., A* **7** (1989), 640.
- (65) Zaera, F., Mechanism for the decomposition of iron pentacarbonyl on Pt(111): evidence for iron tetracarbonyl and iron tricarbonyl intermediates. *Surf. Sci.* **255** (1991), 280.
- (66) Zaera, F., A kinetic study of the chemical vapor deposition of iron films using iron pentacarbonyl. *Langmuir* **7** (1991), 1188.
- (67) Xu, M.; Zaera, F., Mechanistic studies of the thermal decomposition of metal carbonyls on Ni(100) surfaces in connection with chemical vapor deposition processes. *J. Vac. Sci. Technol., A* **14** (1996), 415.
- (68) Mulders, J. J. L.; Belova, L. M.; Riazanova, A., Electron beam induced deposition at elevated temperatures: compositional changes and purity improvement. *Nanotechnology* **22** (2011), 055302.
- (69) Plank, H.; Kothleitner, G.; Hofer, F.; Michelitsch, S. G.; Gspan, C.; Hohenau, A.; Krenn, J. R., Optimization of postgrowth electron-beam curing for focused electron-beam-induced Pt deposits. *J. Vac. Sci. Technol., B* **29** (2011), 051801.
- (70) Reimer, L., *Scanning Electron Microscopy*. 2nd ed.; Springer-Verlag, Berlin - Heidelberg - New York (1998).
- (71) Everhart, T. E.; Thornley, R. F. M., Wide-band detector for micro-microampere low-energy electron currents. *J. Sci. Instrum.* **37** (1960), 246.
- (72) Cazaux, J., Material contrast in SEM: Fermi energy and work function effects. *Ultramicroscopy* **110** (2010), 242.
- (73) Briggs, D.; Seah, M. P. (Eds.), *Practical Surface Analysis, Volume 1 - Auger and X-ray Photoelectron Spectroscopy*. 2nd ed.; John Wiley & Sons Ltd, Chichester (1990).
- (74) Binnig, G.; Rohrer, H.; Gerber, C.; Weibel, E., Surface Studies by Scanning Tunneling Microscopy. *Phys. Rev. Lett.* **49** (1982), 57.

- 
- (75) Sutter, P., Scanning Tunneling Microscopy in Surface Science. In *Science of Microscopy*, Hawkes, P. W.; Spence, J. C. H. (Eds.), Springer Science+Business Media, New York (2007).
- (76) Chen, C. J., *Introduction to Scanning Tunneling Microscopy*. Oxford University Press, New York (1993).
- (77) Tersoff, J.; Hamann, D. R., Theory and Application for the Scanning Tunneling Microscope. *Phys. Rev. Lett.* **50** (1983), 1998.
- (78) Baratoff, A., Theory of scanning tunneling microscopy - methods and approximations. *Physica B+C* **127** (1984), 143.
- (79) Chen, C. J., Microscopic view of scanning tunneling microscopy. *J. Vac. Sci. Technol., A* **9** (1991), 44.
- (80) Ohnishi, S.; Tsukada, M., Molecular orbital theory for the scanning tunneling microscopy. *Solid State Commun.* **71** (1989), 391.
- (81) Tersoff, J.; Hamann, D. R., Theory of the scanning tunneling microscope. *Phys. Rev. B* **31** (1985), 805.
- (82) Kirz, J.; Rarback, H., Soft x-ray microscopes. *Rev. Sci. Instrum.* **56** (1985), 1.
- (83) Raabe, J.; Tzvetkov, G.; Flechsig, U.; Böge, M.; Jaggi, A.; Sarafimov, B.; Vernooij, M. G. C.; Huthwelker, T.; Ade, H.; Kilcoyne, D.; Tyliszczak, T.; Fink, R. H.; Quitmann, C., PoLux: A new facility for soft x-ray spectromicroscopy at the Swiss Light Source. *Rev. Sci. Instrum.* **79** (2008), 113704.
- (84) Stöhr, J., *NEXAFS Spectroscopy*. 1st ed.; Springer-Verlag Berlin Heidelberg (1992).
- (85) Meyer, M. J., *Investigation of biocompatible fibers by nanoprobes*. Master Thesis, Friedrich-Alexander-Universität Erlangen-Nürnberg, Erlangen (2014).
- (86) Stöhr, J., Exploring the microscopic origin of magnetic anisotropies with X-ray magnetic circular dichroism (XMCD) spectroscopy. *J. Magn. Magn. Mater.* **200** (1999), 470.
- (87) Funk, T.; Deb, A.; George, S. J.; Wang, H.; Cramer, S. P., X-ray magnetic circular dichroism - a high energy probe of magnetic properties. *Coord. Chem. Rev.* **249** (2005), 3.
- (88) Oura, K.; Lifshits, V. G.; Saranin, A. A.; Zotov, A. V.; Katayama, M., *Surface Science - An Introduction*. 1st ed.; Springer-Verlag, Berlin - Heidelberg - New York (2003).

- (89) Held, G., Low-Energy Electron Diffraction: Crystallography of Surfaces and Interfaces. In *Methods in Physical Chemistry*, Wiley-VCH Verlag GmbH & Co. KGaA, Weinheim (2012).
- (90) Hesse, M. M., H.; Zeeh, B., *Spektroskopische Methoden in der organischen Chemie*. 7th ed.; Georg Thieme Verlag, Stuttgart (2005).
- (91) Dawson, P. H. (Ed.) *Quadrupole mass spectrometry and its applications*. 1st ed.; Elsevier Scientific Publishing Company, Amsterdam - Oxford - New York (1976).
- (92) Drouin, D.; Couture, A. R.; Joly, D.; Tastet, X.; Aimez, V.; Gauvin, R., CASINO V2.42-A Fast and Easy-to-use Modeling Tool for Scanning Electron Microscopy and Microanalysis Users. *Scanning* **29** (2007), 92.
- (93) Demers, H.; Poirier-Demers, N.; Couture, A. R.; Joly, D.; Guilmain, M.; de Jonge, N.; Drouin, D., Three-dimensional electron microscopy simulation with the CASINO Monte Carlo software. *Scanning* **33** (2011), 135.
- (94) Lukasczyk, T., *Generation of pure iron nanostructures via electron-beam induced deposition in UHV*. Doctoral Thesis, Friedrich-Alexander-Universität Erlangen-Nürnberg, Erlangen (2010).
- (95) Schirmer, M., *Generation of Titanium Oxide Nanostructures via Electron Beam Induced Deposition in UHV*. Doctoral Thesis, Friedrich-Alexander-Universität Erlangen-Nürnberg, Erlangen (2012).
- (96) *Handbuch für die Rasterelektronenmikroskope SUPRA(VP) und ULTRA*. Carl Zeiss NTS, Oberkochen (2004).
- (97) *MULTISCAN STM VT User's Guide Version 1.0*. Omicron Nanotechnology, Taunusstein (2005).
- (98) Friedli, V.; Utke, I., Optimized Molecule Supply from Nozzle-Based Gas Injection Systems for Focused Electron- and Ion-Beam Induced Deposition and Etching: Simulation and Experiment. *J. Phys. D: Appl. Phys.* **42** (2009), 125305.
- (99) Vila-Comamala, J.; Jefimovs, K.; Raabe, J.; Pilvi, T.; Fink, R. H.; Senoner, M.; Maaßdorf, A.; Ritala, M.; David, C., Advanced thin film technology for ultrahigh resolution X-ray microscopy. *Ultramicroscopy* **109** (2009), 1360.
- (100) Diebold, U., The Surface Science of Titanium Dioxide. *Surf. Sci. Rep.* **48** (2003), 53.
- (101) Tromp, R.; Rubloff, G. W.; Balk, P.; LeGoues, F. K.; van Loenen, E. J., High-Temperature SiO<sub>2</sub> Decomposition at the SiO<sub>2</sub>/Si Interface. *Phys. Rev. Lett.* **55** (1985), 2332.

- 
- (102) Raider, S. I.; Flitsch, R.; Aboaf, J. A.; Pliskin, W. A., Surface Oxidation of Silicon Nitride Films. *J. Electrochem. Soc.* **123** (1976), 560.
- (103) Méndez, J.; Luna, M.; Baró, A. M., Preparation of STM W tips and characterization by FEM, TEM and SEM. *Surf. Sci.* **266** (1992), 294.
- (104) Guise, O. L.; Ahner, J. W.; Jung, M.-C.; Goughnour, P. C.; Yates, J. T., Reproducible Electrochemical Etching of Tungsten Probe Tips. *Nano Lett.* **2** (2002), 191.
- (105) Tannenbaum, R.; Bor, G., Selected reactions of cobalt carbonyl complexes placed under vacuum conditions. *J. Organomet. Chem.* **586** (1999), 18.
- (106) Horcas, I.; Fernández, R.; Gómez-Rodríguez, J. M.; Colchero, J.; Gómez-Herrero, J.; Baro, A. M., WSXM: A Software for Scanning Probe Microscopy and a Tool for Nanotechnology. *Rev. Sci. Instrum.* **78** (2007), 013705.
- (107) JC Nability Lithography Systems, Bozeman MT (USA). <http://www.jcnability.com/> (Accessed: 24.04.2014).
- (108) Raith GmbH, Dortmund (D). <http://www.raith.com/> (Accessed: 24.04.2014).
- (109) Helbert, J. N. (Ed.) *Handbook of VLSI Microlithography - Principles, Technology and Applications*. 2nd ed.; Noyes Publications / William Andrew Publishing, Norwich, NY (2001).
- (110) Vollnhals, F., *Titanium(IV)isopropoxide as a precursor for electron beam induced deposition (EBID)*. Bachelor Thesis, Friedrich-Alexander-Universität Erlangen-Nürnberg, Erlangen (2007).
- (111) W. Zhou; Wang, Z. L. (Eds.), *Scanning Microscopy for Nanotechnology: Techniques and Applications*. Springer Science+Business Media, New York (2007).
- (112) Beaulieu, D.; Ding, Y.; Wang, Z. L.; Lackey, W. J., Influence of process variables on electron beam chemical vapor deposition of platinum. *J. Vac. Sci. Technol., B* **23** (2005), 2151.
- (113) Kohlmann-von Platen, K. T.; Buchmann, L. M.; Petzold, H. C.; Brünger, W. H., Electron-beam induced tungsten deposition: Growth rate enhancement and applications in microelectronics. *J. Vac. Sci. Technol., B* **10** (1992), 2690.
- (114) Lipp, S.; Frey, L.; Lehrer, C.; Frank, B.; Demm, E.; Pauthner, S.; Ryssel, H., Tetramethoxysilane as a precursor for focused ion beam and electron beam assisted insulator (SiO<sub>x</sub>) deposition. *J. Vac. Sci. Technol., B* **14** (1996), 3920.
- (115) *Agilent 33120A User's Guide*. Agilent Technologies, Inc., Loveland, CO (2002).
- (116) *SmartSEM Remote Protocol*. Carl Zeiss SMT, Oberkochen (2008).

- (117) *MSCU Technical Reference Manual Version 2.2*. Omicron Nanotechnology, Taunusstein (2006).
- (118) Buchner, F., *STM Investigation of Molecular Architectures of Porphyrinoids on a Ag(111) Surface*. Doctoral Thesis, Friedrich-Alexander Universität Erlangen-Nürnberg, Erlangen (2010).
- (119) Buchner, F.; Kellner, I.; Steinrück, H.-P.; Marbach, H., Modification of the Growth of Iron on Ag(111) by Predeposited Organic Monolayers. *Z. Phys. Chem. (Leipzig)* **223** (2009), 131.
- (120) Vollnhals, F.; Woolcot, T.; Walz, M.-M.; Seiler, S.; Steinrück, H.-P.; Thornton, G.; Marbach, H., Electron Beam-Induced Writing of Nanoscale Iron Wires on a Functional Metal Oxide. *J. Phys. Chem. C* **117** (2013), 17674.
- (121) Pang, C. L.; Lindsay, R.; Thornton, G., Chemical Reactions on Rutile TiO<sub>2</sub>(110). *Chem. Soc. Rev.* **37** (2008), 2328.
- (122) Humphrey, D. S.; Cabailh, G.; Pang, C. L.; Muryn, C. A.; Cavill, S. A.; Marchetto, H.; Potenza, A.; Dhesi, S. S.; Thornton, G., Self-Assembled Metallic Nanowires on a Dielectric Support: Pd on Rutile TiO<sub>2</sub>(110). *Nano Lett.* **9** (2009), 155.
- (123) Strukov, D. B.; Snider, G. S.; Stewart, D. R.; Williams, R. S., The Missing Memristor Found. *Nature* **453** (2008), 80.
- (124) Pang, C. L.; Bikondoa, O.; Humphrey, D. S.; Papageorgiou, A. C.; Cabailh, G.; Ithnin, R.; Chen, Q.; Muryn, C. A.; Onishi, H.; Thornton, G., Tailored TiO<sub>2</sub>(110) Surfaces and Their Reactivity. *Nanotechnology* **17** (2006), 5397.
- (125) Yim, C. M.; Pang, C. L.; Thornton, G., Oxygen Vacancy Origin of the Surface Band-Gap State of TiO<sub>2</sub>(110). *Phys. Rev. Lett.* **104** (2010), 036806.
- (126) Wang, L.-Q.; Baer, D. R.; Engelhard, M. H., Creation of variable concentrations of defects on TiO<sub>2</sub>(110) using low-density electron beams. *Surf. Sci.* **320** (1994), 295.
- (127) Zhang, Z.; Yates, J. T., Effect of Adsorbed Donor and Acceptor Molecules on Electron Stimulated Desorption: O<sub>2</sub>/TiO<sub>2</sub>(110). *J. Phys. Chem. Lett.* **1** (2010), 2185.
- (128) Schirmer, M.; Walz, M.-M.; Papp, C.; Kronast, F.; Gray, A. X.; Balke, B.; Cramm, S.; Fadley, C. S.; Steinrück, H.-P.; Marbach, H., Fabrication of Layered Nanostructures by Successive Electron Beam Induced Deposition with Two Precursors: Protective Capping of Metallic Iron Structures. *Nanotechnology* **22** (2011), 475304.
- (129) Plank, H.; Smith, D. A.; Haber, T.; Rack, P. D.; Hofer, F., Fundamental Proximity Effects in Focused Electron Beam Induced Deposition. *ACS Nano* **6** (2012), 286.

- 
- (130) Bikondoa, O.; Pang, C. L.; Ithnin, R.; Murn, C. A.; Onishi, H.; Thornton, G., Direct Visualization of Defect-Mediated Dissociation of Water on TiO<sub>2</sub>(110). *Nat. Mater.* **5** (2006), 189.
- (131) Dulub, O.; Batzilln, M.; Solovev, S.; Loginova, E.; Alchagirov, A.; Madey, T. E.; Diebold, U., Electron-Induced Oxygen Desorption from the TiO<sub>2</sub>(011)-2×1 Surface Leads to Self-Organized Vacancies. *Science* **317** (2007), 1052.
- (132) Nishigaki, S., Auger Electron Spectroscopy of TiO<sub>2</sub>: Inter- and Intra-Atomic Transitions Connected with the Valence Band. *Surf. Sci.* **125** (1983), 762.
- (133) Göpel, W.; Anderson, J. A.; Frankel, D.; Jaehnig, M.; Phillips, K.; Schäfer, J. A.; Rucker, G., Surface Defects of TiO<sub>2</sub>(110): A Combined XPS, XAES and ELS Study. *Surf. Sci.* **139** (1984), 333.
- (134) Sánchez-Sánchez, C.; González, C.; Jelinek, P.; Méndez, J.; de Andres, P. L.; Martín-Gago, J. A.; López, M. F., Understanding Atomic-Resolved STM Images on TiO<sub>2</sub>(110)-(1×1) Surface by DFT Calculations. *Nanotechnology* **21** (2010), 405702.
- (135) Vollnhals, F.; Wintrich, P.; Walz, M.-M.; Steinrück, H.-P.; Marbach, H., Electron Beam Induced Surface Activation of ultrathin porphyrin layers on Ag(111). *Langmuir* **29** (2013), 12290.
- (136) Love, J. C.; Estroff, L. A.; Kriebel, J. K.; Nuzzo, R. G.; Whitesides, G. M., Self-assembled monolayers of thiolates on metals as a form of nanotechnology. *Chem. Rev.* **105** (2005), 1103.
- (137) Ballav, N.; Shaporenko, A.; Terfort, A.; Zharnikov, M., A flexible approach to the fabrication of chemical gradients. *Adv. Mater.* **19** (2007), 998.
- (138) Eck, W.; Stadler, V.; Geyer, W.; Zharnikov, M.; Götzhäuser, A.; Grunze, M., Generation of surface amino groups on aromatic self-assembled monolayers by low energy electron beams - A first step towards chemical lithography. *Adv. Mater.* **12** (2000), 805.
- (139) Turchanin, A.; Götzhäuser, A., Carbon nanomembranes from self-assembled monolayers: Functional surfaces without bulk. *Prog. Surf. Sci.* **87** (2012), 108.
- (140) Zharnikov, M.; Grunze, M., Modification of thiol-derived self-assembling monolayers by electron and x-ray irradiation: Scientific and lithographic aspects. *J. Vac. Sci. Technol., B* **20** (2002), 1793.
- (141) Buchner, F.; Kellner, I.; Hieringer, W.; Görling, A.; Steinrück, H.-P.; Marbach, H., Ordering aspects and intramolecular conformation of tetraphenylporphyrins on Ag(111). *Phys. Chem. Chem. Phys.* **12** (2010), 13082.

- (142) Gottfried, J. M.; Marbach, H., Surface-Confined Coordination Chemistry with Porphyrins and Phthalocyanines: Aspects of Formation, Electronic Structure, and Reactivity. *Z. Phys. Chem. (Leipzig)* **223** (2009), 53.
- (143) Henderson, M. A.; Ramsier, R. D.; Yates, J. T., Low-Energy Electron Induced Decomposition of Fe(CO)<sub>5</sub> Absorbed on Ag(111). *Surf. Sci.* **259** (1991), 173.
- (144) Sato, S.; Ukisu, Y.; Ogawa, H.; Takasu, Y., Infrared Reflection-Absorption Spectroscopy, X-Ray Photoelectron-Spectroscopy and Temperature-Programmed Desorption Study on the Adsorption and Decomposition of Fe(CO)<sub>5</sub> over Silver Surfaces. *J. Chem. Soc., Faraday Trans.* **89** (1993), 4387.
- (145) Grundmann, M., Formation of epitaxial domains: Unified theory and survey of experimental results. *Phys. Status Solidi B* **248** (2011), 805.
- (146) Snyman, H. C.; Olsen, G. H., Application of Electron-Transparent (111) Silver Platelets as Substrates in Epitaxial Studies. *J. Appl. Phys.* **44** (1973), 889.
- (147) Olsen, G. H.; Snyman, H. C., Interfacial and Morphological Effects in Epitaxial-Growth of Iron on Silver. *Acta Metall.* **21** (1973), 769.
- (148) Buchner, F.; Flechtner, K.; Bai, Y.; Zillner, E.; Kellner, I.; Steinrück, H.-P.; Marbach, H.; Gottfried, J. M., Coordination of iron atoms by tetraphenylporphyrin monolayers and multilayers on Ag(111) and formation of iron-tetraphenylporphyrin. *J. Phys. Chem. C* **112** (2008), 15458.
- (149) Lukasczyk, T.; Flechtner, K.; Merte, L. R.; Jux, N.; Maier, F.; Gottfried, J. M.; Steinrück, H.-P., Interaction of cobalt(II) tetraarylporphyrins with a Ag(111) surface studied with photoelectron spectroscopy. *J. Phys. Chem. C* **111** (2007), 3090.
- (150) Beggan, J. P.; Krasnikov, S. A.; Sergeeva, N. N.; Senge, M. O.; Cafolla, A. A., Control of the axial coordination of a surface-confined manganese(III) porphyrin complex. *Nanotechnology* **23** (2012), 235606.
- (151) Silvers, S. J.; Tulinsky, A., The crystal and molecular structure of triclinic tetraphenylporphyrin. *J. Am. Chem. Soc.* **89** (1967), 3331.
- (152) Zhang, Z. J.; Verma, A. L.; Nakashima, K.; Yoneyama, M.; Iriyama, K.; Ozaki, Y., Substrate-dependent aggregation and energy transfer in Langmuir-Blodgett films of 5-(4-N-octadecylpyridyl)-10,15,20-tri-p-tolylporphyrin studied by ultraviolet-visible and fluorescence spectroscopies. *Langmuir* **13** (1997), 5726.
- (153) Turchanin, A.; Käfer, D.; El-Desawy, M.; Wöll, C.; Witte, G.; Götzhäuser, A., Molecular Mechanisms of Electron-Induced Cross-Linking in Aromatic SAMs. *Langmuir* **25** (2009), 7342.

- 
- (154) Feil, S.; Winkler, M.; Sulzer, P.; Ptasinska, S.; Denifl, S.; Zappa, F.; Krautler, B.; Mark, T. D.; Scheier, P., Single, double and triple ionization of tetraphenyl iron(III) porphyrin chloride. *Int. J. Mass Spectrom.* **255** (2006), 232.
- (155) Arumainayagam, C. R.; Lee, H. L.; Nelson, R. B.; Haines, D. R.; Gunawardane, R. P., Low-energy electron-induced reactions in condensed matter. *Surf. Sci. Rep.* **65** (2010), 1.
- (156) Sanche, L., Low energy electron-driven damage in biomolecules. *Eur. Phys. J. D* **35** (2005), 367.
- (157) Elschenbroich, C., *Organometallicchemie*. 6th ed.; B. G. Teubner Verlag / GWV Fachverlage, Wiesbaden (2008).
- (158) Lane, K. R.; Sallans, L.; Squires, R. R., Gas-Phase Nucleophilic-Addition Reactions of Negative-Ions with Transition-Metal Carbonyls. *J. Am. Chem. Soc.* **108** (1986), 4368.
- (159) Vollnhals, F.; Drost, M.; Tu, F.; Carrasco, E.; Späth, A.; Fink, R. H.; Steinrück, H.-P.; Marbach, H., Electron-beam induced deposition and autocatalytic decomposition of  $\text{Co}(\text{CO})_3\text{NO}$ . *Beilstein J. Nanotechnol.* **5** (2014), 1175.
- (160) Gazzadi, G. C.; Mulders, H.; Trompenaars, P.; Ghirri, A.; Affronte, M.; Grillo, V.; Frabboni, S., Focused Electron Beam Deposition of Nanowires from Cobalt Tricarbonyl Nitrosyl ( $\text{Co}(\text{CO})_3\text{NO}$ ) Precursor. *J. Phys. Chem. C* **115** (2011), 19606.
- (161) Gazzadi, G. C.; Mulders, J. J. L.; Trompenaars, P.; Ghirri, A.; Rota, A.; Affronte, M.; Frabboni, S., Characterization of a new cobalt precursor for focused beam deposition of magnetic nanostructures. *Microelectron. Eng.* **88** (2011), 1955.
- (162) Ade, H.; Hitchcock, A. P., NEXAFS microscopy and resonant scattering: Composition and orientation probed in real and reciprocal space. *Polymer* **49** (2008), 643.
- (163) Zheng, F.; Alayoglu, S.; Guo, J.; Pushkarev, V.; Li, Y.; Glans, P.-A.; Chen, J.-I.; Somorjai, G., In-situ X-ray Absorption Study of Evolution of Oxidation States and Structure of Cobalt in Co and CoPt Bimetallic Nanoparticles (4 nm) under Reducing ( $\text{H}_2$ ) and Oxidizing ( $\text{O}_2$ ) Environments. *Nano Lett.* **11** (2011), 847.
- (164) Kobayashi, M.; Hidai, S.; Niwa, H.; Harada, Y.; Oshima, M.; Horikawa, Y.; Tokushima, T.; Shin, S.; Nakamori, Y.; Aoki, T., Co oxidation accompanied by degradation of Pt-Co alloy cathode catalysts in polymer electrolyte fuel cells. *Phys. Chem. Chem. Phys.* **11** (2009), 8226.
- (165) Morales, F.; de Groot, F. M. F.; Glatzel, P.; Kleimenov, E.; Bluhm, H.; Hävecker, M.; Knop-Gericke, A.; Weckhuysen, B. M., In Situ X-ray Absorption of Co/Mn/TiO<sub>2</sub> Catalysts for Fischer-Tropsch Synthesis. *J. Phys. Chem. B* **108** (2004), 16201.

- (166) Chantler, C. T.; Olsen, K.; Dragoset, R. A.; Chang, J.; Kishore, A. R.; Kotochigova, S. A.; Zucker, D. S. X-Ray Form Factor, Attenuation and Scattering Tables (version 2.1). [Online]. <http://physics.nist.gov/ffast> (Monday, 13-Jan-2014 11:34:29 EST),
- (167) Chantler, C. T., Detailed tabulation of atomic form factors, photoelectric absorption and scattering cross section, and mass attenuation coefficients in the vicinity of absorption edges in the soft X-ray ( $Z = 30-36$ ,  $Z = 60-89$ ,  $E = 0.1-10$  keV) - addressing convergence issues of earlier work. *J. Synchrotron Radiat.* **8** (2001), 1124.
- (168) Chantler, C. T., Theoretical Form Factor, Attenuation, and Scattering Tabulation for  $Z=1-92$  from  $E=1-10$  eV to  $E=0.4-1.0$  MeV. *J. Phys. Chem. Ref. Data* **24** (1995), 71.
- (169) Fernández-Pacheco, A.; Serrano-Ramón, L. E.; Tyliczszak, T.; Chou, K. W.; Córdoba, R.; Szkudlarek, A.; Brien, L. O.; Cz, K.; Ibarra, M. R.; Teresa, J. M. D., Correlation between the magnetic imaging of cobalt nanoconstrictions and their magnetoresistance response. *Nanotechnology* **23** (2012), 105703.
- (170) Fernández-Pacheco, A.; Teresa, J. M. D.; Szkudlarek, A.; Córdoba, R.; Ibarra, M. R.; Petit, D.; O'Brien, L.; Zeng, H. T.; Lewis, E. R.; Read, D. E.; Cowburn, R. P., Magnetization reversal in individual cobalt micro- and nanowires grown by focused-electron-beam-induced-deposition. *Nanotechnology* **20** (2009), 475704.
- (171) Lau, Y. M.; Chee, P. C.; Thong, J. T. L.; Ng, V., Properties and applications of cobalt-based material produced by electron-beam-induced deposition. *J. Vac. Sci. Technol., A* **20** (2002), 1295.
- (172) Nikulina, E.; Idigoras, O.; Vavassori, P.; Chuvilin, A.; Berger, A., Magneto-optical magnetometry of individual 30 nm cobalt nanowires grown by electron beam induced deposition. *Appl. Phys. Lett.* **100** (2012),
- (173) Utke, I.; Michler, J.; Gasser, P.; Santschi, C.; Laub, D.; Cantoni, M.; Buffat, P. t. A.; Jiao, C.; Hoffmann, P., Cross Section Investigations of Compositions and Sub-Structures of Tips Obtained by Focused Electron Beam Induced Deposition. *Adv. Eng. Mater.* **7** (2005), 323.
- (174) Córdoba, R.; Sesé, J.; De Teresa, J. M.; Ibarra, M. R., High-purity cobalt nanostructures grown by focused-electron-beam-induced deposition at low current. *Microelectron. Eng.* **87** (2010), 1550.
- (175) Rao, K. M.; Spoto, G.; Guglielminotti, E.; Zecchina, A., Spectroscopic investigation of the interaction of  $\text{Co}_2(\text{CO})_8$  with  $\text{MgO}$  and  $\text{SiO}_2$ . *J. Chem. Soc., Faraday Trans. 1* **84** (1988), 2195.
- (176) Tannenbaum, R., Polymer Matrix Influence on the Kinetics of Some Fundamental Inorganic Colloidal Reactions. *Langmuir* **13** (1997), 5056.
- (177) Yu, S.-H.; Moraes, K.; Ganguli, S.; Chung, H.; Phan, S.-E.; Selective Cobalt Deposition on Copper Surfaces. World patent WO 2009/134840 A3 (2009).

- 
- (178) Henderson, M. A.; Ramsier, R. D.; Yates, J. T., Minimizing Ultrahigh-Vacuum Wall Reactions of Fe(CO)<sub>5</sub> by Chemical Pretreatment of the Dosing System. *J. Vac. Sci. Technol., A* **9** (1991), 2785.
- (179) Klingenberger, D.; Huth, M., Modular ultrahigh vacuum-compatible gas-injection system with an adjustable gas flow for focused particle beam-induced deposition. *J. Vac. Sci. Technol., A* **27** (2009), 1204.
- (180) *Pressure Gauge Controller Models PGC2 and PGC2D User Manual Issue 1.2*. Arun Microelectronics Ltd., Arundel (1991).
- (181) *Pressure Gauge Controller Model NGC2 User Manual Issue 2.2*. Arun Microelectronics Ltd., Arundel (2009).



## Appendix A – Communication Protocols

### RemCON32 – Carl Zeiss SMT

RemCON32 is a RS-232 terminal server application that provides remote access to the SmartSEM software via a command line interface. The default COM settings are 9600 bps, 8 data/ 1 stop bits, parity/flow control off. The commands are sent in ASCII format with <CR> termination. RemCON32 will return an acknowledge receipt (“@”+<CR> for valid, “#”+<CR> for invalid commands), followed by a completion indicator (“>”+<CR> for successful, “\*”+<CR> for unsuccessful completion).

For full description, refer to the user manual.<sup>116</sup>

<b>Command</b>	<b>Function</b>
EDX1/EDX0	External scan enable/disable
BBLK1/BBLK0	Beam blanking on/off (only in internal scan mode, EDX0)
MAG?	Request magnification
MAG <i>r</i>	Set magnification <i>r</i> ( <i>r</i> as REAL, e.g. “3472.3”)
PIX?	Request pixel size in nm

## NGC2/PGC2 Pressure Gauge Controllers – Arun Microelectronics

The pressure in the preparation and analysis chamber is monitored by ionization pressure gauges, which are controlled by the NGC2 (preparation chamber) and PGC2D (analysis chamber) ion gauge controllers (Arun Microelectronics Ltd.). The pressure can be read digitally using RS-232 connections. Unfortunately, the controllers offer very different serial interface structures.

**The PGC2D controller** transmits a 106 byte wide status report once per second at 2400 bps, 1 start bit, 2 stop bits and no parity/handshaking, ASCII characters only. The following table contains an excerpt of the transmitted information in such a report.

For a full documentation see user manual.<sup>180</sup>

Byte	Content	Comment
1-4	“:...”	Report start
5-11, 12-18, 19-25, 26-32	Four pressure data points of last second	Scientific notation, e.g. “9.2-10”
54	Status	Pressure only valid if “E” (emission)
58	Fault	“ “: no error
102, 103	Checksum	
104-106	ASCII 13,10,0	Report end, <CR><LF><NUL>

*Appendix table A: PGC2D ion gauge controller serial interface excerpt.*

The **NGC2 controller** requires polling of status reports through a connection using 9600 bps, 8 data bits, 1 stop bit, and no parity/handshaking. To request a status report, the command \*S0 is transmitted (max. 10 requests per second). The controller replies with a report containing a “state byte”, an “error byte”, a “relay status byte” (state of the interlock relays), an unused byte followed by 13-byte wide reports *for every installed gauge* including the Pirani gauges etc. The structure of a gauge report is given in the following table. If the subsequent byte after byte 13 of a report is “G”, another gauge report follows. After the individual gauge reports a “units byte” (“M”: mbar; “T”: torr; “P”: Pa), an unused byte and <CR><LF> are added to conclude the status report.

For a full documentation see user manual.<sup>181</sup>

Byte	Content	Comment
1	Header	“G”: indicates (another) 13 byte gauge report
2	Gauge type	“T”: ion gauge (“P”/“M”: Pirani/other)
3	Gauge number	“1”: ion gauge
4	Gauge status	[10000010]: Emission, Filament 1 [10000110]: Emission, Filament 2
5	Gauge error	[00000010]: No error
6-13	Pressure	Scientific notation + <b>comma</b> , e.g. “1.5E-09,”

**Appendix table B:** NGC2 ion gauge controller gauge status report.

### MSCU Piezo stage controller, Omicron Nanotechnology

The movement of the piezo stage can also be controlled via the RS-232 connection. In contrast to the previous interface protocols, the actual command structure is not disclosed. Instead, software libraries (.dll, .lib) are provided for communication purposes. These can be accessed in LabVIEW through special subVIs, which link the respective functions to icons on the block diagram of a VI.

All control functions are of type “INT”, i.e. they return integer values when called. In all cases, a return value of -1 indicates a transmission error. In the following, the some of the available commands are briefly discussed, starting with the communication control functions.

Function	Comment
<i>configcom</i> (int Comport)	Open serial interface on the respective COM port
<i>exitcom</i> (int Comport)	Close serial interface on the respective COM port
<i>getversion</i> (int Comport)	Returns an version number
<i>readbuffer</i> (int Comport)	Returns executions messages from buffer
<i>geterror</i> (int Comport)	Returns an error code (transmission errors only)
<i>getstatus</i> (int Comport)	Returns MSCU status; 0 = no error, 1 = powered down, ...

*Appendix table C: Communication control commands.*

The control commands functions are assigned a (positive) command number. These numbers are contained in the buffer that is read by *readbuffer* (int Comport). Positive numbers indicated execution, while negative numbers indicate that the command was not executed.

Function	#Hex	Comment
<i>setvoltage</i> (int Comport, Voltage)	0x12 (18 <sub>10</sub> )	Set output voltage, 80 to 400 V
<i>setfrequency</i> (int Comport, Frequency)	0x13 (19 <sub>10</sub> )	Set repetition frequency, 50 to 4000 Hz
<i>standby</i> (int Comport, Mode)	0x14 (20 <sub>10</sub> )	Mode 1: enter standby Mode 0: exit standby

continued on next page

table continued

<b>Function</b>	<b>#Hex</b>	<b>Comment</b>
<b><i>singlestep</i></b> (int Comport, Channel, Direction)	0x10 (16 <sub>10</sub> )	Do one step on axis “Channel”, e.g. 1 = x-axis Direction: 1 = forward, -1 = backward
<b><i>dosteps</i></b> (int Comport, Channel, Direction, Steps)	0x11 (17 <sub>10</sub> )	As <b><i>singlestep</i></b> Steps 1 to 32767: perform number of steps Steps -1: perform continuous steps Steps 0: stop moving

**Appendix table D:** MSCU control commands.

The program should be structured in a way that after a control command has been issued, the *readbuffer* function should be polled until successful execution is indicated, i.e. the positive command number is received. Only when this is the case should the next control command be issued.

The detailed description of the RS-232 interface to the MSCU can be found in the respective manual.<sup>117</sup>

## Appendix B – List of Figures

- Figure 2-1: Electron beam induced deposition (EBID) and electron beam induced surface activation (EBISA) processes in comparison. Starting from a clean sample (a) in EBID the surface is irradiated while precursor is supplied (b), leading to the e-beam induced decomposition into volatile fragments and a nonvolatile primary deposit (e). The EBISA process involves an irradiation step under vacuum conditions (c) followed by precursor dosage and surface mediated deposition (d) of a primary deposit (e). In both cases, the primary deposit may grow autocatalytically if further precursor is supplied (f) to form the final deposit (g).....5
- Figure 2-2: Examples of the autocatalytic growth observed for EBID lines prepared from  $\text{Fe}(\text{CO})_5$  on  $\text{SiO}_x(300 \text{ nm})/\text{Si}$  (A) and first published results of successful EBISA and autocatalytic growth on the same system (B). The SEM series A:a-g and A:h-j show EBID lines prepared with two different electron doses and increasing autocatalytic growth times (as indicated). The series B:a-f consists of EBISA lines prepared with increasing PE doses after identical growth times of 270 min. Figures reprinted from Walz et al.<sup>5</sup>..... 10
- Figure 2-3: Most stable structures of  $[\text{Co}_2(\text{CO})_8]$  on fully hydroxylated (a) and partially hydroxylated (b)  $\text{SiO}_2$ , reprinted from Muthukumar et al.<sup>15</sup> The  $\text{Co}_2(\text{CO})_8$  precursor shows only minor interactions with the fully hydroxylated silica (a), but undergoes dissociation into two surface bound  $\text{Co}(\text{CO})_4$  fragments on the partially hydroxylated surface..... 12
- Figure 3-1: Topography contrast in SEM. The top scheme is a cross section of a surface with a flat section (left), a trench, a protruding edge and a rough section (right), while the bottom one represents a schematic graph of the expected image intensity. The electron emission, represented by the black arrows, differs from one surface structure to the other solely due to the topography.....20
- Figure 3-2: One dimensional metal-vacuum-metal tunneling junction (modified from ref 76). The bias voltage  $U$  offsets tip and sample Fermi level by  $\Delta E = eU_T$  with  $eU_T$  being much smaller than the work function  $\Phi$ .....23
- Figure 3-3: Schematic setup of a zone plate based STXM. Reprinted from ref. 85. ....25
- Figure 4-1: Photographs of the preparation chamber with labeled main components. Reprinted from ref. <sup>95</sup>.....31
- Figure 4-2: Photographs of the analysis chamber with labeled main components. Reprinted from ref. <sup>95</sup>.....32
- Figure 4-3: Schematic of the Gemini electron column as used in the MULTILAB system. The electron source is a Schottky type field-enhanced thermionic emitter. The electrons are extracted by an extractor voltage and accelerated to the final energy by the anode (top section). The beam booster adds 8 keV during the transition through the lens system only and acts as an attractive potential for the emitted SEs and BSE to the inlens-detector (“Annular SE-detector”). The beam is focused by a combination of magnetic and electrostatic lenses and feed through the column in a crossover-free trajectory. The deflection of the electron beam is realized via scan coils. Reprinted from ref. <sup>96</sup>.....33
- Figure 4-4: Photograph of the stage assembly of the MULTISCAN STM (a) and schemes of the scanner (b) and coarse drive geometry (c). The main components are indicated. The Y-shaped piezo scanner is comprised of individual piezos for in-plane movement (x/y) that form the arms of the Y while the z-piezo is directly attached to the scanner head that holds the tip assembly. The coarse drive is realized in an  $r, \phi$  geometry (c) using piezo motors as well. Tips assemblies can be exchanged without breaking the vacuum. Photograph and schemes modified from ref. <sup>97</sup>..... 34
- Figure 4-5: Technical drawing (a) and examples (b-d) of sample plates. b) Ta sample plate without specimen, for high temperatures; c) Stainless steel sample plate with windows, used for mounting standard 3 mm TEM samples, e.g.  $\text{Si}_3\text{N}_4$  membrane; d) Sample plate with MgO specimen, mounted by spot-welding it in place using of a support foil. ....35
- Figure 4-6: VT sample holder with integrated filament for heating via electron bombardment: (a) assembled sample holder with  $\text{TiO}_2(110)$  specimen, (b) side view, (c) filament level, (d) contacts. ....37

- Figure 4-7: Photographs of the PoLux beamline at the Swiss Light Source. Left: overview; right: X-ray focusing, sample stage and detector setup, including schematic. .... 38
- Figure 4-8: LEED pattern of a rutile  $\text{TiO}_2(110)$ - $1 \times 1$  surface at an electron energy of 54 eV. The samples was prepared by several (>10) cycles of sputtering and annealing as described above. .... 39
- Figure 4-9: Schematic view of the wire loop setup for electrochemical etching of STM tips from tungsten wire. Reprinted from ref. <sup>104</sup> ..... 41
- Figure 4-10: SE micrographs of an STM tip at increasing magnification. The tip was prepared by electrochemical etching of a tungsten wire using 2 mol/l KOH solution in a two-step rough/fine etching procedure. See text for details. .... 42
- Figure 4-11: Mass spectrum of  $\text{Fe}(\text{CO})_5$  recorded in the gas dosing chamber at a pressure of  $3 \times 10^{-7}$  mbar. Fragment species are indicated for the most prominent m/z features. The natural isotope pattern of iron ( $^{54}\text{Fe}$  ~6%,  $^{56}\text{Fe}$  ~92%,  $^{57}\text{Fe}$  ~2%) is responsible for the peak triplet observed for Fe-containing fragments. .... 43
- Figure 4-12: Mass spectrum of  $\text{Co}(\text{CO})_3\text{NO}$  recorded in the gas dosing chamber at a pressure of  $3 \times 10^{-7}$  mbar. Likely fragment species are indicated for the most prominent m/z features. .... 44
- Figure 4-13: Mass spectrum (log scale) of  $\text{Co}_2(\text{CO})_8$  recorded in the gas dosing chamber at a pressure of  $3 \times 10^{-7}$  mbar. The separations between the peaks correspond to missing atoms or groups of atoms and are indicated by blue (CO), yellow (O) and green (C) markers. .... 45
- Figure 4-14: Setup for the vacuum recrystallization of  $\text{Co}_2(\text{CO})_8$ . The feedstock of  $\text{Co}_2(\text{CO})_8$  is carefully degassed to remove the stabilizing agent (hexane) and slowly heated up to about 35 °C under vacuum. An ice bath is added to the outside of the reaction vessel further up the gas stream. In the course of about 30 min, red  $\text{Co}_2(\text{CO})_8$  crystals are formed at the cool sections. .... 46
- Figure 5-1: Schematic of the internal and external connections of the SEM control electronics used in signal generation. The digital interface (top right) connects to interface card of a PC running the SEM applications (SmartSEM, RemCon32) and supplies configuration data to the internal DACs, which supply the patterns during standard operation. The analog inputs for beam x- and y-deflection accept  $\pm 10$  V input signals via standard BNC connectors. Either type of signal is converted to the appropriate current for driving the magnetic scan coils by the analog scan board. .... 51
- Figure 5-2: Reference systems for the beam position. a) SmartSEM and beam field of view (FOV) in real space coordinates (x|y); b) Proportional deflection and corresponding DC signal ( $U_x|U_y$ ); c) Binary representation (i|k) with n being the bit resolution of the DAC. The binary grid defines all positions on the surface the beam can target without further signal processing. .... 53
- Figure 5-3: Examples of lithographic EBI deposits using the SEM software. (a) Au(111) single crystal surface with a conspicuous crystallite that was decorated with an S-shaped feature by dragging the spot exposure marker manual along the desired path, creating a carbonaceous deposit from residual gases. (b)  $\text{TiC}_x\text{O}_y$  structures by EBID of titanium tetraisopropoxide (TTIP) using the spot, line and image mode of SmartSEM. The blue and green circles and ellipses highlight artifacts (unintended deposits) due to the peculiarities of the scan modes. The red circles mark spot exposures. Reproduced from Schirmer <sup>95</sup> ..... 55
- Figure 5-4: EBI deposits fabricated using Elphy Quantum with artifacts due to missing beam blanker. (a) Fe patterns from  $\text{Fe}(\text{CO})_5$  on Si(100) at 200 K. The white arrow marks the deposit at parking position of the electron beam that is irradiated between end of exposure and the manual beam blank. (b) Complex EBID Fe logo from  $\text{Fe}(\text{CO})_5$  on 0.7 nm  $\text{SiO}_x/\text{Si}(100)$  produced by repeatedly exposing the same structure 1000 times. The white arrow marks one of several circular artifacts due to the stationary, unblanked beam during the data processing of further elements of the pattern. .... 57
- Figure 5-5: Examples of EBI deposits exposed using two HP 33120A arbitrary waveform generators. Left: 2D shape, multi-sweep exposure, TTIP on Si(100); right: multi-sweep line exposures, IPC on 300 nm  $\text{SiO}_x/\text{Si}$ . The image on the left shows a test logo that uses half of the available memory of the AWGs. All lines are single-pixel wide. The artifacts (arrow) are attributed to synchronization issues of the x- and y-ARB. The sweep frequency is 50 Hz with a pixel dwell time of 5.6  $\mu\text{s}$ . The micrograph on the right contains an array of 45  $\mu\text{m}$  wide lines with 625 Hz repetition frequency. The dark areas at the start and end of every line are the

result of intentional, predefined beam parking at those positions. The line segments in the middle remain unaffected by the parking artifacts. ....	59
Figure 5-6: Connection diagram of the NanoScribbler system. RS-232 connections are available for pressure readout of the ion gauge controllers (PGC2/NGC2, Arun Microelectronics Ltd.), for stage control via the Matrix CU, and for SEM control via the RemCON32 server running on the SEM PC. The latter is connected to the SEM electronics via a proprietary interface using a standard SCSI cable. The control voltage connection $U_{DC}$ comprises two separate coax cables (BNC on SEM electronics, SMB on DAC side). ....	61
Figure 5-7: NanoScribbler main window. All lithography tools are accessible from this screen. ....	62
Figure 5-8: Data structures and timeline for exposures with inactive (a) and active oversampling (b, c). Colors indicate identical coordinates. If oversampling is not activated, the dwell time $t_d$ , i.e. the time during which the beam is stationary at (i k), is equal to the sample time $t_s$ . In the case of active oversampling (b, c), identical (i k) values are output for a number of consecutive samples. The sampling frequency is adjusted so that the dwell time is an integer multiple of the sample time (i.e. $t_d = n \times t_s$ ). The multiplier $n$ is referred to as oversampling factor (OSF). Both case a) and b) will yield identical output patterns for different sampling rates, as in both cases $t_d = n \times t_s = 1$ ms. The third case (c) corresponds to the standard use of oversampling: synthesizing dwell times that are incompatible with the DAC board. A $t_d$ of 0.8 ms requires $f_s = 1.25$ kHz, which cannot be selected. Instead, $t_d$ is broken down into four valid $t_s$ -steps of 0.2 ms ( $f_s = 5$ kHz, $t_d = 4 \times t_s = 0.8$ ms) to avoid invalid sampling rates. See text for more detail. ....	66
Figure 5-9: GUI of the Rechteck (“rectangle”) tool. Top left: system parameter collection; top right: position and parameter setup; bottom left: output pattern information. ....	68
Figure 5-10: Standard path (a) and meander path (b) exposure. Full lines represent the active exposure path, while dashed lines show the beam repositioning between subsequent lines. ....	69
Figure 5-11: Exposure GUI. The info box on the left displays a number of details of the currently active pattern if provided by the respective tool. The exposure details box shows the card setup parameters sample rate, loop count and sample count. The options box provides advanced features like SEM control disable (“Work offline”). The status bar displays current status of the DAC. ....	72
Figure 5-12: Line splitting of 45 $\mu\text{m}$ multisweep line exposures on 300 nm $\text{SiO}_x/\text{Si}$ . The micrographs a)-f) show splitting of the multisweep lines for different compensations ( $b=0$ ). The correlation between compensation amplitude and observed line splitting is presented in the graph (h); corresponding images are indicated. The beam positions for the line (x-input) and compensation (y-input) during a sweep the scheme (i). The duration of a single sweep without waiting time was 500 $\mu\text{s}$ , which corresponds to a beam speed of 0.09 m/s. ....	74
Figure 5-13: Beam stability test using a pixel map to fabricate a square outline (1 $\mu\text{m} \times 1 \mu\text{m}$ ). All shapes are irradiated with the same total electron dose, but different dwell times per sweep and sweep counts, as indicated in the images. The pattern is exposed in sequential lines, i.e. the top bar is exposed first, followed by quick jumps from the left to the right vertical line and vice versa until the bottom line is reached. Images d)-f) show that the beam is not able to follow the jumping pattern for per sweep dwell times in the range of 10 $\mu\text{s}$ . The shapes in e) and f) are the result of very fast beam deflection inputs which cannot be followed by the electromagnetic scan system. ....	76
Figure 5-14: Beam stability test using a vector path to fabricate a square outline (1 $\mu\text{m} \times 1 \mu\text{m}$ ). All shapes are irradiated with the same total electron dose, but different dwell times per sweep and sweep counts, as indicated in the images. The pattern is exposed in a continuous path, i.e. the top line is exposed first, followed by the right vertical line top to bottom and so forth. Image f) shows that the beam is not able to follow the vector path for per sweep dwell times in the range of 100 ns. The distorted shape in f) is the result of very fast beam deflection inputs which cannot be followed by the electromagnetic scan system. ....	77
Figure 5-15: Graphical user interface of the stage position readout VI. The current position is displayed in the large text boxes (x/y position). The buttons on the respective right set current position to 0.0 (“Zero”) or to an arbitrary value (“Set” and input box). The vertical bar on the right indicates the current movement speed for manual stage translation using the joystick (see text). The controls on the bottom enable the MATRIX connection via RS-232, the control via the joystick and the software-controlled stage movement (“Automove”). See text for details. ....	79

- Figure 6-1: Line (a-d) and  $2 \times 2 \mu\text{m}^2$  square deposits (e-h) fabricated by EBISA on  $\text{TiO}_2(110)$  using  $\text{Fe}(\text{CO})_5$  as a precursor (approx.  $1.1 \times 10^5$  L). Primary electron doses are indicated on the top right. The line width (FWHM, SEM intensity) increases with PE dose and range from approx. 150 nm (a) to 2.6  $\mu\text{m}$  (d). The central line is a result of activation by PEs, while the fringe is caused by BSE proximity effects. For the square fields, deposit density increases from a loose grain assembly at 0.27 C/cm<sup>2</sup> via a close-packed assembly at 0.55 C/cm<sup>2</sup> to a fused-grain deposit of near-ideal geometry at 1.1 C/cm<sup>2</sup>. At even higher doses proximity effects also cause a fringe growth (3.3 C/cm<sup>2</sup>). Note that scattered iron clusters are found all over the surface without electron exposure, which is attributed to active defects created during sample preparation. .... 87
- Figure 6-2: Local Auger Electron Spectroscopy recorded on the circular structure shown in the inset. The structure was prepared by EBISA and subsequent dosage of 270 min ( $\sim 1.1 \times 10^5$  L) of  $\text{Fe}(\text{CO})_5$ . Evaluation of the peak areas shows a content of >90%at. Fe, <7 %at. O and <3 %at. C. The thickness of the iron structure is estimated to be around 50 nm based on typical growth rates. Substrate-related Ti features are completely attenuated. .... 88
- Figure 6-3: Non-irradiated surface of  $\text{TiO}_2(110)$  after dosage of 270 min ( $\sim 1.1 \times 10^5$  L) of  $\text{Fe}(\text{CO})_5$ . The bright features correspond to Fe crystallites, which nucleate at intrinsic defect sites on the surface and grow autocatalytically while  $\text{Fe}(\text{CO})_5$  is supplied. .... 89
- Figure 6-4: (a) AE spectra of pristine (red) and electron irradiated, reduced  $\text{TiO}_2$  samples in non-derivative mode. The loss of oxygen KLL intensity is a clear indication of oxygen loss, i.e. ESD, while the intensity shift of the titanium LMV peak from lower to higher kinetic energy is an indication of a shift from fully oxidized  $\text{Ti}^{4+}$  towards more reduced states like  $\text{Ti}^{3+}$  or even lower. The gradual shift of the peak shape with increasing electron dose is shown in (b), top to bottom. (c) Quantitative evaluation of the normalized  $\text{Ti}_{\text{LMM}}$  (blue) and  $\text{O}_{\text{KLL}}$  peak areas and apparent O:Ti ratio (green) versus applied electron dose. The apparent O:Ti ratio (green) is set to 2:1 ( $\text{TiO}_2$ ) for very low electron doses, i.e. a pristine substrate. Electron stimulated desorption causes a loss of oxygen atoms, i.e. signal intensity, which simultaneously leads to an increase in the relative intensity of the  $\text{Ti}_{\text{LMM}}$  signal. .... 90
- Figure 6-5: High resolution ST micrograph ( $I = 280$  pA,  $U = 1.2$  V, moderately high pass filtered) of an e-beam line irradiation ( $50 \mu\text{C}/\text{cm}$ ), marked by the large arrow and yellow lines. The surface on the left shows only minor damage; the typical row pattern of the  $\text{TiO}_2(110)$  surface is preserved. Defects include ( $1 \times 2$ ) reconstructed sections (small arrows), dark defects in the row structure and isolated protrusions. On the right, a disordered section running top to bottom was identified as the result of a line irradiation with a primary electron dose of  $50 \mu\text{C}/\text{cm}$ . The ( $1 \times 1$ ) structure is barely retained in the highly damaged area; no characteristic defects can be identified in the irradiated area. The loss of long and short range order corresponds to an electron induced surface amorphisation. .... 92
- Figure 6-6: SEM scan (a) and STM topography (b) of the  $\text{TiO}_2(110)$  surface after line irradiation with  $50 \mu\text{C}/\text{cm}$  and after initial Fe growth from  $\text{Fe}(\text{CO})_5$  (c). The line position is indicated by yellow markers. The strongly contrast enhanced scanning electron micrograph (a) shows a dark feature at the position of the line irradiation, conventionally attributed to carbon deposition from residual gases. STM reveals a high degree of disorder at the line position, while the surrounding surface remains fairly unaffected by the irradiation. Upon exposure to about 10 L of  $\text{Fe}(\text{CO})_5$ , clusters form predominantly at the irradiated surface area (c). Cluster formation next to the line exposures is attributed to defects induced by backscattered electrons, i.e. common proximity effects. .... 93
- Figure 6-7: STM images of a line exposure (right part of the images, marked by black lines) imaged before (a) and after  $\text{Fe}(\text{CO})_5$  dosage (b). White circles in (a) mark the location of corresponding deposits in (b); the inset shows the apparent height profile of the top right Fe cluster marked by the orange arrow. The image shows the known, striped rutile surface with the parallel rows running in [001] direction (top to bottom). The identification of single defects is not possible for the irradiated line structure due to the pronounced disorder. The more intact region on the left shows some isolated bright and dark spots which could be attributed to missing O or OH defects produced by scattering processes, i.e. proximity effects. .... 95
- Figure 6-8: (a) SE micrograph and high magnification image (inset) of the iron layer on the non-irradiated  $\text{Ag}(111)$  surface after dosage of approx.  $\sim 1.1 \times 10^5$  L of  $\text{Fe}(\text{CO})_5$ , and (b) the corresponding Auger electron spectrum. Fe forms needle-like structures, oriented with angles of  $120^\circ$  with respect to each other. The observed features correspond to the known growth mode of Fe on  $\text{Ag}(111)$ . The Auger spectrum shows

- pronounced  $\text{Fe}_{\text{LMM}}$  peaks and a small  $\text{O}_{\text{KLL}}$  contribution ( $< 8 \text{ \%at.}$ ), while the  $\text{C}_{\text{KLL}}$  signal is below the detection limit. The Ag substrate signal is completely damped by the Fe layer. .... 100
- Figure 6-9: (a) STM image ( $U = +1 \text{ V}$ ,  $I = 50 \text{ pA}$ ) of a 2HTPP monolayer on Ag(111); arrows indicate orientations of the square domains. (b) LEED pattern of closed layer of 2HTPP molecules on Ag(111) recorded at  $E = 15.0 \text{ eV}$ . The inset shows a simulated pattern for the  $(1.46, 5.44 | 5.44, 1.46)$  superstructure with color-coded rotational domains. .... 101
- Figure 6-10: SE micrographs of monolayer (a), partial bilayer (b) and multilayer (c) films of 2HTPP and Auger line scan data of the BiL film (d). The monolayer (a) appears as featureless grey area, while the bilayer (b) exhibits a bimodal distribution of greyscales. The Auger data (d) shows that the dark areas correspond to higher carbon intensity (black curve) and significant damping of the Ag signals (red curve). The inverse situation is observed for the bright areas. The dark areas can therefore be identified as second-layer islands of TPP molecules on the first layer (bright). The multimodal appearance of multilayer (c) is attributed to different 2HTPP layer thicknesses on the respective terraces. Note that the contrast of the SEM images was adjusted for visibility such that the grayscale intensities are not directly comparable between images. .... 103
- Figure 6-11: Dot (top row, a-c) and line deposits (bottom row, d-f) prepared by EBID on monolayer (MonoL: a, d), partial bilayer (BiL: b, e) and multilayer (MultiL: c,f) 2HTPP films on Ag(111). The electron dose was 48 nC for the dots and  $8 \mu\text{C/cm}$  for the line structures ( $E = 15 \text{ keV}$ ,  $I = 400 \text{ pA}$ ), while the precursor dose after EBID was approx.  $1.0 \times 10^5 \text{ L}$  for the dots and  $0.95 \times 10^5 \text{ L}$  for the lines. The insets contain higher magnifications of the respective structures. For a given electron dose, reduced structure growth can be observed on the MonoL compared to BiL and MultiL. The appearance of individual clusters on the MonoL surface (a, d) is attributed to incomplete coverage of the reactive silver sites, e.g. step edges, by the porphyrin film. .... 105
- Figure 6-12: Dot (top row, a-c) and line deposits (bottom row, d-f) prepared by EBISA on monolayer (MonoL: a, d), partial bilayer (BiL: b, e) and multilayer (MultiL: c,f) 2HTPP films on Ag(111). The electron dose was 48 nC for the dots and  $8 \mu\text{C/cm}$  for the line structures ( $E = 15 \text{ keV}$ ,  $I = 400 \text{ pA}$ ), while the precursor dose after the surface irradiation was approx.  $1.1 \times 10^5 \text{ L}$  for all structures. The insets contain higher magnifications of the respective structures. For a given electron dose, reduced structure growth can be observed on the MonoL compared to BiL and MultiL. In image (e) structure growth is only observed on the dark, bilayer covered islands. The appearance of individual clusters on the MonoL surface (a, d) is attributed to incomplete coverage of the reactive silver sites, e.g. step edges, by the porphyrin film. .... 106
- Figure 6-13: Diameter of EBID (solid lines) and EBISA (dashed) dot structures for multilayer (MultiL, black), partial bilayer (BiL, red) and monolayer (MonoL, blue) 2HTPP films on Ag(111) versus applied PE dose. The grey line represents the theoretical size limitation due to the BSE proximity effect. EBID deposits can overcome this limitation by FSE proximity effects. The diameters on MultiL and BiL are almost identical ( $\pm 10 \text{ \%}$ ) for EBID and EBISA, while on the MonoL, the diameter is significantly reduced. In general, the EBID deposits are larger than their EBISA counterparts. .... 108
- Figure 6-14: Summary of EBISA-based nanostructure fabrication results on organic layers on Ag(111). On pristine Ag(111),  $\text{Fe}(\text{CO})_5$  is catalytically decomposed to form a closed film of needle-like Fe crystallites (far right), which can be suppressed by a layer of TPP molecules. When these TPP films are irradiated with a focused electron beam, molecules are chemically modified ( $\text{C}_x\text{H}_y\text{N}_z^*$ ) and the films become active towards the decomposition of  $\text{Fe}(\text{CO})_5$ , which facilitates nanostructure growth. This activation is quenched on the monolayer (middle), presumably due to the close proximity to the Ag(111) support. On bi- and multilayer (left) the first molecular layer effectively decouples the activated molecules from the support and avoids the quenching (left). .... 109
- Figure 6-15: Fabrication and secondary/tertiary growth of nanostructures. The deposits can be fabricated by electron irradiation of a surface in the presence of a precursor (EBID) to form a thin primary deposit (a, top). In the absence of a precursor (a, bottom), some surfaces can undergo selective electron beam induced surface activation (EBISA), also yielding a primary deposit upon post-exposure to the precursor. If the primary deposits are exposed to the precursor in a successive step, autocatalytic decomposition can lead to further secondary autocatalytic growth of the deposit (b). In the case that a different precursor is supplied, tertiary autocatalytic growth can occur, leading to a layered nanostructure (c). The icons in b) and c) will be used to indicate the respective process throughout this publication. .... 112

- Figure 6-16: SEM of  $2 \times 2 \mu\text{m}^2$  deposits prepared by EBID and autocatalytic growth using  $\text{Co}(\text{CO})_3\text{NO}$  on a 100 nm  $\text{Si}_3\text{N}_4$  membrane (a, c) and corresponding high resolution data (b, d). The total PE dose is  $0.55 \text{ C}/\text{cm}^2$ , applied in one sweep with a dwell time of 0.5 ms (a) or in ten sweeps with a dwell time of 0.05 ms per sweep (c). In the single top-to-bottom sweep case (a) the top edge appears brighter and is surrounded by a pronounced bright fringe, while the bottom edge fades into the background. This behavior is attributed to proximity effects caused by electron scattering at already deposited material. In the case of multisweep irradiations, the deposit presents a more uniform distribution of material. The lower dwell time per sweep hinders the formation of a pronounced starting edge deposit, reducing the proximity effects. The high resolution images b) and c) also confirm the granular nature of the autocatalytically grown  $\text{CoO}_x\text{N}_y\text{C}_z$  deposit. The less pronounced granularity observed in d) is attributed to the lower growth time (a/b: 260 min, c/d: 220 min)..... 115
- Figure 6-17: SEM micrograph of square EBID structures of different sizes and primary electron doses (as indicated), prepared on a 100 nm  $\text{Si}_3\text{N}_4$  membrane using  $\text{Co}(\text{CO})_3\text{NO}$ . The structures were prepared in one experimental run, from left to right, top to bottom. After the EBID step, the precursor was further supplied to allow for autocatalytic growth. The total growth time increases from 198 min (bottom right structure) to 230 min (top left structure). The minimum electron dose for detectable deposition is  $\sim 0.05 \text{ C}/\text{cm}^2$ , while a dose of  $0.5 \text{ C}/\text{cm}^2$  marks the start of proximity effect-induced loss of structure definition (fringe surrounding bottom right structure). ..... 116
- Figure 6-18: Nanostructures prepared by EBID plus autocatalytic growth using  $\text{Co}(\text{CO})_3\text{NO}$  on  $\text{Si}_3\text{N}_4$  with different growth times, as indicated below the images. The electron dose during EBID was  $0.2 \text{ C}/\text{cm}^2$  for the structures in the right column of every image; the dose of the lower left square was  $0.1 \text{ C}/\text{cm}^2$ . The insets show higher magnification images of the respective structures directly below. With increasing growth time the images appear brighter, and the granular nature of the deposits is more pronounced..... 117
- Figure 6-19: (left) Co L-edge X-ray absorption spectra of deposits prepared on a  $\text{Si}_3\text{N}_4$  membrane by EBID ( $0.2 \text{ C}/\text{cm}^2$ ) plus autocatalytic growth using  $\text{Co}(\text{CO})_3\text{NO}$ , with different growth times (indicated by colors); the spectra were vertically shifted to a common pre-edge baseline; (right)  $\text{L}_3$  edge of the deposits at an enlarged photon energy scale, along with the spectrum of a Co layer produced by PVD as reference (grey). ..... 118
- Figure 6-20: XAS evaluation of the growth of Co-containing deposits by EBID plus autocatalytic growth upon  $\text{Co}(\text{CO})_3\text{NO}$  dosage. a) Optical density (left vertical axis) and apparent Co thickness (right vertical axis) of  $4 \times 4 \mu\text{m}^2$  squares vs. growth time and PE dose during EBID. b) and d) detailed graphs of the observed growth behavior; the color code identifies the respective data set. c) STXM micrograph (transmitted intensity) of a set of deposits prepared with different PE doses, but the same growth time of  $\sim 160$  min obtained at a photon energy of 780.4 eV. See text for the definition of the apparent Co thickness. .... 121
- Figure 6-21: Optical density at the Fe  $\text{L}_3$  edge at 708.7 eV (left vertical axis) and average thickness of the iron layer (right vertical axis) of various  $\text{CoO}_x\text{N}_y\text{C}_z$  / Fe nanostructures versus autocatalytic growth time for  $\text{Fe}(\text{CO})_5$ . The different symbols indicate different primary electron (PE) doses. Above  $0.05 \text{ C}/\text{cm}^2$ , the thickness/optical density increases linearly with the growth time at a rate of  $0.5 \pm 0.1 \text{ \AA}/\text{min}$  irrespective of the applied PE dose. Lower PE doses (red, black) exhibit reduced thickness. .... 124
- Figure 6-22: Optical density at the Co  $\text{L}_3$  edge and apparent cobalt thickness of  $\text{CoO}_x\text{N}_y\text{C}_z$  layers grown autocatalytically from  $\text{Co}(\text{CO})_3\text{NO}$  on Fe layers plotted against the Fe layer thickness. The Fe layers were prepared by EBID and autocatalytic growth using  $\text{Fe}(\text{CO})_5$ . In a second step,  $\text{Co}(\text{CO})_3\text{NO}$  was dosed for 210 min to produce the  $\text{CoO}_x\text{N}_y\text{C}_z$  layers via (auto-)catalytic decomposition. The optical density and thickness are corrected to account for the absorption of the Fe deposit underneath (see text). The OD of the cobalt containing layer is almost independent of the Fe layer thickness for Fe layers thicker than 4 nm. .... 125
- Figure 6-23: Scheme (left) and image of the reduced-length tubing for the  $\text{Co}_2(\text{CO})_8$  precursor. In the standard setup, the leak valve (A) connects to precursor via the length of the gas line ( $>2$  m). The new setup introduces a T-junction to directly attach the precursor container (C) via a bellows-sealed valve (B) and adds another valve (D) to seal of the remaining gas line during precursor dosing. The length of the line is reduced to about 15 cm. .... 130
- Figure 6-24: SEM images of a Co-rich EBID deposit prepared from  $\text{Co}_2(\text{CO})_8$  (a) and of the non-irradiated a silicon surface (b). The bright square was irradiated with a primary electron dose of  $1.4 \text{ C}/\text{cm}^2$  at a precursor background pressure of  $3.0 \times 10^{-7}$  mbar. Note that the image contrast and brightness cannot be directly compared..... 131

Figure 6-25: Auger electron spectra (as recorded, top, and smoothed & differentiated, bottom) of the nanostructure prepared by EBID using  $\text{Co}_2(\text{CO})_8$  as a precursor (black curves) and of the non-irradiated silicon surface after precursor dosage (red curves). The deposit contains 75% cobalt, approx. 15% carbon and 10% oxygen (+/- 5%)..... 132

## Danksagung

Zum Abschluss möchte ich mich bei allen bedanken, die auf die eine oder andere Weise zum Gelingen dieser Arbeit beigetragen haben.

Als erstes gilt mein Dank Herrn Professor Dr. Hans-Peter Steinrück und PD Dr. Hubertus Marbach für die Chance, diese Doktorarbeit am Lehrstuhl für Physikalische Chemie II in der EBID-Gruppe anzufertigen. Die offenen Gespräche und wissenschaftlichen Diskussion waren immer hilfreich und haben einen großen Beitrag zum Erfolg dieser Arbeit geleistet.

Weiterhin gilt mein Dank der EBID-Gruppe: Thomas Lukasczyk, Michael Schirmer, Marie-Madeleine Walz, Martin Drost und Fan Tu, sowie Andreas Späth für seine Hilfe bei den Synchrotronexperimenten. Ohne die großartige Arbeitsatmosphäre und den heiteren, traurigen, spannenden, langweiligen, interessanten und vor allem freundschaftlichen Momenten wäre die Zeit nur halb so schön gewesen.

Aus dem gleichen Grund möchte ich auch bei allen aktuellen und ehemaligen Kollegen und Freunden am Lehrstuhl für die schöne Zeit, die Gespräche, die Begegnungen, die Feiern, die Unterstützung in allen Belangen und die vielen, vielen gemeinsamen Tassen Kaffee bedanken. Besonders erwähnen möchte ich Hans-Peter Bäumler und Bernd Kreß, deren allzeit kompetente und prompte Hilfe bei technischen Schwierigkeiten unersetzlich ist. Mein Dank gilt auch dem Werkstattteam, das die vielen kleinen Projekte und Umbauten möglich gemacht hat.

Bei der Studienstiftung des deutschen Volkes und der Graduate School Molecular Science (GSMS) der FAU Erlangen-Nürnberg möchte ich mich für die Förderung während der Doktorarbeit bedanken.

Abschließend möchte ich mich bei meinen Eltern, meinem Bruder und meinen Freunden bedanken, die mit mir diesen Weg gegangen sind, immer ein offenes Ohr hatten und ohne die diese Arbeit unmöglich gewesen wäre.